https://ntrs.nasa.gov/search.jsp?R=19750012093 2020-03-23T00:07:54+00:00Z

NASA TECHNICAL MEMORANDUM

December 1974

NASA TM X-64882

MSFC SKYLAB GROUND-BASED ASTRONOMY PROGRAM

Skylab Program Office

FEB 1975
RECEIVED
NASA STI FACILITY
INPUT BRANCH

NASA

George C. Marshall Space Flight Center

Marshall Space Flight Center, Alabama

(NASA-TM-X-64882) MSFC SKYLAB GROUND-BASED ASTRONOMY PROGRAM (NASA) 324 p HC $9.25 CSCL 03A

N75-20165

Unclas

G3/89 09687

MSFC - Form 3190 (Rev June 1971)

TECHNICAL REPORT STANDARD TITLE PAGE

1. REPORT NO. NASA TMX-64882	2. GOVERNMENT ACCESSION NO.	3. RECIPIENT'S CATALOG NO.
4. TITLE AND SUBTITLE MSFC Skylab Ground-Based Astronomy Program		5. REPORT DATE December 1974
		6. PERFORMING ORGANIZATION CODE
7. AUTHOR(S) B. J. Duncan		8. PERFORMING ORGANIZATION REPORT #
9. PERFORMING ORGANIZATION NAME AND ADDRESS George C. Marshall Space Flight Center Marshall Space Flight Center, Alabama 35812		10. WORK UNIT NO.
		11. CONTRACT OR GRANT NO.
		13. TYPE OF REPORT & PERIOD COVERED Technical Memorandum
12. SPONSORING AGENCY NAME AND ADDRESS National Aeronautics and Space Administration Washington, DC 20546		14. SPONSORING AGENCY CODE

15. SUPPLEMENTARY NOTES

Prepared by Space Sciences Laboratory

16. ABSTRACT

The Skylab Ground-Based Astronomy Program (SGAP) was conducted to enhance the data base of solar physics obtained during the Apollo Telescope Mount (ATM) mission flown in conjunction with the Skylab orbital station. Leading solar physicists from various observatories obtained data from the ground at the same time that orbital data were being acquired by ATM.

The acquisition of corollary solar data from the ground simultaneously with the ATM orbital observations helped to provide a broader basis for understanding solar physics by increasing spectral coverage and by the use of additional sophisticated instruments of various types. This report briefly describes the individual tasks and the associated instrumentation selected for this ground-based program and contains as appendices, the final reports from the Principal Investigators.

17. KEY WORDS Apollo Telescope Mount, Photoheliograph, Telescope, X ray, Spectrograph, Spectrometer, Spectrophotometer, Coronagraph, Spectroheliogram	18. DISTRIBUTION STATEMENT Unclassified - Unlimited Bill J. Duncan B. J. Duncan

19. SECURITY CLASSIF. (of this report) Unclassified	20. SECURITY CLASSIF. (of this page) Unclassified	21. NO. OF PAGES 324	22. PRICE NTIS

MSFC - Form 3292 (Rev December 1972)

For sale by National Technical Information Service, Springfield, Virginia 22151

Table of Contents

		Page
Abstract		i
Acknowledgment		ii
Table of Contents		iii
List of Figures and Tables		iv
Section 1	Introduction	1
Section 2	University of Hawaii Multichannel Coronal Spectrophotometer	6
Section 3	LMSC Spectra-spectroheliograph	10
Section 4	NBS Radiometer Calibrations of ATM Experiments	14
Section 5	CIT Vacuum Photoheliograph	17
Section 6	LMSC Filter Studies in HeI and CaII at Rye Canyon	21
Section 7	UCSD Solar Infrared Observations	24
Section 8	LMSC Studies of Helium Emission in Visible and UV	26
Section 9	Uttar Pradesh Observatory Molecular Line Observations	27
Section 10	Johns Hopkins Radio Burst Spectral Observations	29
Appendix A	University of Hawaii Final Report	35
Appendix B	LMSC Spectra-spectroheliograph Final Report Volume I	62
Appendix C	CIT Final Report	120
Appendix D	LMSC Filter Studies - Final Report	138
Appendix E	UCSD Report, "Direct Observation of Temperature Amplitude of Solar 300-Sec. Oscillations	179
Appendix F	LMSC Helium Emission Studies - Final Report	187
Appendix G	Johns Hopkins Solar Radio Observations - Final Report	285

PRECEDING PAGE BLANK NOT FILMED

List of Figures & Tables

		Page
Figure 1.1	Spectral Relationships	5
Figure 2.1	Mees Solar Observatory	7
Figure 2.2	Coronal Spectrophotometer	7
Figure 2.3	Optical System	8
Figure 3.1	S^2HG Data Collection System	11
Figure 3.2	Typical S^2HG Solar Spectra	11
Figure 3.3	S^2HG Data Reduction System	13
Figure 5.1	26-inch Photoheliograph Assembly	18
Figure 5.2	Optical Layout of 65cm Telescope	19
Figure 5.3	Big Bear Lake Observatory	20
Figure 6.1	Lockheed Solar Spars	22
Figure 7.1	UCSD Telescope at Mt. Lemmon, Arizona .	25
Figure 10.1	Block Diagram of the 565-1000 MHz High Time Resolution Solar Spectrum Analyzer	30
Figure 10.2	Solar Radio Burst Spectrum	31
Figure 10.3	APL Sixty-Foot Radio Burst Antenna . . .	32
Table 1.1	Project Summary Chart	2

SECTION 1. INTRODUCTION

After the National Aeronautics and Space Administration (NASA) Office of Space Science (OSS) announcement of opportunities for participation in the Apollo Telescope Mount (ATM) solar physics mission on Skylab in January 1971 and the receipt of resultant proposals, an ad hoc committee of solar scientists from throughout the United States selected a number of efforts to be pursued. These programs involved some X ray-instrumented rocket flights as well as the ground-based observational efforts that the Marshall Space Flight Center (MSFC) was asked to manage. The rocket flight tasks were managed directly from NASA headquarters.

Because of its scientific nature, the Skylab Ground-Based Astronomy Program (SGAP) was assigned to MSFC's Space Sciences Laboratory, where the author was project manager, Dr. Mona Hagyard was project scientist, and individual task scientists (see Table 1.1) were responsible for the selected efforts as contracting officer's representatives (COR).

Nine tasks were funded, with the participating astronomical observatories and their associated projects as follows:

A. The University of Hawaii constructed a photoelectric differential coronal photometer for an observational investigation of coronal active regions. This instrument measures simultaneously the intensities of several visible coronal lines suitably chosen for their diagnostic properties. Physical properties are studied to determine from this primary data the rates of energy loss and gain from the active regions and the effects of flare events on the corona. The Principal Investigator (PI) was Dr. John Jefferies.

B. Lockheed Missiles and Space Company (LMSC) operated, at Kitt Peak Observatory's McMath solar telescope, a system called spectra-spectroheliography that is capable of mapping the physical parameters of the solar atmosphere. In addition to the Kitt Peak solar telescopes and vacuum spectrograph, a wide-exit aperture and a specially constructed movie camera capable of rapid film advance were used to obtain spectral maps of regions of the solar disk with high spatial resolution (to one-half arc second). A high-speed microdensitometer-computer system was added to allow rapid analysis of the spectral data to obtain solar velocity and magnetic field maps of regions of interest. Dr. Alan Title was the Principal Investigator.

C. The National Bureau of Standards (NBS) was to upgrade calibration capabilities in support of ATM-related measurements as a part of the SGAP program in the following areas:

1. A hydrogen arc source of known radiant flux for the calibration of spectrometric-detector systems over the region of 500 to 3700 Å was developed.

INSTITUTION	INVESTIGATOR	DESCRIPTION	CONTRACTING OFFICER REPRESENTATIVE
University of Hawaii	Jefferies	Construction & operation during ATM of photo-electric differential coronal photometer in various simultaneous visible lines.	J. McGuire
Lockheed Missiles and Space Company	Title	Addition of microdensitometer/computer system to S^2Hg & modeling of solar data.	B. Duncan
National Bureau of Standards	Wiese - Madden	Develop H_2 arc UV calib. source (500-3700Å). Study contamination effects on photocathode response in VUV (500-1500). Develop synchrotron calib. capability (600 - 200 Å).	R. Linton
California Institute of Technology	Zirin	Construct equatorial mount and vacuum system, & install 65 cm FVU photoheliograph at Big Bear. Purchase and install at Big Bear, filter & IR vidicon for 10830 Å He & 3933 Å Ca-K line filtergrams.	E. Reichmann
Lockheed Missiles and Space Company	Martin-Ramsey	Observations of D_3 line of HeI (5876 Å) (photographic). Filter studies in CaII (8542 Å).	E. Miller
University of California at San Diego	Hudson	Construct beam switching radiometer for the 60" Mt. Lemon telescope for meas. at 1 mm - 1 u & observations during ATM.	W. Fountain
Lockheed Missiles and Space Company	Kulander	Theoretical study of He emission in visible ($HeI-_{D3}$@5876 Å) and UV (HeI @ 584 & 537 Å).	Dr. Hagyard
Uttar Pradesh State Observation (India)	Pande	Equipment procurement & loan to allow observations for molecular line studies.	E. Miller
Johns Hopkins University	Gotwols	Observation & analysis of 565-1000 MHz spectra from APL 60' dish.	C. Baugher

Table 1.1 Project Summary Chart

2. A study was conducted to determine the effects on photocathodes caused by the removal or addition of monolayers of contaminants in vacuum; the wavelength region of interest was 500 to 1500 Å.

3. A capability was established for radiometric calibration by utilization of the NBS synchrotron facility. Windowless diodes were developed as transfer standards in this spectral range. Drs. W. Wiese and R. Madden were the Principal Investigators.

D. The California Institute of Technology installed the 65-cm FVU (functional verification unit) photoheliograph at its observatory at Big Bear Lake in California. The installation of the new vacuum photoheliograph provides Big Bear with a large-aperture telescope capable of fully exploiting the site's excellent observing conditions. The new unit was used in conjunction with ATM for extremely high resolution studies of active regions. Provisions were made for use of various cameras and detector systems as well as feeding a vacuum spectrograph at the Coudé focus. Filtergrams were made in lines extending from the 3933 Å calcium K-line to the 10830 Å helium line. Dr. Harold Zirin was the Principal Investigator.

E. The Lockheed Solar Observatory at Rye Canyon prepared both of its spar telescope systems for observations during the ATM mission. On one spar, studies in the D_3 line of HeI were to direct attention to observing solar flares and transient events during periods of high disk activity and to prominence observations during periods of low disk activity. On the other spar, a telescope was fitted with a filter for high resolution photographic studies in CaII at 8542 Å. This line is believed to originate at a higher level in the solar atmosphere than the H-α line and should be extremely valuable in relating the ATM X ray and XUV data to filtergrams and spectroheliograms taken at wavelengths originating at lower levels in the chromosphere. Drs. S. Martin and H. Ramsey were the Principal Investigators.

F. The University of California at San Diego built a beam-switching photometer system for infrared observations of solar flares. The observing site is at Mt. Lemmon, Arizona, with observations to extend from the 700-μ region down to possibly 1 μ, utilizing the 60-inch Cassegrainian telescope. These infrared continuum observations should define the solar spectrum well enough to allow differentiating among the major theories of white-light flare emission. Dr. Hugh Hudson was the Principal Investigator.

G. The LMSC at Palo Alto, California, conducted a theoretical study of helium visible and ultraviolet emissions from solar active regions. Calculations of the statistical equilibrium populations for a 19-level HeI and a 10-level HeII ion were performed. Results of these studies should allow the interpretation of line observations in terms of electron density and temperature profiles for the active regions. Dr. J.L. Kulander was the Principal Investigator.

H. The Uttar Pradesh State Observatory in India was to study dissociation and excitation equilibria of various molecules in the photosphere, spots, and faculae. Detection equipment was supplied to India on loan for an observational program using their existing horizontal solar telescope and its associated spectrograph, with the goal of improving available models of the solar atmosphere parameters which influence these studies. Dr. M. C. Pande was the Principal Investigator. No final report was required from this effort, although publications in the scientific journals are anticipated.

I. The Applied Physics Laboratory (APL) of Johns Hopkins University performed, during the ATM mission, an observational program of high time-resolution spectral observations of solar radio bursts in the 500- to 1000-MHz range. With the 0.01 sec time resolution available from their spectrograph and 60-ft diameter antenna, it should be possible to determine whether a finite frequency drift rate is present in the radio bursts. This, in turn, would affect models of the emission mechanism and electron densities in the source region. Mr. B. Gotwols was the Principal Investigator.

The nature of the SGAP program was to provide corollary data for postmission analyses in conjunction with the ATM. As such, it complements those programs, such as the National Oceanic and Atmospheric Administration (NOAA) effort, which were designed to provide the real-time, or near-real-time, data required by the ATM mission.

The ATM instruments were designed to take advantage of orbital altitude to obtain data in the X ray and ultraviolet portions of the spectrum where atmospheric absorption limits observations from the earth. The SGAP observations extended the spectral coverage of events observed by the ATM by utilizing atmospheric windows in the visible, microwave, and infrared portions of the spectrum. Figure 1.1 shows the spectral ranges covered in relation to each other.

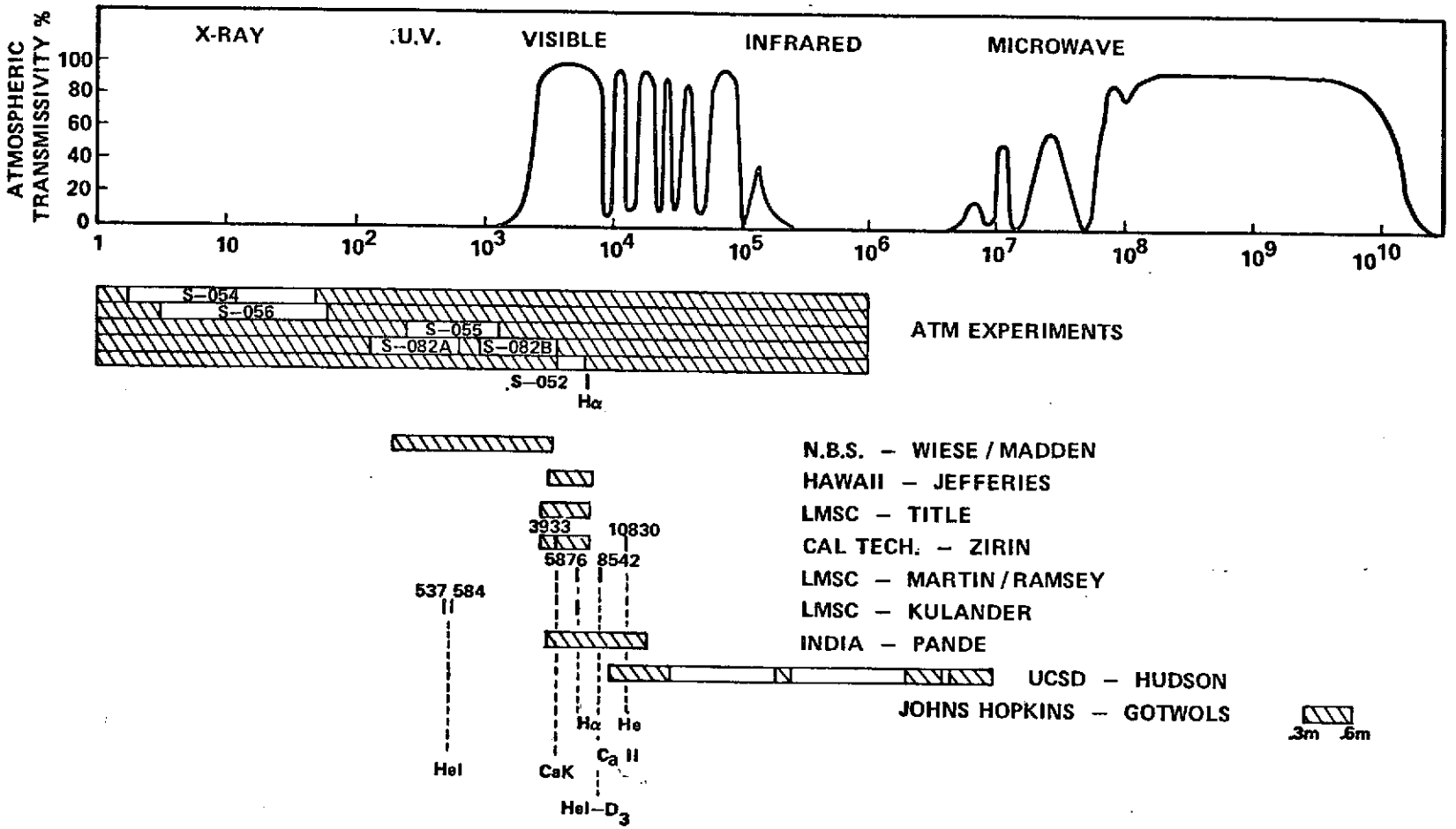

Figure 1.1 Spectral Relationships

SECTION 2. UNIVERSITY OF HAWAII MULTICHANNEL CORONAL SPECTROPHOTOMETER

The Principal Investigator for this experiment was Dr. John T. Jefferies, with Drs. Frank Orrall, Jack Zirker, and Don Landman as co-investigators. The University of Hawaii instrument measured forbidden line (magnetic dipole) radiation in the visible and near infrared spectral regions from some of the same ions that emit the permitted line radiation observed by the ATM instruments. A number of prominence line intensities with temporal and spatial resolutions comparable to that of the ATM equipment are measured. Selected line intensities, together with neighboring sky and continuum background, were digitized and recorded on magnetic disk while the spectrophotometer scanned the image of a coronal region. In this way, simultaneous, monochromatic, high spatial and temporal resolution coronal region images were obtained. The data, reduced in real-time with a PDP 11/45 computer system, were then available for immediate analysis. Certain forbidden line ratios are sensitive to electron density changes over relatively narrow temperature ranges while other line ratios are insensitive to density and may be used to fix the temperature or composition. Diagnostic methods utilizing line ratios have been developed and applied by the experimenters. The temperature, density, and composition of the active regions can thus be determined, thereby providing inputs for physical models of the active regions as functions of time and activity. These physical models can be used to determine the rates of energy loss by radiation and conduction, and the coronal energy balance can be studied.

The apparatus was designed to record simultaneously many 0.33μ to 1.1μ line intensities in order to eliminate systematic errors in obtaining line intensity ratios resulting from seeing and sky transparency fluctuations during a measurement. The spatial resolution obtainable by the instrument is on the order of 5 arc seconds. The instrument's relatively high temporal resolution capability enables following closely the time variations of physical properties of active regions.

Figure 2.1 is an overall view of the instrument. It is roughly 25 cm in diameter by 4.4 m long and is mounted on one face of the 3.6-m spar at the Mees Solar Observatory (Figure 2.2). The gimbal mounting allows programmed spatial scanning within 3 $R_\odot$ with the stepping motor translation drives designed to provide 1.66 arc second/step motions. Scanning is under computer control so that rectangular, circular, etc., rasters can be programmed and used as desired.

The optical system, shown schematically in Figure 2.3, consists of a coronagraph telescope, reimaging optics, component wheel, spectrometer, and shutter/sun-positioner. The detector is a thermoelectrically cooled silicon vidicon camera tube placed at the spectrometer's output focal plane, located behind the spectrometer. After exposure, the duration of which can be arbitrarily selected, the target is read out in a slow-scan mode (approximately 2 seconds/frame), with the video signals amplified, digitized, and routed via CAMAC to the computer. Any pixel set (up to 256 x 384 at 12 bits/pixel) can be selected by the program

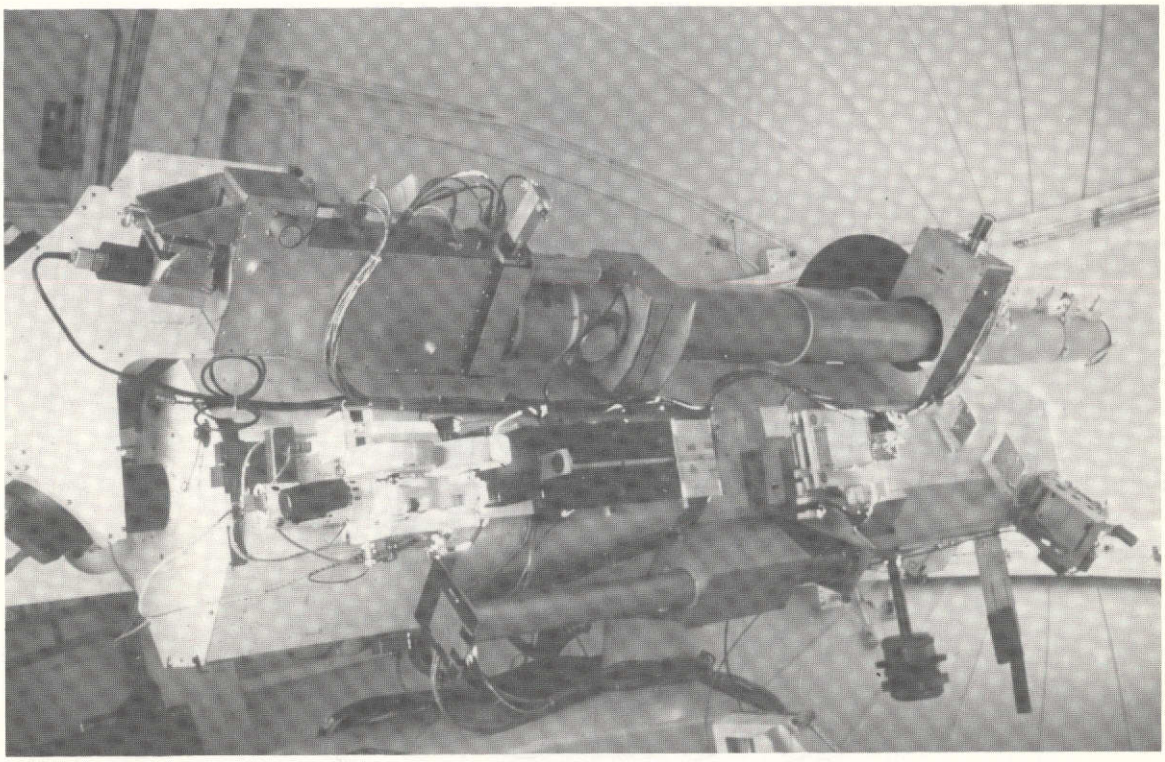

Figure 2.1 Coronal Spectrophotometer

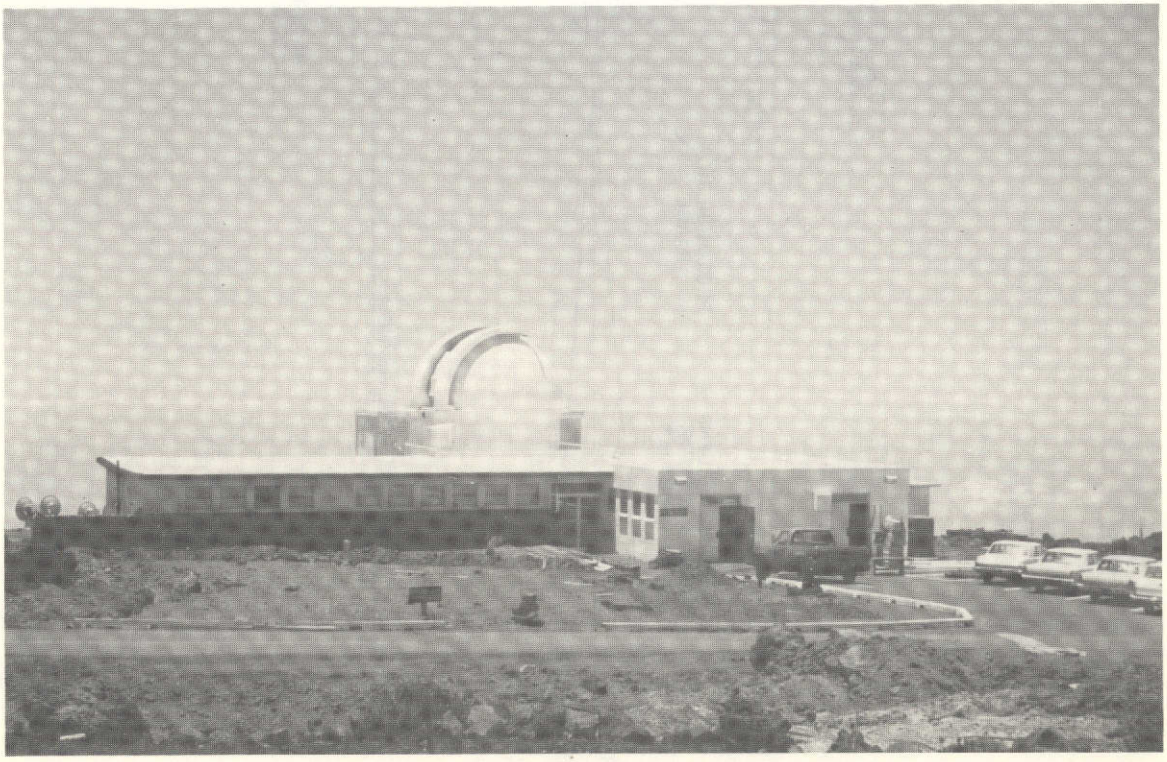

Figure 2.2 Mees Solar Observatory

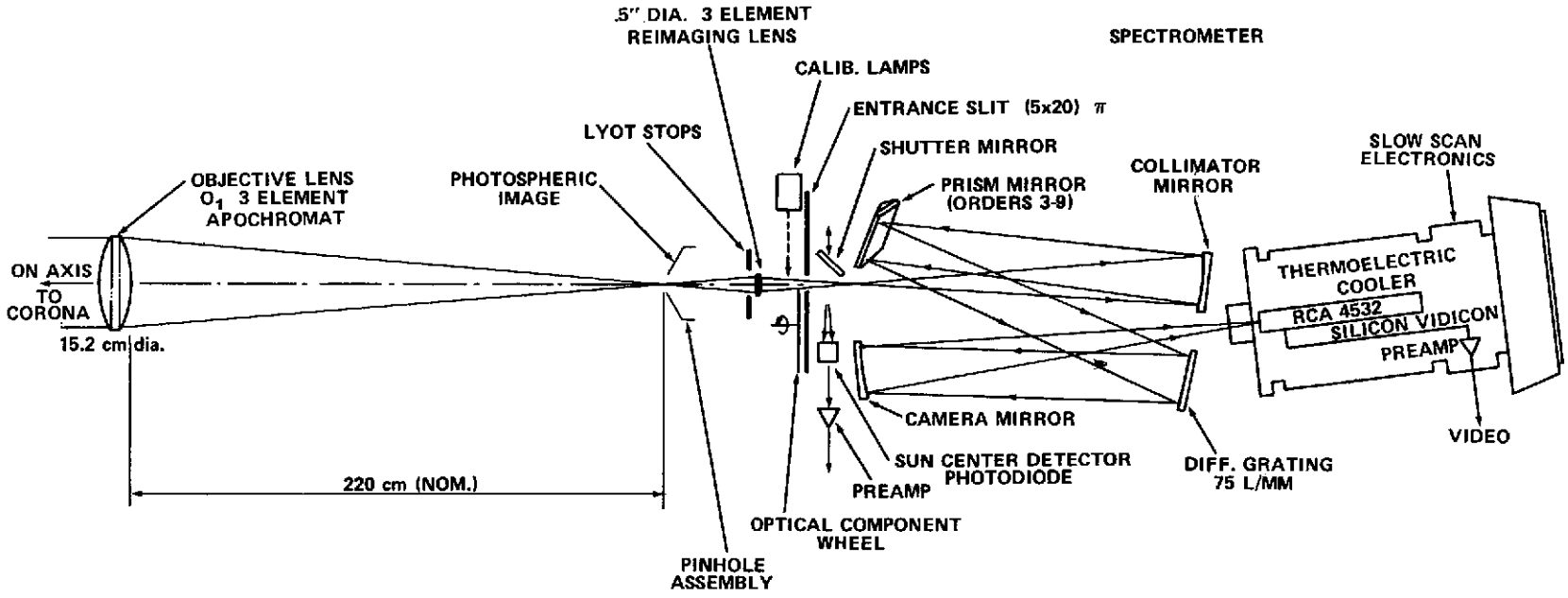

Figure 2.3 Optical System

for processing. The data acquisition and control system (DACS) is configured around a PDP 11/45 computer with 24K words of memory. Peripherals include teletype, line printer, DEC tape, and disk units. All other interfacing, such as CRT display, motor controls, etc., is via a CAMAC system to take advantage of data-way standardization. The DACS control functions include: telescope pointing; vidicon exposure, read-out, and erasure; pixel selection and data transfer; and on-line reduction with associated CRT displays. A more complete instrumentation description is contained in Appendix A.

SECTION 3. LOCKHEED SPECTRA-SPECTROHELIOGRAPH

Dr. Alan Title was the Principal Investigator for this effort involving spectra-spectroheliography (S^2HG), an extension of spectroheliography (SGH). In both S^2HG and SHG, the solar image is moved with respect to the entrance slit of a spectrograph and recorded on film which is simultaneously being moved with respect to the exit slit. The most important difference is that S2GH records a wide spectral region and SHG records only a narrow band of wavelengths. Following is a brief description of the system's operation, taken largely from Dr. Title's original experiment proposal.

Ordinarily, spectroheliograms are made by fixing both the film and the sun's image and moving the spectrograph. Exposure is through a narrow exit slit. The result is a photograph of the sun with variations in density representing variations in the intensity of solar radiation (integrated over a small fixed wavelength band). It is difficult to determine from a single spectroheliogram whether these changes in density are due to Doppler shifts, Zeeman splittings, or variations in continuum intensity or line strength. Various techniques using combinations of spectroheliograms have been developed in an attempt to distinguish physical effects. The S^2HG system allows simultaneous collection of the data needed for these various studies.

The S^2HG spectrograph (Figure 3.1) has a wide exit aperture and a digitally controlled, stepping motor driven movie camera capable of rapidly advancing the film. In recording spectra, the spectrograph remains stationary and the sun's image is allowed to drift past the entrance slit. A single frame of the film is exposed while the sun moves a fixed distance with respect to the entrance slit. The film is then rapidly advanced and the next frame exposed. Thus, S^2HG spectra are recorded in a series of frames on the film, each frame containing the entire spectral profile along a line on the sun's disk (Figure 3.2). Since successive frames contain spectral profiles for adjacent solar regions, the film contains the spectral line profile for each position on a two-dimensional grid on the solar disk. By inserting quarter or half-wave plates and a polarization-dependent beam splitter into the system, one obtains spectral profiles in polarization pairs, as shown in the figure.

If a line displays a Zeeman effect and the spectra have been recorded in right and left circular polarizations, longitudinal magnetic field maps can be constructed. If Zeeman sensitive lines are photographed in several pairs of linear polarizations, then transverse magnetic field maps can be constructed. S^2HG magnetic field maps yield resolutions as high as one-half arc second under favorable seeing conditions.

Velocities to about 7 meters per second absolute can be measured by comparing the spectra against a standard line inserted into the spectrograph by a laser or atomic absorption cell. Operating in the velocity field mode, the S^2HG observations cover a region of 1 x 2 arc minutes in

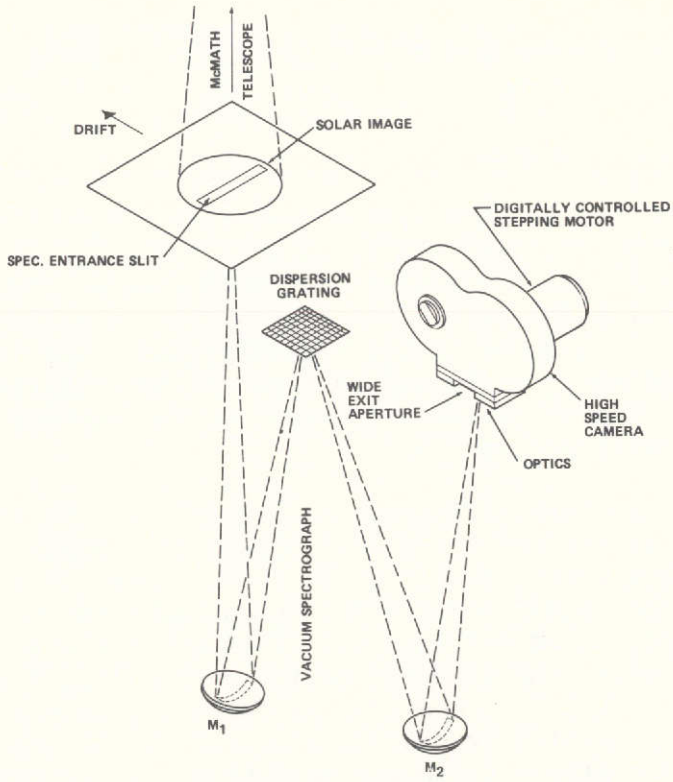

Figure 3.1 S^2HG Data Collection System

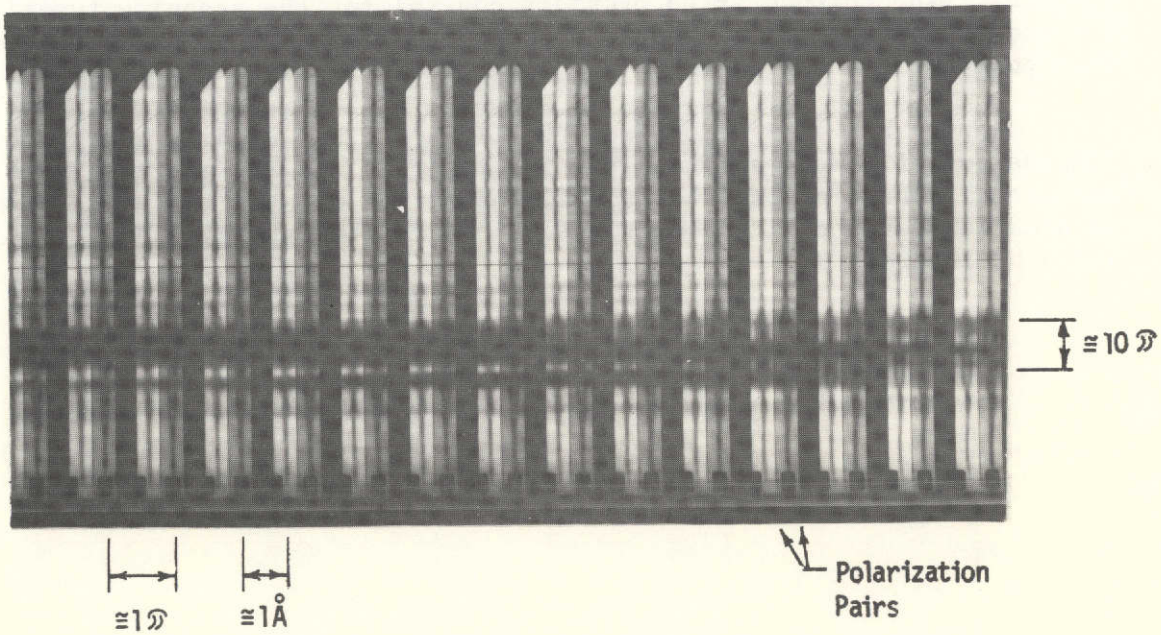

Figure 3.2 Typical S^2HG Solar Spectra

less than 15 seconds. This enables studying the velocity field development in regions of substantial physical extent. Using beam splitters and folding optics allows simultaneous recording of spectra of two or more lines formed at different heights for studies of changes in phase and amplitude with height.

The S^2HG cameras were mounted on instruments at the McMath Solar Tower at Kitt Peak National Observatory in Arizona. At Kitt Peak the large spectrograph has a dispersion of 0.14 Å/mm at λ5250 (5th order), so that 20μ corresponds to 0.00276 Å at λ5250. A shift of 20 microns corresponds to 71 gauss or to 157 meters/second. The location of the peaks can be reliably determined to a micron by comparison with adjacent points, so that fields could be measured to an accuracy of 3.5 gauss and velocity of 7 meters/second.

Due to a fortunate coincidence, fifth order Fe λ5250.2 (5 x 5250.2 = 26251.0) and fourth order H-alpha λ6562.8 (4 x 6562.8 = 26251.2) are nearly coincident in the spectrograph focal plane. Hence, a dichroic beam splitter that separates red and green light and the normal polarization beam splitter used for magnetic field studies make it possible to simultaneously study the spectral region surrounding H-alpha and the magnetic field in λ5250. When S^2HG is operating in the H-alpha mode, it is possible to conveniently study a spectral region 3.3 Å wide, centered on H-alpha, which allows following velocities in H-alpha for ± 75 km/second.

The S^2HG film is scanned by a Photometric Data Systems Model 1010G microdensitometer whose output is encoded digitally and fed to a PDP 11/45 computer. The computer also provides control for the scanning functions. The microdensitometer is capable of scanning some 6000 points per second, with positional encoding to an accuracy of one micron.

Appendix B is Section I of Dr. Title's final report, containing discussions of theory and results. Sections II and III of the report are not included herein, but they contain operation manuals and programming information for the microdensitometer and computer system, should outside users be interested.

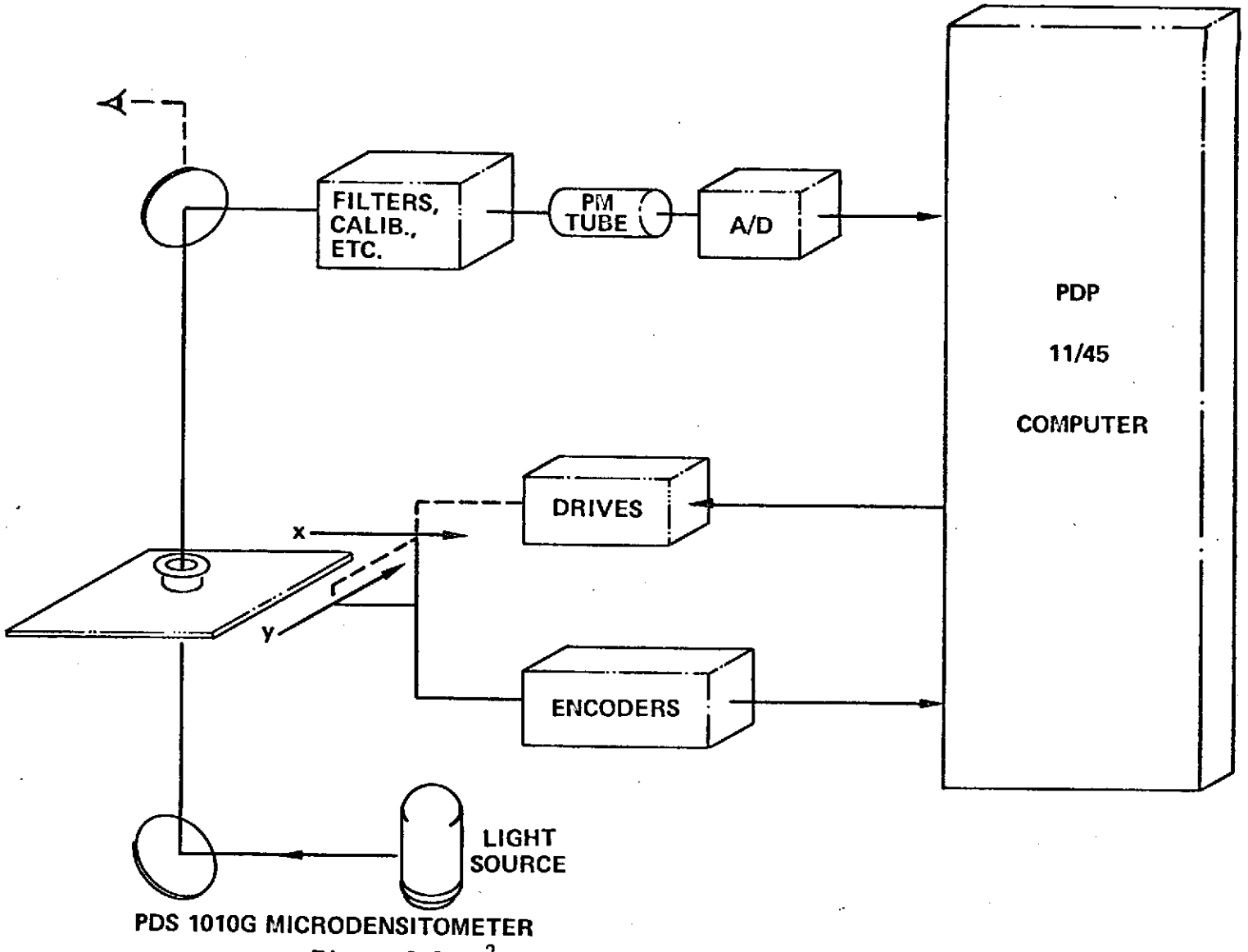

Figure 3.3 S^2HG Data Reduction System

SECTION 4. NBS RADIOMETRIC CALIBRATION OF ATM EXPERIMENTS

The National Bureau of Standards participated in the SGAP program, although not for ground-based observations per se, but rather to enhance their capabilities to provide calibration services to the ATM and its associated rocket programs in the ultraviolet wavelength region.

The NBS effort was divided into three distinct phases as follows:

A. Continued development work on a hydrogen arc plasma source of known radiant flux for the calibration of spectrometric-detector systems over the wavelength region of 500 to 3700 Å.

B. The second part of the program was a study of the effect of ultra-high vacuum and particular contaminants on the sensitivity of photocathodes in the windowless region of the vacuum ultraviolet (VUV). These investigations of the cause of observed changes in windowless photomultiplier response in space help establish a greater integrity of calibration from the laboratory to a space environment.

C. The third part of the program was the development of calibration capability at the NBS Synchrotron Ultraviolet Radiation Facility (SURF) for the purpose of extending radiometric calibrations to shorter wavelengths. For certain applications the calculability of this source can be utilized for direct calibrations. Also, work was done toward the development of diode detectors as transfer standards for the wavelength region shorter than 600 Å.

The H_2 arc is capable of producing accurate continuous emission in the VUV at reasonable temperatures. The known frequency distribution of the continuum emitted from a pure hydrogen plasma, with the emissivity exactly calculable, allows calibrations using the continuum intensities at any wavelength, with accuracies dependent on the accuracy of the plasma diagnostics. Extensive numerical calculations of the continuous emission of hydrogen from 950 Å to 3650 Å have been performed by NBS under the assumption that a hydrogen arc plasma is in local thermal equilibrium (LTE) and at atmospheric pressure. The accuracy of the calculations is estimated to be within 2 percent. The main uncertainty originates from the high density plasma corrections.

The arc was initially operated at 13,000 °K, being an excellent standard down to about 1600 Å where molecular Lyman band emission begins. Atomic line radiation is also present from a few Lyman lines in the 1216 Å to 950 Å region. Modification of the arc for operation at higher temperatures up to 25,000 °K allowed an extension of the calibration range down to 1100 Å in that the molecular line emission became insignificant due to dissociations.

The arc is wall-stabilized by a stack of electrically insulated, water-cooled disks with an axial bore of a few millimeters. Ring electrodes allow emission to be observed axially. Provision is also made for side-on observations. For wavelengths below 1100 Å, the LiF window is removed, requiring a differential pumping system. Measurements are then possible down to about 500 Å, although inaccuracy increases as wavelength decreases.

Utilizing the H_2 arc, calibration should be reliable to an accuracy of about 15 percent from 1650 Å through 6000 Å. Inaccuracy will increase as wavelength decreases to about 25 or 30 percent at 500 Å wavelength.

The photocathode contamination study's objective was to understand the effects on the performance of photocathodes caused either by removal or addition of surface monolayers of contaminating substances. The tests were carried out in vacua of 10^{-10} torr, over the wavelength region 500 to 1500 Å, and include the energy analysis of the photo-emitted electrons for diagnostic purposes. A number of contaminating gases were used with the element tungsten as a VUV calibration detector on the photocathode. Tungsten was used since its physical properties are well known. Induced contaminants included the common gases O_2, H_2, N_2, etc., and such things as methanol, aldehydes, acids, esters and ketones.

Surfaces were prepared in the atomically-clean state and, subsequently, exposed to controlled amounts of known contaminating gases measuring concurrently the changes in photoelectron yield. The main constituents evolved during the outgassing of space plastics were of relatively high molecular weights. However, contamination effects of these species can probably be partially understood by a study of these related lighter hydrocarbons. During these experiments, the energies of the photoelectrons were measured to determine both the cause of the changes in yield which are observed and the origin of the photoelectrons (e.g., the photocathode proper or the contaminating layer).

Results of these studies have application to contamination of such photocathodes used as photomultipliers for the far (windowless) ultraviolet when exposed to outgassing of various space vehicle sources and to the "clean-up" of such surfaces as the exposure to the hard vacuum of space continues.

NBS has a unique facility which allows the sample photocathode to be exposed to far UV radiation in the windowless region without destroying the required hard vacuum. It consists of a gas discharge light source connected through a two-stage differential pumping unit to a high vacuum-normal-incidence VUV monochromator. This monochromator, of stainless steel with metal O-rings, has a 10-inch diffusion pump. The bakable experimental chamber fastens to the exit slit of the monochromator and, with a high-speed pump and LN_2 baffle, maintains 1×10^{-10} torr with the light source

running. A sample manipulator allows two samples to be studied simultaneously and independently heated for cleaning. An electron energy analyzer is a part of the main experimental unit.

The third part of the NBS program was to establish a capability for the radiometric calibration of ATM experiments from 600 Å to 200 Å by utilization of the NBS Synchrotron Ultraviolet Radiation Facility (SURF). The approach was two-pronged: First, calibration procedures were developed using synchrotron radiation as a calculable standard source of flux for experiments where this approach is feasible; and second, synchrotron radiation was utilized as a continuum light source with a monochromator and an absolute detector for the calibration of transfer standard diode detectors.

Synchrotron radiation is a strong source of continuum radiation which is highly collimated (f/360), linearly polarized and of calculable intensity, assuming that the number of electrons circulating (electron current) is known. This effort involved determination of the electron current as a measure of the proportional radiation intensity, and careful definition of the photon beam collection geometry. Also involved was the fitting of a test port with a grazing incidence monochromator which is rotatable about the optic axis--required by the polarization of the beam and optical systems to be tested--and the associated test fixtures and electronics.

The high collimation of synchrotron radiation requires optical systems of large angular aperture to be scanned. These problems may restrict the instruments for which this calibration technique is applicable. In the second approach SURF acts as the continuum source of VUV flux to be used for the calibration of transfer standard detectors. The NBS currently supplies two types of photodiodes, one with a window for the wavelength region of 1200 Å up to 2400 Å, and a windowless one extending from about 1200 Å down to below 600 Å. This effort involved development of a transfer standard to extend calibration to shorter wavelengths. Work concentrated on Al_2O_3 photocathodes because of their comparative stability of photoelectron yield with temperature. The primary standard for diode testing is a specially constructed double-ionization chamber. Aluminum itself is transparent to this short wavelength radiation; hence, the oxide is used to eliminate natural oxidation and resultant change of photoelectric yield with time.

SECTION 5. CAL TECH VACUUM PHOTOHELIOGRAPH

The California Institue of Technology had a twofold effort in the SGAP program: mounting the 26-inch photoheliograph functional verification unit, including its own specially constructed vacuum tank onto the telescope mount yoke at Big Bear Lake Observatory, and the construction and placing into operation of a special new birefringent filter for observations in the 10830 Å line of helium. Dr. Harold Zirin was the Principal Investigator for this effort, and Richard Proutt was the experiment manager.

Among the necessary efforts in the study of Solar Physics is the observation and understanding of successively smaller structural detail on the sun's surface. The Big Bear Lake site was selected initially for its excellent "seeing" conditions and the fact that some of the best resolution work to date had come from that site. Installation of the 26-inch photoheliograph was intended to take advantage of this "seeing" by providing good optics with a large aperture.

The 26-inch photoheliograph is a Gregorian telescope which was expressly designed for future space flights. The instrument (Figure 5.1) was built as a functional verification unit with special attention to reducing the effect of solar heating on the various mirrors. The paraboloidal primary mirror is coated with a special high reflectance silver coating which greatly reduces thermal distortion of the shape of the primary mirror. An image of the sun is formed at a diagonal heat stop mirror which rejects all the solar energy except that from a small field approximately 5 arc minutes on the side which is only 3.3 percent of the sun's area. This image is then enlarged by an ellipsoidal secondary mirror and reflected by two diagonal mirrors which direct the image to a location where it may be studied (Figure 5.2). The entire instrument, up to the cameras, is enclosed in a vacuum tank with a vacuum entrance window and exit windows so that all effects due to air currents inside the telescope structure may be eliminated. The vacuum tank was mounted in the existing fork mounting at the Big Bear Solar Observatory, along with two other vacuum telescopes, a 10-inch refractor and an 8.6-inch refractor, which simulated the ATM hydrogen-alpha telescope. The beam from the 26-inch telescope may either be utilized directly or may be diverted through a pair of mirrors to the Coudé focus of the telescope, where a powerful Littrow spectrograph enables spectrograms to be made of various selected features on the sun. Alternate observations using narrow-band birefringent filters with spectrograph observations and observations using a video magnetograph allow the determination of magnetic fields in near real time. Another instrument used with the 26-inch system is the universal birefringent filter which enables observations in any spectral line from 4000 to 7000 angstroms. These systems obtain long-term observations of the various features that were observed from the ATM so that their background, history, and fine structure can be better understood. The 26-inch photoheliograph is theoretically capable of resolution down to 0.2 arc seconds at H-alpha.

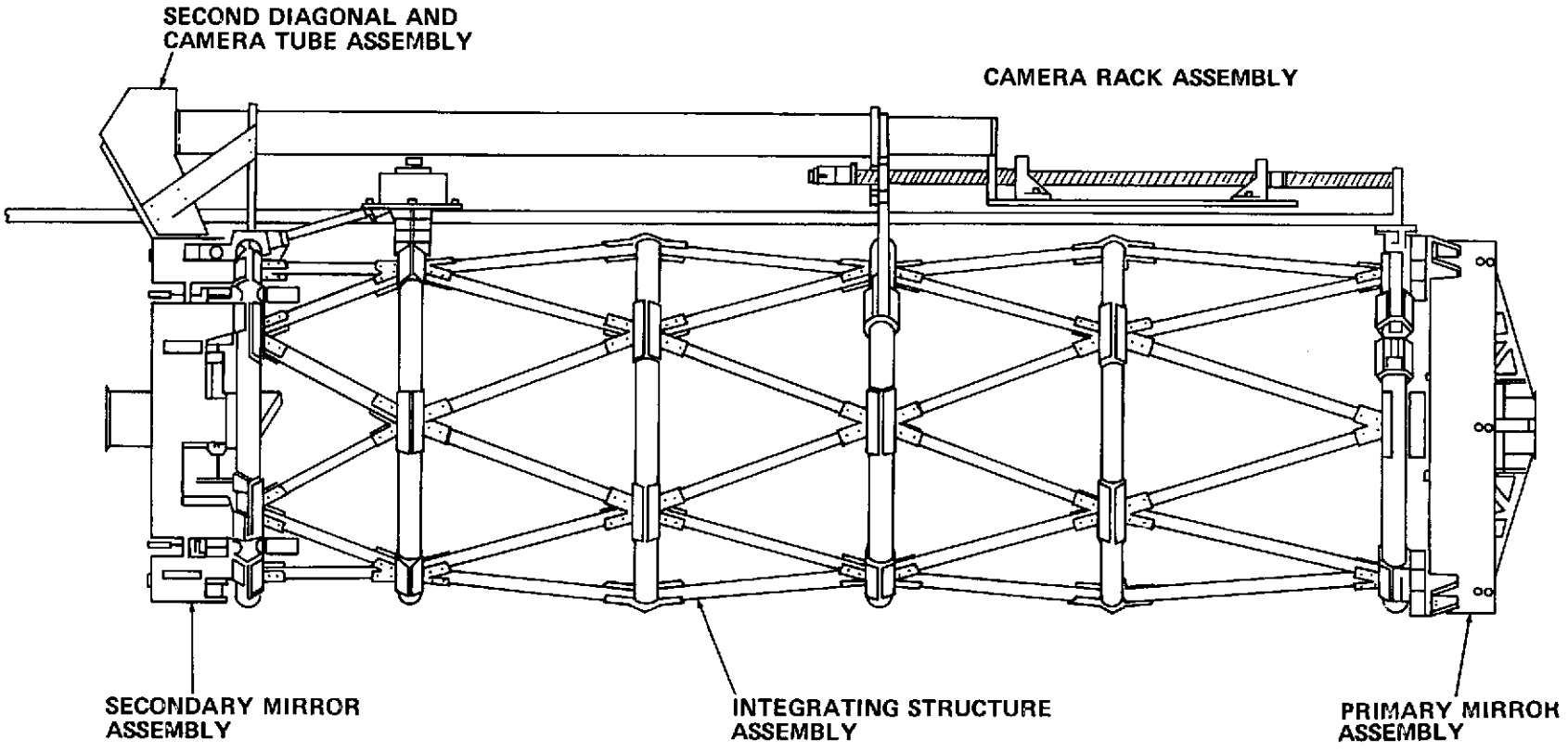

Figure 5.1 26-Inch Photoheliograph Assembly

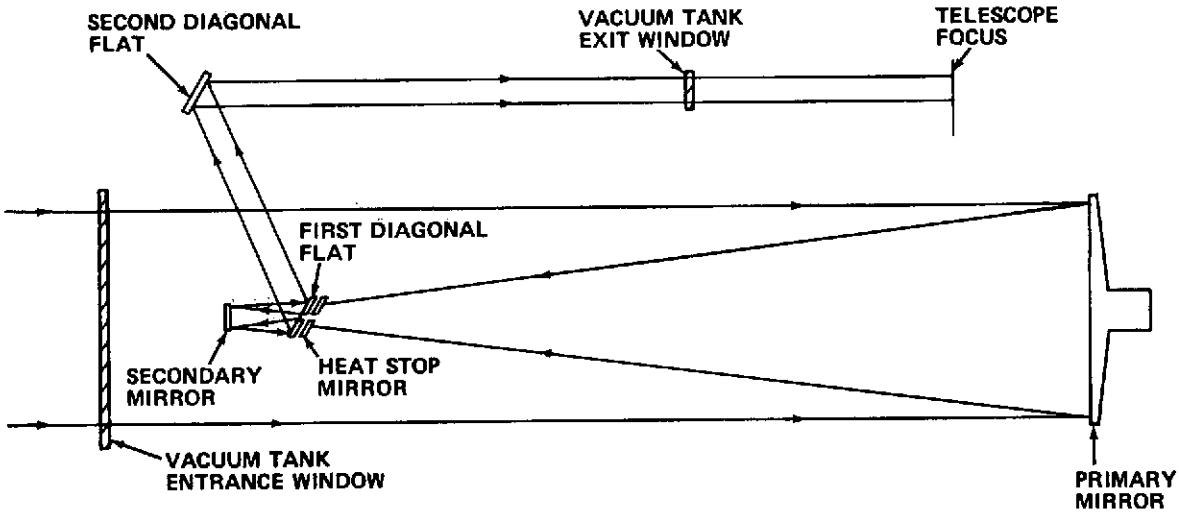

Figure 5.2 Optical Layout

An automatic alignment system has been provided which is designed to keep the telescope in good alignment at all times despite changes in temperature and the like. Many of the apparent larger scale phenomena that are observed with lower resolution originate in smaller features. In particular, solar granulation is made up of structures only a few hundred kilometers across, yet these are thought to be one of the main mechanisms by which the chromosphere and corona of the sun are heated. Similarly, solar spicules, which are only a few hundred kilometers across, extend upward into the atmosphere and are thought to play an important role in the transition between the chromosphere and the corona. Inside sunspots many features which are near the limit of resolution appear to play an important role in the growth of magnetic fields and the occurrence of flares. Therefore, high resolution observations of what is occurring inside these features give physical insight into what is happening and complement and extend the ATM data even though the features that were observed by ATM scientific experiments were, in general, more coarse than those which are resolved by the system discussed here.

A 10830 Å birefringent, narrow band filter was especially designed and constructed for observations at this infrared wavelength, which is the only helium line observable on the disk of the sun. Since helium is difficult to excite, it is seen only where the temperature is high. Thus, it provides an opportunity to observe the chromosphere on the disk without interference from photospheric radiation below, since the photosphere is

cooler. Because of problems with the filter, no simultaneous observations could be made with ATM, although postmission observations will be made and reported. These observations are complementary to the extreme ultraviolet (XUV) data from the ATM experiments in that they also look at the hotter part of the solar atmosphere. The instrumental setup for 19830 Å observations includes, in addition to the filter and telescope, a CO_2 cooled RCA infrared image converter tube and a 35mm camera for recording the image.

Appendix C is the Cal Tech final report describing installation and initial results of the photoheliograph at Big Bear Observatory.

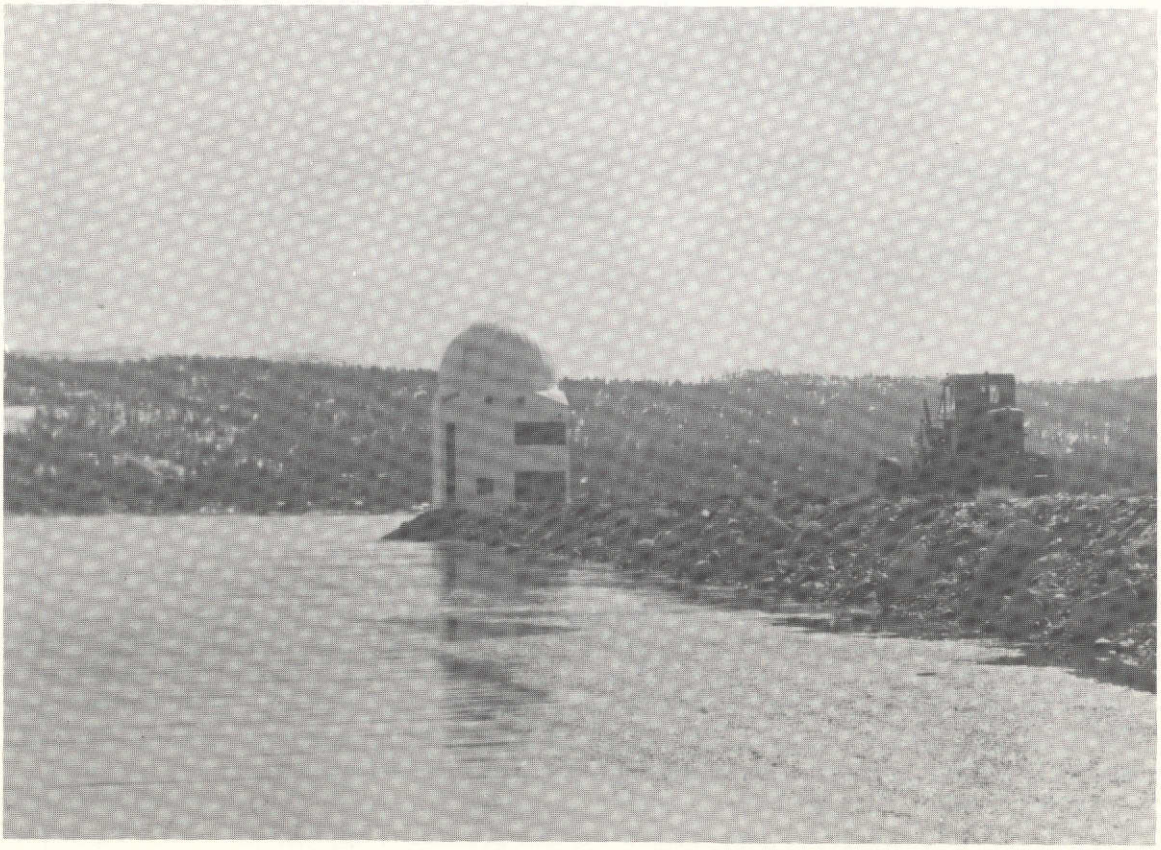

Figure 5.3 Big Bear Lake Observatory

SECTION 6. LOCKHEED FILTER STUDIES IN HeI AND CaII AT RYE CANYON

The Lockheed SGAP effort included research programs involving disk and limb observations in the D_3 line of HeI and high resolution observations in the infrared CaII line at 8542 Å. The two programs had complementary objectives. Drs. Sara Martin and Harvey Ramsey were the Principal Investigators.

During periods of high solar activity on the disk, the HeI observations were directed toward photographing solar flares and transient events. Effort was made to take these D_3 observations simultaneously with ATM spectra and spectroheliograms at X ray and XUV wavelengths. During periods of low disk activity, the effort was concentrated on acquiring prominence observations for correlation with ATM coronagraph observations.

The infrared CaII observations were high resolution, time-lapse photographs of only selected active centers or comparable sized areas of the solar surface. These observations were taken during the ATM observing periods (primarily the second manned mission) as well as several days after the ATM observations in order to acquire a reasonable chronology of the active regions for which X ray and XUV spectroheliograms were taken from space. The CaII and HeI filtergrams taken in conjunction with the ATM X ray and XUV spectroheliograms permit study of the origin of features at different levels in the solar atmosphere.

The HeI program consisted of building and testing a filter for the D_3 ($2^3P - 3^3D$) neutral helium line at 5876 Å and placing it in operation on one of two solar spar telescope systems at the Rye Canyon Observatory (Figure 6.1). The filter was mounted on the 28-inch diameter, 12-foot long spar which contains four optical systems, each occupying one quadrant of a cross formed by radial struts around a 5-inch center tube which contains the guiding optics. The narrow band 0.4 Å filter is used with a 7 Å blocking filter. A second 7 Å blocking filter was mounted in a full disk occulting system for studies of limb prominences. The narrow band filter permits referencing of oppositely polarized transmission peaks of 0.4 Å separated by 0.8 Å which allows referencing centerline D_3 and continuum at $\pm$ 0.8 Å or determining Doppler differences at $\pm$ 0.4 Å subtraction techniques. The line is seen to appear in either emission or absorption against the photosphere during flares; the strength relative to the continuum is used to infer electron density in the emitting volume.

Mounted on the other solar spar system at Rye Canyon was the optical system and 0.25 Å tunable filter for the infrared CaII line high resolution observations at 8542 Å. This solar spar system is slightly larger (14-foot length and 36-inch diameter) but otherwise very similar to the other spar. The CaII line is believed to originate at a higher level in the solar atmosphere than H-alpha. Therefore, these observations should prove extremely valuable in relating the ATM X ray and XUV data to H-alpha filtergrams and to spectroheliograms taken at wavelengths originating at lower levels.

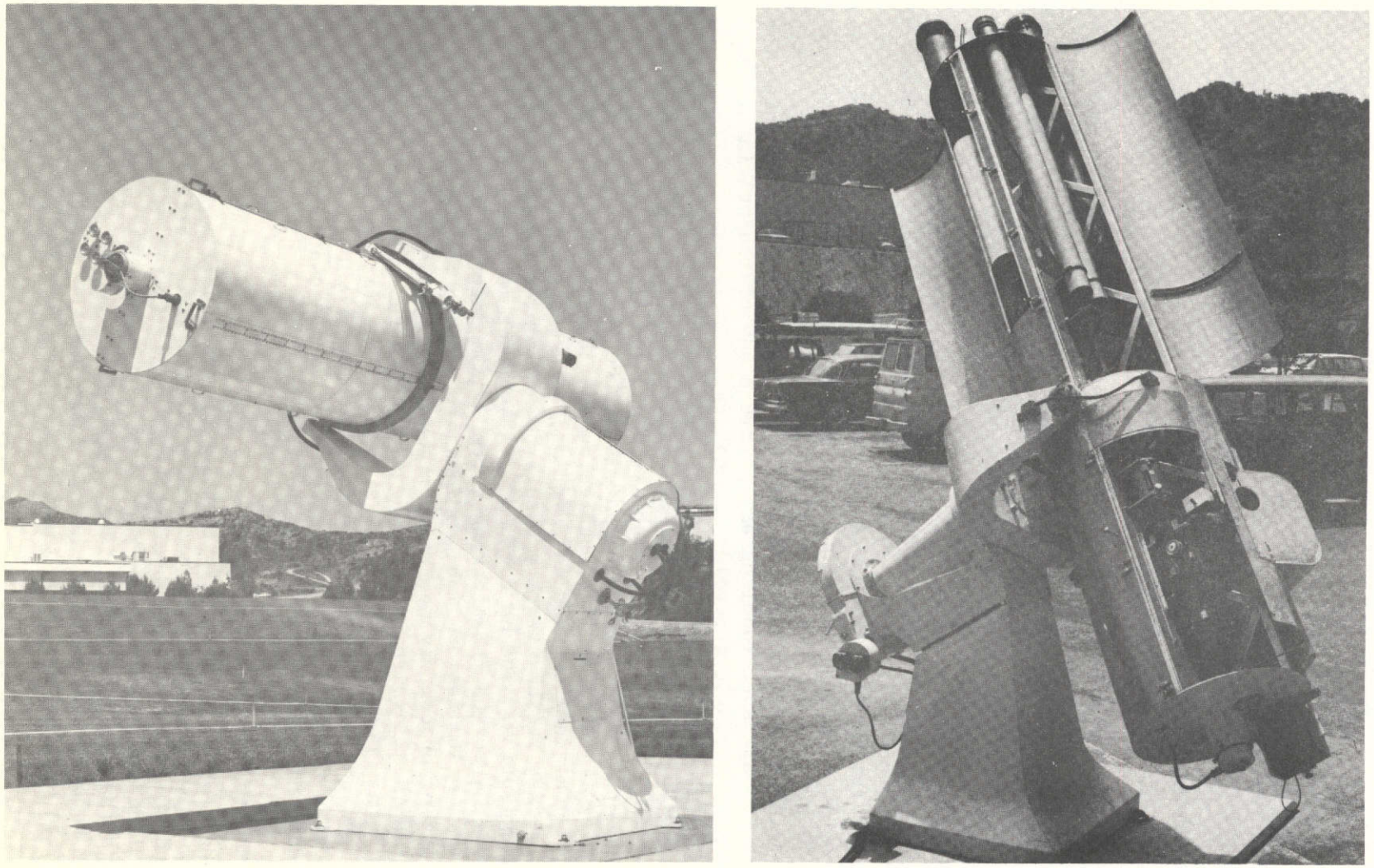

Figure 6.1 Lockheed Solar Spars

This task provided the photography of CaII features with excellent spatial resolution and permitted the recording of all except the most rapid changes in solar flares and accompanying transient events. The optical system included, in addition to the 0.25 Å birefringent filter with polarizing beam splitters, a 10-inch objective lens and a broadband blocking filter mounted on the track which served as the optical bench, as well as the camera system for data taking on infrared film. A visual monitoring system consisting of a conventional television camera and monitor was provided for operator convenience.

Instrumentation and observations are described in Appendix D.

SECTION 7. UNIVERSITY OF CALIFORNIA AT SAN DIEGO (UCSD) SOLAR INFRARED OBSERVATIONS

The objective of the UCSD observations was to explore the last remaining unknown region of the solar flare electromagnetic spectrum, the infrared wavelengths between 1μm and 1 mm. Flares appear prominently at almost all other wavelengths, and historically the development of observational techniques for each wavelength has revealed phenomena of major importance. Indeed, the X ray flare observations within the last decade have completely changed the accepted picture of solar flare energetics.

Atmospheric opacity limits ground-based observations to certain regions of the infrared spectrum. Out to about 25μ one finds numerous transparent "windows"; between 25μ and 100μ, however, the sun would not be detectable even at excellent mountaintop sites. Longward of 100μ, atmospheric transmission windows are narrow and require narrow-band detection to exploit them fully. In the present series of observations the 25μ and 300 to 1000μ regions were explored. Observations were primarily from Mt. Lemmon, Arizona, although a two-week run was scheduled at Mauna Kea, Hawaii.

Infrared detection generally involves "sky cancellation" to help remove the effects of emissions from the atmosphere and various parts of the telescope. With the 60-inch Mt. Lemmon telescope at submillimeter wavelengths, angular resolution is good enough to permit two beams on the solar disk. Chopping between them cancels both the background signal and the quiet solar signal, so that a source of transient activity in one beam (e.g., a flare) can be recognized by its time profile. At the longer wavelength end of the infrared spectrum, phenomena similar to those in the millimeter-wave region of radio observations were expected. In this region both impulse and gradual bursts are found, arising apparently from distinct emission mechanisms. The nature of the emission mechanism of the impulsive component remains unclear, and the submillimeter observations should help in understanding it. In the 1 to 30μm range, a most interesting phenomenon is the "white-light" flare. Understanding the white-light flare phenomenon potentially has very great importance, partly because of its close relationship with the energy release in the "flash phase" of the flare, and also because the visible continuum may also represent a large fraction of the flare energy. Infrared observations provide the crucial test to decide among different emission mechanisms. Solar flare infrared continuum might arise from any layer of the solar atmosphere above the level of the temperature minimum, below which the optical depth becomes large. This region includes the site of H-α flare emission. Possible emission processes would include white-light continuum, thermal continuum from the H-α source, thermal continuum from hot regions, non-thermal Bremsstrahlung, and synchrotron emission. A great deal of the justification for this effort was the possibility, however slight, for obtaining data on a white light flare in order to choose between these mechanisms. Although this did not materialize, numerous subflares were observed, and an important new phenomenon was discovered: temperature fluctuations associated with the 300-second oscillations of the solar atmosphere. Appendix E describes this discovery.

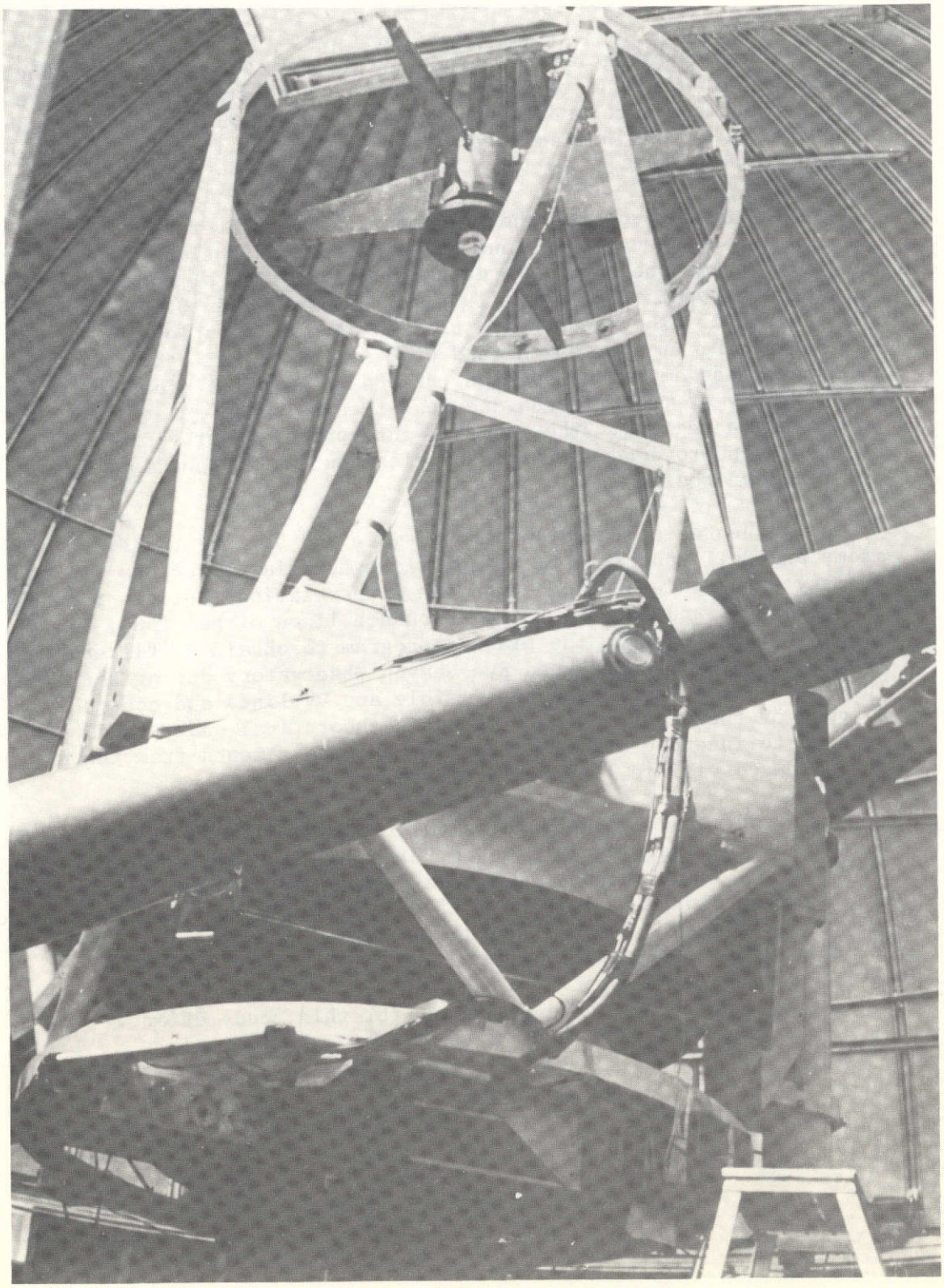

Figure 7.1 UCSD Telescope at Mt. Lemmon, Arizona

SECTION 8. LMSC STUDIES OF HELIUM EMISSION IN VISIBLE AND UV

This was a theoretical study by Dr. J.L. Kulander of Lockheed, the objective of which was to develop a better understanding of active solar region phenomena such as flares, prominences, and filaments through observations of visible and ultraviolet emissions from helium in the regions of interest.

The study provided the framework for the interpretation of and correlation between the various emission and absorption features found in active solar phenomena. A detailed calculation of the statistical equilibrium populations for a 19 level HeI atom and 10 level HeII ion was conducted. The results are used to develop relationships between the visible D_3 line emission (and 4686 Å line of HeII) and important UV resonance line emissions such as the 584 Å and 537 Å lines of HeI for a wide variety of temperatures and densities as would be anticipated in solar active regions. The specific interpretation of visible HeI D_3 line observations provided estimates of electron density and temperature in solar active regions.

A theoretical study of the visible and UV line radiation of HeI atoms and HeII ions from flare and flare associated regions was made. Primary emphasis was placed upon the interrelations between the HeI - D_3 line (5876 Å) and the first two resonance lines of HeI (584, 537 Å). This emphasis resulted from the planned program to obtain D_3 filtergrams on a patrol basis at the Lockheed Rye Canyon Observatory during the ATM mission. The calculations include other visible and UV lines and continua. The purpose of the program was to obtain a theoretical understanding which can be used to interpret the simultaneous UV measurements from the ATM and the ground-based visible line measurements.

A code was developed to calculate the radiation fields and populations of the individual terms in HeI and II through principal quantum number n = 4. A plane-parallel model was used, with solutions analyzed for electron densities 10^{10} to 10^{14} cm^{-3} and electron temperature from 10^4 to 5×10^4 °K. Optical depths and some line intensities are presented for a 1000 kilometer thick layer.

Appendix F is the final report for this study effort.

SECTION 9. MOLECULAR LINE OBSERVATIONS AT UTTAR PRADESH, INDIA

The Uttar Pradesh State Observatory (UPSO) in India is doing a study of dissociation and excitation equilibria of various molecules in the photosphere, spots, and faculae, using data obtained during the Skylab mission. Detection equipment was supplied to India on loan for an observational program at the Manora Peak facility using their existing horizontal solar telescope and its associated spectrograph with a view toward improving available models of the solar atmosphere's parameters which influence these studies. Dr. M.C. Pande was the Principal Investigator.

The solar group at UPSO is investigating the following types of problems concerning the sun during the ATM mission:

A. A comparative study of the dissociation and excitation equilibria of various molecules in the photosphere, spots and faculae. Theoretical studies concerning these have previously been undertaken based on various available models of these features. The present effort is based on an observational program using a spectrograph in conjunction with the horizontal telescope.

B. Center-to-limb variations of the atomic and molecular lines in the spectra of photospheric and active regions and their intercomparison.

The equipment complement of the horizontal solar telescope and its associated spectrograph includes:

A. Image-forming optics, including a 46-cm coelostat and a 27-cm, f/66 skew cassegrain telescope capable of forming an 18-cm image of the sun.

B. A spectrograph employing a 127 x 203 mm^2 plane reflection grating with 600 lines/mm blazed at 2.5μ and a 25-cm, f/36 camera giving a dispersion of 1.2 Å/mm in the first order. In this program spectral orders up to the fifth order were used. The recording facilities were provided for photoelectric spectrophotometry (with scanning facilities in the fourth order at speeds varying between 1 Å in 768 seconds to 120 Å/minute) and photography. Simultaneous spectrophotometry in different spectral regions, not exceeding four in number, is possible, in the region 3000 to 9000 Å.

Instrumentation which was placed on loan to Uttar Pradesh for observation in the ATM time frame includes:

A. Refrigerated photomultiplier tube chambers to reduce dark current noise in the detection.

B. PbS detectors to extend the spectral coverage into the infrared.

C. An image intensifier tube to allow prominence and weak emission line studies.

D. Film magazine adaptable to the image tube, film, and associated electronics.

Although no report to NASA was required for this equipment loan, publications in the open literature are expected covering the Skylab and subsequent time frame observations. The basic Skylab program was center-to-limb variations of Mg triplett, Na, D_1 and D_2 lines, C_2 bands, MgH, and CH 4300 Å region on each clear day for photospheric and spot spectra.

SECTION 10. JOHNS HOPKINS RADIO BURST SPECTRAL OBSERVATIONS

The Applied Physics Laboratory (APL) of Johns Hopkins University performed an observational program during the ATM mission of high time resolution spectral observations of solar radio bursts in the 500 to 1000 MHz range. Bruce Gotwols was the Principal Investigator. With the high time resolution available from their spectrograph and 60-foot diameter antenna, the observational goal was to determine the presence or absence of frequency drift in solar radio bursts and associated implications on models of the emission mechanisms and electron densities in the source region. Observations during ATM were principally a continuation of earlier work; hence, no instrumentation development was required for this project.

A principal goal of the 565 to 1000 MHz spectral observations was to utilize the extremely high 0.01 second time resolution of the APL spectrum analyzer to determine if, in fact, there is a finite frequency drift rate in the radio bursts from the sun. A finite drift rate would strongly imply an emission mechanism operating at or near the local plasma or gyro frequency. Electrons travelling radially outward from the photosphere with velocities of appreciable fractions of the speed of light should traverse the distance from the 1000 MHz to 500 MHz plasma levels on the order of a tenth of a second, thus allowing an unambiguous conclusion as to the presence or absence of a finite frequency drift rate.

It is also possible to obtain a time history of the activity at any selected frequency within the passband of the spectrum analyzer. From the lifetime of a drifting burst at a particular frequency, the surrounding plasma temperature may be determined, and from the frequency drift rate the density gradient can be estimated. Thus, data are provided for modeling the physical parameters of the corona-chromosphere transition region where at least some of these bursts are thought to originate.

The antenna is a 60-foot diameter paraboloid mounted on an X-Y mount with computer generated pointing control. Focal length is 25-feet, at which a cavity backed spiral, with right-hand circular polarization is located.

The radio frequency section of the receiver is antenna mounted, behind the paraboloid, as is the intermediate frequency amplifier. The remaining portions of the spectrograph are located in an instrumentation trailer adjacent to the antenna. Figure 10.1 is a block diagram of the complete spectrum analyzer. The minimum detectable signal is approximately 20×10^{-22} watts/m^2/Hz.

The data recording was accomplished by letting the log amplifier output modulate the intensity of the spot on a high resolution cathode ray tube. Simultaneously the spot is driven laterally in synchronization

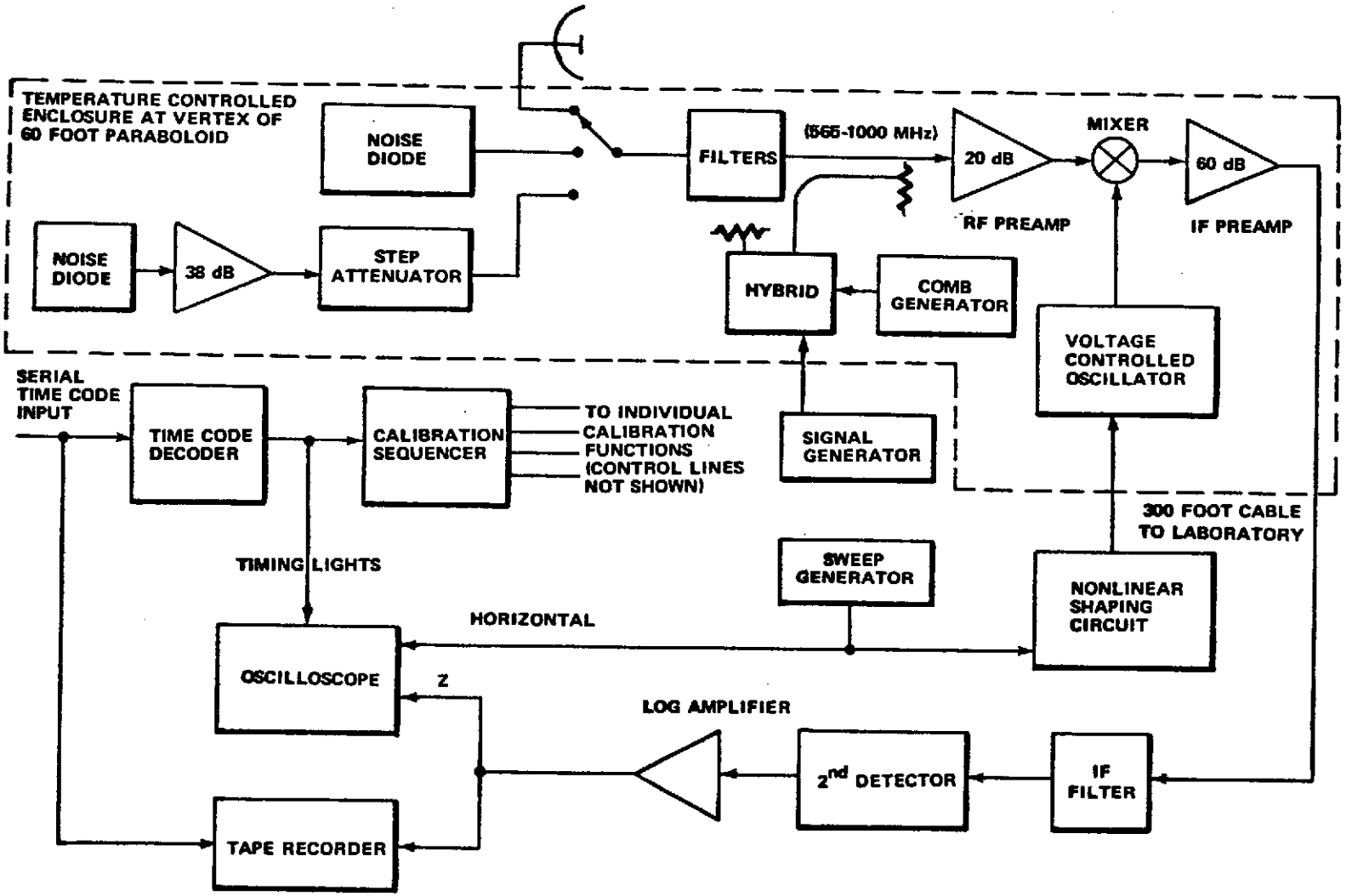

Figure 10.1 Block Diagram of the 565-1000 MHz High Time Resolution Solar Spectrum Analyzer

with the local oscillator tuning of the spectrum analyzer and photographed with a continuously moving 35mm camera film. Figure 10.2 is a typical recording. The spectrum analyzer output was also recorded on magnetic tape in analog form. Appendix G discusses results of this task.

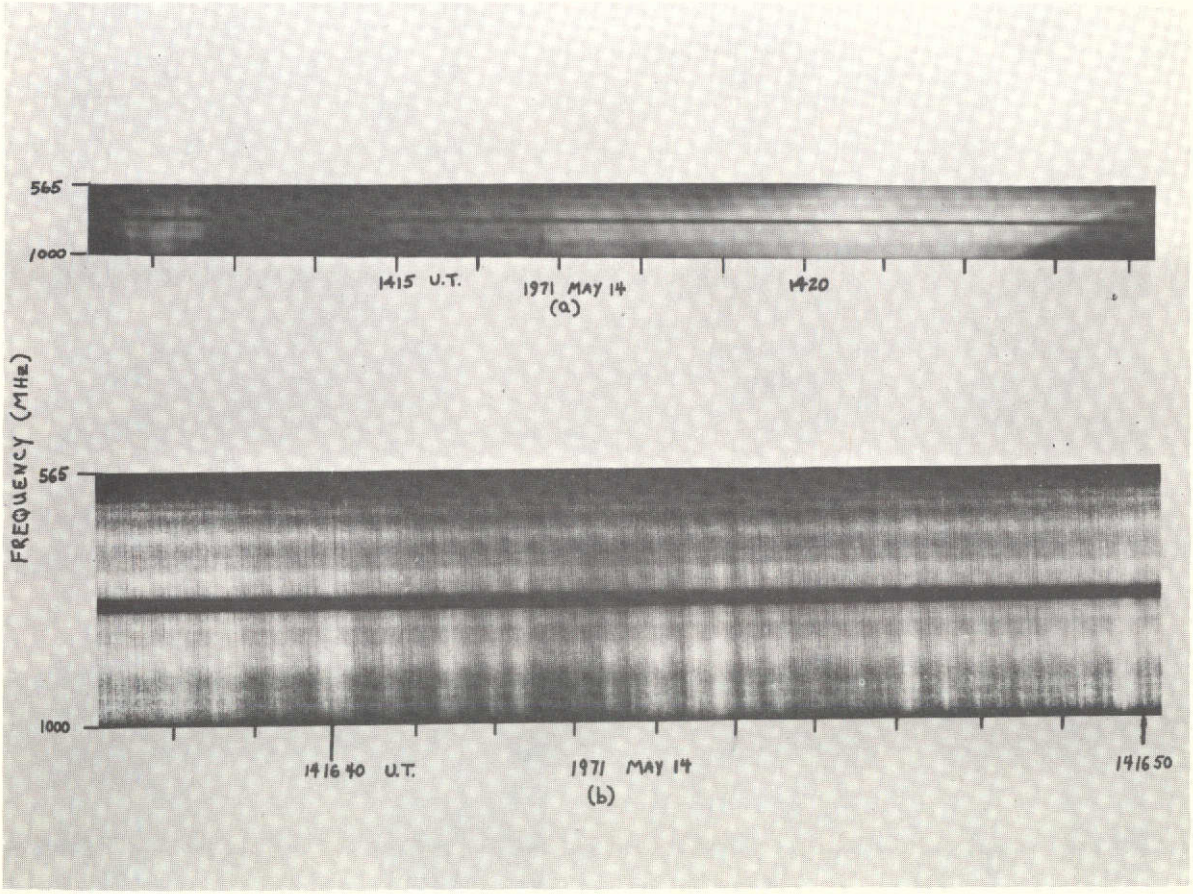

Figure 10.2 Solar Radio Burst Spectrum

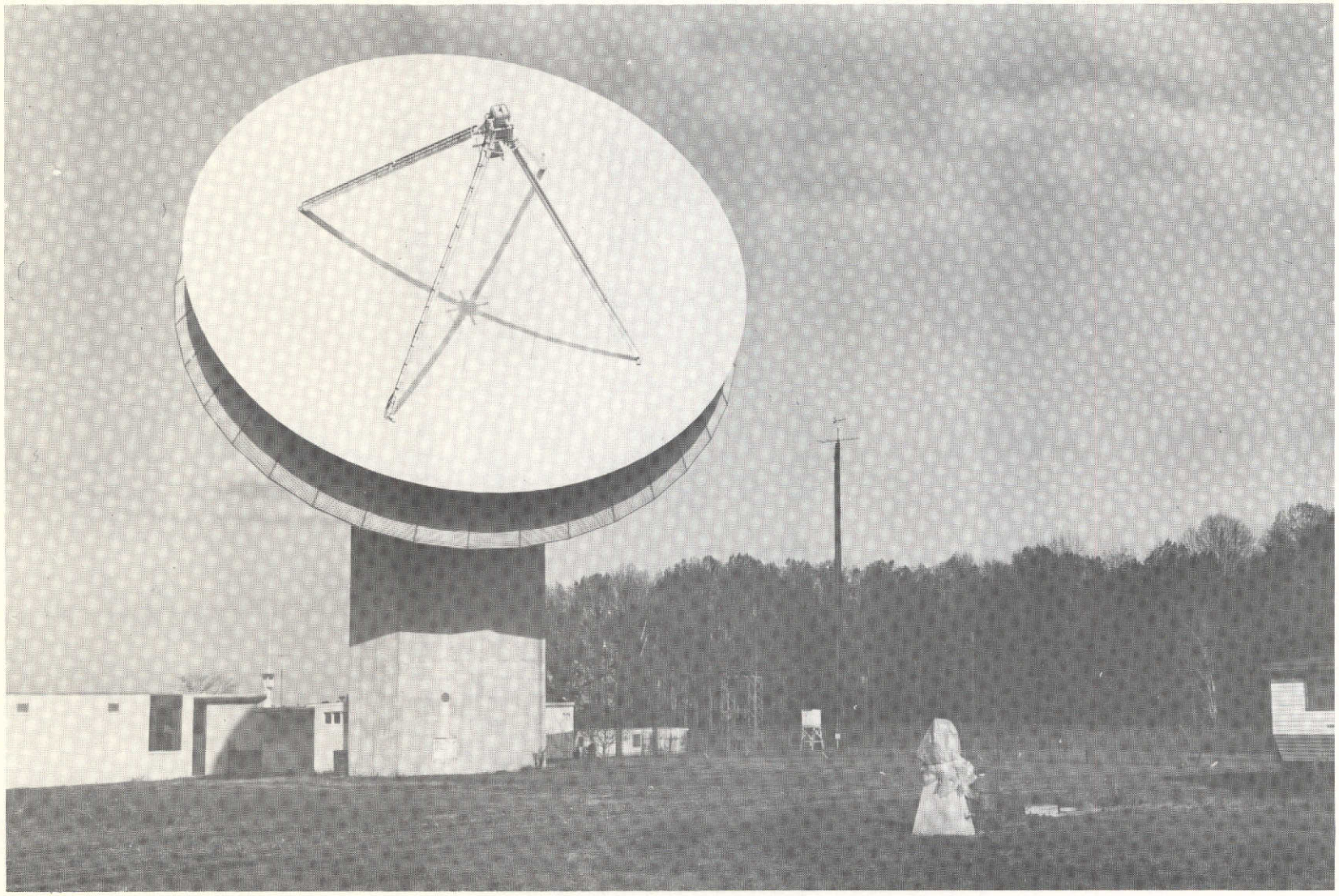

Figure 10.3 APL Sixty Foot Radio Burst Antenna

This page intentionally left blank

This page intentionally left blank

Appendix A

University of Hawaii
Final Report

PRECEDING PAGE BLANK NOT FILMED

INSTITUTE FOR ASTRONOMY
UNIVERSITY OF HAWAII
2840 Kolowalu Street
Honolulu, Hawaii 96822

March 3, 1974

APOLLO TELESCOPE MOUNT OF SKY LAB MISSION-A

Contract No. NAS8-27950

FINAL REPORT
for period
November 3, 1971 - March 2, 1974

Prepared by:
John T. Jefferies
Principal Investigator

for

George C. Marshall Space Flight Center
Huntsville, Alabama 35812

INTRODUCTION

The multi-channel coronal spectrophotometer system described in this report was conceived as part of the 1973 SKYLAB mission ground-based solar observational support. Much of the Apollo Telescope Mount instrument package aboard SKYLAB was configured especially to investigate coronal physics via high spatial and temporal resolution observations of the line radiation in the XUV and EUV spectral regions. Our apparatus was designed to complement that work by measuring, in coordination with the SKYLAB scientific schedule, the corresponding forbidden line radiation in the visible and near-visible spectral regions, together with a number of prominence line intensities, with resolutions comparable to that of the ATM equipment.

The instrument was in operation on a daily basis throughout the mission. However, due principally to limiting signal-to-noise capability, sparse coronal activity and spotty weather conditions, our observationsal program was only partially successful. By far, our most scientifically significant results were obtained during the second manned mission. When appropriate, supplementary observations were made using our other existing instrumentation: 10-inch coronagraph-coudé spectrograph and Hα Zeiss system, Hα flare patrol camera, K-line telescope, Hα and green-line dual coronagraphs, and polarimeter-photometer.

Two papers describing the multi-channel coronal spectrophotometer system have been presented: one was published in Astronomical Observations with Television-Type Sensors, University of British Columbia (1973), and the other was delivered at the Solar Physics Divisions meeting of the American Astronomical Society, 9-11 January 1974 (paper P4).

Anticipating the analysis of the coronal observations, we also carried out new Fe^{+12} excitation equilibrium calculations based on our improved ground configuration proton impact excitation rates. Three papers describing this work have been published in Solar Physics.

The succeeding sections to this report describe, in turn, the multi-channel coronal spectrophotometer system's design and operation, the observations made with the system, and the proton impact excitation calculations. The Appendix contains copies of the scientific papers resulting from the work performed under this contract.

Photographs of the spar-mounted instrument (with the two-dimensional vidicon detector unit) and the data-acquisition and control system are shown in Figures 1 and 2, respectively.

II. INSTRUMENT DESIGN AND OPERATION

The projected scientific programs constrained the instrument system design in several directions:

(a) To have the facility of measuring simultaneously as many coronal and prominence emission lines as possible, the apparatus had to be sensitive and achromatic over a very wide spectral range. In particular, we desired the capability of measuring simultaneously the three Fe^{+12} lines: $\lambda\lambda$3388, 10747 and 10798. For obtaining line intensity ratios, the feature of simultaneity eliminates any systematic errors resulting from sky transparency and seeing fluctuations throughout a measurement;

(b) To be able to derive meaningful physical models from the data, the instrument required a spatial resolution sufficient to resolve the intrinsic filamentary structure of coronal active regions (typical diameters $\geq 5''$);

(c) To enable close time-variation observations of the physical properties of active regions, the instrument was designed with as high a temporal resolution capability as possible; and

(d) To maximize scientific throughput a data-acquisition and control system with on-line reduction and display facilities was required. To allow for the possible coordinated operation of several solar telescope systems it was desired that the DACS have multiprogramming capability.

The following subsections describe in turn the various apparatus subsystem design characteristics and functioning.

A. MECHANICAL CONFIGURATIONS

Figure 3 shows an overall mechanical view of the instrument. It is $\sim$25 cm in diameter by $\sim$4.4 m long, constructed principally of aluminum, and mounted on one face of the 3.6-m spar at the Mees Solar Observatory. It consists successively of an on-axis coronagraph telescope, a spectrometer, and a silicon-vidicon camera tube detector unit. The gimbal mounting permits 5/6 $''$/step spatial scanning via computer driven stepping motors. The limits of travel are $\sim$3 $R_\odot$ from the sun center. Various component motions (dust cover, shutter, diffraction grating, optical component wheel and objective lens focus) are driven by computer-controlled synchronous motor (cf. Figure 9).

B. OPTICAL CONFIGURATION

The optical system, shown schematically in Figure 4, is comprised of an achromatic coronagraph telescope, reimaging lens, optical component wheel, calibration light sources, shutter/sun-positioner and spectrometer.

(1) Coronagraph Telescope

As indicated in Figure 4, the coronagraph telescope is used on-axis so that when observing the corona, the disk's image is occulted by the side of the pinhole assembly. Scattered light in the field is minimized by appropriate baffling in the telescope tubes.

The objective lens is a three-element (FK-5/KZFS-N4/F-7) oiled (DC 510, 50CS) apochromat with a 15.2-cm working aperture and 220-cm nominal back focal length (i.e., f/14.5). It is color corrected (with no aspheric surfaces) for "out of focus" to better than two Rayleigh limits throughout the spectral range $0.3\mu<\lambda<1.1\mu$.

The pinhole acts as a field lens to "form an image" of the O_1 aperture on the Lyot stop located just in front of the reimaging lens. (Only the O_1 aperture diffraction image was masked out; it did not appear necessary to stop the images from O_1 surface reflections.) The most effective pinhole diameter corresponds to $\sim 30''$; diffraction from smaller pinholes increases the stray light in the field, while the larger the pinhole, the less close in to the solar limb one can observe. The reason for the latter circumstance is that the instrument's aperture stop is the spectrometer entrance slit and photospheric light passed by the pinhole is scattered into the field by the reimaging optics. A set of interchangeable pinholes with assorted diameters were fabricated; most observations were made with the 30" and 40" ones.

A value of $\sim 30\times10^{-6} I_{\odot}$ was estimated for the O_1 scatter using a bench test after initial assembly of the lens, when presumably it was optimally clean. In actual operation, the estimated scattering after average use was about twice the above value. This result was obtained by comparing multi-channel coronal spectrophotometer observations of the green coronal emission line Fe^{+13} 5303A with those made simultaneously by the coronal polarimeter-photometer (also mounted on the spar). During one cleaning operation (on 23 June 1973), the oil voided out between the lens elements. In the process of reassembly a relatively deep scratch developed in the rear junction and for subsequent observations a small stop was placed at the position of the Lyot stop to mask out the image of the scratch. With this stop in place, the scattering figure did not appear to be degraded over the earlier value.

(2) Reimaging Lens

This lens is used to relay the coronal light to the spectrometer entrance slit and, as mentioned above, supports the Lyot stop on its face. It is a triplet (BK-6/fluorite lBK-6) achromat designed to produce with minimal aberration an image with 5" equivalent to 25μ, a scale determined principally by the vidicon read beam diameter.

(3) Optical Component Wheel

This rotatable wheel is used to position under programmable control a selection of assorted optical components just in front of the spectrometer entrance slit. These components, equally spaced in eight slots around the wheel, include polarizers, spectral filters, neutral density filters used for system intensity calibration via the intensity at the center of the sun's disk, and a small mirror to direct light from the calibration lamps through the spectrometer.

(4) Calibration Light Sources

Provision was made for the concurrent mounting of two types of spectral calibration lamps: pencil discharge and hollow cathode, and either type can be selected by means of a flippable mirror. These lamps are used for system spectral calibration.

(5) Shutter/Sun-Positioner

The computer controlled shutter is situated right behind the spectrometer entrance slit. The shutter's front face is polished and angled so that when the shutter comes on-axis, light is deflected onto a photo-diode. The amplified signal is read by the computer through a 12-bit ADC (cf. Figure 7) and is used for programmable sun-centering of the telescope axis by monitoring the gross change in light when crossing the limb.

(6) Spectrometer

The spectrometer, which is $\sim$66 cm long, is shown schematically in Figure 5. The collimator and camera mirrors are f/8 off-axis paraboloidal sections with focal lengths of $\sim$61 cm. The diffraction grating (75 groove/mm, $6^{\circ}28'$ blaze angle, 3.0μ 1st order Littrow blaze wavelength) produces dispersion in the plane of the figure while the prism/mirror separates the overlapping grating orders by providing dispersion perpendicular to this plane. The spectrum is thereby presented to the vidicon target in the form of bands corresponding to the low orders in an echelle-type format. Using orders 3 to 9 and remaining near the blaze, the entire spectral range of interest $\sim$0.3μ-1.1μ can be covered, with much overlap, on the active target area with three grating orientations. The spectrometer has a low dispersion ($\sim$1A/25μ in 6^{th} order ($\sim$5000A)) so that with the target formatting used ($\sim$33μx33μ pixels) only line intensity and not line shape information can be obtained. As noted above, the spectrometer entrance slit defines the aperture stop and for all data were fixed at 5"x20"; with respect to the sun the slit orientation remains fixed, independent of telescope pointing.

C. DETECTOR :

Two versions of the detector unit were used during the research period. The active component in each case was a silicon-vidicon camera tube, chosen because of its extremely wide spectral response ($\sim$0.3μ-1.1μ) and relatively high quantum efficiency over this range. An RCA 4532 tube with filament light shield was used throughout. The tube's target was situated in the spectrometer output focal plane. The earlier less versatile version was used throughout the first two manned flights; the final unit was in operation subsequently. We describe the latter unit first.

The final detector assembly is shown in outline form in Figure 6. The Unit is thermoelectrically cooled to $\sim -6^{\circ}$ C to reduce leakage current and enable extended exposure times. (The fan mounted on the back of the unit was disconnected because it introduced some noise into the video signal. This resulted in a vidicon operating temperature $\sim 9^{\circ}$ C warmer than we had anticipated with correspondingly larger leakage currents.) An evacuated double quartz window is mounted in front of the tube to prevent frosting on the tube's entrance window. In operation, light integration times for weak emission lines in the corona are limited to $\sim$15sec by leakage current and scattered light in the field.

A block diagram of the detector control electronics is shown in Figure 7. The vidicon control unit at the right supplies all the camera tube operating voltages (filament, grids, forms, etc.) as well as the control pulses (clock, frame and line retrace). The vidicon is operated in a slow-scan mode, the scan rate being determined by the video digitization rate together with computer housekeeping time. Horizontal and vertical deflection currents are generated via a crystal oscillator driving scalers connected to DACs. The fast axis of the scan consists of 256 pixels covering $\sim$8.9 mm on the target in a direction approximately perpendicular to the spectral orders. The slow scan axis consists of 384 lines covering $\sim$13.0 mm. With our 12-bit ADC, a scan rate of 20 μsec/pixel is appropriate so that this arrangement therefore produces a raster scan over $\sim$116 mm^2 of target area with a resolution of 98,304 pixels in $\sim$2.1 sec (including retrace time). Provision is made for the PDP-11/45 computer to read the deflection scalers so that it can check the read beam position at any time. The read beam may also be programmably blanked or unblanked at the beginning of any frame.

The video output signal is amplified, digitized and input to the PDP-11/45 via a CAMAC input register. To enable real-time monitoring of the system, the video is both displayed line by line on a CRT and routed into a Hughes scan converter for regular TV display.

As a figure of merit for the system, we have found that the limiting factor in detecting weak spectral lines with the detector as it now stands is the presence of electrical noise in the video signal leading to unit signal-to-noise ratio for an $\sim 5 \times 10^{-6} I_{\odot}$ green-line intensity with an $\sim$12 sec integration time. This figure should be capable of much improvement, since we do not even approach the detector preamplifier noise specification limits.

Until the above detector system was ready, we configured a preliminary system around an SSR, Inc. Optical Multichannel Analyzer. This system was similar to the final one, differing principally in the target read out format and rate. With the OMA the target is divided electronically into 500, $\sim$25μ wide channels and upon readout, which is at the rate of 32.8 msec/frame, the signal in each channel is added together. Since this device provides only a one-dimensional array of channels for data taking, while the spectrometer presents the spectrum in a two-dimensional format, the camera tube was oriented with the channels along the grating dispersion direction and order separation was accomplished by physically marking the target to accommodate the desired set of spectral features. Thin copper masks were fabricated by photo-etching holes in the appropriate places using standard electronic circuit board lay-out techniques,

ORIGINAL PAGE IS
OF POOR QUALITY

and mounted up against the vidicon faceplate. The OMA console unit contains all the necessary power, scanning, leakage and background subtraction, amplifying, digitizing and memory electronics to operate the vidicon. Various features (e.g., frame blanking) were programmably controlled. Provision was made for local cooling of the vidicon target by ~10-15° C by enabling the mounting of an annular thermoelectric unit on top of the mask; however, this was not done during observations since the specially ordered thermoelectric module was not available until after our final detector was ready.

There are several major disadvantages of this system when compared to the two-dimensional one: (1) different observing programs require changing physical masks; (2) spectral lines of interest falling on the same channels in different orders get summed over when reading out the vidicon; (3) adding in the masked out portion of the target signal during channel read out to the very much smaller unmasked portion degrades severely the signal-to-noise ratio; and (4) intensity calibration complications due to the very slight moving of the spectrum relative to the mask as the telescope changes position through the day. Even though the preliminary system had in practice a noise figure comparable to that quoted above for the two-dimensional version, in principle the latter system should be at least an order of magnitude better.

D. DATA-ACQUISITION AND CONTROL SYSTEM

The DACS is configured about a Digital Equipment Corporation PDP-11/45 computer and is equipped with 40K of core memory, a teletype, two disk cartridge drives and a dual DEC tape drive. All major user defined peripherals, including a CRT point plot display, character generator, light pen and Printer 100 char/sec printer are interfaced via a CAMAC standard dataway controlled by a Borer type 1533 crate controller. The computer configuration is shown in Figure 8. As displayed schematically in Figure 9, all electro-mechanical instrument functions are controlled by the PDP-11/45 via CAMAC interfaces to stepping and synchronous motor drivers. Both detector systems were interfaced to the computer via CAMAC modules and the arrangement for the two-dimensional vidicon unit is given in Figure 7. (In these Figures: I(o)R = input (output) register; PPG - programmed pulse generator; and 4BD = fourfold busy-done.)

An enormous amount of software was written to implement the various system aspects. To effect the functions of calibration and telescope raster scanning, a large assortment of CAMAC handlers were assembled into a coherent, interactive system of operational subrontines. Using these basic assembly routines, a wide variety of FORTRAN software was developed for DACS purposes, including calibration, telescope scanning, sun-centering, focus, etc., programs. Separate complete operating systems had to be prepared for each of the two detector packages.

All software was run under the PDP-11/45 Disk Operating System Monitor and not, as we had originally planned, under the RSX 11-D Real-Time Executive Operating System. The latter system enables a foreground/background multiprogramming capability. DEC was simply not able to deliver the RSX 11-D in time for incorporation into the system. In fact, DEC's delay of several months in their initial delivery of the PDP-11/45 seriously undermined our

development timetable. In practice, we have had an ongoing difficulty with the DOS: the monitor "bombs" frequently and erratically, causing loss of system parameters (telescope position, etc.) and data; DEC has not been able to solve this problem.

While the flexibility deriving from the standardization and modularity inherent to the CAMAC scheme has proved extremely valuable in interfacing the variety of components to the PDP-11/45, we did run into a few unnecessary problems particularly with regard to implementing the two-dimensional detector unit, as outlined in Quarterly Status Report #8. In addition, the Printer-100 printer has had a somewhat spotty mechanical history; when it is down we are forced to fall back on TTY output, greatly slowing down data acquisition (i.e., telescope raster scanning) speed as well as inconveniencing software development.

III. OBSERVATIONS

Throughout the report period we have used the multi-channel coronal spectrophotometer system, with both detector assemblies, to perform a variety of prominence and coronal observations. In addition to the usual prominence emission lines, the most significant lines that we have observed are Fe^{+9} 6374 A, Fe^{+10} 7892 A, Fe^{+13} 5303 A and He 10830 A. Whenever possible, we coordinated our observations with those of SKYLAB as relayed via WWVH.

Most of the coronal observations were made either with the 5303 A line alone or with the 5303 A and 6374 A lines simultaneously; the signal-to-noise ratio for the 7892 A line was generally too poor to give much more than an indication of its presence. We were not successful in detecting the Fe^{+12} 10747 A and 10798 A lines, even after careful searching in regions where there was substantial 5303 A and 6374 A emission; the system sensitivity at these wavelengths, however, is clearly evidenced by the relative ease with which the 10830 A line is observed.

The great majority of our scientifically meaningful observations were obtained during the second manned mission. During the first mission there were no particularly relevant events for us to look at in relation to the SKYLAB observational programs and our work was principally of a diagnostic and instrumental shakedown nature. The unexpected delay in making operational the new two-dimensional vidicon detector system, coupled with generally poor weather throughout the third manned mission, precluded any scientifically significant output during that period.

The next four figures depict data obtained using the OMA adapted detector system; similar observations have been performed with the two-dimensional system. In Figure 10, we show a typical prominence spectrum and illustrate the sensitivity to He 10830 A. A RG-10 high-pass colored glass filter was inserted in front of the reimaging lens to very strongly attenuate the Hα line, rendering its intensity comparable to that of the 10830 A line. The relatively long signal averaging in this case resulted from a combination of using the RG-10 filter and the desire to bring out the He 6678 A line. Note that the line shapes are instrumental.

Figure 11a shows a spectrum that includes the three coronal lines 5303 A, 6374 A and 7892 A, together with Hα. The gross pedastral structure is due to scattered light delimited by the target mask slots and somewhat obscures the 6374 A line which falls on a slot edge in this arrangement. In Figure 11b, we show the 5303 A and 6374 A signals with a different mask/grating positioning. Here orders 5 and 6 are both allowed to pass through the target mask over the spectral region indicated. (While this circumstance of overlapping orders reduces the signal-to-noise ratio in the derived line intensities, the close lateral proximity of the two lines made it necessary to record

simultaneous line intensities in this manner. This situation is completely obviated by the two-dimensional detector system.) Signals are shown for two different coronal positions. Again, the line shapes are instrumental.

Figures 12 and 13 show the results of a two-dimensional coronal scan simultaneous in 5303 A and 6374 A. In Figure 12, the data are plotted as a ρ,θ raster with the numbers denoting the absolute emission line intensities, calibrated via the measured intensity at the center of the sun's disk, and with isophote contours drawn in; in Figure 13, the same data are redrawn as curves of line intensity versus θ at each of the various values of ρ. (Note: $\rho = R/R_{\odot}$ = distance from sun center in solar radii, and θ = geocentric position angle measured counterclockwise from north.) As described above, the spatial resolution, determined by the spectrometer entrance slit, was $5'' \times 20''$. The telescope is mounted on the spar so that the orientation of this slit has its long side tangent to the solar limb at $\theta = 135^{\circ}$; the orientation is independent of telescope pointing.

IV. CALCULATIONS

A principal function of the multi-channel coronal spectrophotometer was to observe forbidden line intensities from coronal ions. Some ions especially, such as Fe^{+12} with three such observable transitions ($\lambda\lambda$3388, 10747, and 10798), are particularly suitable for coronal region diagnostics, provided the line intensity ratios can be reliably related back to the ionic excitation distribution. The various proton collisional excitation rate constants are significant elements in this reduction and since many of them had not been calculated with sufficient detail previously, we embarked upon a program of doing so for the most important cases. Three papers reporting on this work--two describing proton excitation calculations in Fe^{+12} and Fe^{+13}, and the third applying these results to determining the Fe^{+12} excitation equilibrium--were published in Solar Physics and are reproduced in the Appendix to this report.

FIGURE CAPTIONS

1. Multi-channel coronal spectrophotometer mounted on the Mees Solar Observatory 3.6-m spar.

2. Data-acquisition and control system.

3. Overall mechanical view of the instrument.

4. Schematic drawing of the optical system.

5. Schematic drawing of the spectrometer.

6. Two-dimensional silicon-vidicon detector assembly.

7. Block diagram of the two-dimensional detector unit and sun-centering photo-diode electronics and system integration.

8. Block diagram of the computer configuration.

9. Block diagram of the electromechanical instrument control electronics and system integration.

10. Data of 24 June 1973, 2:05 uT; p = 1.04, $\theta = 262^{\circ}$; 3000 frame x 32.8 msec/frame; RG-10 filter; Aperture: 5" x 20".

11. (a) Spectrum showing the three coronal lines 5303 A, 6374 A and 7892 A, together with Hα. Data of 5 September 1973, 21:34 uT; p = 1.04, $\theta = 296^{\circ}$; 1000 frame x 32.8 msec/frame; Aperture: 5" x 20".
    (b) Spectrum showing the 5303 A and 6374 A lines with the target slot/spectrum configuration used for simultaneous scan observations. Data of 11 September 1973, ∿21:25 uT; 500 frame x 32.8 msec/frame; Aperture: 5" x 20".

12. Simultaneous 5303 A and 6374 A emission line scan. Data of 18-19 September 1974, 23:19-00:01 uT; the numbers denote absolute line intensity in units of erg cm^{-2} sec^{-1} $ster^{-1}$; $\Delta I_{abs} = \pm 15\%$, $\Delta I_{rel} = \pm 15$ erg cm^{-2} sec^{-1} $ster^{-1}$; $R_{\odot} = 956.7''$.

13. Same data as for Figure 12.

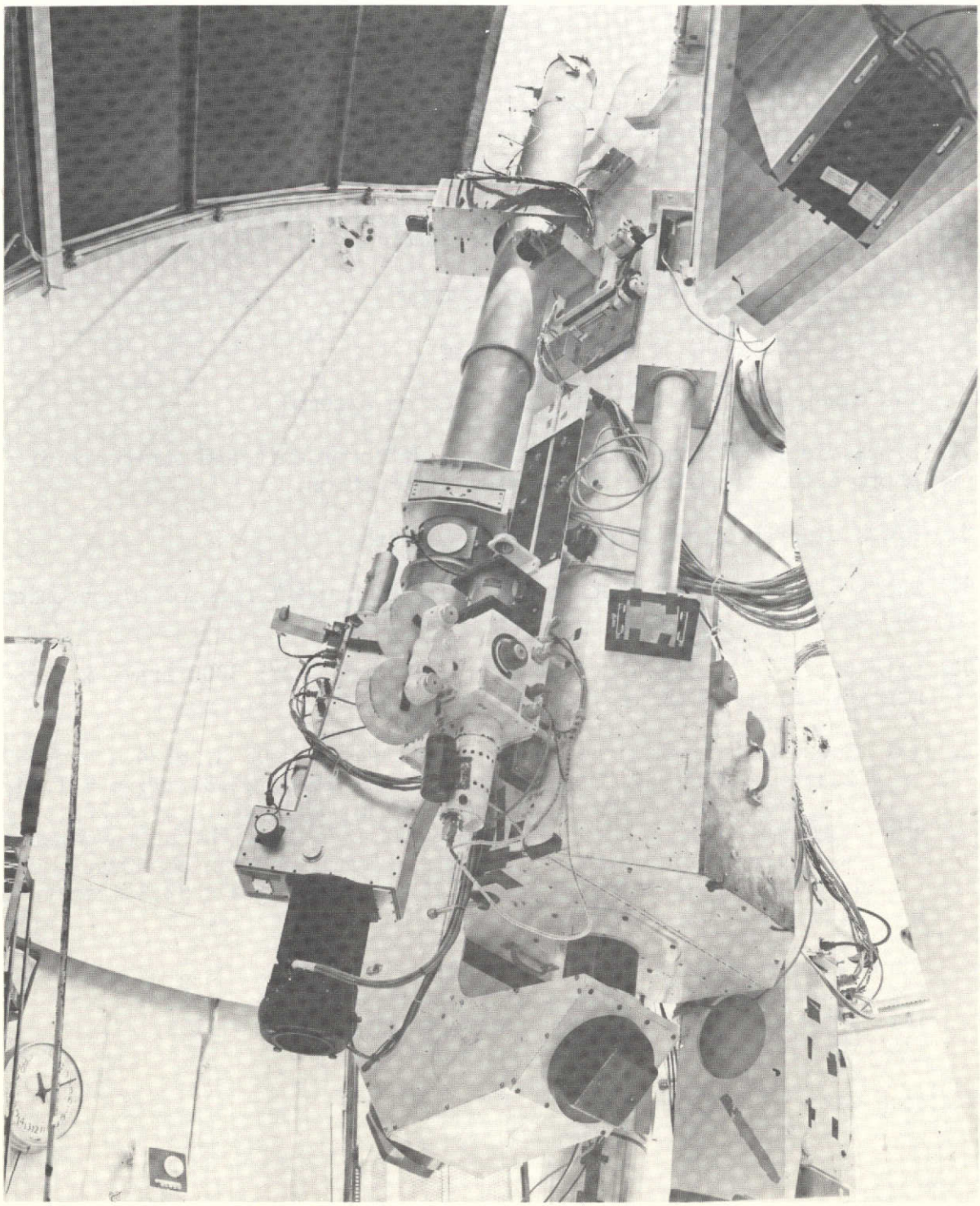

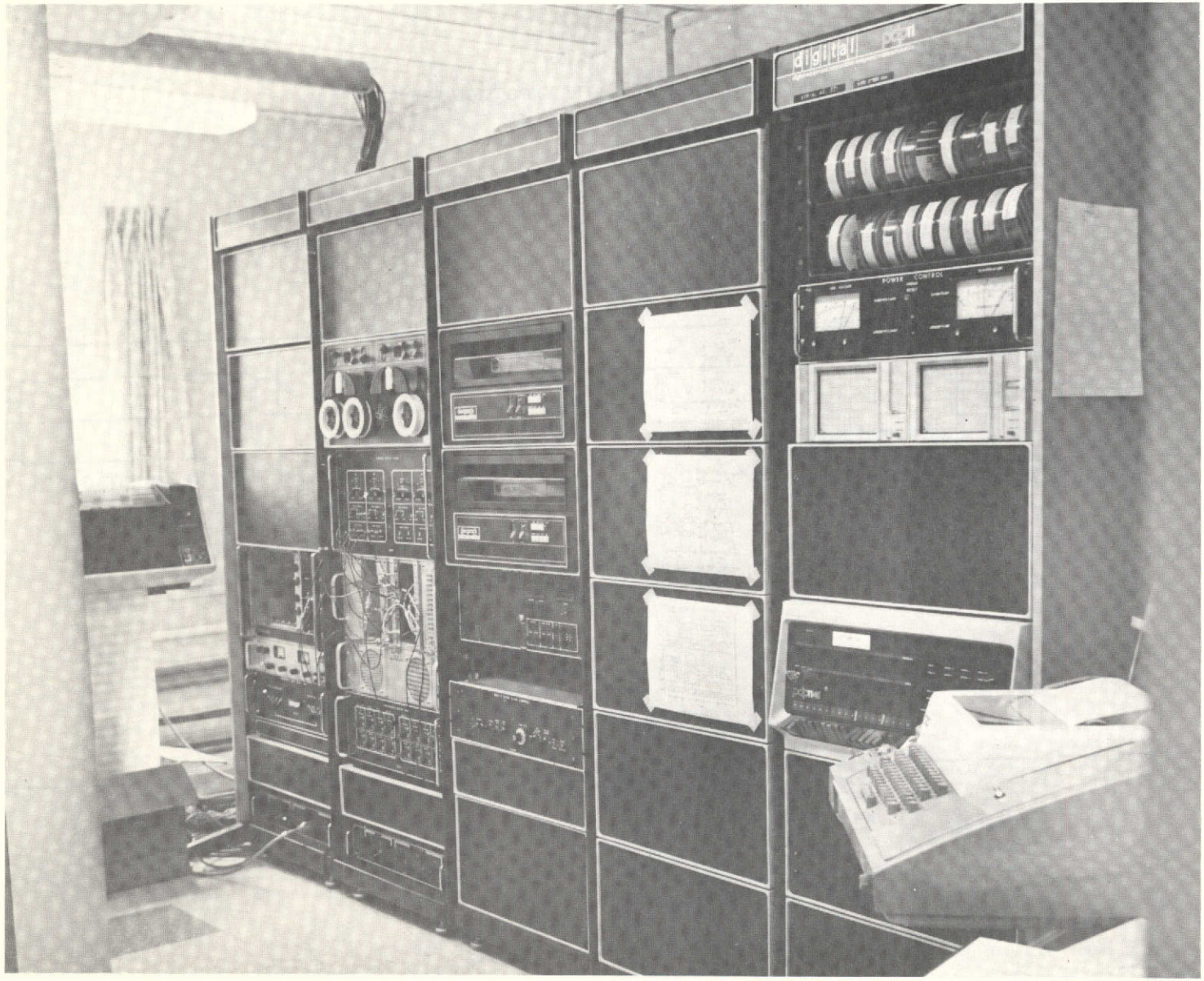
digital
POWER CONTROL

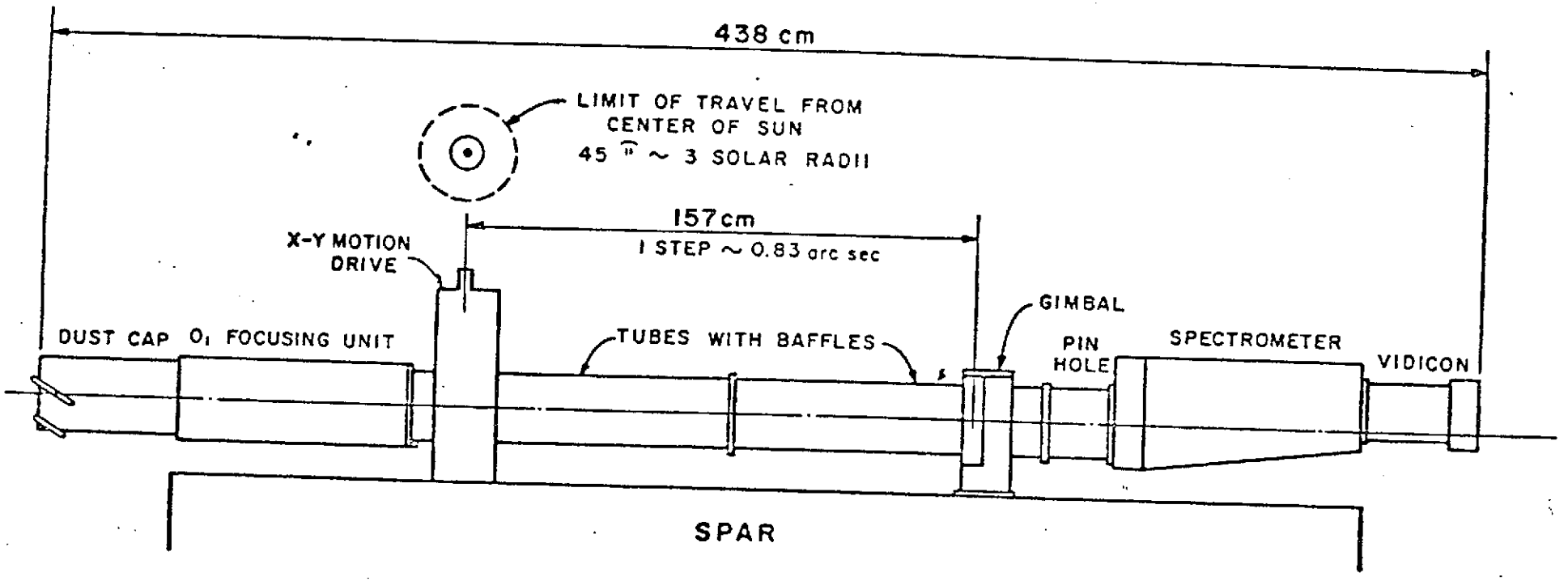

Figure 3.
Overall mechanical view of the instrument.

ORIGINAL PAGE IS
OF POOR QUALITY

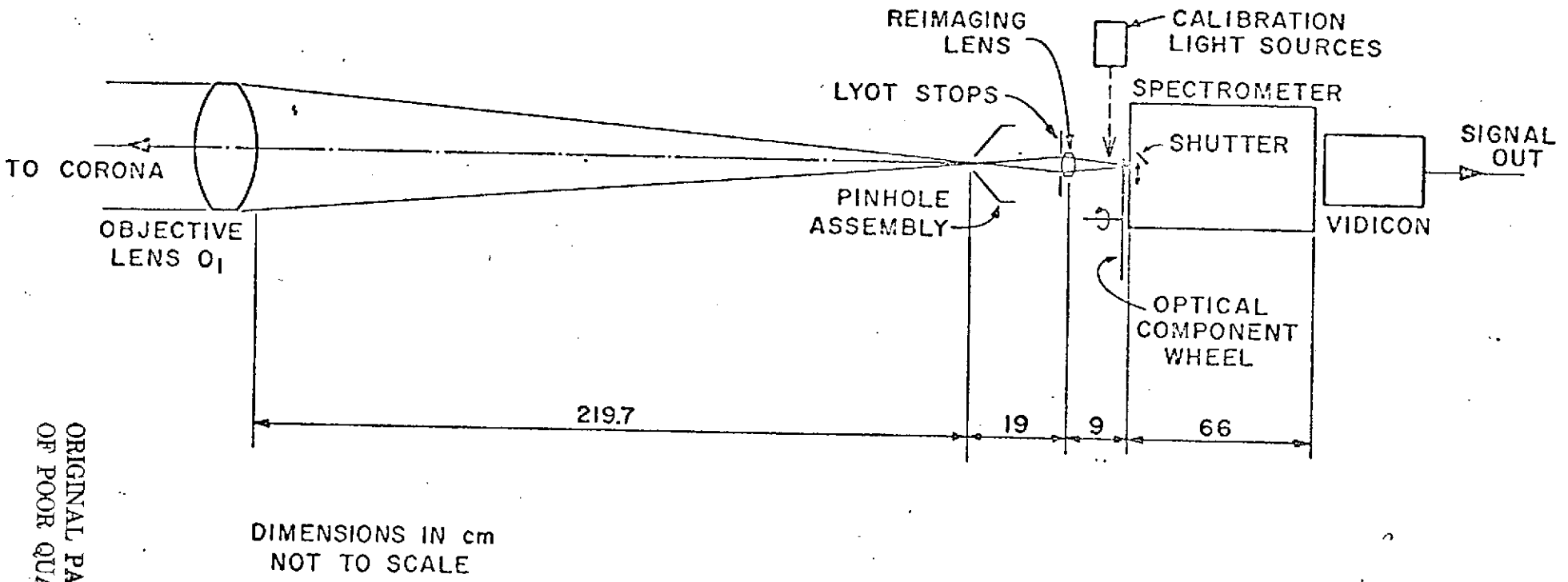

Figure 4.
Schematic drawing of the optical system.

ORIGINAL PAGE IS
OF POOR QUALITY

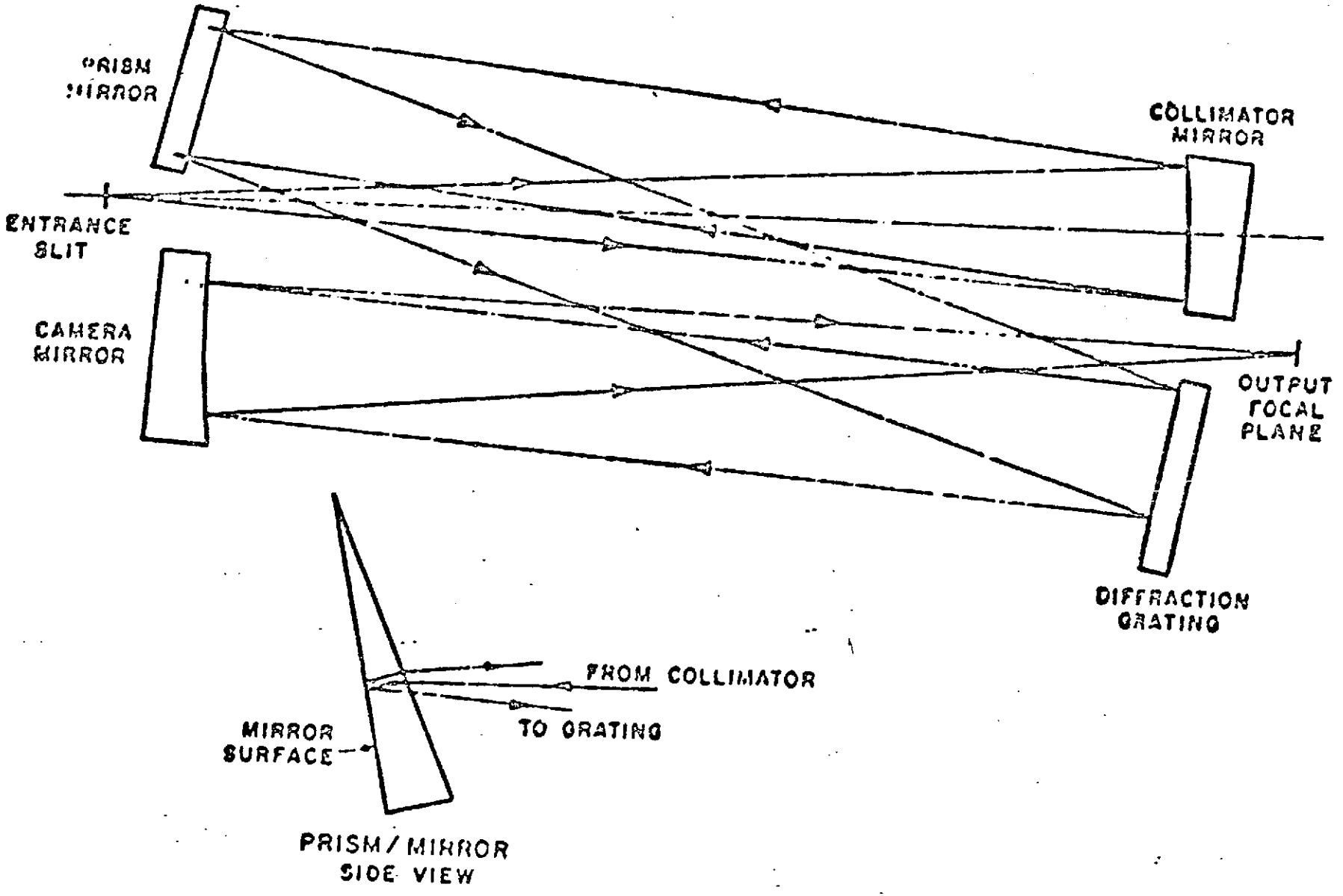

Figure 5.
Schematic drawing of the spectrometer.

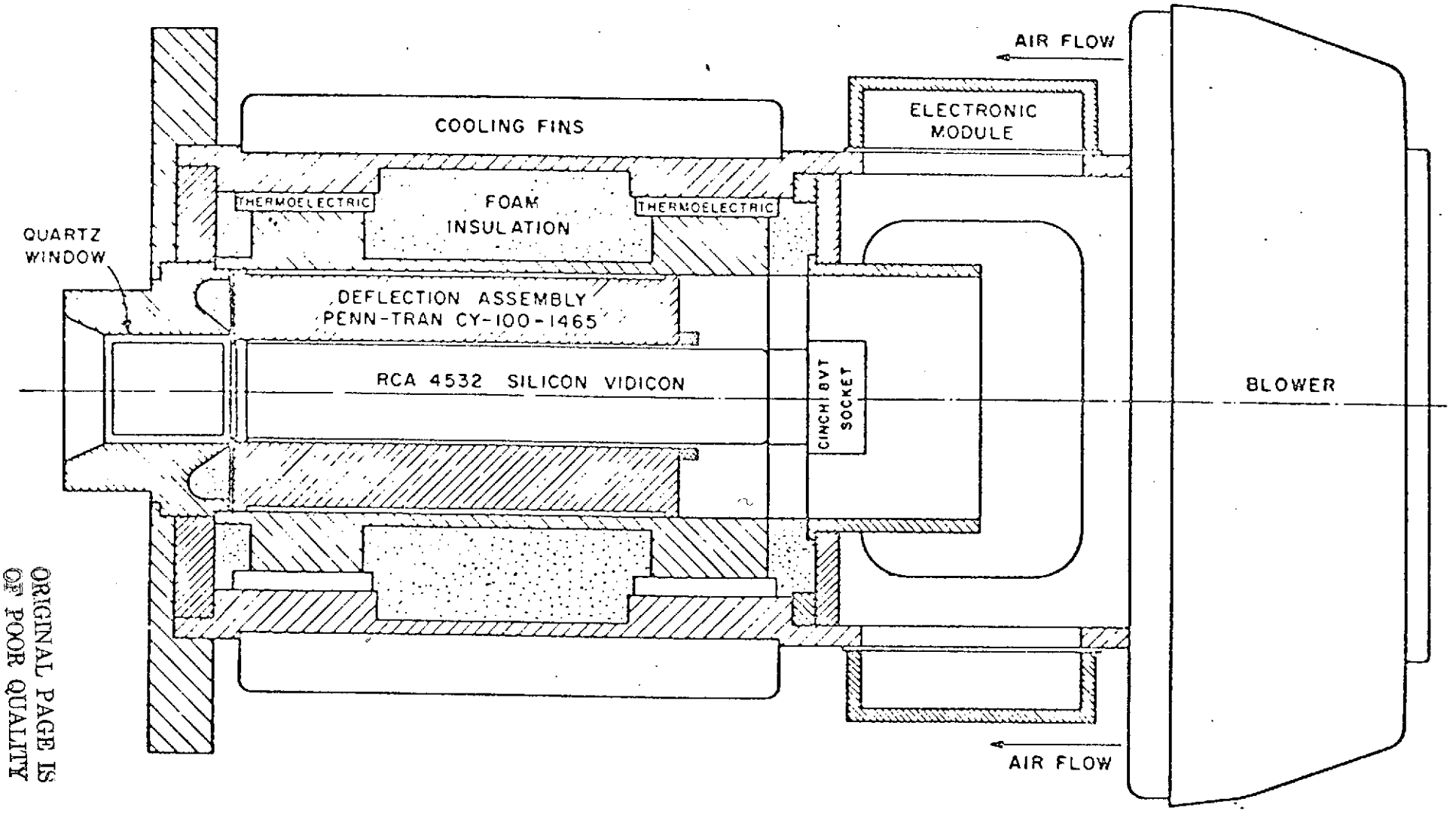

Figure 6.
Two-dimensional silicon-vidicon detector assembly.

ORIGINAL PAGE IS OF POOR QUALITY

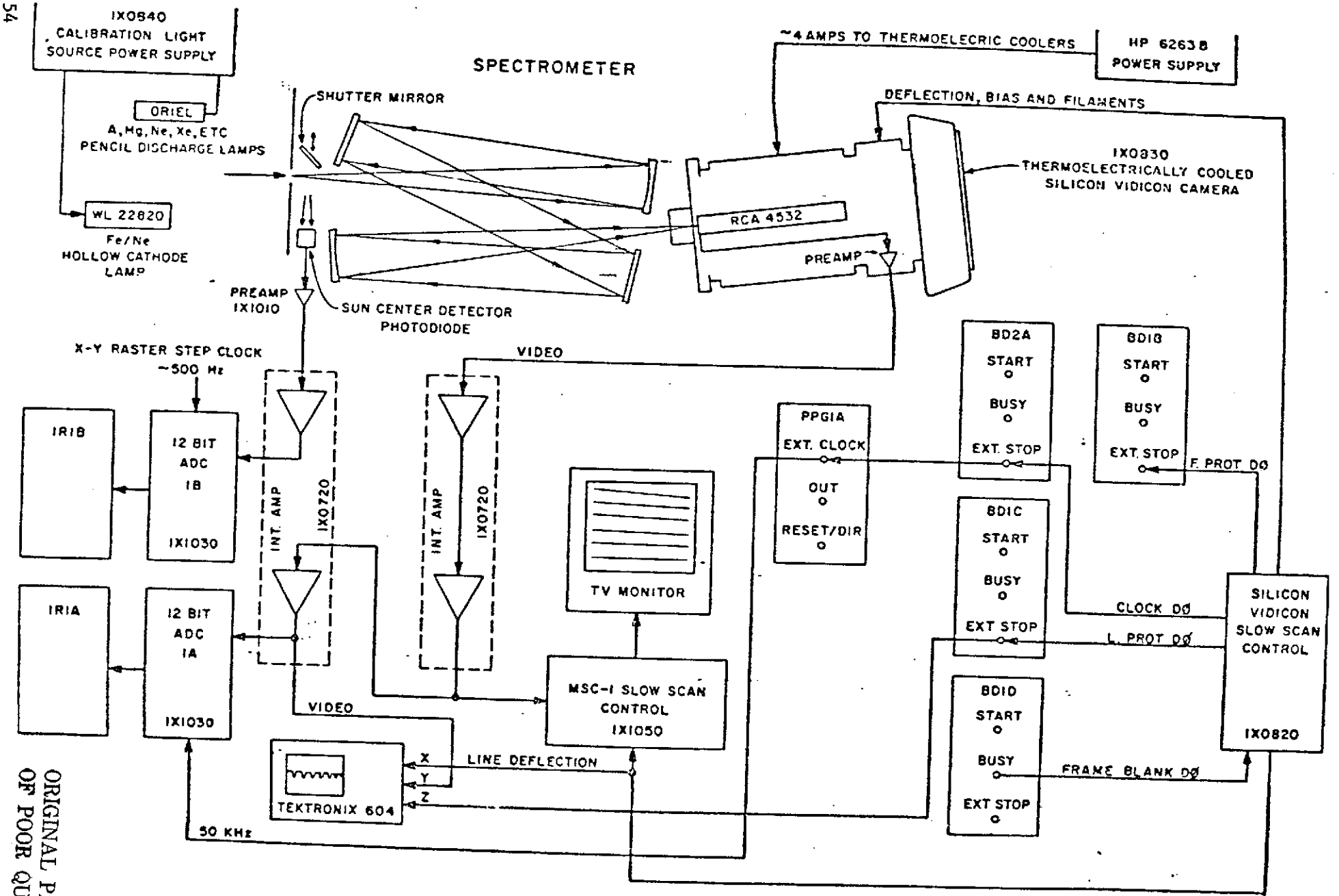

Figure 7.
Block diagram of the two-dimensional detector unit and sun-centering photo-diode electronics and system integration.

ORIGINAL PAGE IS
OF POOR QUALITY

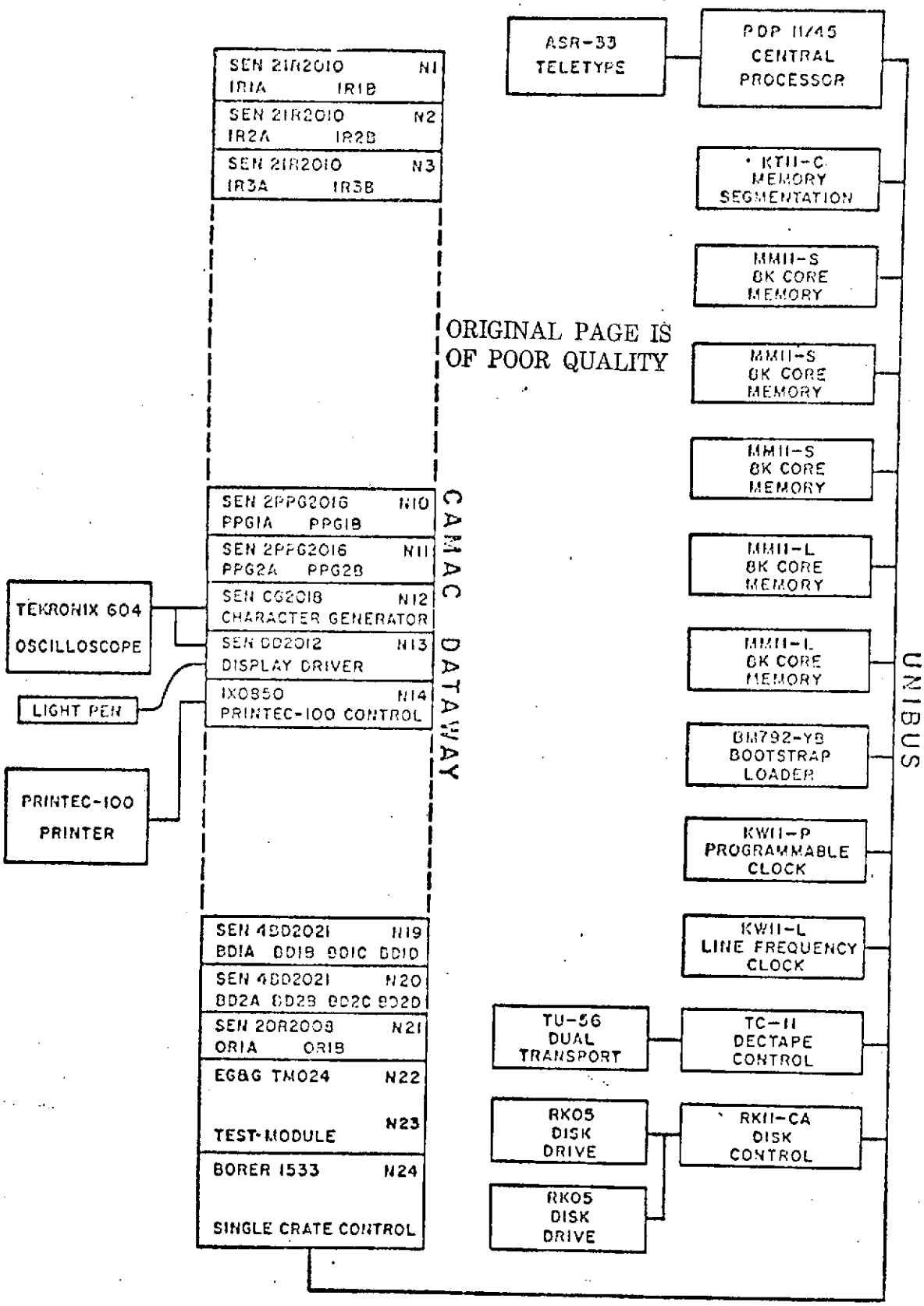

ORIGINAL PAGE IS
OF POOR QUALITY

Figure 8.
Block diagram of the computer configuration.

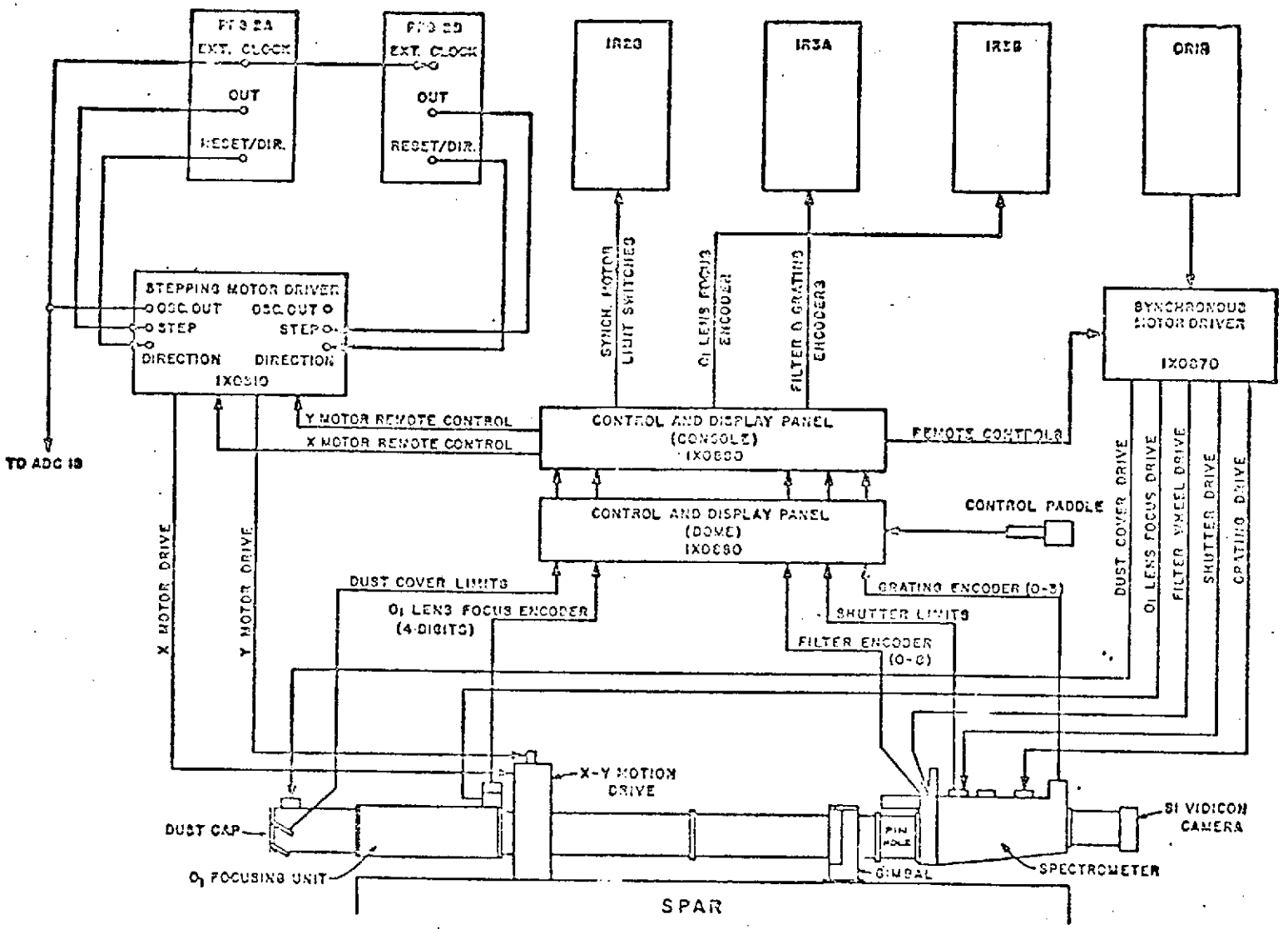

Figure 9.
Block diagram of the electromechanical instrument control electronics and system integration.

ORIGINAL PAGE IS
OF POOR QUALITY

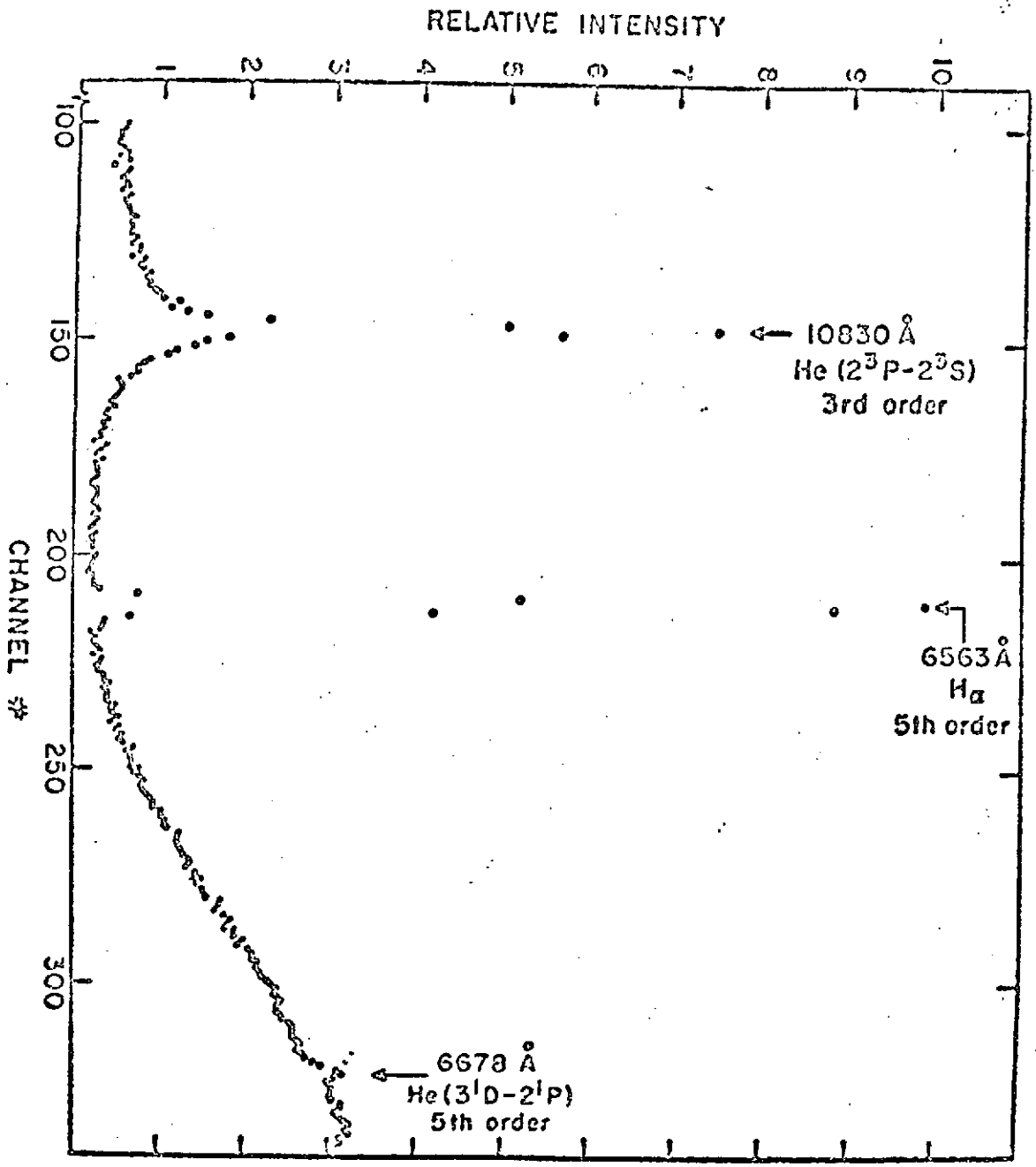

Figure 10.
Data of 24 June 1973, 2:05 uT; p = 1.04, θ = 262°; 3000 frame x 32.8 msec/frame; RG-10 filter; Aperture: 5″ x 20″.

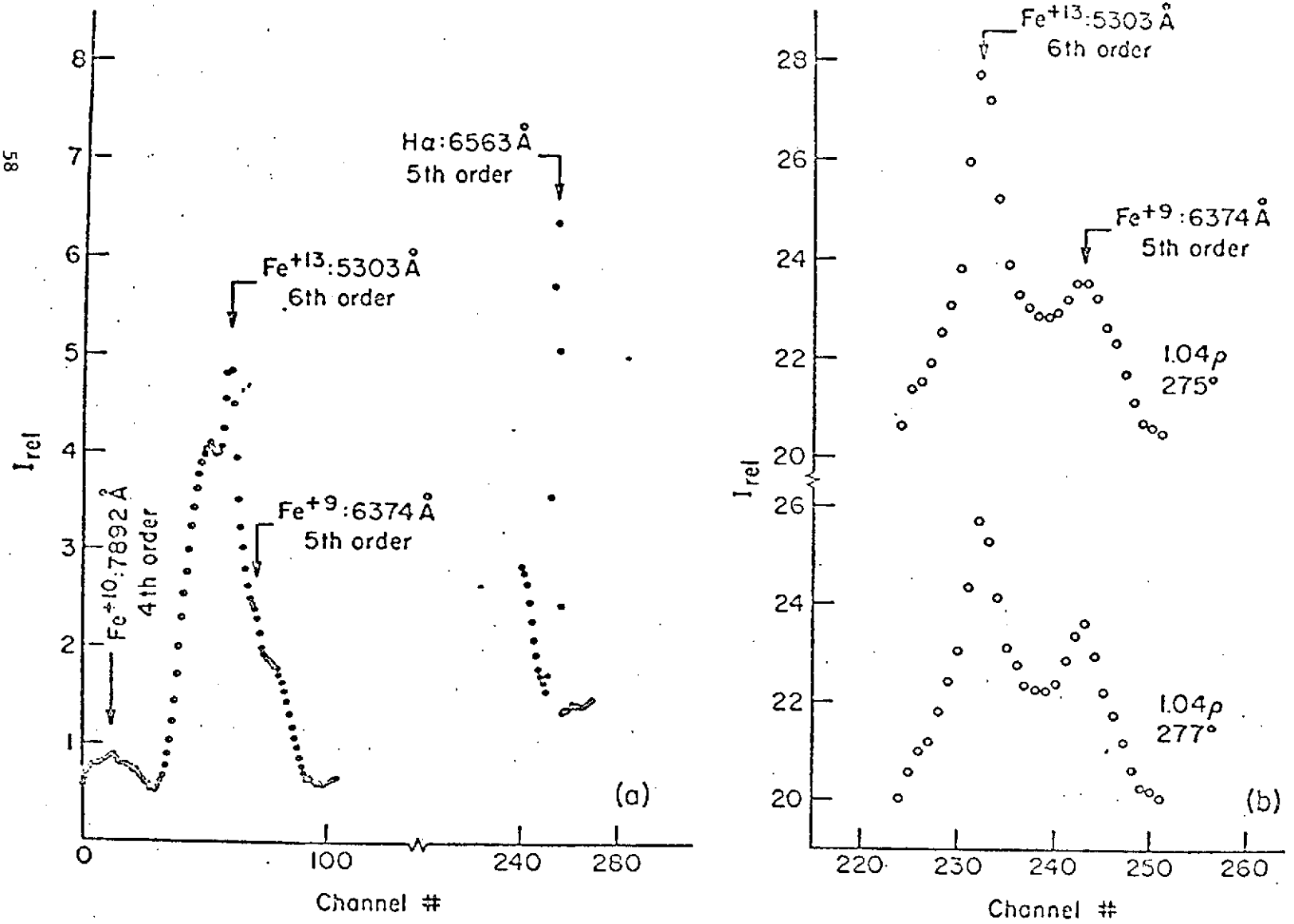

Figure 11.

(a) Spectrum showing the three coronal lines 5303 A, 6374 A and 7892 A, together with Hα. Data of 5 September 1973, 21:34 uT; p = 1.04, θ = 296°; 1000 frame x 32.8 msec/frame; Aperture: 5" x 20".

(b) Spectrum showing the 5303 A and 6374 A lines with the target slot/spectrum configuration used for simultaneous scan observations. Data of 11 September 1973, ∿21:25 uT; 500 frame x 32.8 msec/frame; Aperture: 5" x 20".

ORIGINAL PAGE IS
OF POOR QUALITY

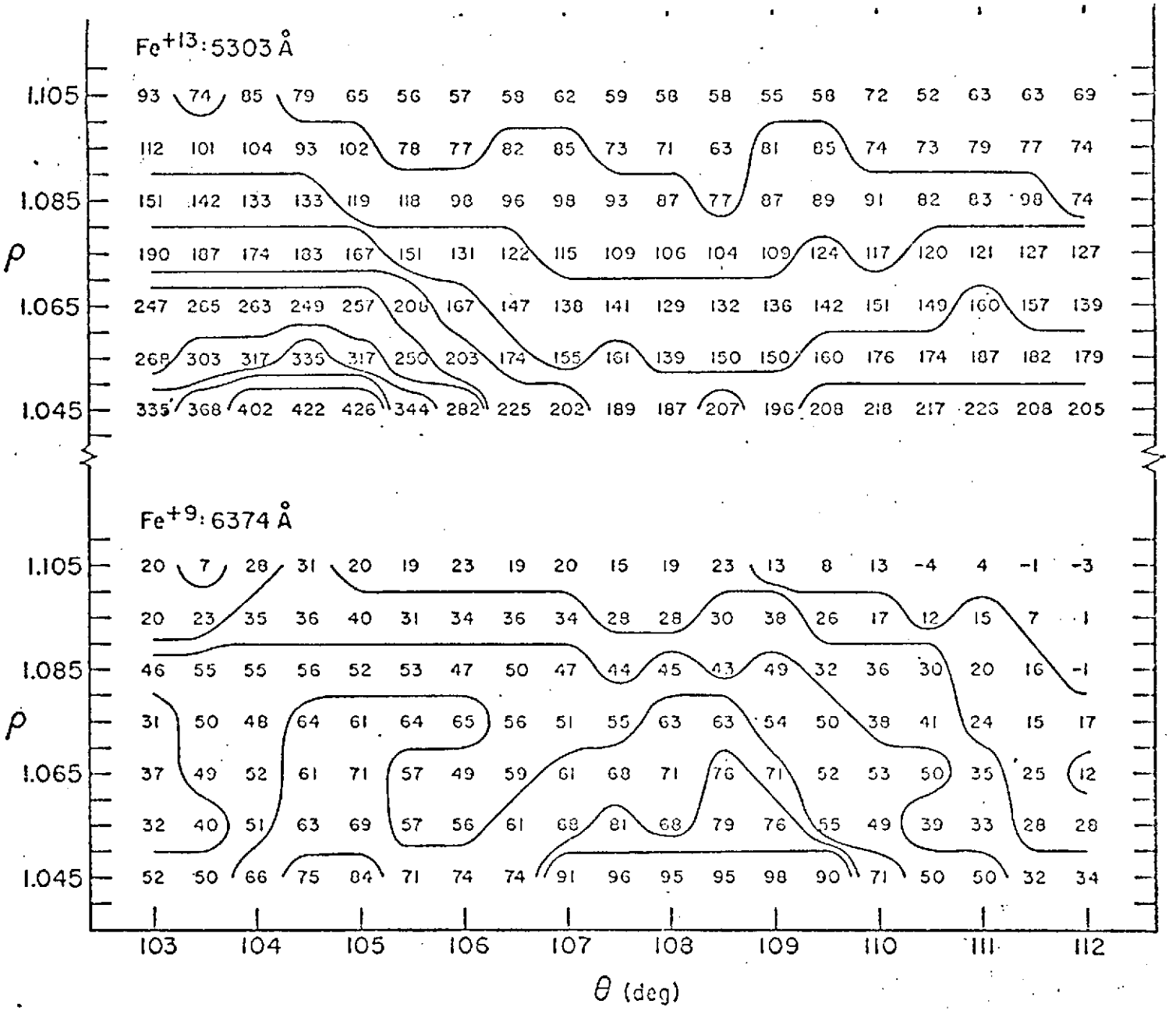

Figure 12.
Simultaneous 5303 A and 6374 A emission line scan. Data of 18-19 September 1974, 23:19-00:01 uT; the numbers denote absolute line intensity in units of erg cm^{-2} sec^{-1} $ster^{-1}$; $\Delta I_{abs} = \pm 15\%$, $\Delta I_{rel} = \pm 15$ erg cm^{-2} sec^{-1} $ster^{-1}$; $R_{\odot} = 956.7''$.

ORIGINAL PAGE IS
OF POOR QUALITY

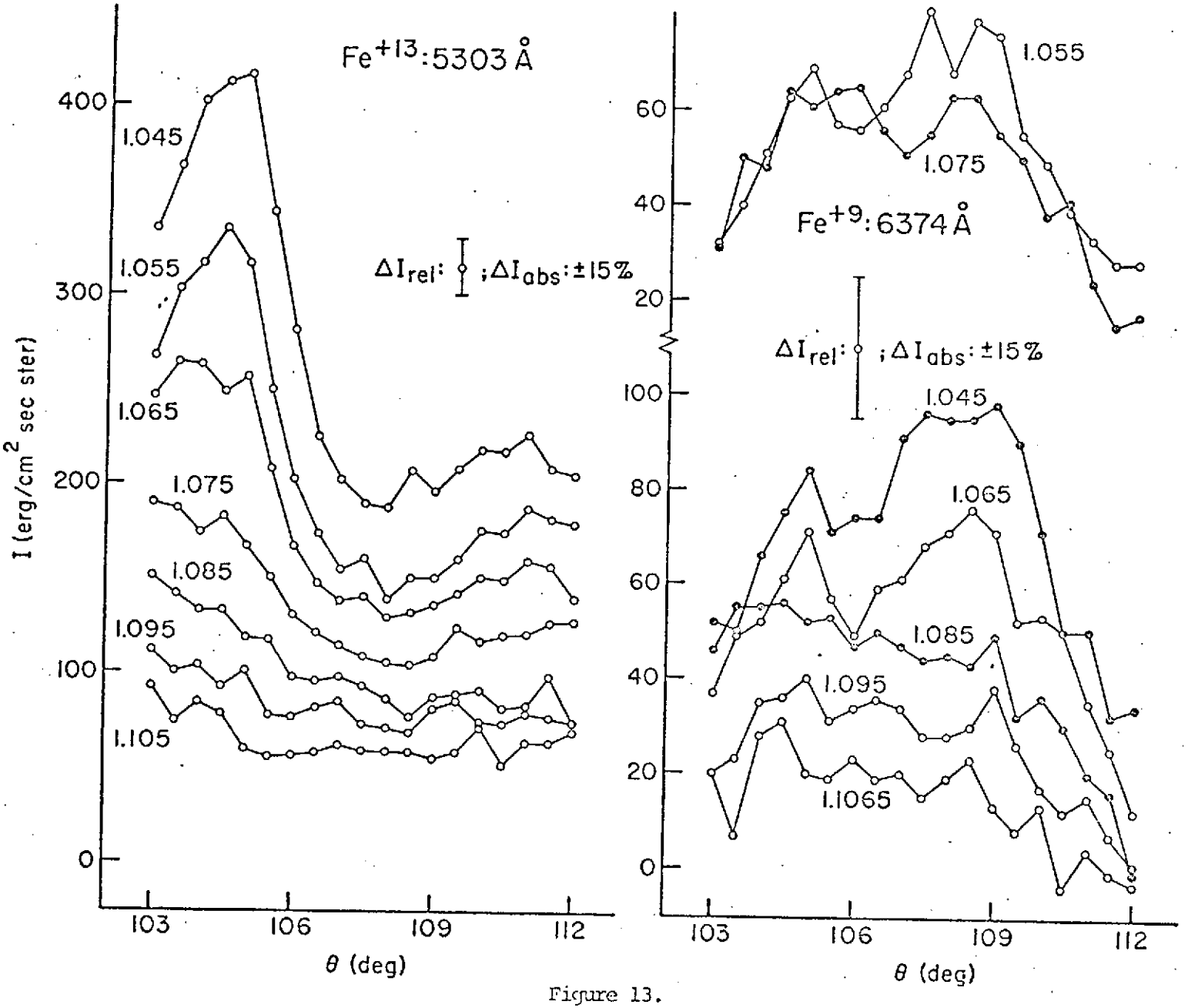

Figure 13.
Same data as for Figure 12.

PUBLICATIONS

The scientific papers that have resulted from the work performed under this contract are reprinted in this Section. They include, in order:

1. D. A. Landman, F. Q. Orrall, and R. Zane, "Astronomical Observations with Television-Type Sensors," University of British Columbia (1973), p. 255.

2. D. A. Landman, F. Q. Orrall, and R. Zane, Solar Physics Division meeting of the American Astronomical Society, 9-11 Jan. 1974, paper P4 (Abstract only).

3. D. A. Landman, Solar Physics 30, 371 (1973).

4. G. D. Finn and D. A. Landman, Solar Physics 30, 381 (1973).

5. D. A. Landman, Solar Physics 31, 81 (1973).

Appendix B

LMSC Spectra-Spectroheliograph Final Report

FINAL REPORT

Section I

THE SPECTRA SPECTROHELIOGRAPH SYSTEM

May 1974

Prepared for

George C. Marshall Space Flight Center
Huntsville, Alabama 35812

Contract No. NAS8-28018

Principal Investigator: Dr. A. M. Title

Lockheed Solar Observatory
Lockheed Palo Alto Research Laboratory
3251 Hanover Street
Palo Alto, California 94304

TABLE OF CONTENTS

		Page
SECTION I		
	THE SPECTRA SPECTROHELIOGRAPH SYSTEM	
A.	SUMMARY	1
B.	MEASUREMENT OF MAGNETIC FIELDS BY FOURIER TRANSFORM TECHNIQUES	3
	APPENDIX I	29
	APPENDIX II	37
C.	CONTOUR MAPS OF A HIGH GRADIENT REGION	47
D.	DATA REDUCTION PROCESS	51
E.	THE FLARE OF 5 SEPTEMBER 1973 - A FILM	57
SECTION II		
	OPERATORS MANUAL FOR THE MAGNETOGRAPH PROGRAM	
SECTION III		
	OPERATORS MANUAL FOR MICRODENSITOMETER CONTROL PROGRAM	

A. SUMMARY

The basic objective of the contract was to create a system capable of producing maps of the magnetic field straight from spectra. The theory of the extraction of magnetic field information is contained in Section I in Part B on measurement of the magnetic field by fourier transform techniques. Part C contains contour maps of a high gradient magnetic field region. Section II is an operators manual, program description, and the Fortran coding for the implementation of the measurement procedures. Section III is an operators manual for microdensitometer which also contains the machine coding for the control computer.

Data on the magnetic field was taken at Kitt Peak during the first and second manned Skylab missions. Due to construction of a new solar magnetic field measuring facility at Kitt Peak maintenance of the main Kitt Peak Solar telescope suffered. Unfortunately during the period of reduced maintenance the main heliostat drive developed severe shake problems in light to moderate winds. The amplitude of the oscillation of the image was often 30 arc seconds and could exceed an arc minute. Because the oscillations were an appreciable fraction of a sun spot diameter there was little point to observing during the third manned mission.

In addition to the data taken at Kitt Peak, Lockheed Observatory operated its multislit spectrograph during the Skylab mission. On 5 September 1973 at 18:00 UT there was a class 1B flare that was well covered by the Skylab instruments as well as the Lockheed multislit system. Because of the basic similarity of the multislit and the spectroheliograph data it was reasonably straightforward to produce densitometer tracings of the flare region. A description of the flare reduction procedure is contained in Part D of Section I.

The densitometer traces of the flare represent the first ground based record of the hydrogen alpha spectrum with such complete temporal and

spatial resolution. In order to demonstrate and properly illustrate the spatial and temperal development of the Hα flare a short movie has been produced. The movie includes the original multislit data and the tracings of the flare region. Part E of Section I is a description of the movie.

In addition to the solar useage of the densitometer we have actively encouraged use of the system by outside users and have made the operating system of the densitometer generally available. The manufacturer of the densitometer now distributes program TRACE as contained in Section III as the normal operating system for desk based PDP-11 systems. Two systems, one at JPL and the other at Nice Observatory in France, are in operation. The National Science Foundation has funded the University of California, Berkeley, to essentially duplicate the Lockheed system. The Naval Observatory Station at Flagstaff is also in the process of acquiring a duplicate of the Lockheed system.

Students and staff of the Universities of California and Southern California and the Center for Astrophysics have used the system. One of the users was able to trace an image tube echelle spectra. The automatic tracing of the echelle plate would have been impossible on any other densitometer. The special curve following routines that adjoin program TRACE 3 which make echelle tracing possible will be published shortly. When the routines are in final form they will be supplied to the TRACE user's group.

B. MEASUREMENT OF MAGNETIC FIELDS BY FOURIER TRANSFORM TECHNIQUES

1. INTRODUCTION

Although there are currently a number of instruments that measure the longitudinal component of the solar magnetic field, there are very few systems that attempt to measure the vector field. The measurement of the vector field can be especially difficult in and around sunspots. We shall present in this paper a method for the measurement of the vector field in high field regions. The method is based on the fourier transform properties of circularly and linearly polarized spectra arising from simple Zeeman triplets.

Beckers[1] has briefly noted that Fourier spectroscopy and the resulting fourier transformed profiles are useful for directly determining field properites. In the discussions below we will amplify on the advantages and some of the shortcomings of the analysis of the transformed profiles. It will be demonstrated that when Zeeman splitting is on the order of half of the full width at half maximum (FWHM) of the basic line profile, then the magnitude of the field, the inclination of the field, the azimuthal angle of the field, and the velocity can be determined independent of the shape of the line profile, if the line profile obeys certain reasonable assumptions. In the sections on analysis of the errors in the fourier transform method, what constitutes a reasonable line profile will be discussed.

The methodology presented here has been successfully implemented. The basic data are pairs of spectra in right and left circular polarized light and three pairs of orthogonal linear polarizations. The data acquisition system is called a spectra-spectroheliograph and has been discussed in some detail by Title and Andelin[2]. Data are microdensitometered and digitized using a filter densitometering system described by Schoolman[3]. The digitized data are organized, reduced to absolute intensities, and analyzed with a set of programs described by November[4]. In this paper we shall not present actual magnetograms. The magnetograms will be discussed in a series of papers on the vector field in sunspots.

2. FOURIER TRANSFORM PROPERTIES

Circular Polarizations

For a normal absorption Zeeman triple in unpolarized light, the profile has the form:

$$p\,(\lambda-\lambda_o) = M(\lambda) - A'\left[f(\lambda-\lambda_o+\Delta) + h(\lambda-\lambda_o-\Delta)\right] - B\,g(\lambda-\lambda_o), \qquad (1)$$

where λ_o is the central wavelength of the line in the absence of a field; $M(\lambda)$ is the continuum intensity; f,h and g are the individual profiles of the displaced and undisplaced components; Δ is the Zeeman splitting; and A' and B are parameters that depend on the angle of the field and the properties of the atmosphere.

In the region of a line, we shall assume a constant continuum intensity. Then, for convenience, we drop the constant and treat the profile as an emission profile. Further, we shall assume:

$$f(\lambda-\lambda_o) = g(\lambda-\lambda_o) = h(\lambda-\lambda_o), \qquad (2)$$

and that the profiles are symmetric:

$$f(\lambda-\lambda_o) = f(\lambda_o-\lambda). \qquad (3)$$

Using assumptions (2) and (3) and dropping the continuum intensity, the Zeeman profile observed in unpolarized and right and left circularly polarized light can be written:

$$p(\lambda-\lambda_o) = A'\left[f(\lambda-\lambda_o+\Delta) + f(\lambda-\lambda_o-\Delta)\right] + B\,f(\lambda-\lambda_o) \qquad (4)$$

$$p_{\begin{pmatrix}RCP\\LCP\end{pmatrix}} = \begin{pmatrix}A\\C\end{pmatrix} f(\lambda-\lambda_o+\Delta) + \begin{pmatrix}C\\A\end{pmatrix} f(\lambda-\lambda_o-\Delta) + B\,f(\lambda-\lambda_o) \qquad (5)$$

where

$$A' = A + C.$$

The fourier transforms of equations (4) and (5) are:

$$p(t) = [2(A+C)\cos\Delta t + B]\,\tilde{f}(t) \tag{6}$$

$$p_{\binom{RCP}{LCP}}(t) = [(A+C)\cos\Delta t + B]\,\tilde{f}(t)\ (\pm)i(A-C)\sin\Delta + \tilde{f}(t), \tag{7}$$

where:

$$\tilde{f}(t) = \int_{-\infty}^{\infty} f(u)\, e^{iut}\, du. \tag{8}$$

The tilde indicates a fourier transformed function. A catalog of circularly polarized profiles and the real and imaginary parts of their fourier transform is contained in Appendix I.

If the fourier transform of the basic profile (equation 8) does not have any zero crossings, and the field is not purely transverse (i.e., $A \neq C$), then the first zero of the imaginary part of the fourier transform of either circularly polarized profile yields the separation of the Zeeman components. That is, at:

$$\Delta t_1 = \pi,$$

$$\sin \Delta t_1 = 0$$

and

$$\Delta = \pi/t_1. \tag{9}$$

Since delta is directly proportional to the magnitude of the field strength, the zero crossing of the imaginary part directly determines the field strength. The fourier transforms of common profile functions, Lorentzian, Gaussian and Voight profiles, have no zero crossings.

If (A+C) is greater in magnitude than B, then the real part of equation (7) or equation (6) can be used to obtain the field strength. Since (A+C) is greater than B, the first zero occurs when:

$$\Delta t_2 = \pi/2 + \epsilon, \tag{10}$$

and the second zero when:

$$\Delta t_3 = \frac{3}{2}\pi - \epsilon, \tag{11}$$

where ϵ is smaller than $\pi/2$.

Hence,

$$\Delta = \frac{2\pi}{(t_2 + t_3)} \quad . \tag{12}$$

In addition, the fourier transform of the circular polarized profiles readily yields the inclination of the field. The slope at the origin of the imaginary part of either circular polarization transform (equation 7) is:

$$C_1 = (A-C)\ \Delta\ \tilde{f}\ (o), \tag{13}$$

while the value of the real part of the transform at the origin is:

$$C_o = (A+B+C)\ \tilde{f}\ (o). \tag{14}$$

The ratio of C_1 to C_o is then independent of the profile shape:

$$C_1/C_o = \frac{(A-C)}{(A+B+C)}\ \Delta. \tag{15}$$

Since delta is known from the value of the zero crossing, a quanity SS may be defined such that

$$SS = C_1/C_o\ \Delta$$

$$SS = \frac{(A-C)}{(A+B+C)} \quad . \tag{16}$$

The value of $\Delta t_1/2$ is $\pi/2$, hence the cosine at $\Delta t_1/2$ is zero while the sine is unity. Therefore, the ratio of the real and imaginary parts of equation (7) yields:

$$C_2 = \pm\left(\frac{B}{A-C}\right) . \tag{17}$$

Again, using the assumption that (A+C) is greater than B, the first zero of the real part of the transform occurs when:

$$\cos(\Delta t_2) = \left(\frac{-B}{A+C}\right). \tag{18}$$

Combining (17) and (18), we obtain:

$$C_3 = (\mp) \left(\frac{A-C}{A+C}\right). \tag{19}$$

For most models of line formation, the quantity C_3 is directly related to the cosine of the angle of inclination. C_3 has the additional advantage that it is independent of the central component.

When the Seares' relations are valid,

$$A = 1/4\ (1 \pm \cos\gamma)^2 \tag{20}$$

$$B = 1/2\ \sin^2\gamma \tag{21}$$

$$C = 1/4\ (1 \pm \cos\gamma)^2, \tag{22}$$

where γ is the inclination of the field to the line of sight.

Using Seares' relation, result (16) is just:

$$SS = \cos\gamma. \tag{23}$$

Besides yielding the magnitude and inclination of the field, the sum of the right and left circular polarizations determine the Doppler shift. The fourier transform of the sum (the unpolarized Zeeman profile), is a symmetric function about the central wavelength of the profile. Hence its transform is real. Therefore, the fourier transform with respect to any other wavelength λ_s must be of the form:

$$\tilde{p}_s\ (t) = e^{ist}\ \tilde{p}\ (t), \tag{24}$$

where

$$s = \lambda_s - \lambda_o. \tag{25}$$

Since p(t) is real, the inverse tangent of the ratio of the imaginary and real parts of $p_s(t)$ yields the offset, s:

$$s = \tan^{-1} [\mathrm{Imag}\ (\tilde{p}_s[t]) \ / \ \mathrm{Real}(p_s[t])\ ]. \tag{26}$$

The velocity shift with respect to the undisplaced wavelength λ_o is:

$$v = sc/\lambda_o, \tag{27}$$

where c is the velocity of light.

Linear Polarizations

Using the same assumptions as used in equation (4) for circularly polarized light, Zeeman profiles observed through a linear polarizer at angle phi with the projection of B in the azimuthal plane has the form

$$p_\varphi\ (\lambda) = E_\varphi\ [f(\lambda-\lambda_o+\Delta) + f(\lambda-\lambda_o-\Delta)] + F_\varphi\ \ f(\lambda-\lambda_o), \tag{28}$$

where E_φ and F_φ are functions of gamma and phi. The fourier transform of equation (28) is:

$$\tilde{p}_\varphi(t) = [2E_\varphi\ \ \cos\Delta t + F_\varphi\ ]\ \tilde{f}(t). \tag{29}$$

In the case that Unno's relations[6] hold:

$$E_\varphi = \alpha/4(1 + \cos^2\gamma - \sin^2\gamma\ \sin 2\varphi) \tag{30}$$

$$F_\varphi = \beta/2(1 + \sin 2\varphi)\ \sin^2\gamma\ , \tag{31}$$

where α and β are functions of the absorption parameters that describe the line and of the angle γ. For weak lines, α and β are unity.

It is useful to analyze the sum and difference of orthogonal pairs of linearly polarized profiles. Using relations (30) and (31), the sum and difference transforms are:

$$\tilde{p}_{S\,\varphi}(t) = [\alpha(1 + \cos^2\gamma)\cos\Delta t + \beta\sin^2\gamma]\,\tilde{f}(t), \tag{32}$$

$$\tilde{p}_{D\,\varphi}(t) = [-\alpha(\sin^2\gamma\sin 2\varphi)\cos\Delta t + \beta\sin^2\gamma\sin 2\varphi]\,\tilde{f}(\epsilon). \tag{33}$$

A catalog of linear polarization profiles and their sum and difference fourier transforms is contained in Appendix II.

If β is less than or equal to α, the sum transform will be zero for the values of t symmetric about $\Delta t = \pi$. That is, at:

$$\Delta t_3 = \pi - \epsilon\ ,$$

and $$\Delta t_4 = \pi + \epsilon,$$

the sum transform is zero. Hence:

$$\Delta = \pi/(t_3 + t_4). \tag{34}$$

Then, given the value of Δ, the sum and difference transforms can be compared at t_2 such that Δt_2 is $\pi/2$. Then:

$$\left.\frac{p_{S\,\varphi}}{p_{D\,\varphi}}\right|_{\Delta t_2=\pi/2} = \sin 2\varphi\ . \tag{35}$$

Hence, a pair of linear polarizations can yield the azimuthal angle of the field. Because of the possibility that the field is 0 or 90° (parallel or perpendicular) to the analyzer, it is useful to analyze several orthogonal pairs. Also, since the sum profile is a symmetric function, the velocity shift can also be obtained with a pair of linear polarizations.

3. ACCURACY AND LIMITATIONS OF THE FOURIER TRANSFORM METHOD

Total Field Strength

From the discussion above, the magnitude of the magnetic field, the angle to the line of sight, the azimuthal projection, and the line of sight velocity are readily available from the fourier transforms of the line profiles. However, as with any measurement method, there are problems that occur because of both random and systematic errors. The fourier transform method is remarkably insensitive to some classes of error or noise and sensitive to others.

The measurement of Δ, and hence the total field strength, $|B|$, is straightforeward. It depends only on the zero crossing of the imaginary part of the circular polarization transform. The accuracy of the zero crossing technique increases as the magnetic splitting increases with respect to the width of the basic profile. The fundamental reason for the improvement in accuracy with large splitting to width ratio is that the larger the splitting, the lower the spatial frequency at which the zero crossing occurs, while the narrower the profile, the higher in spatial frequency its transform has significant amplitude. Because of its fundamental importance, the ratio of splitting to full width at half maximum (FWHM) shall be defined as:

$$Q = \Delta/\mathrm{FWHM}. \tag{36}$$

The amplitude of the imaginary part of a circular polarization transform is proportional to cosine gamma. Thus, the zero crossing determination will also depend on cosine gamma.

In order to get some measure of the effectiveness of the transform technique, a program was written to create artificial profiles that could then be subjected to various sytematic and random effects that

simulate some solar and measurement problems. To check the validity of the zero crossing procedure, Zeeman profiles were constructed using the Sears relations and Gaussian and Lorenzian profiles. The profiles so constructed were subjected to random noise proportional to the maximum signal value of the undisturbed profile. These synthetic profiles were then transformed and analyzed for the first zero crossing. By repeated evaluation of the same profile subjected to random noise, it was possible to calculate the standard deviation of the zero crossing versus percentage noise in the profile. The procedure was carried out for a variety of gammas and splitting-to-width ratios for both Gaussian and Lorentzian line shapes.

Upon completion of the analysis, it was found that, if the error in the zero crossing was normalized by cosine gamma, the percent error of the zero crossing was a function only of the ratio of the splitting to the width of the line profile, so that for a noise $n(P_{max})$ in the profile:

$$N_B \frac{n(B)}{B} = \frac{n(P_{max})}{P_{max}} N \cos \gamma, \tag{37}$$

where N_B is the noise reduction and $n(B)$ is the standard deviation in the measurement of B. Shown in Figure 1 is the noise reduction factor, the ratio of the noise in the profile to the noise in the zero crossing, versus Q, the ratio of the splitting to the full width at half maximum (FWHM) for Gaussian and Lorentzian profiles. From the figure it is seen that when the field is vertical at a magnetic splitting equal to FWHM, the noise in the measured field is reduced by a factor of 12 (Gaussian) from the noise in the profile. For a 60° inclination of the field, the reduction factor is 6 and for 75°, it is 3.

In order to measure $|B|$, the position of the unpolarized line center must be known accurately because an error in the center position will be reflected as an error measured in the splitting. For a pure longitudinal field, an error in the line center position will cause an

error of equal magnitude in the splitting for a single circular polarization. However, the centering error will cause an equal but opposite error in the splitting inferred from the opposite circular polarization. Thus, at least for longitudinal field, the mean splitting obtained from the sum of the right and left circular profiles will have the correct value.

For other than pure longitudinal fields, the centering error is somewhat more complex. From equation (24) in the presence of a centering error, s, and a splitting, Δ, the condition for the zero of the imaginary parts of the transform is:

$$A \sin t(s + \Delta) + C \cos t(s - \Delta) + B \sin ts = 0. \tag{38}$$

Since, in the absence of a centering error, the zero of the imaginary part occurs when:

$$\Delta t_1 = \pi,$$

in the presence of a small error condition (38) occurs when

$$\Delta t_s = \pi + \zeta t, \tag{39}$$

where ζ is just the splitting error.

Substituting (39) into (38) yields the relation between the centering and splitting error:

$$\Delta \sin t(s + \zeta) + C \sin t(s - \zeta) - B \sin ts = 0. \tag{40}$$

If the errors are small, then:

$$\zeta = \frac{(A + C - B)}{(A - C)} s. \tag{41}$$

Using the Seares relations, equation (40) becomes:

$$\zeta = \pm(\cos \gamma)s. \tag{42}$$

From results(41) and (42), the splitting error averages to zero when the splittings obtained from the right and left circular polarizations are averaged. Further when Seares relations hold, the error in $|B|$ caused by a centering error is diminished by the cosine of the inclination.

One of the assumptions of the fourier transform technique is that all three of the Zeeman components have the same profile shape. However, if the undisplaced profile is symmetric it may differ from the shape of the displaced components without affecting the value of the zero crossing because the imaginary part of the circular transform is free of all profile components that are symmetric about the profile center. The lack of dependence on the central component is very useful because it means scattered photospheric light or the existence of molecular lines centered on the profile do not affect the value of $|B|$.

Another transform assumption is that the profile shape is symmetric about the undisplaced center. There are at least two physical conditions which can cause line profile asymmetry - magnetic field gradients and velocity field gradients. Magnetic field gradients cause mirror asymmetry in the displaced profiles. That is, the profile displaced to high wavelengths is the mirror image of the component shifted to shorter wavelengths. In the case of the mirror asymmetry, the profile can be considered to be made of a sum of profiles that are shifted by differing amounts. Since the fourier transform procedure is a linear process, the zero crossing will reflect a weighted average magnetic splitting. In the case of a velocity gradient asymmetry, all three profiles are asymmetric in the same direction. The first effect of a velocity gradient will be an error in the center wavelength of the sum line profile. As discussed above, if

simultaneous profiles are obtained in right and left circular polarizations, the velocity error will increase the field estimated from one profile and decrease the field from the other. The order of the error will be the same, so that the average of the right and left circular polarization fields will be a good estimate of $|B|$ and the difference will be a measure of the velocity gradient error.

Even if the line profiles are symmetric and well centered, the fourier transform can still yield erroneous results for $|B|$ if there exist photometry errors. To get an idea of the magnitude of this error, profiles of the form:

$$p_\delta(\lambda) = p(\lambda)^{1+\delta} \tag{43}$$

were analyzed. It is clear that for pure longitudinal fields that the value of the zero crossing is unaffected by δ. However, as the field inclination increases, the effect of non-zero δ on the zero crossing increases. On the other hand, as Q increases, the effect of non zero δ should decrease, since the profile components overlap region decreases. Shown in Figure 2 are plots of percent error in the zero crossing versus inclination of field for $\delta = -.05$ and $-.1$ for $Q = .5$. Shown in Figure 3 are plots of percent error in the zero crossing verus Q for the same values of δ for a field inclination of 82°. Negative values of δ cause an increase in the splitting values while positive values cause a decrease of splitting. For values of $\delta < |.08|$ the magnitude of the crossing error is nearly independent of sign of δ. Note that the values of Q and γ used in Figures 2 and 3 respectively were chosen to illustrate maximal error sensitivity.

In practice, it should be possible to correct the photometry so that the error in δ is less than $|.05|$.

4. THE INCLINATION OF THE FIELD

Once the value of $|B|$ is known, the inclination can be determined as indicated by the series of results (17), (18) and (19). Result (19) yields cosine γ independent of the value of the central component and

only requires Unno's relations to hold. However, since result (19) is independent of the central component, it cannot be expected to be of much value for small values of the ratio A/C. For inclinations of less than 45°, $A/C < .03$. But by 60°, $A/C = .11$. Thus, it should not be surprising if the accuracy of cosine γ markedly deteriorates at inclinations of less than 45°.

For angles of inclination less than 45°, the slope at the origin of the imaginary part of the transform can be utilized. However, not only does this method require that Seares relation hold, but perhaps more importantly, introduces dependence on the strength of the possibly contaminated central component. Another method of obtaining cosine γ is to take advantage of the properties of linear polarization transforms, since these depend on sine gamma.

The method used to obtain result (19) can be improved upon. Since the value of Δ is known, the ratio of the real to the imaginary part of the transform can be multiplied by $\sin \Delta t$ to create a function:

$$RS(t) = \frac{(A+C)\ \cos t\Delta + B}{(A-C)} . \tag{44}$$

The integral of the product of $RS(\Delta t)$ and the first two Legendre polynomials properly normalized over the range in Δt for 0 to π yield

$$\int RS(\Delta t)\ d(\cos\Delta t)\ P_o = \left(\frac{B}{A+C}\right) \tag{45}$$

$$\int RS(t)\ d(\cos\Delta t)\ P_1 = \left(\frac{A+C}{A-C}\right) . \tag{46}$$

Since the Lengendre polynomials are orthogonal functions, the integrals of $RS(\Delta t)$ times higher order polynomials yield information on the degree of asymmetry and or differences between the central and displaced components in the line profiles.

The value of the integral approach of equation (46) is that a significant portion of the transformed function is used rather than the single point which is used for result (19). However, the formation of

$RS(\Delta t)$ entails dividing out a denominator that can take on zero values. By use of Gaussian quadrature, the points at which $RS(\Delta t)$ can become large can be avoided without loss of numerical accuracy. When the correlation coefficient of the error in $|B|$ and the error in cosine γ are evaluated from profiles subjected to random noise, for inclination greater than 45° and $Q > .5$, the correlation coefficient is less than .01.

Using the random synthetic profile program, the noise in cosine gamma was evaluated. As with the error in $|B|$, the noise in cosine γ is reduced by a factor normalized by cosine gamma. Thus, for an amount of noise $n(P_{max})$:

$$N_\gamma \frac{n(\cos \gamma)}{\cos \gamma} = \frac{n(P_{max})}{P_{max}} \cos \gamma, \tag{47}$$

and

$$n(\cos \gamma) = \frac{n(P_{max})}{P_{max} N_\gamma} . \tag{48}$$

Thus, the error in cosine gamma is independent of gamma. Shown in Figure 4 is a plot of N_γ versus Q. Relations (47) and (48) hold for angles greater than 45°. For angles less than 45°, methods for determining cosine γ from result (46) fail.

Since it is not until slightly under 15° that the ratio:

$A/B < .03$,

it can be expected that result (23) is useful between 15° and 45° for determining cosine γ. Numerical experiment in fact shows that the slope of the imaginary part of the transform is useful for inclination less than 45°.

The polynomial measurement of cosine gamma is only weakly dependent on differences in shape between the central and displaced components, and errors introduced by such differences are manifested in the coefficients of the higher order Legendre polynomials in the expansion of $RS(\Delta t)$. Also, as with

$|B|$ errors in centering the line cause equal and opposite effects on the value of cosine gamma measured. As a consequence, the average value of cosine gamma will be a good estimate even in the presence of a centering error.

Photometry errors cause a somewhat different effect on cosine gamma than on the measurement of $|B|$. As shown in Figure 5, the percent error in cosine gamma versus inclination of field only slowly increases with angle, while as shown in Figure 6, the error in cosine gamma versus Q does not decrease with Q as does the error in $|B|$, but rather increases. Further, as seen from Figures 5 and 6, the size of the error in cosine γ is only a slowly varying function of both gamma and Q. Shown in Figure 7 is a plot of the error in gamma versus gamma for a ten percent error in cosine γ. Figure 7 deomonstrates that estimates of the inclination of larger angles are almost certainly correct while the accuracy of angles less than 40° is extremely sensitive to photometry.

5. DISCUSSION

From the arguments above there are two major advantages of the fourier transform method. The first is that the magnitude of the field can be measured independent of the shape of the profile. The second is that for large fields, the magnitude of the field can be measured with an accuracy which is a factor of 10 to 25 better than that of the basic line profile. Since measurement accuracy depends on the square of the number of photons counted, the factor of 10 to 25 increase in accuracy represents a factor 100 to 625 in observing time required.

The main disadvantage to the method is a possible systematic photometry error. At present, we can measure the field in sunspots relatively to an accuracy of about one percent, with a possible systematic error of 5 percent. Cosine γ can be measured relatively to 3 to 4 percent and absolutely to 8 to 10 percent.

The fourier transform method does not require a great deal of computer time. This is not because a fast fourier transform method is used, but rather because a relatively few fourier components need be evaluated to find the zero crossing. Usually less than ten fourier components must be evaluated. For just a few transforms it is sufficient to determine the sines and cosines recursively.

REFERENCES

1. Beckers, J.M., I.A.U. Symposium No. 43, Solar Magnetic Fields, R. Howard, ed., page I

2. Title, A.M., and J.P. Andelin, Jr., ibid, page 298

3. Schoolman, S., Program TRACE, Lockheed Report for NAS8-28018

4. November, L., Operator's Manual for Microdensitometer Program, Lockheed Final Report for NAS8-28018

5. Seares, F.H., "The Displacement-Curve of the Sun's General Magnetic Field," in Astrophys J. 30, 99

6. Unno, W., "Line Formation of a Normal Zeeman Triplet," Pub. Astron. Soc. Japan 8, 108, 1956

FIGURE CAPTIONS

Figure 1. Noise reduction in zero crossing from noise in profile data versus the ratio of splitting/FWHM. Curve (a) is for Gaussian profiles while (b) is for Lorenzian profiles.

Figure 2. Percent error in zero crossing versus inclination of the field for photometric errors of size δ, for $Q = .5$.

Figure 3. Percent error in zero crossing versus splitting FWHM for several photometric errors for a field inclination of 82.82° ($\cos \gamma = .125$).

Figure 4. Noise reduction in the measurement of cosine gamma versus splitting/FWHM.

Figure 5. Percent error in cosine gamma versus gamma for photometric errors of size δ for $Q = 1.5$.

Figure 6. Percent error in cosine gamma versus splitting/FWHM for photometric errors of size δ for a field inclination of 82.82°.

Figure 7. Percent error in angle versus angle for a 10 percent error in cosine gamma.

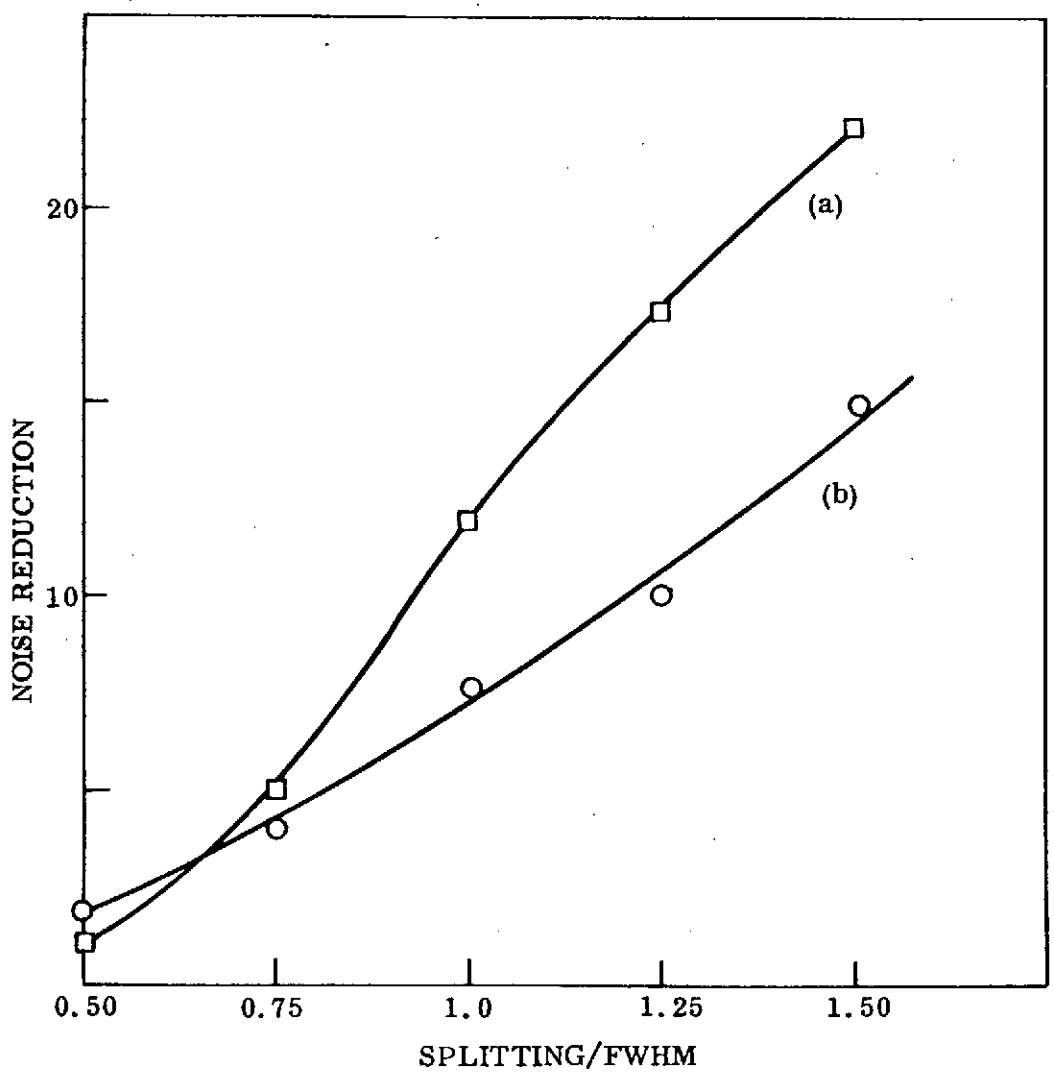

Figure 1

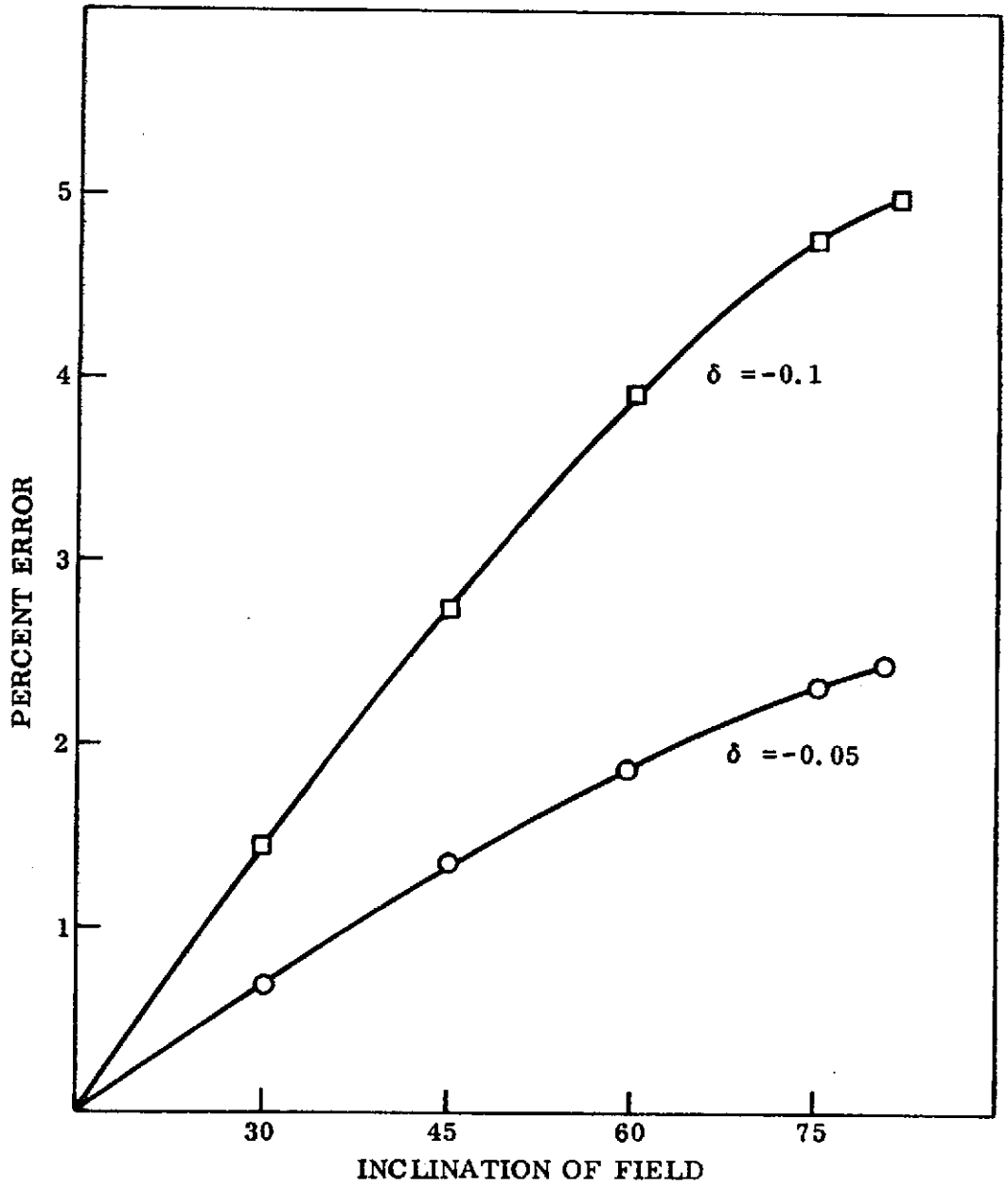
PERCENT ERROR
5
4
3
2
1
δ =-0.1
δ =-0.05
30
45
60
75
INCLINATION OF FIELD

Figure 2

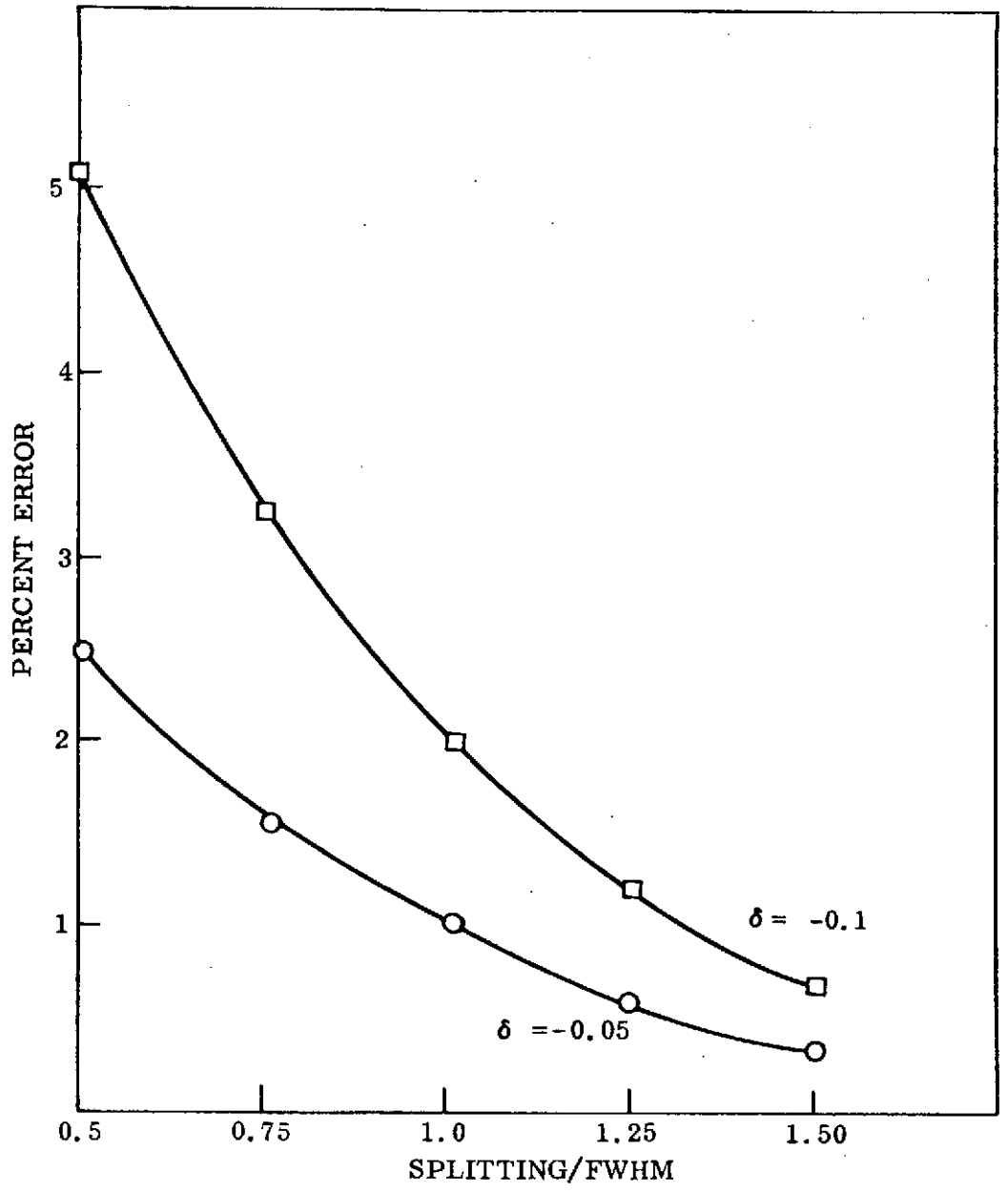
PERCENT ERROR
5
4
3
2
1
0.5
0.75
1.0
1.25
1.50
SPLITTING/FWHM
δ = -0.1
δ =-0.05

Figure 3

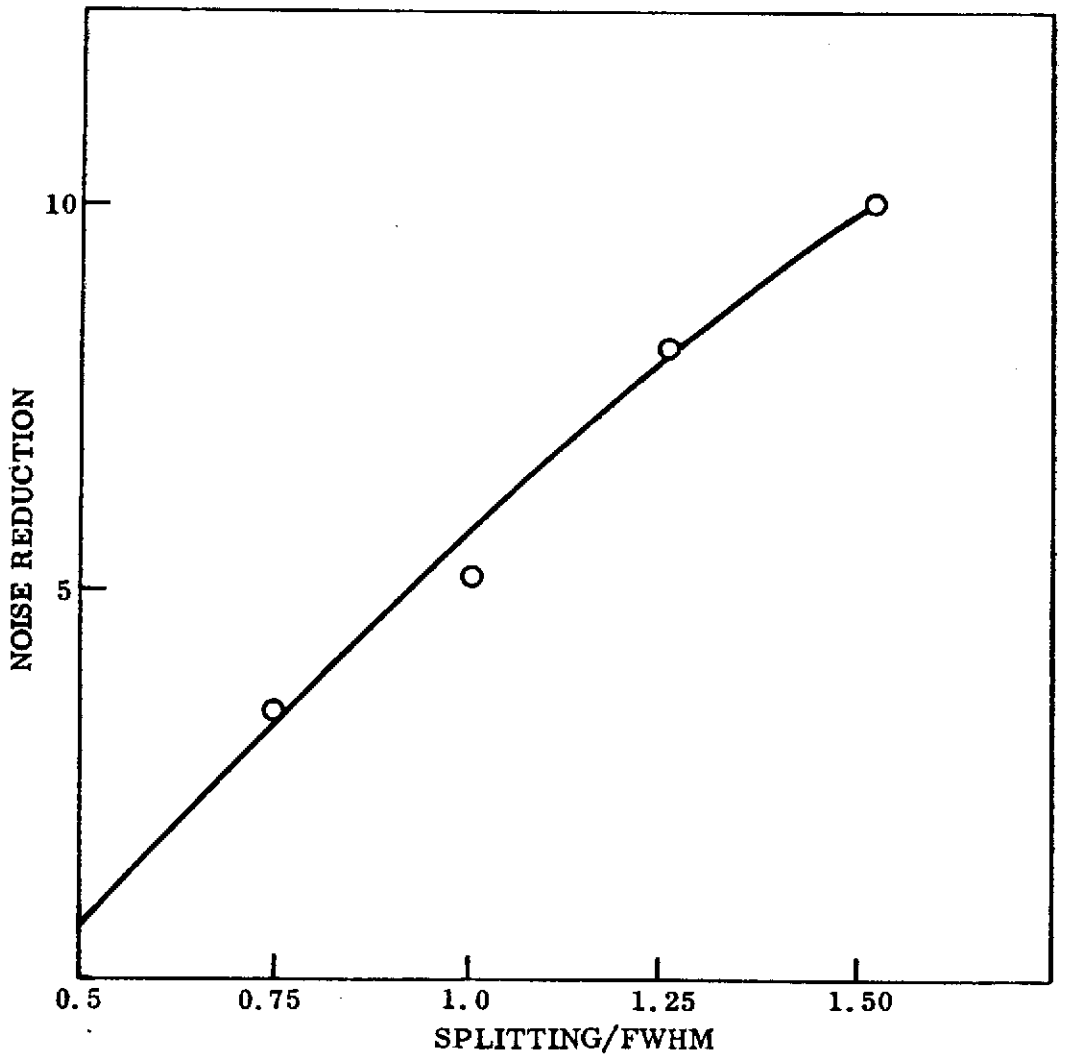

Figure 4

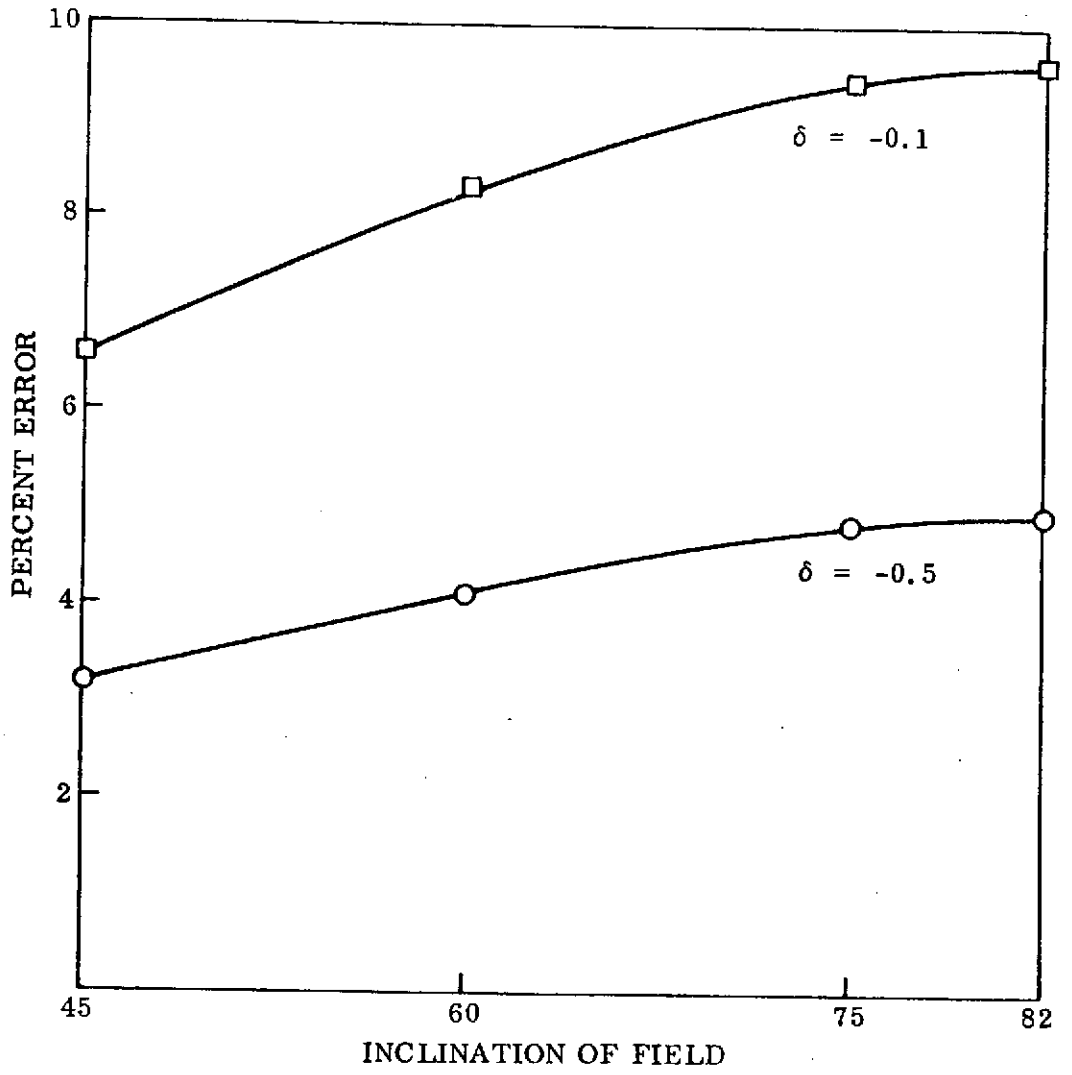
10
8
6
4
2
PERCENT ERROR
δ = -0.1
δ = -0.5
45
60
75
82
INCLINATION OF FIELD

Figure 5

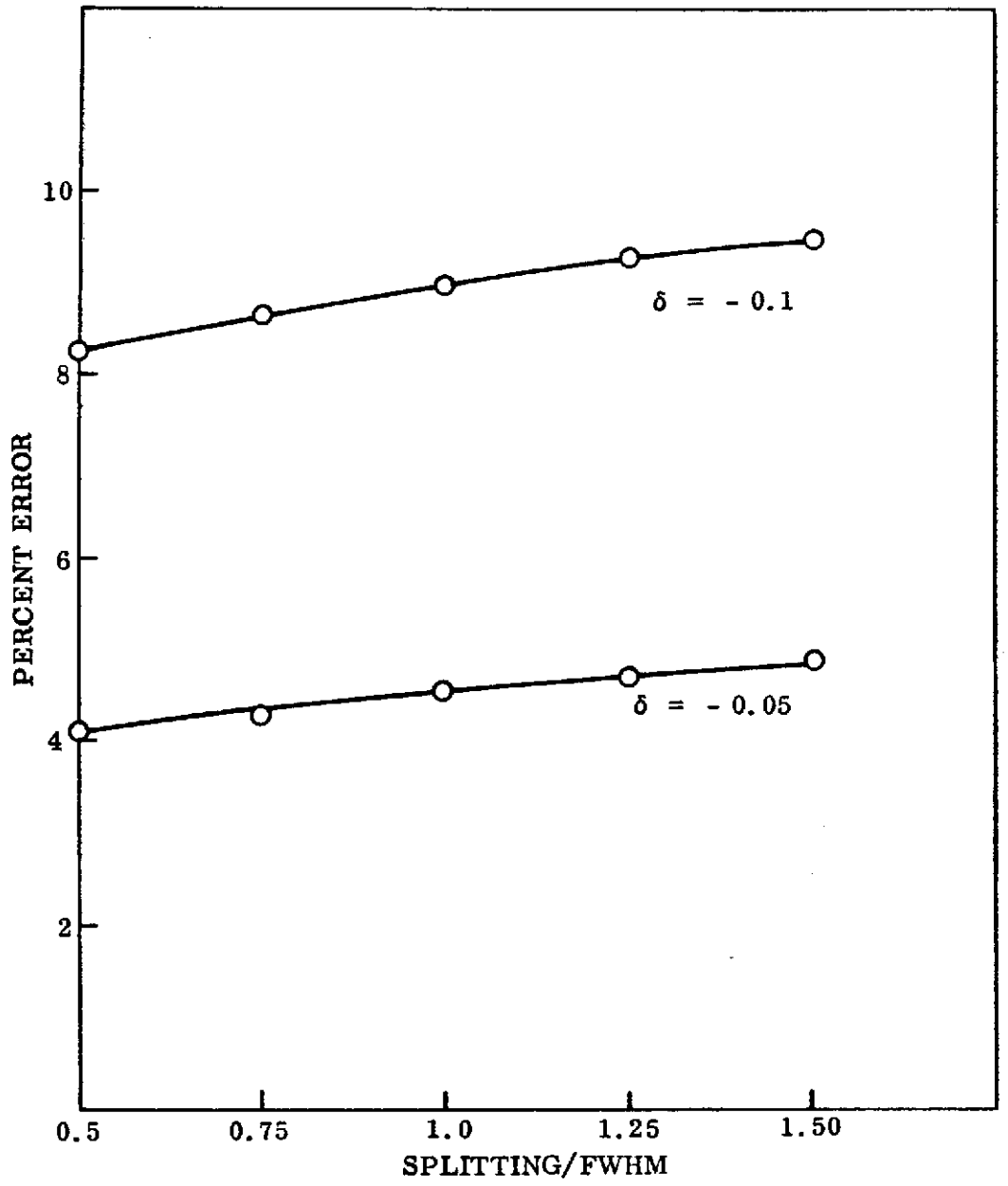
10
8
6
4
2
PERCENT ERROR
δ = - 0.1
δ = - 0.05
0.5
0.75
1.0
1.25
1.50
SPLITTING/FWHM

Figure 6

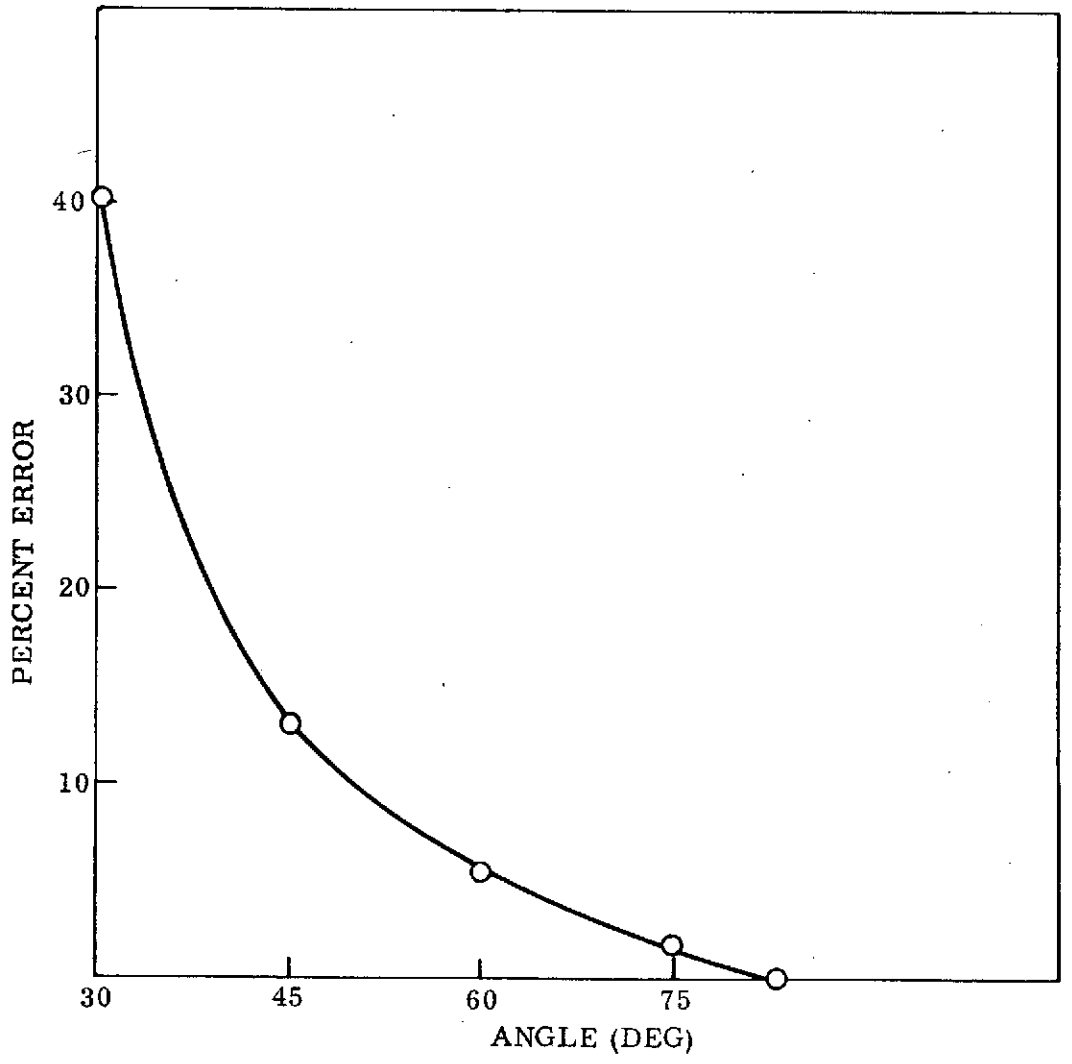

Figure 7

APPENDIX I

Shown in Figures A1 through A6 are plots of Gaussian based Zeeman profiles in a single circular polarization and the corresponding real and imaginary parts of the profiles' fourier transform. The set of figures include profiles with inclinations to the vertical from 0° to 75° in 15° steps of .25. Seares' relations were used for the relative amplitudes of the three Zeeman components. The profiles are normalized so that peak amplitude at zero inclination is unity. The transforms are normalized so that the amplitude of the real part of the transform is unity at zero spatial frequency. On an individual figure which covers a single field inclination each row contains a profile and the corresponding real and imaginary transforms. Successive rows on a given figure are for successively higher ratios of Q, the ratio of splitting to FWHM.

Figure A1

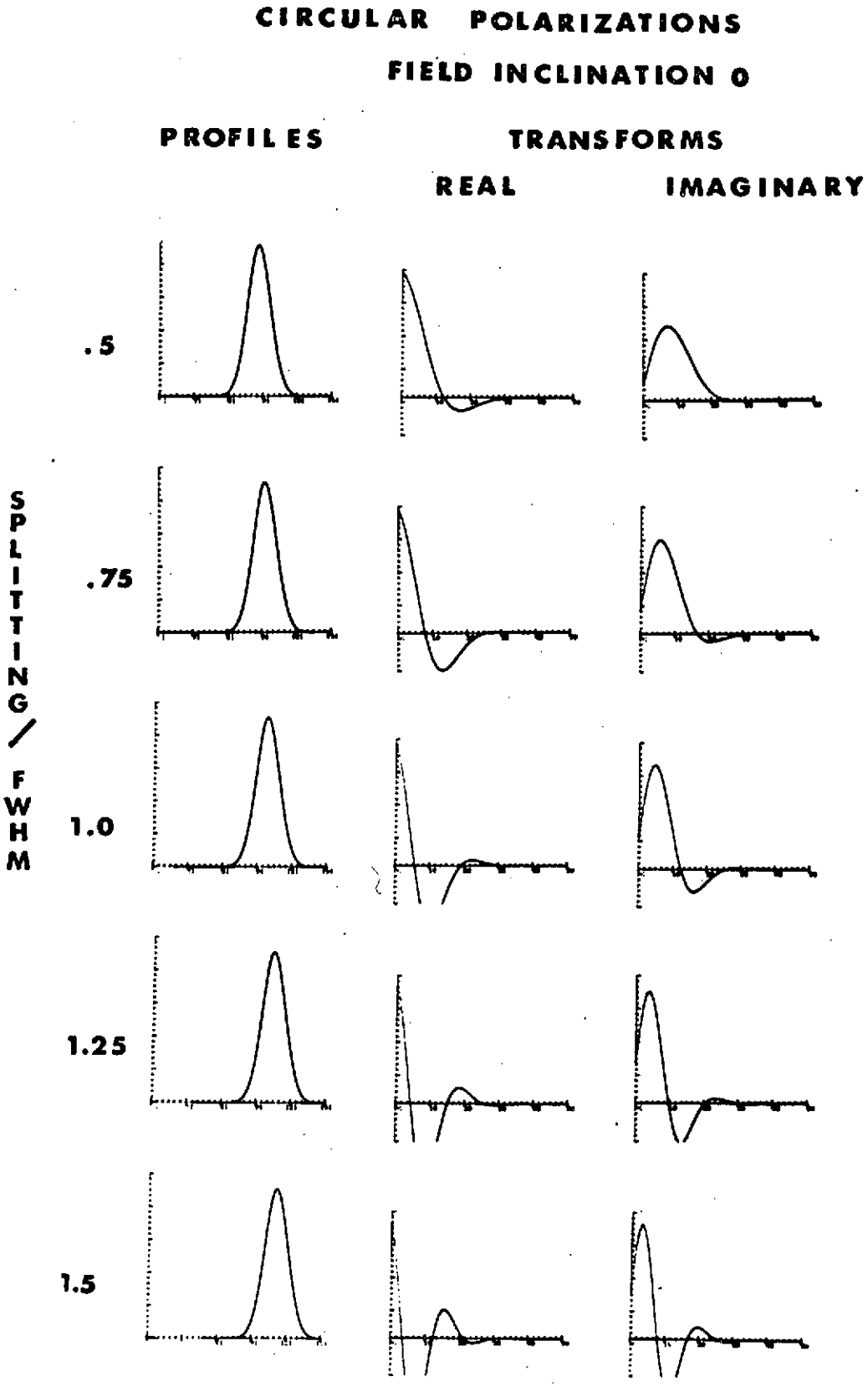
CIRCULAR POLARIZATIONS
FIELD INCLINATION 0
PROFILES
TRANSFORMS
REAL
IMAGINARY
SPLITTING / FWHM
.5
.75
1.0
1.25
1.5

Figure A2

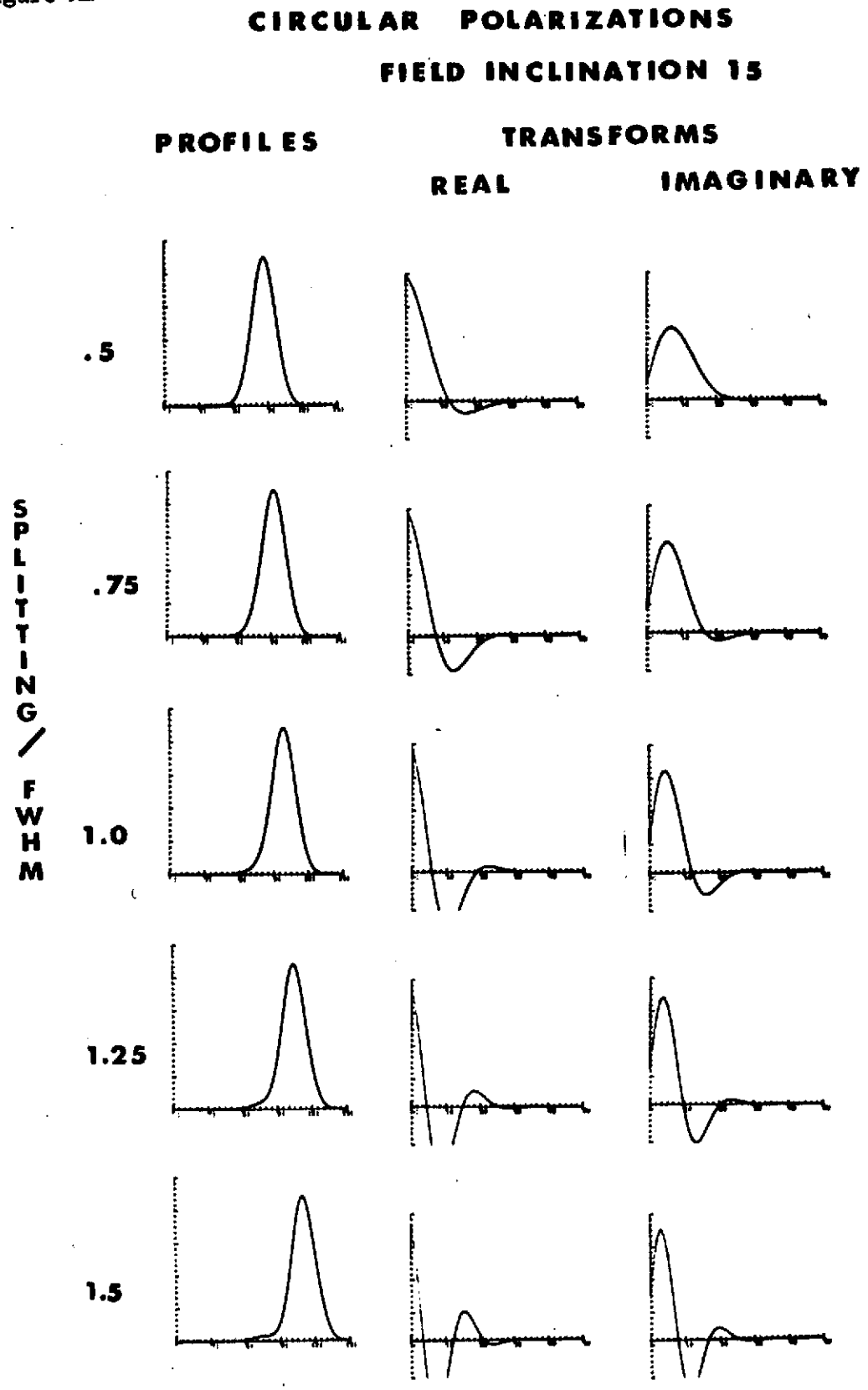
CIRCULAR POLARIZATIONS
FIELD INCLINATION 15
PROFILES
TRANSFORMS
REAL
IMAGINARY
SPLITTING / FWHM
.5
.75
1.0
1.25
1.5

Figure A3

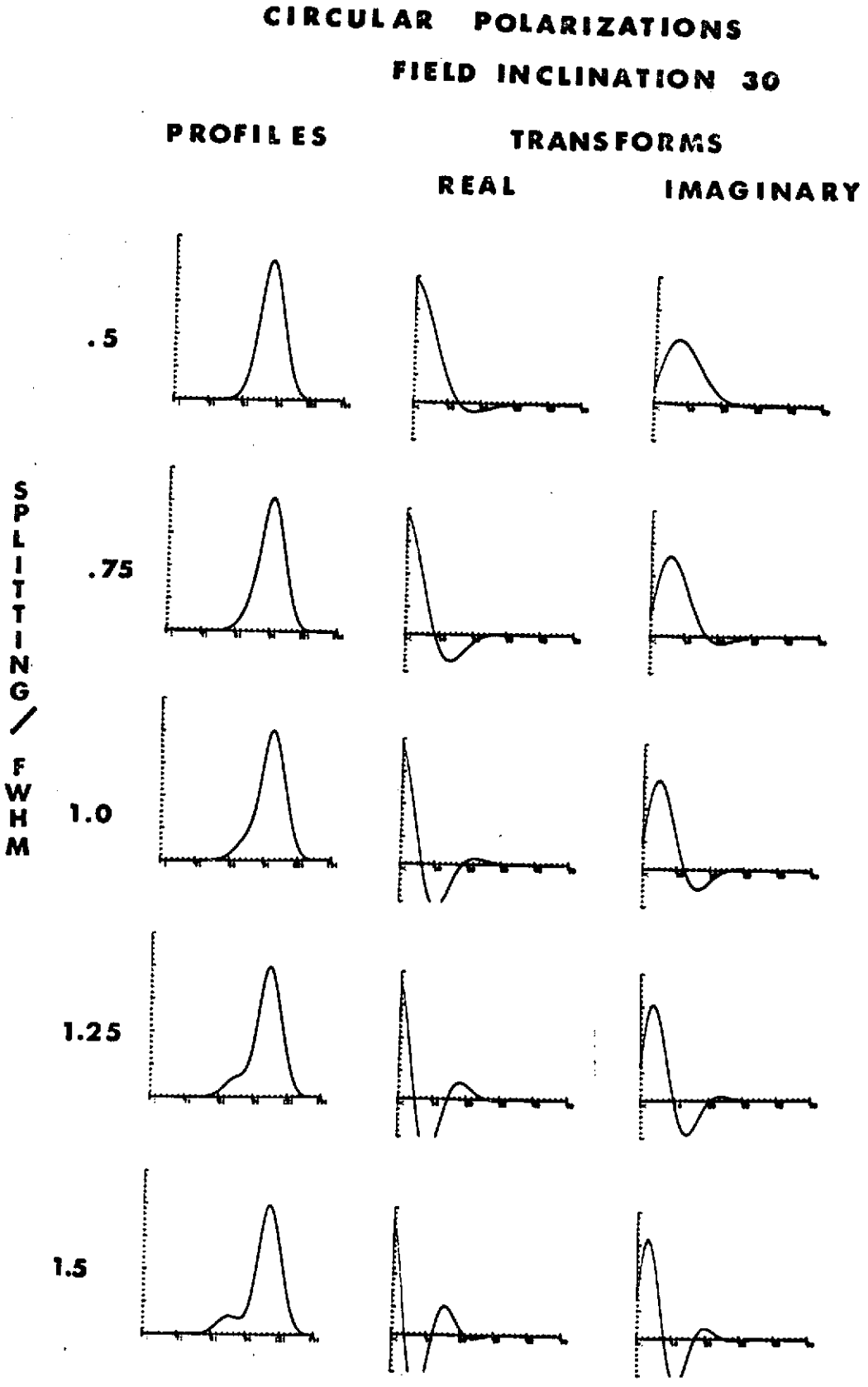
CIRCULAR POLARIZATIONS
FIELD INCLINATION 30
PROFILES
TRANSFORMS
REAL
IMAGINARY
SPLITTING / FWHM
.5
.75
1.0
1.25
1.5

Figure A4

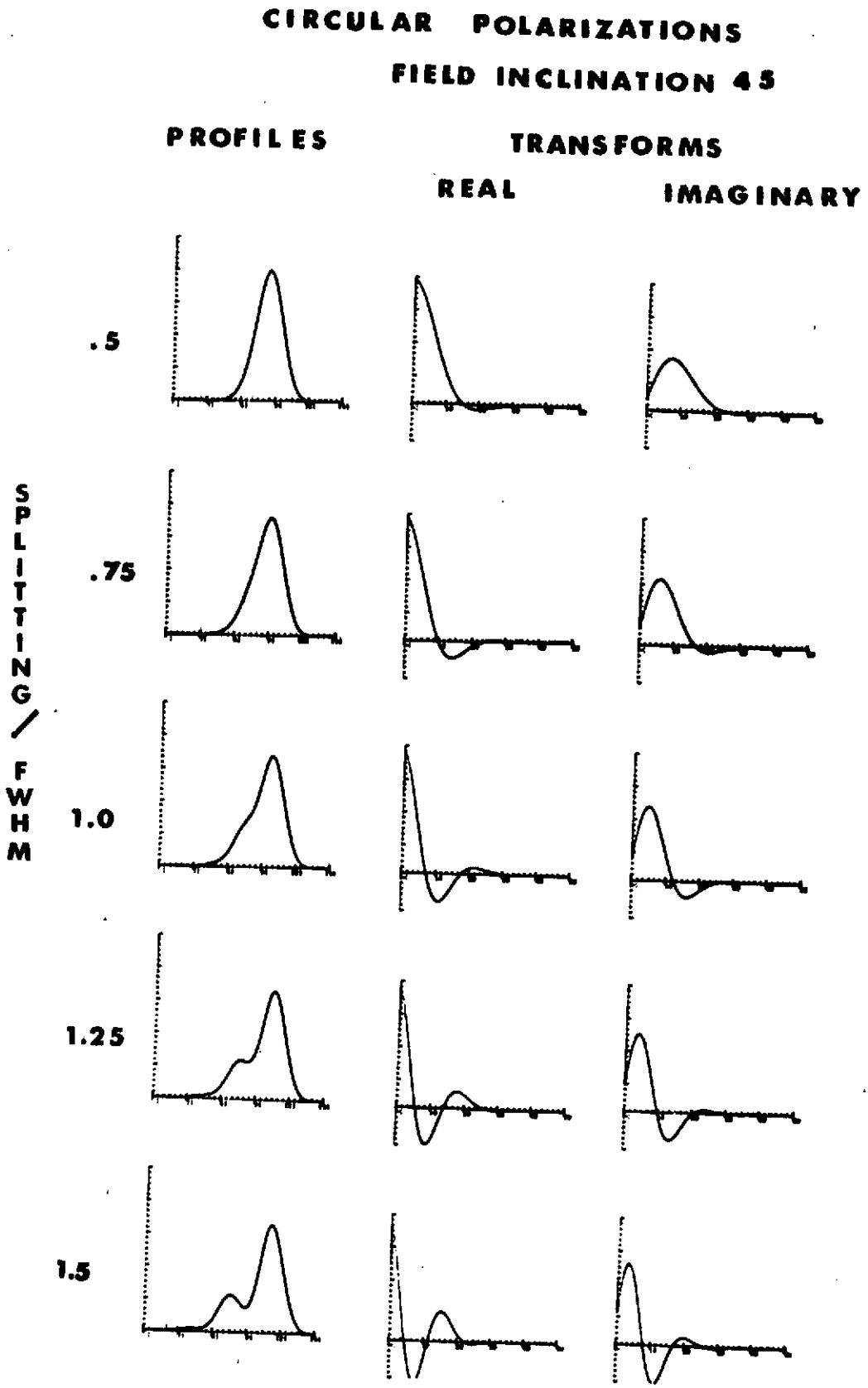
CIRCULAR POLARIZATIONS
FIELD INCLINATION 45
PROFILES
TRANSFORMS
REAL
IMAGINARY
SPLITTING / FWHM
.5
.75
1.0
1.25
1.5

Figure A5

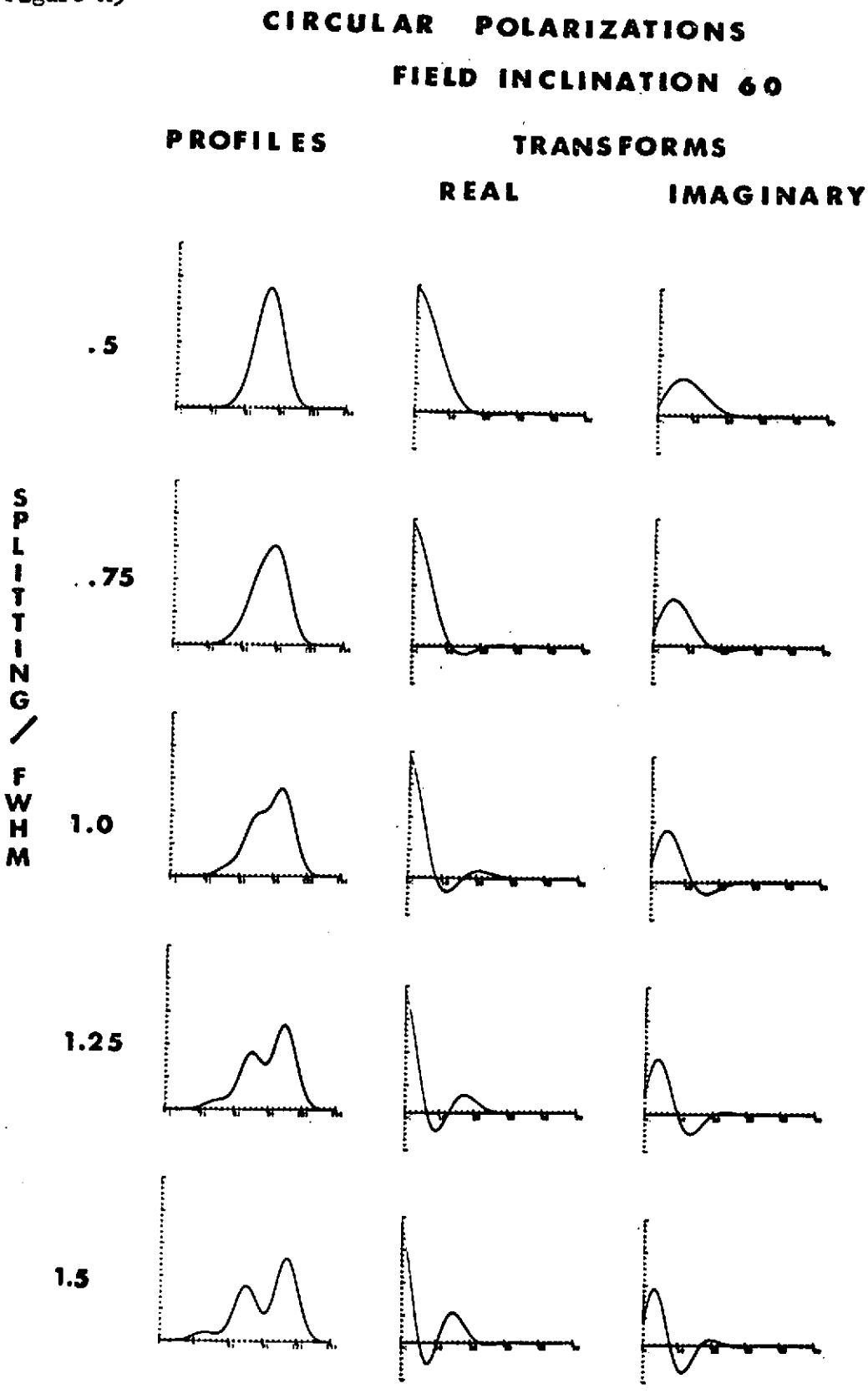
CIRCULAR POLARIZATIONS
FIELD INCLINATION 60
PROFILES
TRANSFORMS
REAL
IMAGINARY
SPLITTING / FWHM
.5
.75
1.0
1.25
1.5

Figure A6

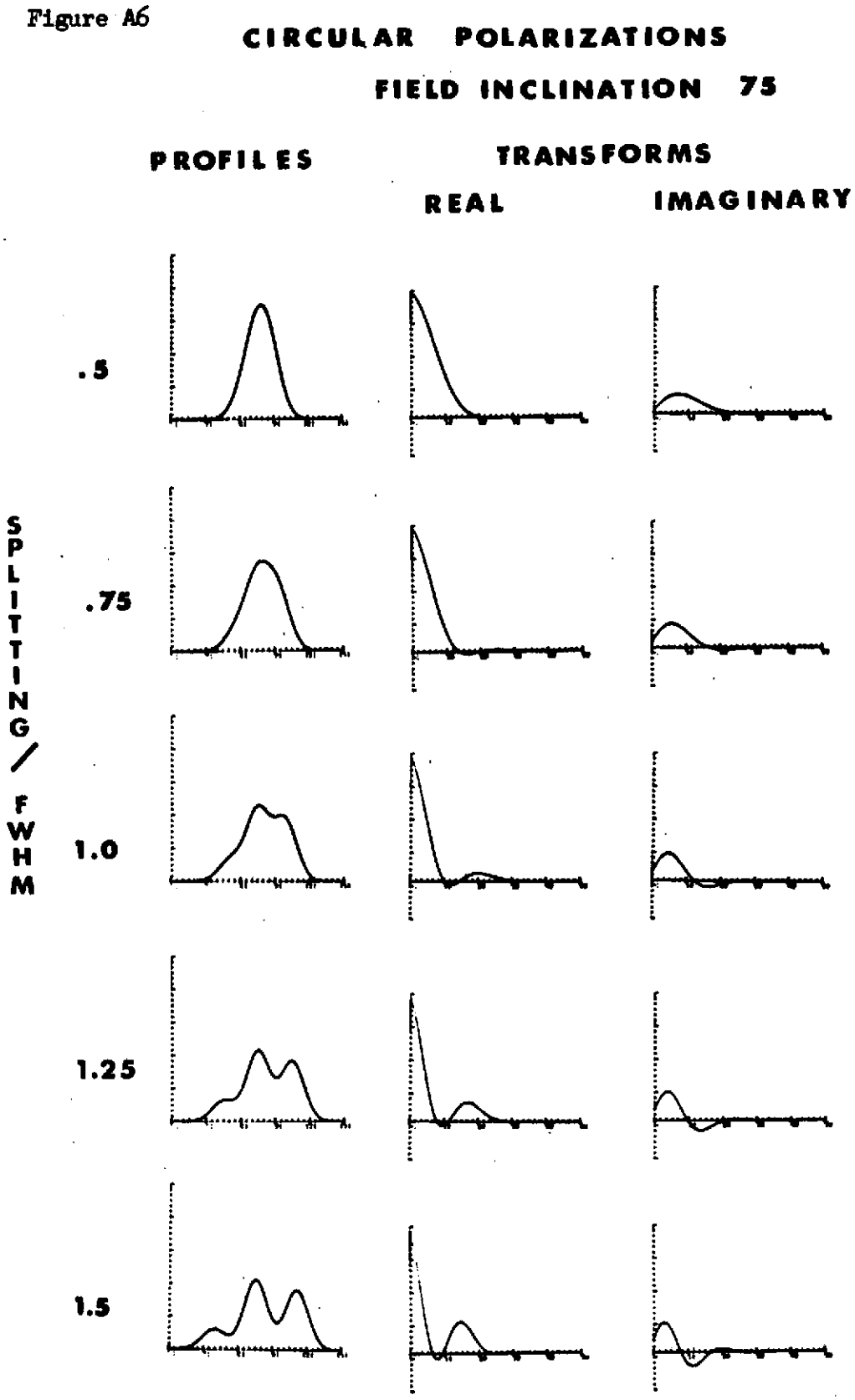
CIRCULAR POLARIZATIONS
FIELD INCLINATION 75
PROFILES
TRANSFORMS
REAL
IMAGINARY
SPLITTING / FWHM
.5
.75
1.0
1.25
1.5

APPENDIX II

Shown in Figures A7 through A15 are plots of Gaussian Zeeman profiles in pairs of orthogonal linear polarizations and the fourier transforms of the sum and differences of the pairs. The profiles and their transforms are organized differently from the circular case and a smaller fraction of the possible angular and splitting combinations are shown. Included are inclinations from the vertical from 30 to 90° in 30° steps, orientations with respect to the azimuthal projection of the field from 45° to 90° in 15° steps at three splitting to FWHM ratios. Each figure represents a single inclination from the vertical and a single splitting to FWHM ratio. The first two columns contain the profile at ± 45° to the azimuthal projection of the field. In the third column of the first row is the transform of the sum profile. The difference profile is zero and is not shown. Further since the sum profile is the same for all azimuthal orientations it is only shown in row one. All successive rows contain profiles in orthogonal polarizations at the indicated angles to the azimuthal projection of the field and the fourier transform of the difference profile.

Figure A7

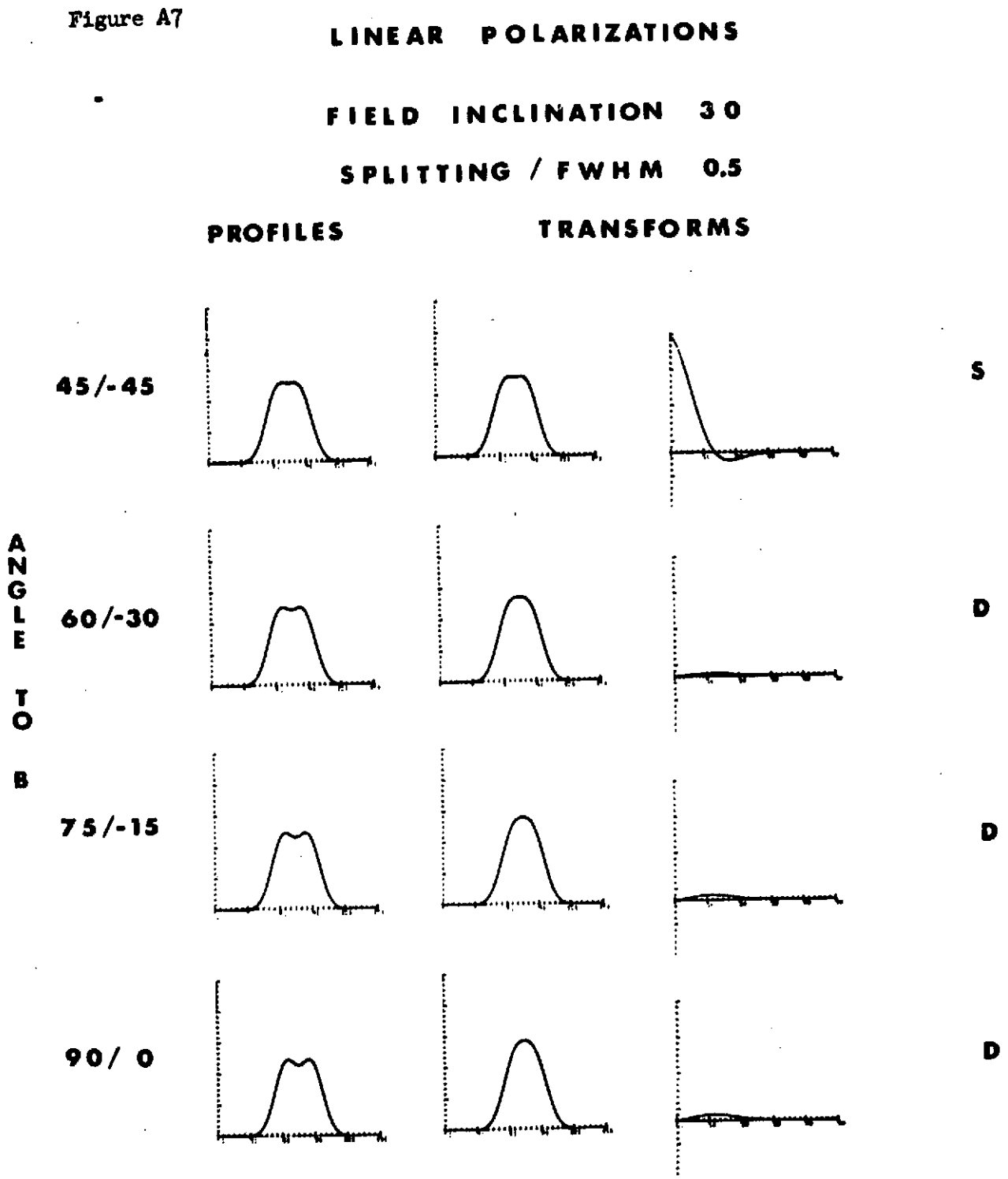
LINEAR POLARIZATIONS
FIELD INCLINATION 30
SPLITTING / FWHM 0.5
PROFILES
TRANSFORMS
ANGLE TO B
45/-45
60/-30
75/-15
90/ 0
S
D
D
D

Figure A8

LINEAR POLARIZATIONS

FIELD INCLINATION 30

SPLITTING / FWHM 1.0

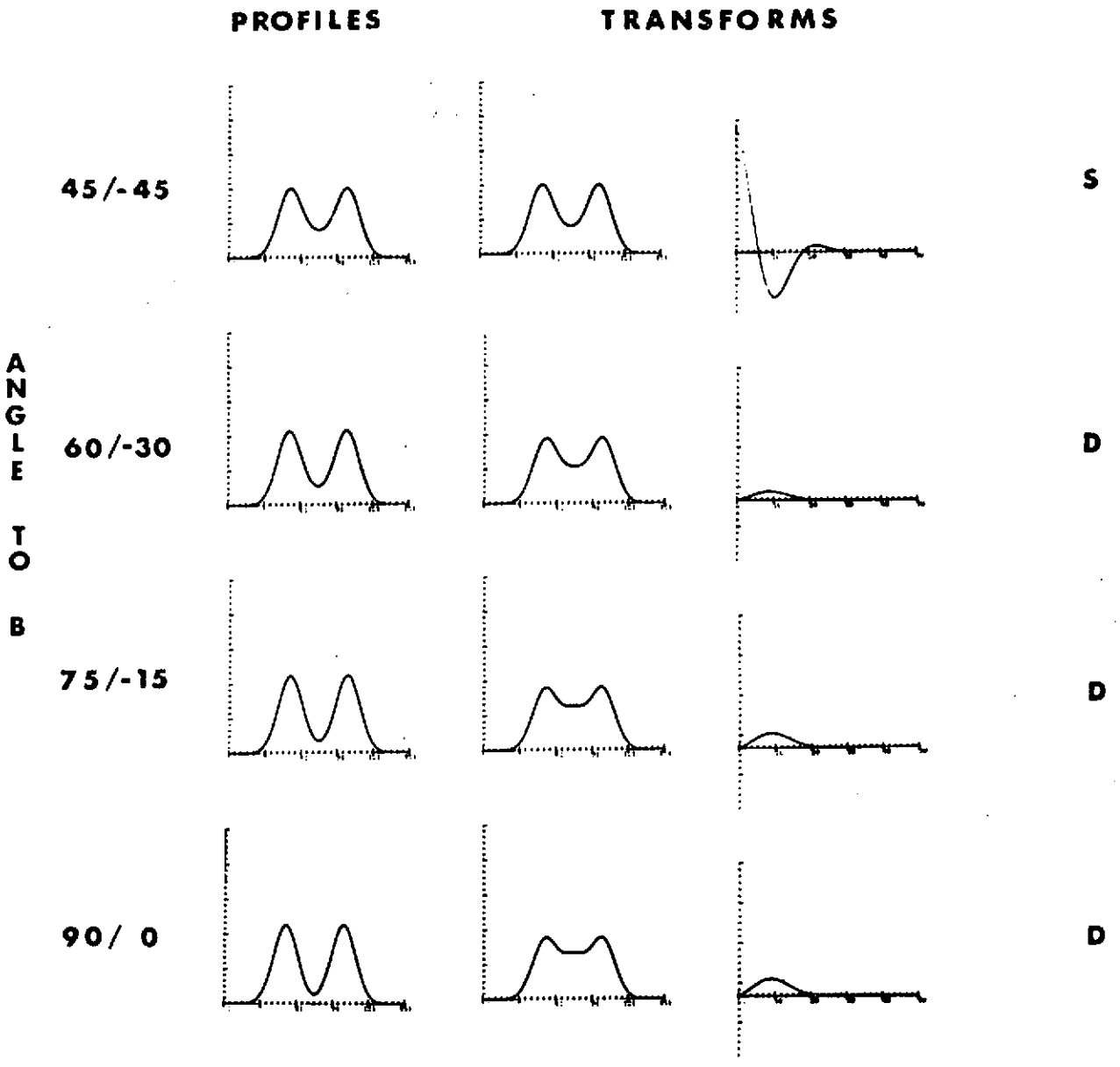

Figure A9

LINEAR POLARIZATIONS

FIELD INCLINATION 30

SPLITTING / FWHM 1.5

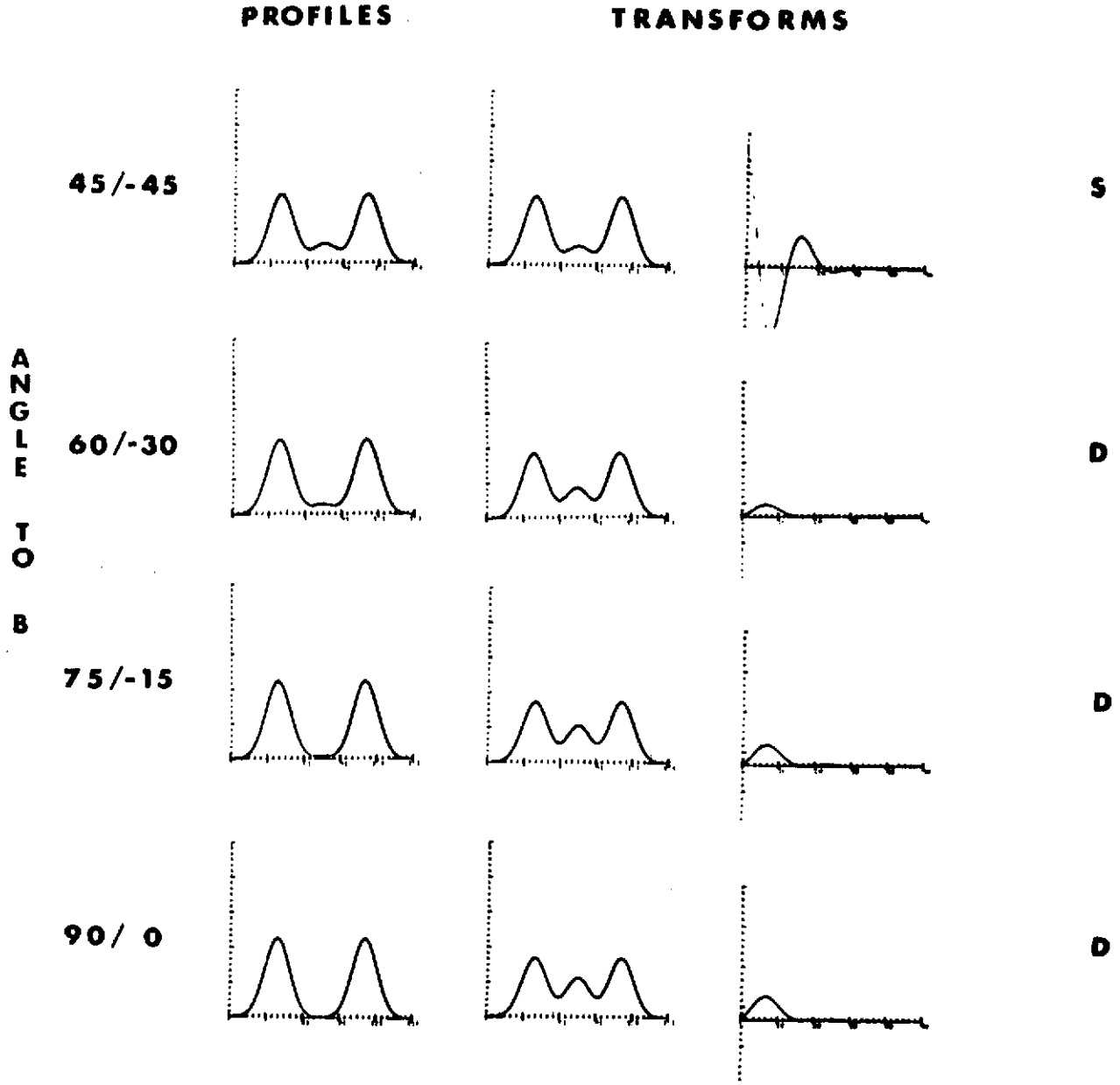

Figure A10

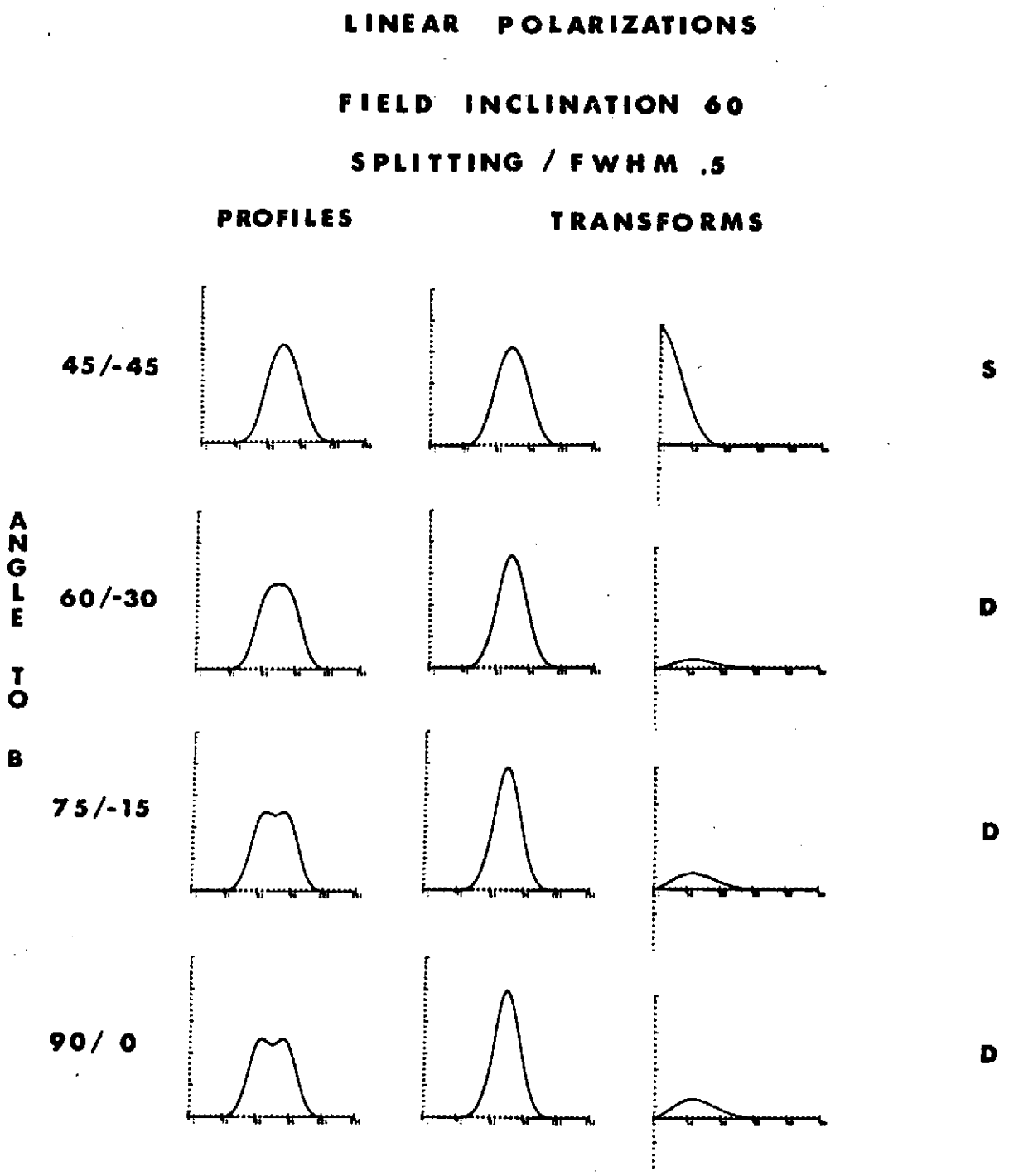
LINEAR POLARIZATIONS
FIELD INCLINATION 60
SPLITTING / FWHM .5
PROFILES
TRANSFORMS
ANGLE TO B
45/-45
60/-30
75/-15
90/ 0
S
D
D
D

Figure A11

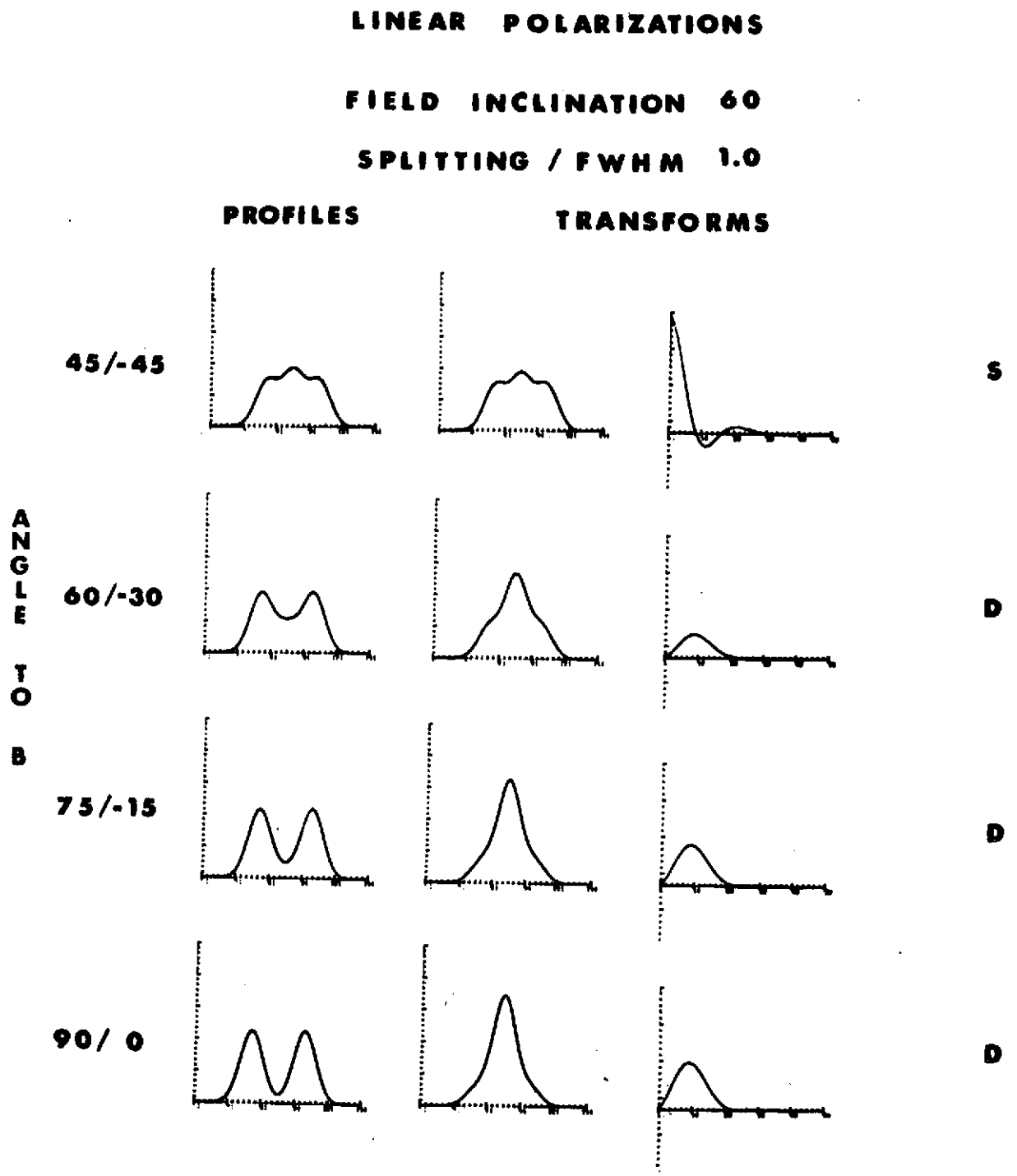
LINEAR POLARIZATIONS
FIELD INCLINATION 60
SPLITTING / FWHM 1.0
PROFILES
TRANSFORMS
ANGLE TO B
45/-45
60/-30
75/-15
90/ 0
S
D
D
D

Figure A12

LINEAR POLARIZATIONS

FIELD INCLINATION 60

SPLITTING / FWHM 1.5

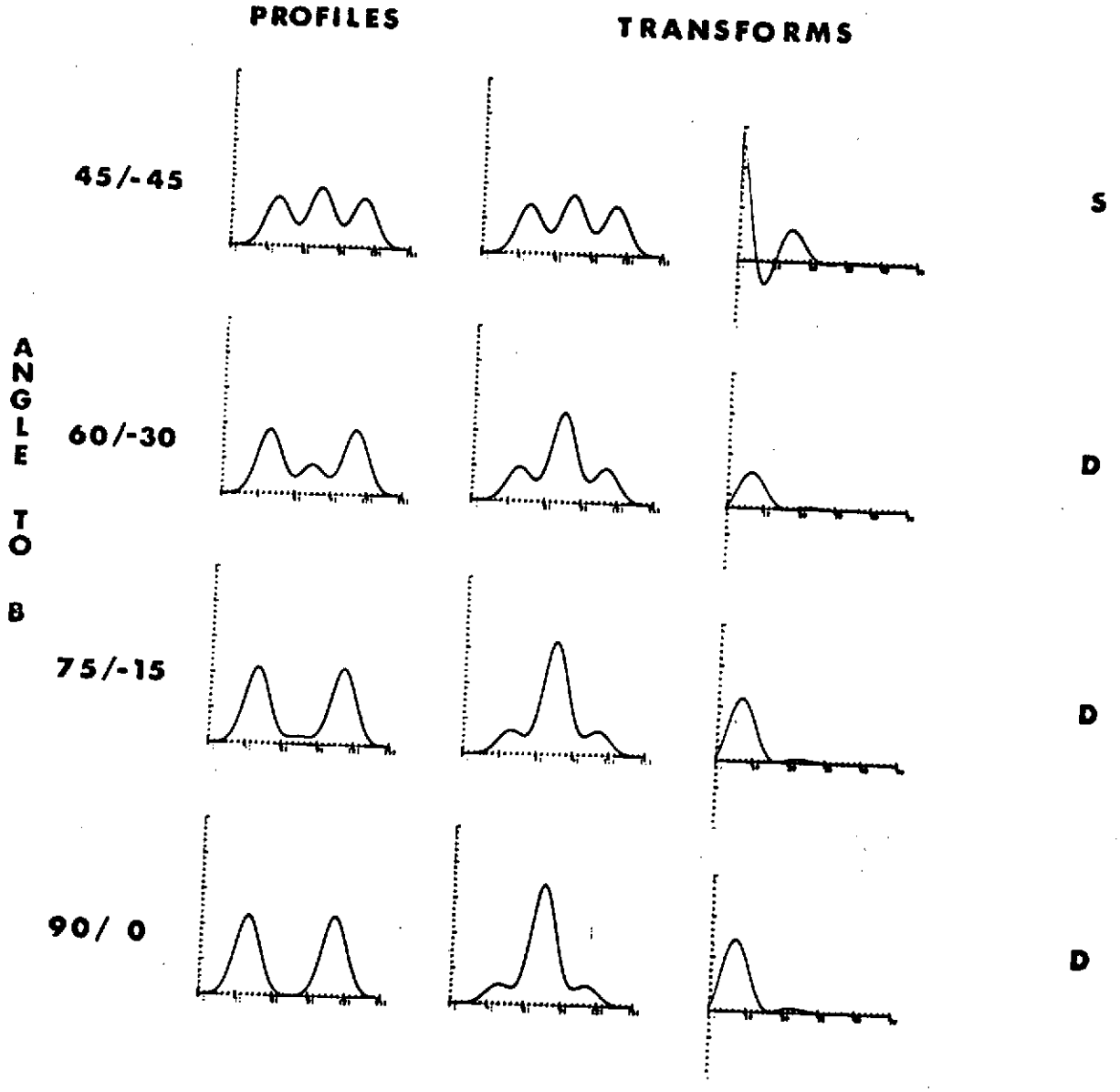

Figure A13

LINEAR POLARIZATIONS

FIELD INCLINATION 90

SPLITTING / FWHM .5

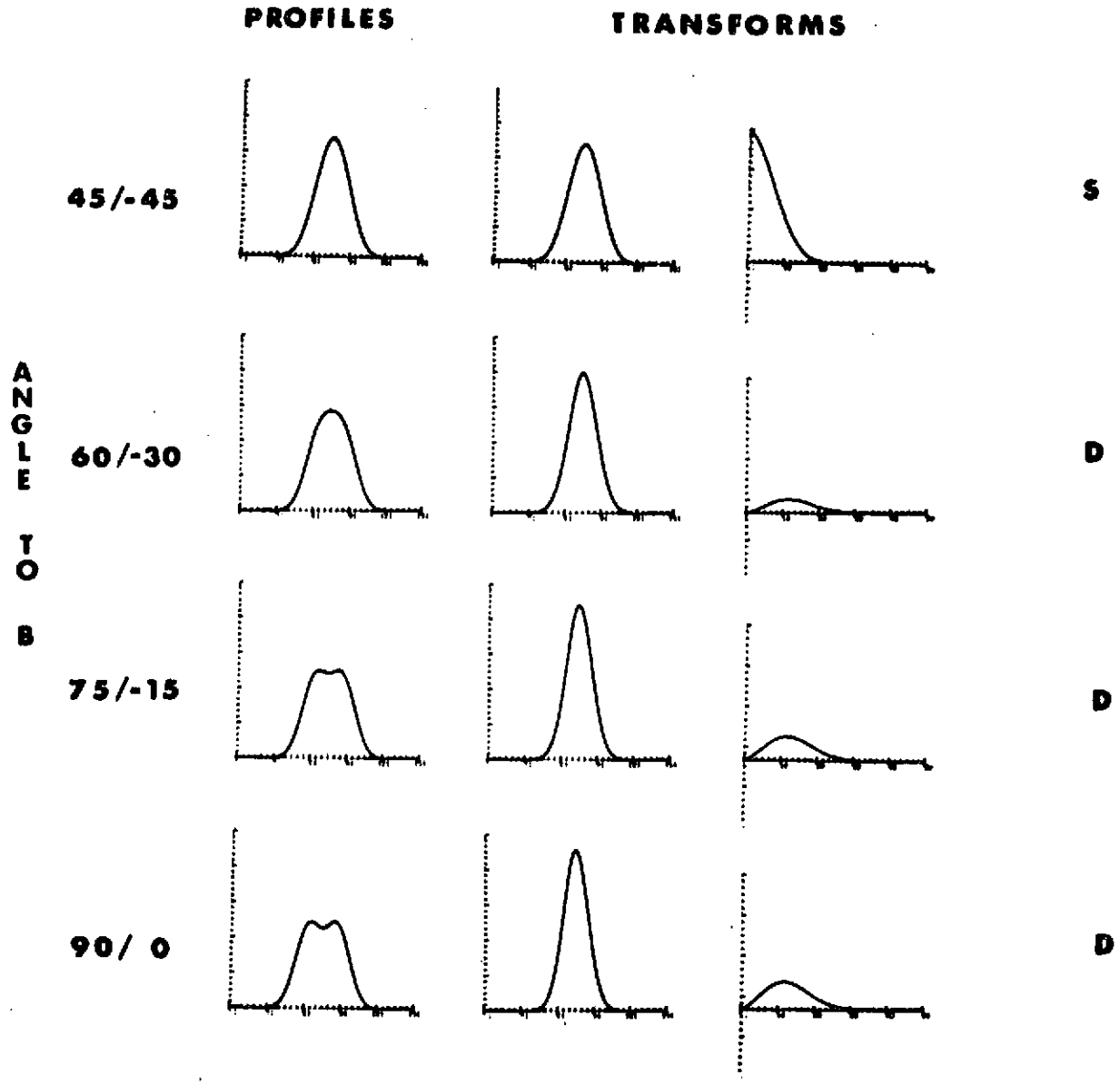

Figure A14

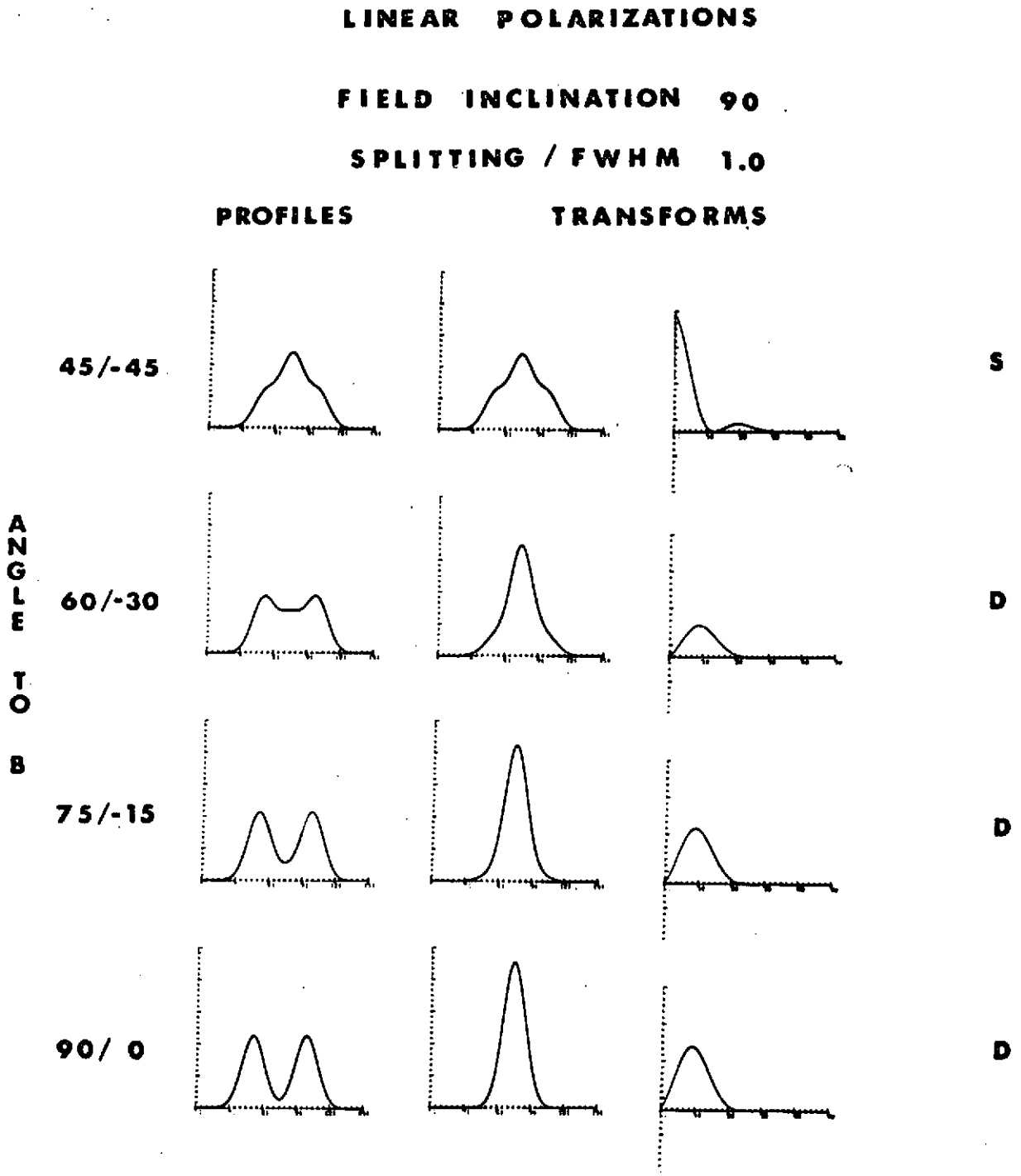
LINEAR POLARIZATIONS
FIELD INCLINATION 90
SPLITTING / FWHM 1.0
PROFILES
TRANSFORMS
ANGLE TO B
45/-45
60/-30
75/-15
90/ 0
S
D
D
D

Figure A15

LINEAR POLARIZATIONS

FIELD INCLINATION 90

SPLITTING / FWHM 1.5

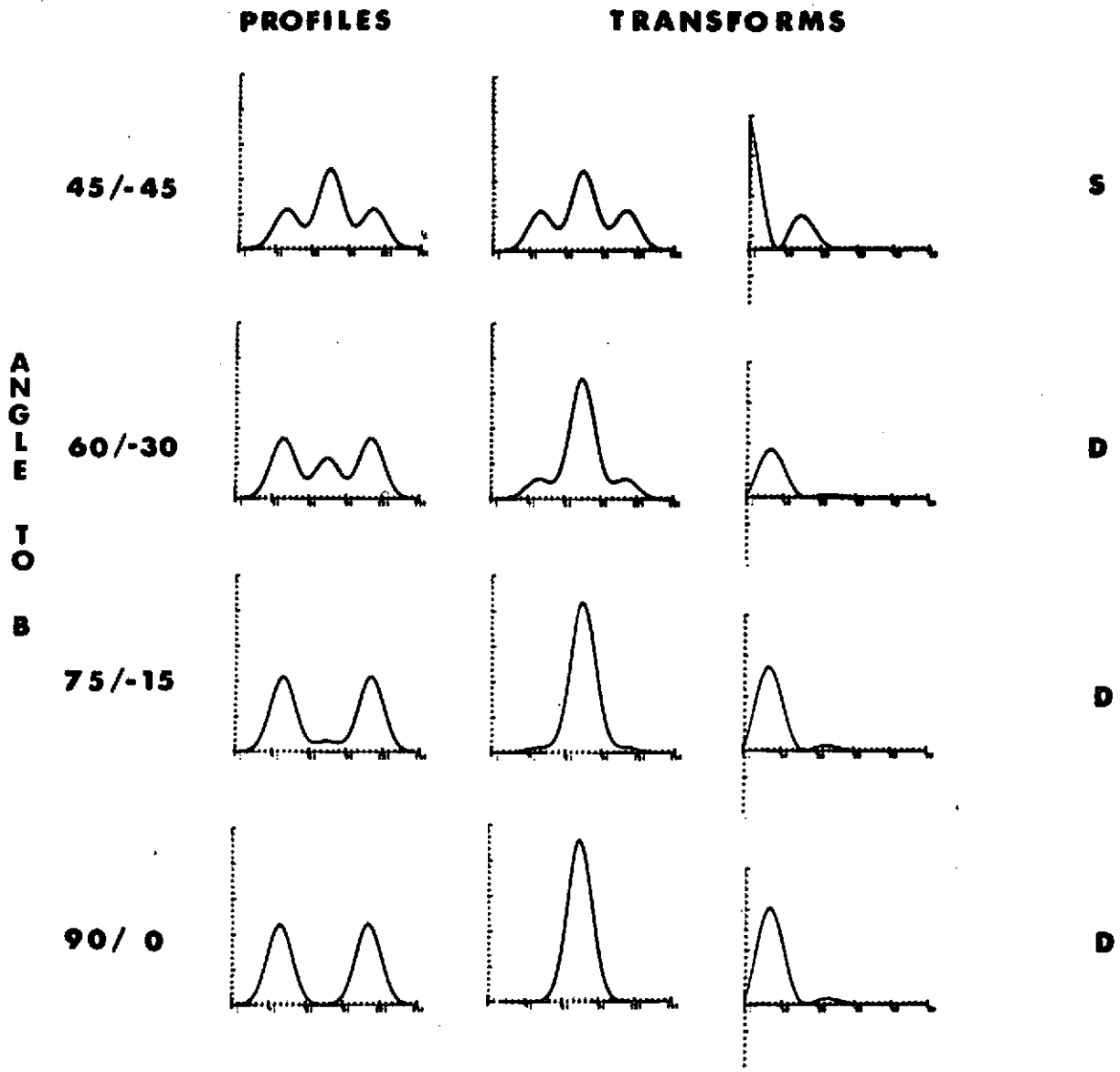

C. CONTOUR MAPS OF A HIGH GRADIENT REGION

In the first paper on the Spectra-Spectroheliograph a sequence of original data was shown that apparently exhibited field reversal at a field strength of over 2000 gauss. In the course of all our observations this region presented the most complex magnetic structure. It was therefore chosen as the final test for the data reduction procedures.

Shown in Figures 8a and b are contour maps of the magnetic field strength ($|B|$), and the continuum intensity for the high gradient region. Corresponding points in 8a and b as well as 9a, b, and c, represent identical points on the surface of the sun. The field strength is shown in hundreds of gauss. The continuum intensity is in arbitrary units; however, lower numbers indicate lower intensities. The regions with intensities below 30 are umbral. Figures 9a, b, and c show contour maps of the longitudinal component of the field ($B \cos \gamma$), the inclination of the field (γ), and the line of sight velocity (V). The longitudinal component of the field is given in hundreds of gauss. The inclination of the field is given in degrees from the vertical. The velocity is in kilometer per second, positive downward.

Comparison of Figures 8a and 9a shows that the maximal field strength occurs where the longitudinal field is zero. For convenience the contour of zero longitudinal field is shown on the field strength map (8a) and is marked by zeros at the outside of the map boundaries. It is clear from 8a that there exist gradients of the order of 6000 gauss/arc second in the magnitude of field in the neighborhood of the zero longitudinal field contour. The maximum gradient in the longitudinal component of the field is approximately 700 gauss/arc second.

Comparison of Figures 9a and 9b shows that, at least for this region, the contours of the longitudinal field inside the spot are dominated by the inclination of the field. Figure 9c indicates that the velocity toward the surface apparently increases as the field inclination becomes more vertical.

The data reduction for the contour maps was performed completely automatically. The film was traced using the roster features of program TRACE in less than five minutes. The data on the computer was reorganized under a program called PASS2 (see Section 2) in a running time of 8 minutes. Then the data for the maps were created by PASS3 in slightly under 20 minutes.

FIGURE CAPTIONS

Figure 8. Contour map of Sunspot High Gradient Region. a - Magnitude of the field in hundreds of gauss. b - Continuum intensity in arbitrary units.

Figure 9. Contour map of Sunspot High Gradient Region. a - Longitudinal component of the field (B cos γ). b - Inclination of field to line of sight (γ). c - Line of sight velocity (positive downward).

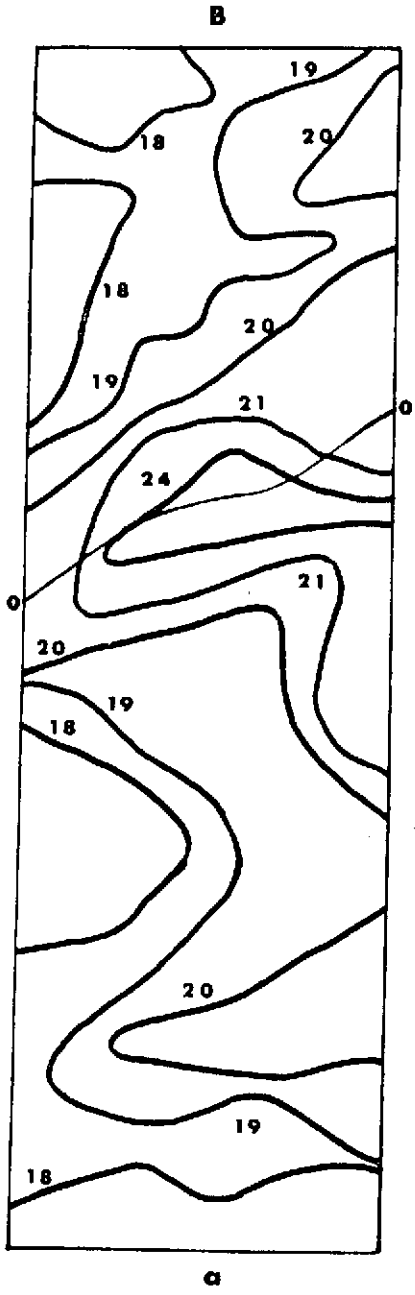

Figure 8a

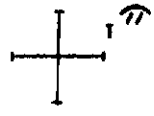

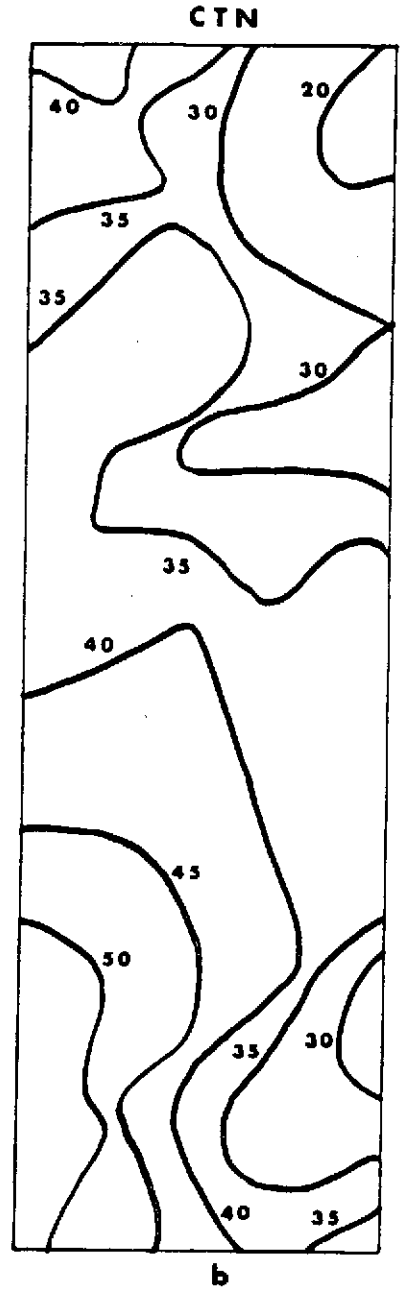

Figure 8b

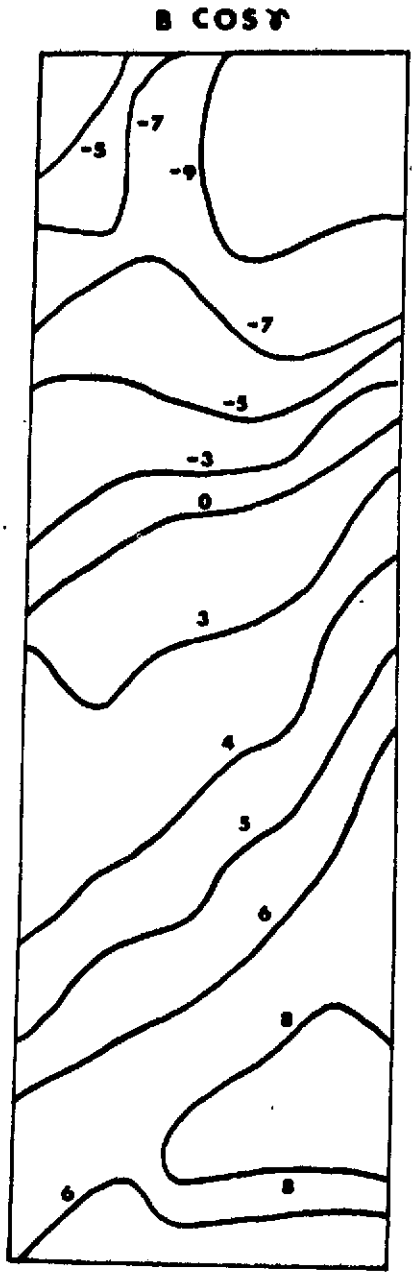

a

Figure 9a

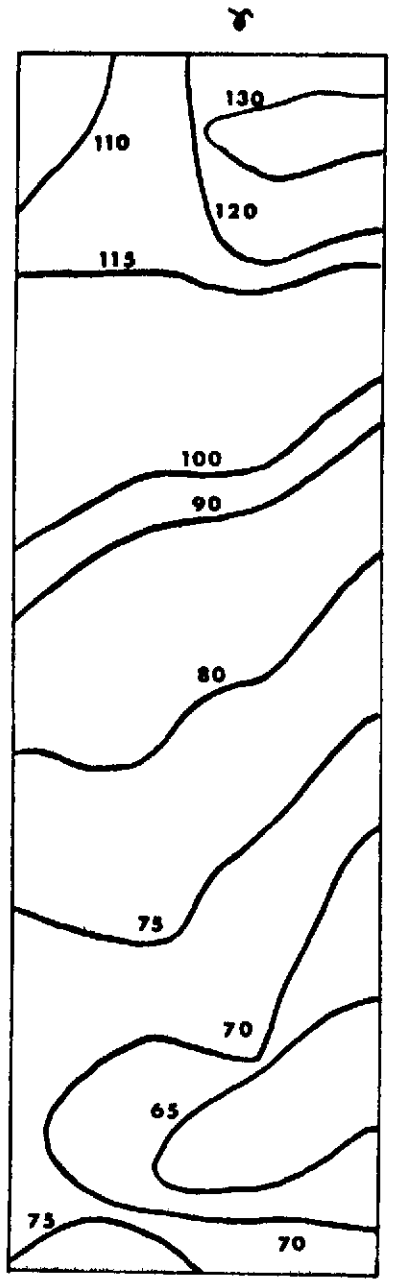

b

Figure 9b

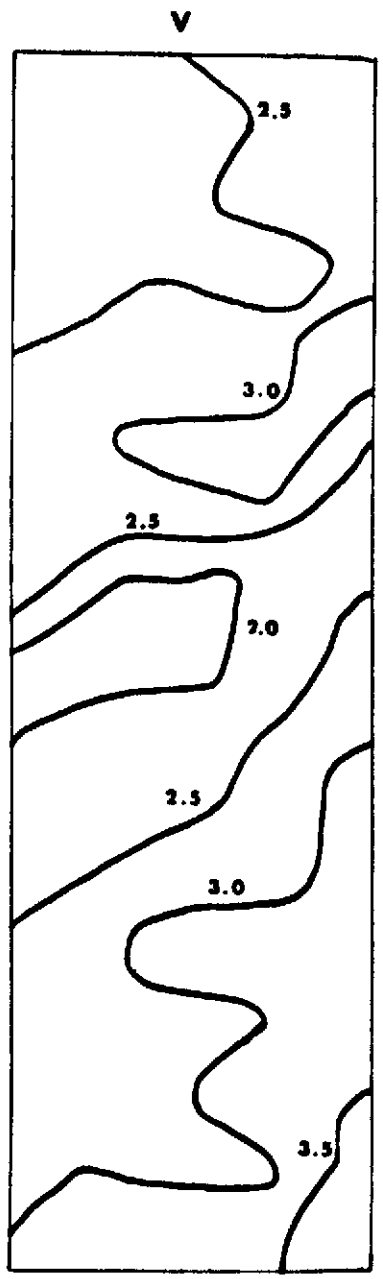

c

Figure 9c

D. DATA REDUCTION PROCESS

As an illustrative example, let us consider the reduction of the Hα spectra of the flare of 5 September 1973 as recorded by Lockheed's multi-slit spectrograph (MSS). This event was seen and studied by Skylab. A sample of the MSS data is shown in Figure 10. The MSS differs from a conventional spectrograph in that many entrance slits are placed at the solar image. A 7 Angstrom blocking filter centered on Hα is introduced into the beam to prevent the spectra from the several slits from overlapping.

The spectra were first digitized with the PDS microdensitometer. (The densitometer, the associated PDP-11 computer, and the control software which facilitates the use of the densitometer, are described in detail elsewhere in this report.) A total of 43 frames (taken at 15 second intervals) were traced. This covered the period from just before the onset of the flare to well into the declining phase. On each frame, 70 positions along the slit were traced, each separated by about one arc second. A calibrated step wedge was also traced. The data were in the computer's disk memory.

The processing of the numerical data proceeds in three steps. First, the raw digital data are converted to relative intensity values, using the step wedge results and the known characteristic curve of the film. Next, the profile of the 7 Å blocking filter was divided out, thereby recreating the original solar spectral profile. Finally, the results are displayed and compared in several ways.

One obvious display is the comparison of a profile to the pre-flare profile at the same location. This can be done both for successive positions along the slit and for successive times at a given slit location. An example is shown in Figure 11. The drawings are made with a computer-controlled CRT.

We have found that a particularly useful display is produced by stacking the profiles diagonally one behind the other. This gives a perspective view of the flare spectrum along the slit. Examples from selected frames are shown in Figure 12. Moreover, when these perspective views are projected cinemagraphically, the spectral dynamics of the entire event become clear. This display is included in the 16 mm film which is appended to this report.

FIGURE CAPTIONS

Figure 10. Multislit spectrograph in Hα for the flare of 5 September 1973.

Figure 11. Flare profile (solid line) compared to the preflare profile (dotted line).

Figure 12. Perspective view of the flare spectrum along the slit. Each frame shows the spatial distribution.

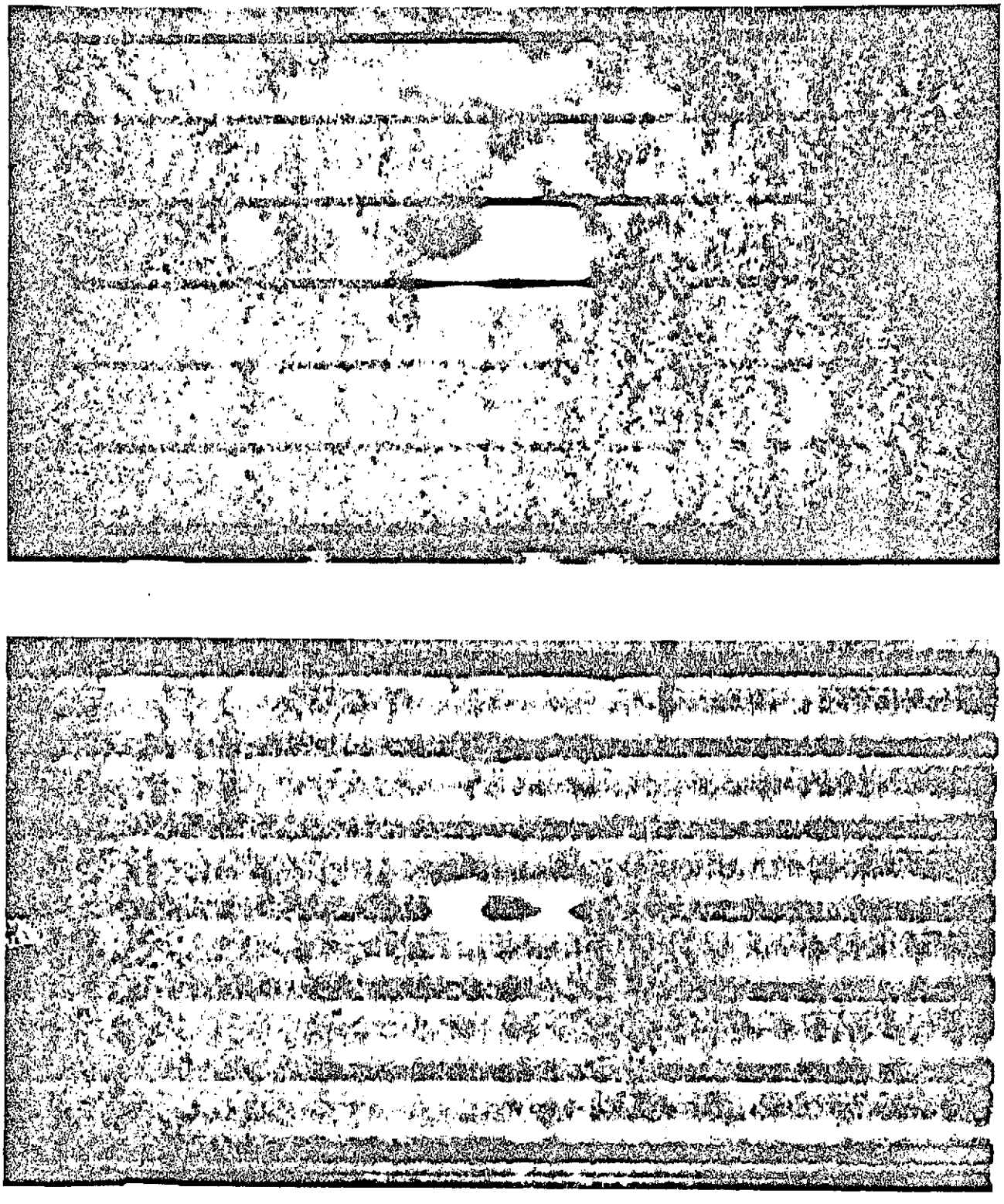

Figure 10

ORIGINAL PAGE IS
OF POOR QUALITY

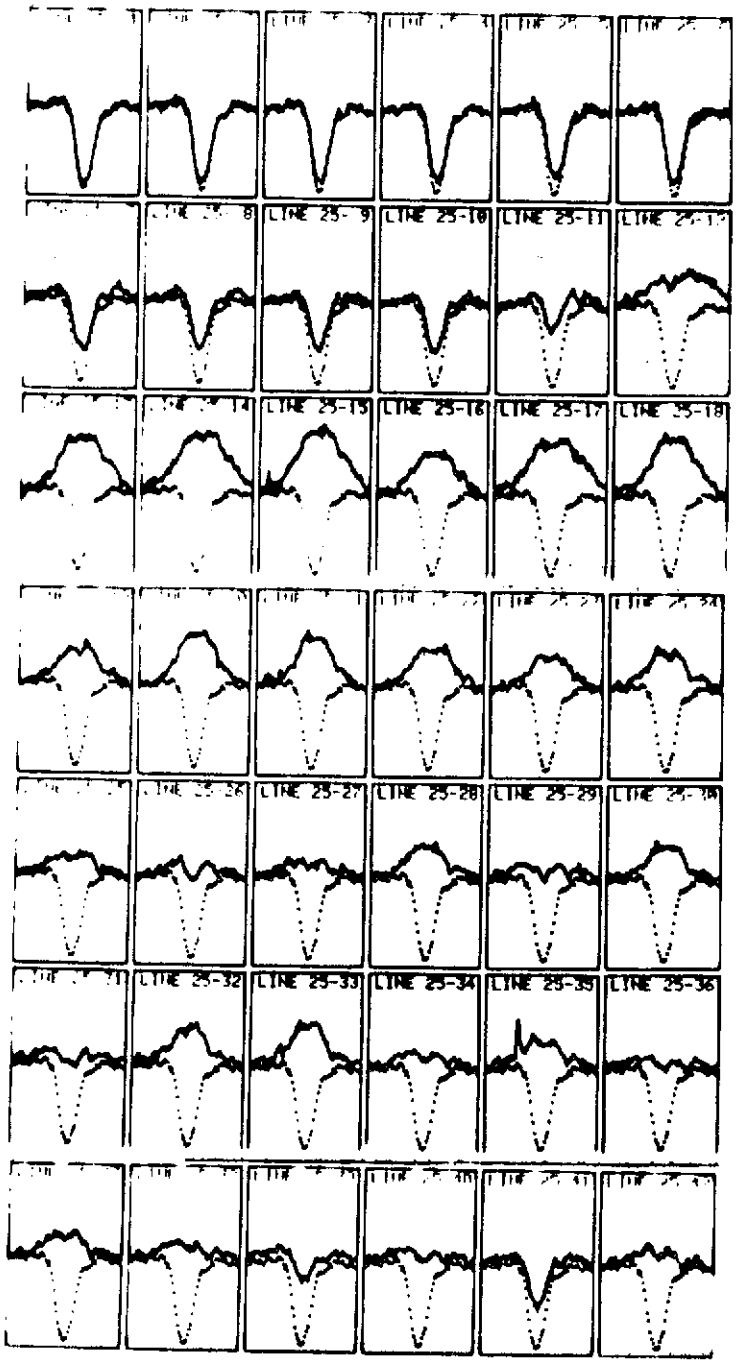
LINE 25-9
LINE 25-10
LINE 25-11
LINE 25-15
LINE 25-16
LINE 25-17
LINE 25-27
LINE 25-28
LINE 25-29
LINE 25-32
LINE 25-33
LINE 25-34
LINE 25-35
LINE 25-36

Figure 11

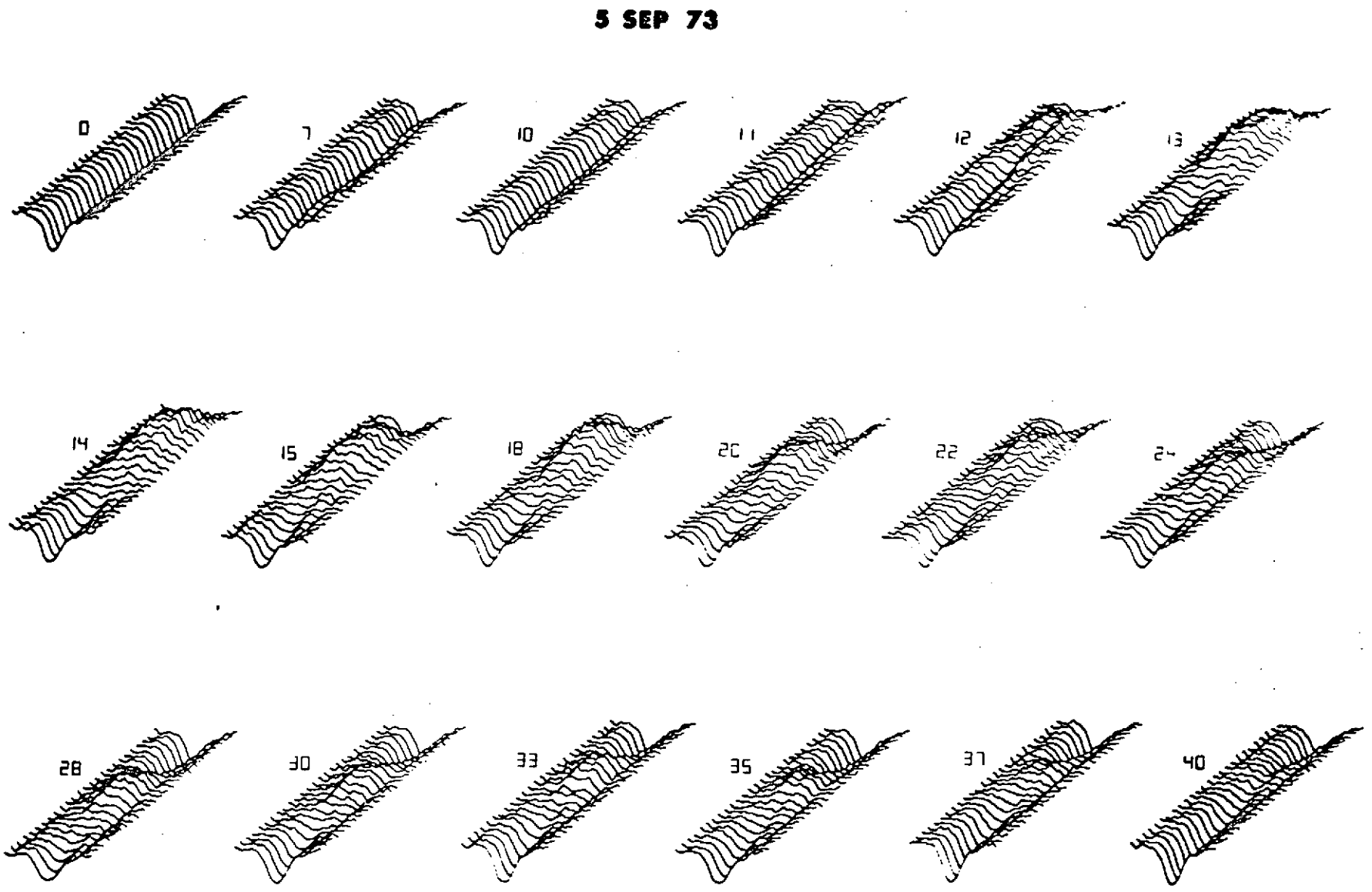

Figure 12

E. THE FLARE OF 5 SEPTEMBER 1973 - A FILM

The accompanying 16 mm film shows the solar flare of 5 September 1973 (a Skylab event) as recorded and measured by the Lockheed Solar Observatory. The film consists of six sequences, each covering approximately the same period of time, but each showing the event in a different way. Only when all of these aspects, plus others not detected at Lockheed, are taken into account can a coherent picture of the flare process be assembled.

Sequence 1. This shows a direct view of the flare as seen through a filter centered on Hα (the Balmer-α line of neutral hydrogen at 6563 Å). The pictures were taken by the slit monitor camera of the multi-slit spectrograph. The vertical black lines are the entrance slits of the spectrograph.

Sequence 2. This shows a series of Hα spectra as recorded by the multi-slit spectrograph. A 7 Å filter, centered on Hα is placed in the optical path. Thus, each entrance slit produces a segment of spectrum about 7 Å wide. The slits are sufficiently separated that there is only a small overlap between adjacent segments. The vertical dark lines seen in the pictures are each the core of the Hα line coming from a single slit. As the sequence progresses, the bright flare can be seen in emission (bright) in the center of Hα. The rapidly moving surges appear in absorption (dark) and are Doppler-shifted away from the core of the line. Blue (shorter wavelength) is to left, red to the right.

Sequence 3. The flare is seen through a narrow filter centered 1.2 Å to the blue (short wavelength) side of the center of Hα. Thus, features which are rising from the sun and are thereby Doppler-shifted toward the blue will appear prominently.

Sequence 4. This is similar to Sequence 3, except that the filter sits on the red side of Hα, so that falling features appear prominently.

ORIGINAL PAGE IS
OF POOR QUALITY

Sequence 5. This is a repeat of parts of sequences 1 (slit monitor) and 2 (multi-slit spectra). The arrow indicates the slit along which the flare spectrum has been digitized. In the multi-slit spectra sequence, note that the bright flare emission occurs at two slightly separated positions along the slit.

Sequence 6. This shows, in animation, the spectral dynamics of the flare. The data were digitized with the PDS microdensitometer, scanning perpendicular to the slit. After reduction, the individual traces along the slit were drawn on a CRT stacked one "behind" the other, so as to give a perspective view of the spectral intensity along the slit. The sequence is divided into two parts, each taken from one of the two bright emission features indicated in Sequence 5. Note that the center of the line goes into smooth emission in the first part, while a "self-reversal" absorption profile persists at line center in the second part.

Appendix C

California Institute of Technology
Final Report

BIG BEAR SOLAR OBSERVATORY, HALE OBSERVATORIES

CALIFORNIA INSTITUTE OF TECHNOLOGY

1201 EAST CALIFORNIA BLVD.

PASADENA, CALIFORNIA

"HIGH RESOLUTION GROUND BASED OBSERVATIONS IN SUPPORT OF THE APOLLO TELESCOPE MOUNT"

Contract NAS8-28028

FINAL REPORT

12 September 1974

Prepared for: George C. Marshall Space Flight Center
Huntsville, Alabama 35812

Prepared by: Richard A. Prout, Project Manager
12 September 1974

FOREWORD

This program to obtain high resolution ground based observation in support of the Apollo telescope mount was conducted for the George C. Marshall Space Flight Center under contract NAS 8-28028. This program was performed under the technical direction of:

E. Reichmann
Code S&E - SSL-TE
George C. Marshall Space Flight Center
Huntsville, Alabama 35812

This program was performed with the assistance of:

Ball Brothers Research Corporation, Boulder, Colorado
Muffoletto Optical Company, Baltimore, Maryland
Corning Glass Works, Corning, New York
Haskell Shapiro, Engineering Consultant,
Corona del Mar, California
Spectra Optics, La Crescenta, California

and others too numerous to mention without whose assistance this project could not have been carried out.

ABSTRACT

This program has resulted in the installation of a 65 cm Photoheliograph Functional Verification Unit (FVU) in a major solar observatory. The program also has led to development of a 10" vacuum refractor telescope and a 10830 Å birefringent filter for obtaining Helium line observations. The telescope cluster, which also includes a previously developed 8.6" Singer-Link vacuum refractor and a Hasselblad white light telescope, is being used in a daily program of solar observation. The 10" and 8.6" vacuum refractors were used to obtain high resolution ground based observation in support of the Apollo Telescope Mount. Results were facsimile transmitted directly from the Big Bear Solar Observatory to the Lyndon B. Johnson Space Center at Houston, Texas during the course of the ATM mission.

I Introduction and Historical Background

1. Big Bear Solar Observatory (BBSO) Description and Capabilities

In full operation at the start of the SGAP program, Big Bear Solar Observatory (BBSO), located in Big Bear Lake in California's San Bernardino Mountains, possessed two excellent 10" refracting telescopes, an 8.6" Singer Link vacuum refractor used to obtain Skylab astronaut training data, a small Hasselblad white light full disc telescope, a spectrograph fed by a 10" telescope through Coude' mirror and a video magnetograph. The telescope drive system which is of the declination/right ascension design possessed a principal guider with offset control affecting all telescopes except the 8.6" Singer Link which possessed its own guider enabling it to always point at the sun's center. The BBSO dome and dome shutter are independently guided. BBSO possessed a variety of 1/4 Å and 1/2 Å H-α filters and a 0.3 Å calcium K-line filter. During the course of the SGAP program a Universal Birefringent Filter tunable for wavelengths between 4000 and 7000 Å was delivered and its checkout begun.

2. 65 cm Photoheliograph Functional Verification Unit (FVU) Description and Status

A 65 cm photoheliograph development program was conducted by JPL and Caltech under contracts sponsored by NASA headquarters during the time period from 1966 through 1973. The 65 cm photoheliograph flight hardware, which was initially proposed for an ATM-B mission that never materialized, was not built but a Functional Verification Unit (FVU) was designed and fabricated complete with flight quality CER-VIT optical elements. The FVU is a 65 cm aperture Gregorian design with an Invar, low thermal coefficient of expansion, truss structure used as a base for mounting of the optical elements. Its 250 cm focal

length f/3.85, primary mirror is coupled with an ellipsoidal secondary mirror possessing a 13 times magnification ratio which yields an effective telescope focal length of 3250 cm. Due to design and fabrication constraints, of the 65 cm primary mirror aperture approximately 2.5 cm at the outer edge is masked off and lost due to the beveled rim and slightly turned down edge which remained after polishing was completed. Therefore, although the FVU effective local ratio was designed to be f/50, it is closer to f/55 in actual operation. The theoretical diffraction limit for a primary mirror of this dimension is approximately 0.2 arc seconds for high contrast targets. Due to problems encountered in polishing and mounting the primary mirror, its resolution is somewhat reduced from the theoretical limit since LUPI-grams obtained during tests indicate that it possessed a surface good only to approximately 1/5 to 1/6 wave peak to peak. A diffraction limited primary mirror should possess a surface figure good to from 1/8 to 1/10 wave peak to peak.

3. Installation of the 65 cm Photoheliograph FVU at BBSO

It became clear quite early in the 65 cm FVU program that Big Bear possessed seeing sufficiently good that imagery nearing the FVU's resolution limit might be obtained frequently during the summer months and occasionally although less frequently in the winter months. It was also apparent that the integration of the 65 cm FVU into the telescope cluster at BBSO would represent the least costly and most timely means for obtaining operational experience with a telescope of this design. As it turned out, interference testing of the FVU in full simulation of the sun, relative to total energy and collimation angle, and vacuum conditions of space would have been more costly than mounting the FVU at BBSO and using it as a ground based telescope where meaningful solar data could be obtained as well.

It was therefore proposed to MSFC as part of the SGAP program to install the 65 cm FVU on a modified mount at BBSO, providing as a part of this new installation one of the existing BBSO 10" refractors, the existing 8.6" Singer Link vacuum refractor, and the Hasselblad white light telescope. The new design was to provide a Coude' capability so that the 65 cm FVU could be used to feed the spectrograph on command. In addition a Helium 10830 Å birefringent filter was proposed for development. A Proposal was submitted, revised and resubmitted to MSFC and a contract to accomplish this installation prior to the launch of the Skylab ATM mission was awarded to Caltech in early 1972. The following sections describe the work that was accomplished under that contract.

II Scope of Work Accomplished

The scope of work that was accomplished is described in the following sections divided on the basis of major subsystems:

1. 65 cm Photoheliograph FVU Subsystems

In order to use the 65 cm FVU at BBSO the following modifications and newly developed equipment items were required.

A. A vacuum tank of sufficient size to enclose the entire telescope less camera rack and provide an operating environment at several millimeters of mercury pressure or less. In association with the vacuum tank, an aperture window was required possessing sufficient quality in transmission that the 65 cm FVU image quality would not be compromised.

B. A new vacuum guide telescope was required to provide pointing accuracy and stability of better than one arc second.

C. An aperture shutter was required to protect the 65 cm FVU structural elements in the case where inadvertent mispointing might have caused the primary mirror's image of the sun to fall on portions of the secondary assembly not protected by the heat stop mirror.

D. As time progressed it became obvious that an extension sunshade was also necessary to protect the large aperture window from high thermal inputs at its edge which were conducted from the front of the vacuum tank which was exposed to the direct sun.

After competitive procurements Ball Brothers Research Corporation (BBRC), Boulder, Colorado was selected to construct the vacuum tank and Muffoletto Optical Company, Baltimore, Maryland was awarded a contract to provide the entrance aperture window. Selection in both cases was based on price, familiarity with the existing 65 cm FVU and its interface requirements, and the historical reputation of both contractors for meeting specifications. The window was fabricated of Corning BSC 52 glass possessing extremely low inhomogeneity. To aid in testing, a wedge was purposely ground and polished between the window surfaces so that light reflected from each of the surfaces could be caused to produce a regular interference pattern that could in turn be used to evaluate the transmissive properties of the window once the surface quality was known. As it turned out, producing the window was much more difficult and time consuming than had ever been imagined. Its late delivery eventually caused the entire program to slip so that data from the newly modified telescopes was available only during the third of the astronaut visits to Skylab/ATM. However, data from existing telescopes was collected during each of the two prior crews visits so no operational time was lost during the first two manned portions of the Skylab/ATM flight program.

The new guide telescope was mounted within the 42" diameter vacuum tank on the FVU structure to minimize effects of any mechanical misalignments between telescope and vacuum tank. This necessitated provision of a separate guide telescope aperture window in the vacuum tank.

Valving and a high capacity pump had previously been procured by JPL. It was tested, repaired and installed at BBSO with the pump exhaust vented through the concrete dome walls. A molecular sieve was procured to prevent any backstreaming of contaminants in case of failure of the pump with the valve open. A long corrugated stainless steel flexible tube was procured and installed on hangers near the pump for ready connection to the vacuum tank when pumping is necessary. The vacuum system holds exceptionally well. Pumpdown is accomplished no more frequently than once a week or so, as long as the tank isn't deliberately vented for maintenance. Vacuum within the specified range is achieved within less than one-half hour after pumping starts. All vacuum system specifications were exceeded and the system works very satisfactorily.

On the 65 cm FVU itself, both the second diagonal mirror assembly and instrumentation rack assembly were removed from the integrating structure. The second diagonal mirror assembly has been remounted in a hat section on the sun end of the 42" vacuum tank where it redirects the beam to the coude'. The second diagonal mirror has been provided with two axis motor driven tilt capability for remote alignment and eventual image motion compensation drive. The instrumentation rack was redesigned in three sections and these are mounted on the underside of the rear of the 42" vacuum tank directly rearward of the Coude'. Flip mirror and beamsplitter assemblies have

ORIGINAL PAGE IS
OF POOR QUALITY

been mounted to feed any of three optical benches with provision for other benches if desired. Typically the Zeiss Universal Birefringent Filter is placed on the east bench and an H-α filter on the west bench. The center bench has less clearance but has been used for a motor driven Nikon camera and could be used for a TV monitor.

2. 10" Vacuum Refractor

Although the objective and field lenses for the 10" telescope already existed in the original mount, a new structure had to be constructed to position and hold these elements. The decision was made to make the 10" refractor also a vacuum telescope using the objective as the entrance aperture. It was also recommended that independent guiding and offset drive be provided in a gimballed mount so that the 10" vacuum refractor could be made to point at the opposing limb of the sun if the main mount and 65 cm FVU were trained on one limb of the sun. The amount of travel required was twice that required for the Singer Link telescope. In addition a sunshield and split beam optical bench were provided to improve image quality and utilization respectively. Furthermore, an achromatizing lens was introduced so that image size identical to that obtained in H-α could be obtained from the calcium K-line filter. The following equipment was provided:

A. A vacuum tank of sufficient size to hold and position the objective lens, field lenses, and achromatizing lens complete with suitable access ports for maintenance and adjustments.

B. A sunshield and dust cover for the sun end of the vacuum tank.

C. An independent vacuum guide telescope to be strapped to the 10" refractor provided with a translating sensor unit to be used for offset pointing.

D. Micrometer/motor drive units for guiding and providing offset pointing capability. Worm drive has provided improved stability under external loads whether disturbances were due to wind or observer operation.

E. A vacuum qualified motor driven field lens and adjustable field stop assembly combined on one optical bench.

F. A manually retractable achromatizing doublet lens designed by Dr. Ira Bowen of The Hale Observatories staff to provide identical magnifications for H-α and Calcium K-line images.

G. A dual optical bench with beamsplitter assembly that can accept spectral or neutral density beamsplitters for simultaneous recording by two camera systems.

H. Valving and a vacuum gauge for use with the high capacity rotary pump used on the 42" vacuum chamber.

All of the above elements were built at Caltech with the exception of the achromatizing lens. The system was integrated without difficulty, holds vacuum almost indefinitely and in short has been remarkably trouble free. It has been operational since first pumpdown at BBSO with the exception of time required to install a flip mirror replacing the beamsplitter feeding the side by side optical benches. The flip mirror reduces efficiency losses and other side effects generated by spectral and neutral density beamsplitters. The 10" vacuum refractor is usually provided with an H-α filter on one bench and the Leighton Videomagnetograph on the straight through bench. Its guider system appears to somewhat damp out guiding disturbances and mispointing occasionally seen in the 65 cm FVU guider.

3. 8.6" Singer Link Vacuum Refractor

The 8.6" Singer-Link Vacuum Refractor was originally piggy-backed on the first telescope installation at BBSO. It has always provided independent guiding and offset pointing so that it can constantly guide on the sun's center. Accordingly, only minor modifications were necessary to gimbal and mount the Singer Link in position at the side of the 10" refractor and under the declination axis. The vidicon camera and beamsplitter were rotated 120° to avoid interference with the 10" telescope and the BBSO mounting pier.

4. Integrating Structure

An integrating structure was required to mate the 42" vacuum tank containing the 65 cm FVU, the 10" vacuum refractor and the 8.6" Singer Link vacuum refractor with the existing BBSO pier and right ascension and declination drive assemblies and axis. Fabrication alignment of this integrating structure was critical if it were to accept the existing declination axis and properly align the 65 cm FVU and its Coude' system. The Coude' system is of necessity an important part of the integrating structure. The Coude mirrors are self aligning for changes in declination. They are passively driven by mechanical coupling to the telescope base near the existing spectrograph. The Coude' system, because of its location, is extremely difficult to gain access to. It operates in vacuum which makes alignment access even more difficult than it would be just due to structural requirements. The system works but will eventually receive added modifications to improve alignment accessability and to add additional alignment adjustments.

Calculations of telescope pointing extremes and seasonal variation of declination coupled with telescope configuration

showed that the northeast and northwest surfaces of the BBSO pier and mounting plate assembly needed to be shaved to provide adequate clearance in normal operation. A concrete sawing firm was contracted with to accomplish this task after the old telescope was dismantled and prior to installation of the new telescope cluster. Adequate clearance is now available for midsummer operations encompassing any of the allowable telescope pointing attitudes.

5. Hasselblad White Light Telescope and Systems Accessories

The Hasselblad White Light Telescope which is mounted on two separate optical benches was mated to the 42" vacuum tank containing the 65 cm FVU. A broadband 500 Å bandpass green interference coating was applied to the objective lens in hopes that a greater degree of protection would be afforded the various neutral density and spectral filters placed in the beam near the camera. The shutter was retained. Even with the interference coating, experience has shown that the heat load on these thin filters is too great if left in the beam for very long. As long as the shutter is used for protection, no breakage occurs. Therefore, while the interference coating provides additional protection for everything in the image field of the objective, use of the objective shutter is still required between exposures to prevent inadvertent damage.

Optical finders including a rifle sight have been added to the 42" vacuum tank and the 10" telescope to aid in initial pointing and boresighting.

Racks have been provided on the 42" vacuum tank for mounting lead weights necessary for telescope balance when instrumentation is moved or replaced by instrumentation of different mass or cg.

6. 10830 Å Birefringent Filter

A 10830 Å helium line birefringent filter was procured under

terms of this contract. The filter was originally specified to provide half height bandwidth at 10830 Å not exceeding 0.6 Å. It was specified to be tunable over a spectral range of 20 Å centered at 10830 Å . Spectral nonuniformity at any point in the 30mm clear aperture was not to exceed ± 0.1 Å. Each filter cell was to be capable of independent adjustment so that the filter might be fine tuned at its equilibrium temperature. The filter was to reject all side bands over the actinic range of the silicon matrix television camera tube. All air to glass surfaces were to be anti reflected for 10830 Å and exhibit 1/10 wave flatness. All internal optical surfaces were to be oil contacted. The filter was to incorporate a contrast element whose inner order separation is 5/7 the 32n element giving a bandpass of 7/5 times that of the smallest element. The filter was to utilize two concentric heating shells, the outer shell to provide the inner shell with a stable temperature hold within which to operate. The outer shell was to be thermostated at 40°c ± 0.03°c. The filter was to operate on 24 volts D.C. A revision later changed the half height bandwidth specifications at 10830 Å to not exceeding 0.3Å .

As a result of competitive procurement Douglas Martin doing business as Spectra Optics of La Crescenta, California was awarded a contract to construct this filter on April 21, 1972. On March 5, 1973 Spectra Optics delivered the completed filter for acceptance testing. Utilizing the Hale Laboratory spectrograph, it was determined that the filter met specifications and it was stored awaiting completion of the telescope cluster at BBSO. When it became possible to check out the 10830 Å filter at BBSO using the spectrograph there, no transmission could be observed at all using the silicon vidicon camera. The filter was returned to Spectra Optics for examination. It was found that the polaroids had all deteriorated and had become

individually opaque. Whether this was a reaction with the oil immersion bath or simply deterioration due to extended storage at 46°c was not determined but the latter reason is suspected.

Polaroid supplied Spectra Optics with an improved substrate material which was tested at elevated temperatures for a period of months with no detectable change in transmission. With new polaroids made from the new substrate material the filter has been reassembled. It is now undergoing alignment. Fine tuning will be completed by October 1, 1974 at which time the 10830 Å filter will be redelivered to Caltech for acceptance testing at BBSO. However, due to the unfortunate and unsuspected substrate materials problem, no 10830Å observations were obtained during the Skylab/ATM mission. Results obtained through the 10830Å filter will be reported on as they become available.

7. Controls

Controls have been essentially totally reworked from the original telescope due to changes and additions to drive functions, camera controls, filter controls, offset capability, flip mirror positioning and the like. A controller has been built for the 65 cm FVU system that will allow programming, in the proper sequence, flip mirrors and cameras once a preset frame rate and bench holding time have been selected. The controls and intercabling work have not been completed even though the telescope systems are operational. Modifications, improvements, and additions will continue to change control needs. Computer control, while temporarily shelved, will eventually be implemented, possibly to simulate control functions for astronauts on early shuttle/pallet missions. The controls, like the instrumentation will always be dynamically changing as improvement in filters, cameras, electronic circuitry, etc. occur.

8. Installation

To allow installation by a truck mounted crane (rather than a barge which would be far more costly) the causeway at BBSO was widened and improved prior to teardown of the old telescope. Teardown of the old telescope was a cooperative project among scientists, staff and summer students. It required approximately two days. Shipment from Caltech to BBSO and crane installation of the major new telescope and mount mechanical elements on the existing declination bearings required just one very long day. Mechanical assembly and alignment was completed within two months although some redesign was necessary along the way. The installation of cabling and controls as well as diligently checking out the equipment during this process has never really ended. The 8.6" Singer Link Refractor and the 10" vacuum refractor were operational during the final Skylab manned mission. Although data was obtained from the 65 cm FVU during this time frame, seeing problems coupled with frustrating delays in obtaining proper alignment and focus of all optical elements prevented obtaining really high resolution imagery until late spring and early summer of 1974, nearly a year behind schedule. Imagery obtained now makes it all seem worthwhile but there were many times in between where progress seemed agonizingly slow to all of the staff who devoted long hard hours to this impressive task. The accompanying photographs will testify to what was accomplished and the quality of data presently obtainable.

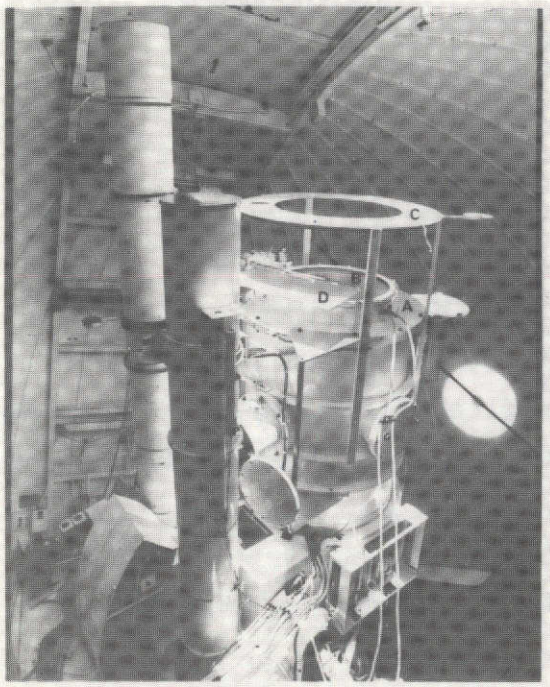

Detail of Front End of 65 cm Telescope showing:
A. Vacuum Tank B. Aperture Window C. Sunshade D. Safety Shutter.

View of Telescope Cluster:
A. 10 inch B. 8.6 inch C. 65 cm D. Hasselblad white Light.

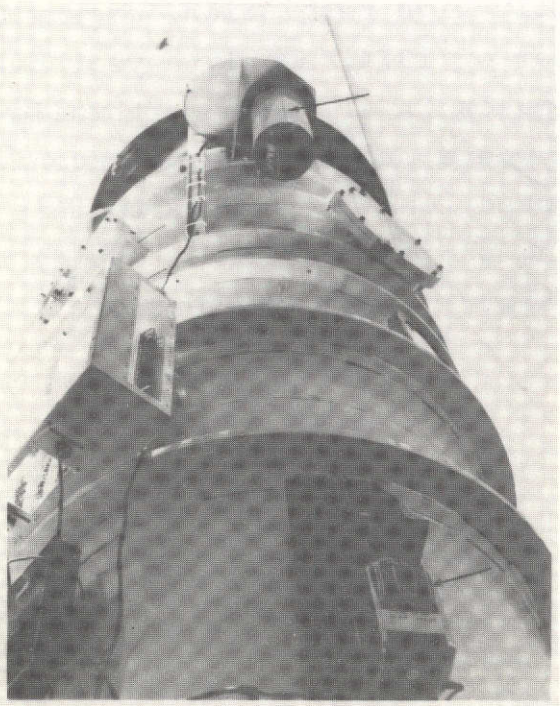

Mounting Details: White Light/full disk Telescope with Hasselblad Camera.

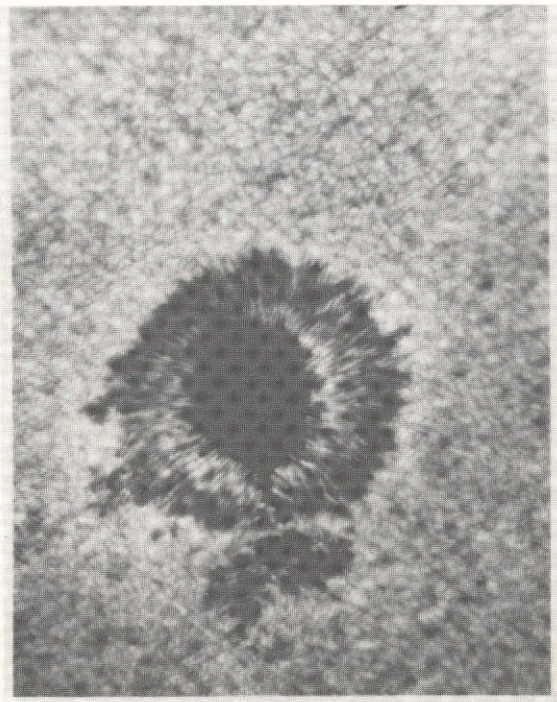

65 cm Telescope
White Light image of sunspot showing
high resolution granulation and penumbral structure.

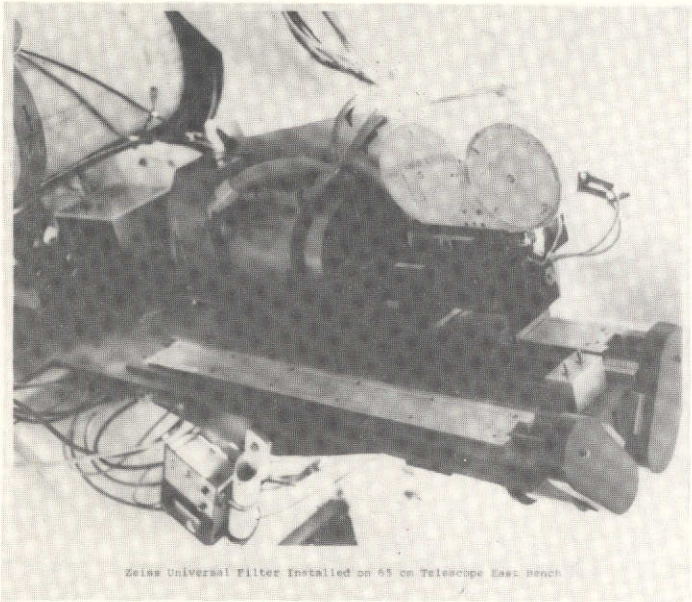

Zeiss Universal Filter Installed on 65 cm Telescope East Bench

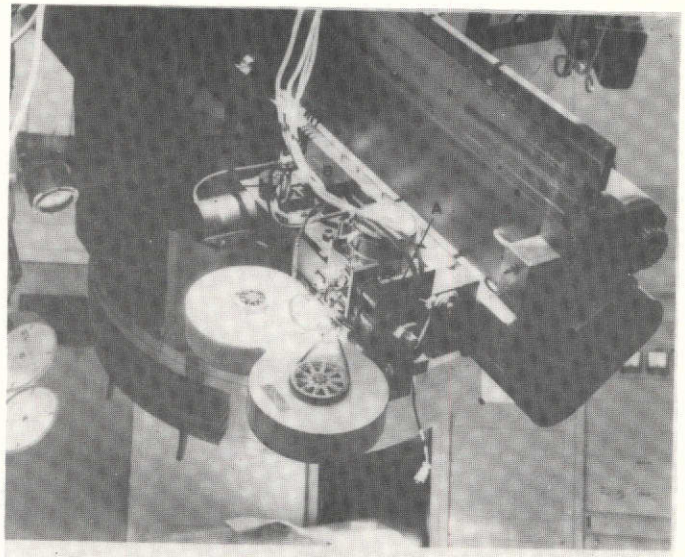

65 cm Telescope East Optical Bench showing: A. Mitchell Stop Action Camera
B. Auto Exposure Control

Photographs by Laboratory of Sunspots

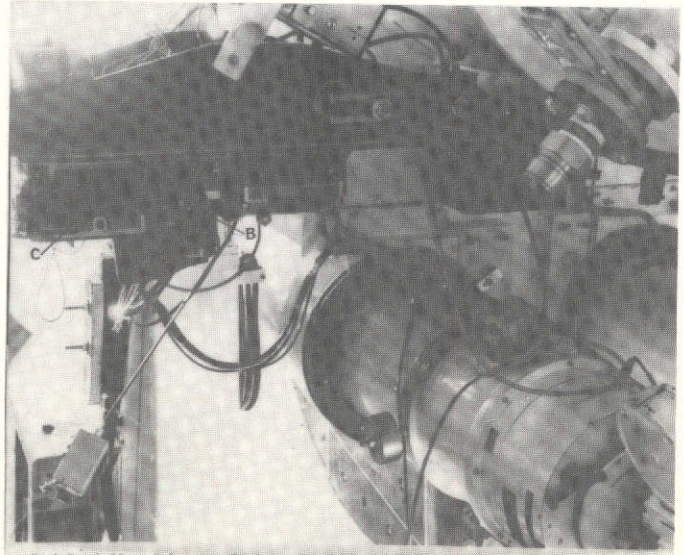

East Bench 65 cm Telescope showing: A. Halle H-α Filter B. Auto Exposure Control
C. Mitchell Stop Action Camera (with film magazine removed).

Appendix D

LMSC Filter Studies
Final Report

FINAL REPORT

FILTER STUDIES IN HeI AND CaII

LMSC/D401258 April 1974

Prepared by: Harry E. Ramsey
Sara F. Martin

Address: Lockheed Solar Observatory
Plt. 2, Bldg. 243
Rye Canyon Research Center
Lockheed-California Company
P. O. Box 551
Burbank, California 91503

Submitted to: National Aeronautics and Space Administration
Marshall Space Flight Center
Huntsville, Alabama 35812

Contract No.: NAS 8-28021

PREFACE

This is the final report for contract NAS 8-28021, "Filter Studies in HeI and CaII," submitted in accordance with the terms of the contract. Herein, we describe ground-based observational programs conducted during Skylab using filters constructed for the D_3 line of HeI and the infrared CaII line at 8542Å.

TABLE OF CONTENTS

Section		Page
	PREFACE	i
	TABLE OF CONTENTS	ii
	LIST OF ILLUSTRATIONS	iii
1	THE D_3 HeI FILTER OBSERVATIONS	1
	1.1 Summary of the HeI Program	1
	1.2 Hours of D_3 Observations	2
	1.3 Preliminary Results	2
	1.3.1 Visible Activity in D_3	2
	1.3.2 Pre-flare Filament Darkening and the Brightening of Ascending Prominences in D_3	10
	1.3.3 Sunspot Changes and D_3 Activity	11
	1.3.4 The D_3 Chromosphere at the Limb	19
2	THE CaII OBSERVATIONS AT 8542Å	21
	2.1 Objectives	21
	2.2 Description of the Filter	21
	2.3 The Observational Program	22
	2.4 Preliminary Results of the CaII Observations	25
	REFERENCES	35

LIST OF ILLUSTRATIONS

Figure		Page
IA	Two bright ribbons of D_3 emission in the Imp. IB flare of 11 April 1973, move apart at 8 km/sec. D_3 absorption obscures underlying sunspots.	4
IB	Classed as Imp. IIB, the second flare of 11 April 1973 has extensive ejecta (2022:30) and is visible entirely in absorption. The two later sub-flares at 2105:00 and 2132:00 are noticeably darker in D_3 absorption than the second major flare.	5
IC	Enlargement of the Imp. IIB flare, 11 April 1973, especially at 2032:00, resolves fine parallel filaments connecting dark strings of points. One string, the lower, moves as a sharply defined front, away from the other string.	6
II	A pre-flare filament darkening (1934:30) and abrupt disappearance with an Imp. IIB flare. Bright arches appearing abruptly in the post-maximum phase (2003:15) are probably the tops of a "complex coronal loop system."	8
III	At D_3 + .8Å (A) sub-flares are rarely visible. They are best observed at "line center" (B). The Hα flare is red-shifted ~ .8Å (D) at a place where D_3 is darkest at line center. The brightest Hα (C) and darkest D_3 do "not" coincide.	9
IV	A rapidly ascending prominence observed in D_3 (upper), brightens dramatically in a manner qualitatively consistent with that observed in Hα (lower).	12
V	D_3 events associated closely with rapid spot changes in a growing region, 5 August 1973.	14
VI	On the next day, 6 August 1973, several small spots suddenly appear, with an Imp. I flare. Rapid spot growth occurs again later in the day with a second D_3 event.	15

LIST OF ILLUSTRATIONS (Cont'd)

Figure		Page
VII	Small spots suddenly appear and grow at either end of a D_3 event.	16
VIII	Under more questionable seeing conditions, a small spot appears in the penumbra of a larger spot, near the terminal of a D_3 event.	17
IX	A small filamentary appendage accompanies a dying spot, while nearby a spot grows, with a D_3 event.	18
X	The D_3 chromosphere appears as an elevated shell (White, 1963) very much brighter above an active region.	20
XI	CaII active regions seen near the west limb.	24
XII	A flare-associated wave in CaII (8542Å) and Hα. Bottom row is Hα + 1.2Å.	26
XIIIA	Beginning of Imp. IB flare on 5 September 1973 with eruption of a filament.	27
XIIIB	Erupting filament associated with flare on 5 September 1973.	28
XIIIC	Surge developing with the flare and erupting filament on 5 September 1973.	29
XIIID	Slowing and reversal of surge direction - after the end of the flare on 5 September 1973.	30
XIV	Flare in CaII showing suggestion of fine structure.	31
XV	Dark borders are seen around plage of all active regions in CaII at 8542Å.	32
XVI	Development of an active region at 8542Å.	34

SECTION 1

THE D_3 HeI FILTER OBSERVATIONS

1.1 Summary of the HeI Program

The D_3 HeI system began first operation in April, 1973, and has functioned successfully, with some changes and improvements added between manned Skylab missions, to the present, April, 1974. We obtained over 12,000 feet of 35 mm time-lapse films in D_3 at mostly 15 sec. intervals, with emphasis in observation during the three manned periods of Skylab.

The first D_3 filter completed was a .4Å (half-width) birefringent filter, using, as an experiment, polyvinyl alcohol wave plates, prepared and mounted in a technique described by Title (1974). This filter began operation in April, 1973, and functioned quite well through the first and second manned Skylab missions. After the second mission, the D_3 filter was completely rebuilt in a new design utilizing alternating inefficient polaroids, developed and described by Title (1974). This design resulted in a filter transmission increase of better than a factor of two, with equal or improved filter contrast. At this time the filter was also modified to provide a continuous reference at 5876 + .8Å. For the final Skylab mission, we obtained simultaneous pictures at 15 sec. intervals at D_3 and D_3 + .8Å.

Some technical difficulties were encountered during missions, but in general the D_3 program has been exceptionally successful. It has yielded a wealth of observational data for analysis and correlation with Skylab observations.

For the final Skylab mission we also set up a full limb eclipsing system in D_3 to record prominence activity in D_3 with Hα, most especially ascending and active prominences.

1.2 Hours of D_3 Observations

On the following page is a list of days with hours of observation with the D_3 large-scale system during the three manned Skylab missions.

1.3 Preliminary Results

1.3.1 Visible Activity in D_3

A detailed comparison of all D_3 events with Hα has not yet been made. Such comparison was deliberately omitted in hopes of more effectively assessing the nature of visible activity in D_3 without bias from the more visible Hα flares.

For this reason we use the term D_3 events on activity except in the obvious cases of major flares.

D_3 Emission

Less than 10% of all D_3 events observed with a .4Å filter against the solar disk are visible at any time in emission. Intense emission well above continuum intensity is even less frequent and limited to only major flares classed invariably as bright in Hα.

"Bright emission" in D_3 can be described as four distinct features of flares:

(1) Bright localized centers. These abruptly with flare start and occur adjacent to sunspots (LMSC/695791) (Harvey and Milkey, 1972) with lifetimes on the order of 20 minutes.

(2) Moving ribbons. Two bright parallel ribbons start close together and move apart, completely analogous to many flares observed in Hα (Dodson, 1960) (Morton and Malville, 1963). In Figure IA, the D_3 flare ribbons expand or move apart at a velocity of 8 km/sec., consistent with Hα flares observed.

HOURS OF D_3 OBSERVATIONS

L. S. D_3

Date	May 1973		June 1973		July 1973		August 1973		September 1973		October 1973		December 1973		January 1974		February 1974	
	Start	End	Start	End	Start	End	Start	End	Start	End	Start	End	Start	End	Start	End	Start	End
1					1505	2500	1535	2457	1620	2320	1736	2448						
2			2024	2153	1528	2558	1455	2507	1504	2518							1652	2210
3			1511	2116	1453	2438	1518	2532									1652	2135
4			1530	1740			1513	2250	2043	2432	2404	2446					1846	2308
5					1505	2604	1704	2400	1957	2156								
6			1722	1833	1654	2505	1634	2612	1511	2306								
7			1528	2542	1551	2417	1643	2457	1632	2354								
8			1500	2520	1534	2500	1558	2305	1716	2429			1641	2344				
9			1551	2150	1501	2425	1502	2235	1606	2418			1650	2340				
10			1514	2230	1519	2326	1502	2415	1805	2224			1954	2345				
11			1700	2550	1442	2405	1513	2500										
12			1544	2402	1500	2145	1504	2300	1535	2250					2025	2107		
13			1534	2311	1725	2302	2158	2219	1827	2301					1756	2209		
14					1710	2250	1959	2300	1908	2233					2224	2400+		
15			1432	2450	1527	2420	2019	2256	1836	2428	1545	2340			1706	2410		
16			1509	2425	1518	2254	1459	2535	1703	2245								
17	1740	2000	1505	2337	1521	2315	1502	2413	1528	2324			1935	2320				
18			1501	2225			1517	2500	1549	2158			1727	1909	1945	2226		
19	1836	2233	1536	2238	1458	2347	1504	2502										
20	1506	2237	1450	2532	1535	2240							1810	2400				
21	1726	2207	1522	2527	1514	2415	1811	2108	1855	2334			1745	1850	1714	2200+		
22	1756	2230	1543	2237	1510	2400	1720	2210					2036	2110				
23	1527	2131	1520	2246	1748	2309			1614	2330								
24	1835	2230	1504	2547					1710	2412			1901	2235	1952	2327		
25			1511	2620	1501	2410					1813	2225			1650	2215		
26	1511	2430	1551	2510	1501	2401							1724	2057				
27	1500	2436	1511	2602	1507	2338	2346	2405			1609	1731			2016	2238		
28	1546	2459	1444	2532	1520	2500	1518	2358	1547	2442	1705	2403			1755	2232		
29			1445	2434	1515	2440	1533	2400+	1518	2427								
30	1523	1626	1519	2350	1541	2518	1514	2400±	1533	2240								
31					1509	2412	1640	2240							1655	2215		

NOTE: No L.S. D_3 in November, 1973

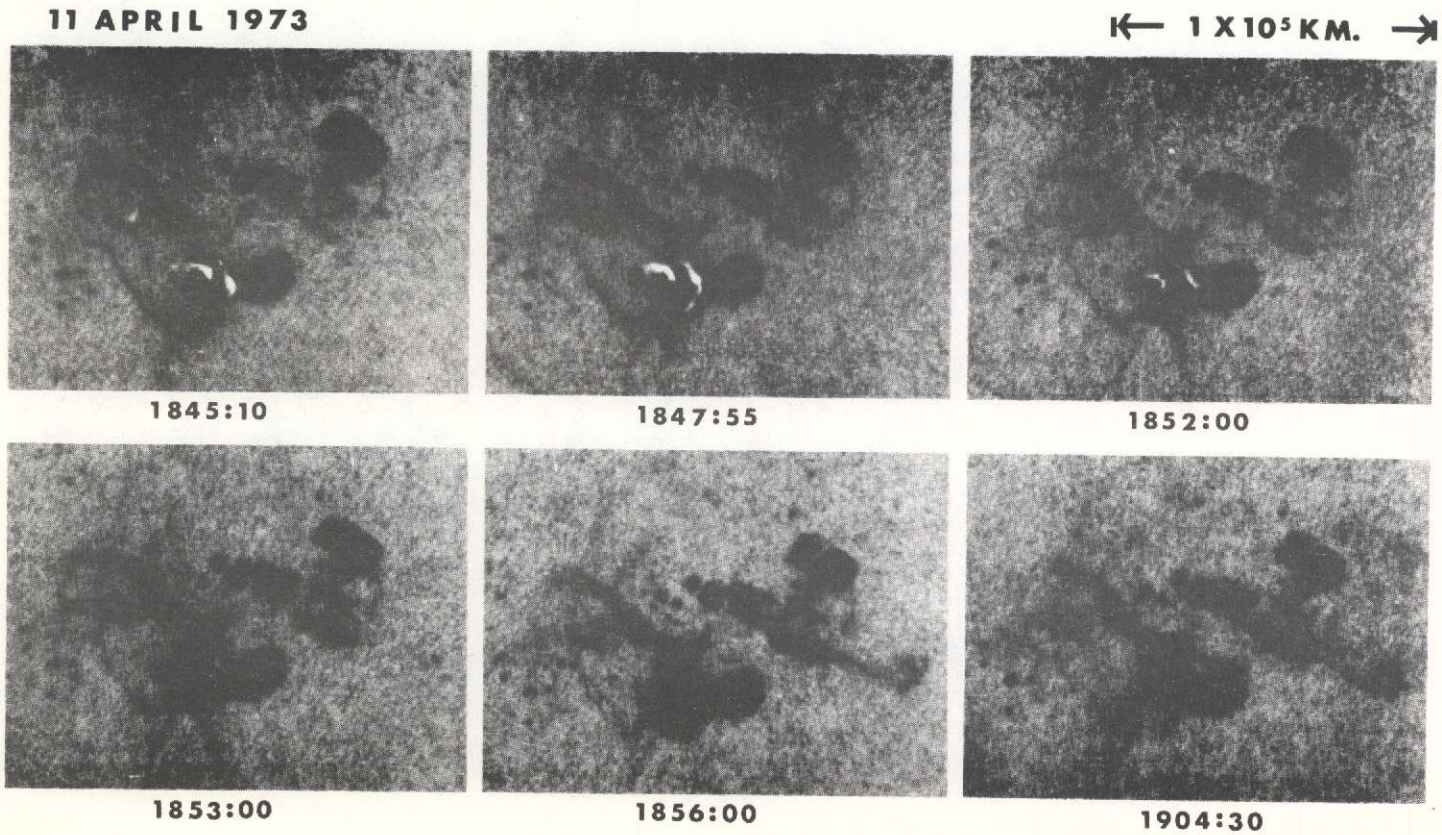

Figure IA. Two bright ribbons of D_3 emission in the Imp. IB flare of 11 April 1973, move apart at 8 km/sec. D_3 absorption obscures underlying sunspots.

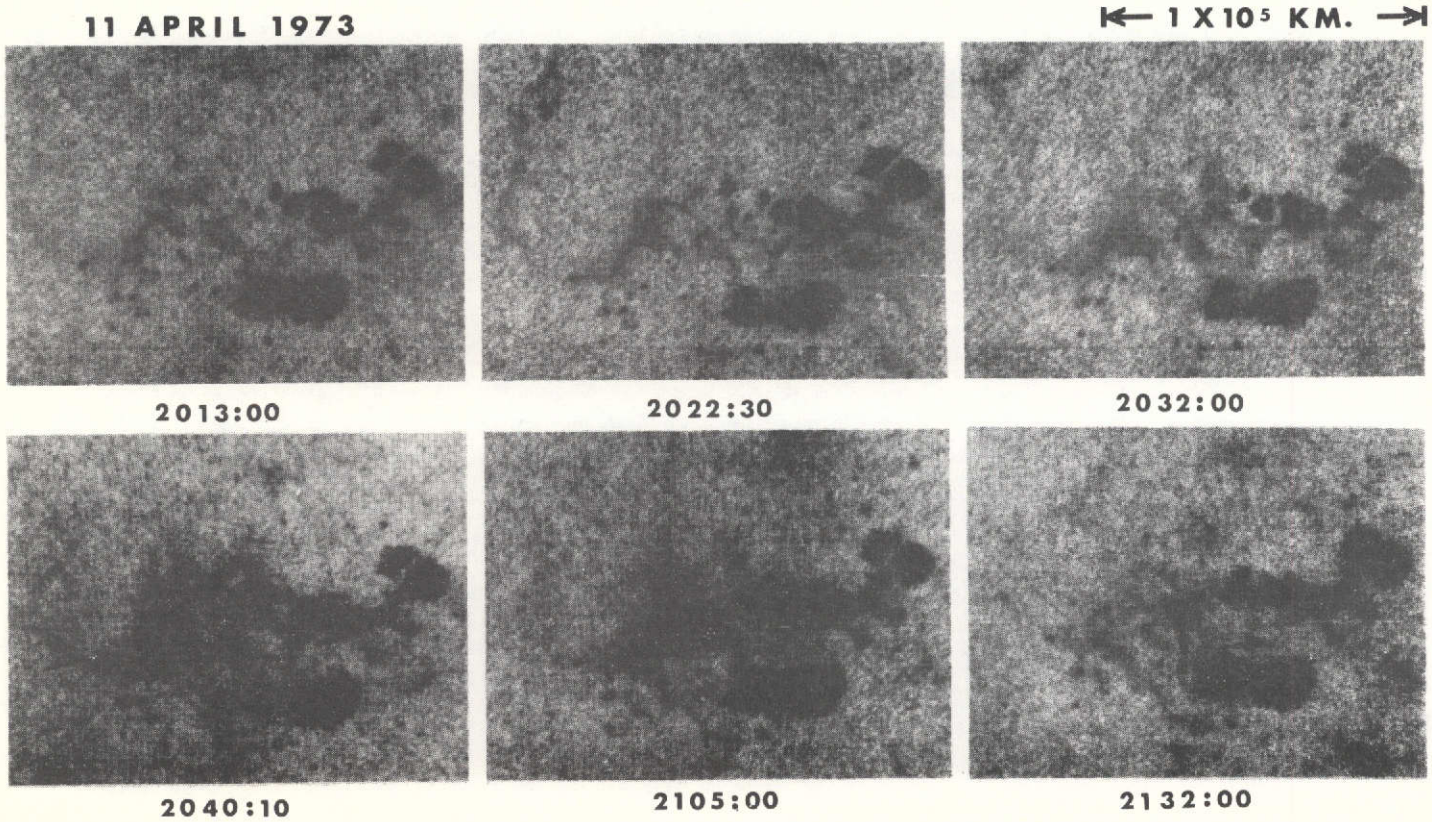

Figure IB. Classed as Imp. IIB, the second flare of 11 April 1973, has extensive ejecta (2022:30) and is visible entirely in absorption. The two later sub-flares at 2105:00 and 2132:00 are noticeably darker in D_3 absorption than the second major flare.

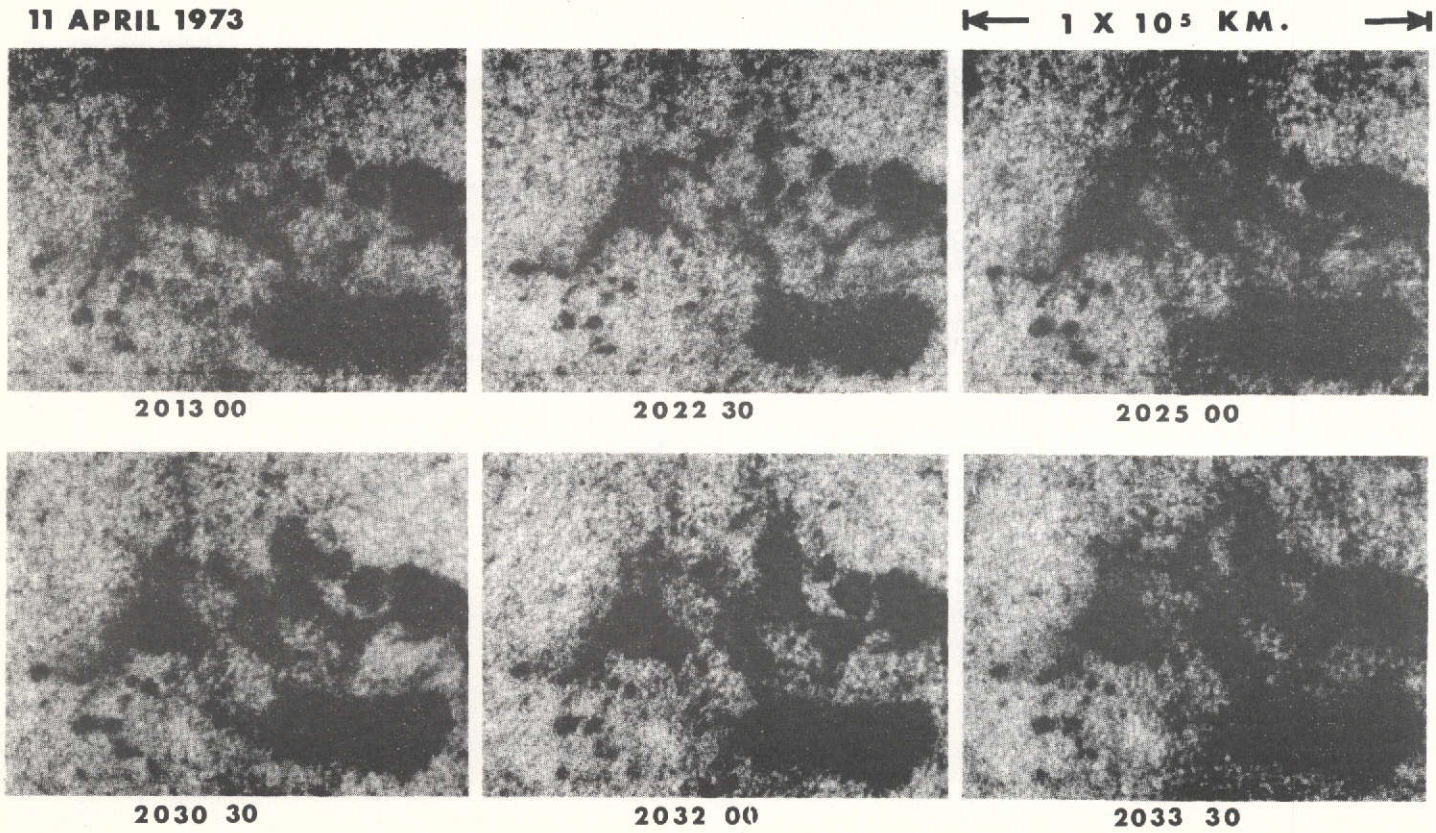

Figure IC. Enlargement of the Imp. IIB flare, 11 April 1973, especially at 2032:00, resolves fine parallel filaments connecting dark strings of points. One string, the lower, moves as a sharply defined front, away from the other string.

(3) Multiple arch condensations. A localized parallel system of bright arches appears in the post maximum phase of a major flare and coincides almost certainly to the tops of a complex "coronal loop system." (Figure II)

(4) Short-lived emission centers. These low intensity emission centers are observed adjacent to spots at the initial phase of major flares and also with the beginning of emission loops (Figure II) limb.

The visibility of "faint emission" in D_3 flares may increase as a function of proximity to the limb. Several sub-flares near the limb were seen in emission indicating that a sizeable number of D_3 events are invisible against the brighter center of the solar disk. This may be the case in Figure III. The red-shifted bright feature in the Hα spectrum (D), typical of many Hα flares, in not visible at D_3 + .8Å (A). Note the brightest part of the Hα flare (C) does not coincide spatially with the darkest D_3 absorption (B).

D_3 Absorption

Almost all Hα flares of any consequence probably have a period of limited visibility in D_3 in absorption when observing with a filter of .5Å or less and under good seeing conditions. We judge this by the large numbers of D_3 events observed with the improved filter of .4Å half-width.

Besides long-lived absorption features in D_3 such as bright plage or active filaments, there are five distinguishable types of distinct, transient D_3 activity.

(1) Arch condensations. The majority of small events are observed as arch shape condensations, with one or both ends terminating at sunspots. With many events observed simultaneously at D_3 and D_3 + .8Å, this absorption is best observed at line center, and is rarely visible at D_3 + .8Å (Figure IIIA and B). This differs from Hα flares which exhibit a marked preference for the red wing.

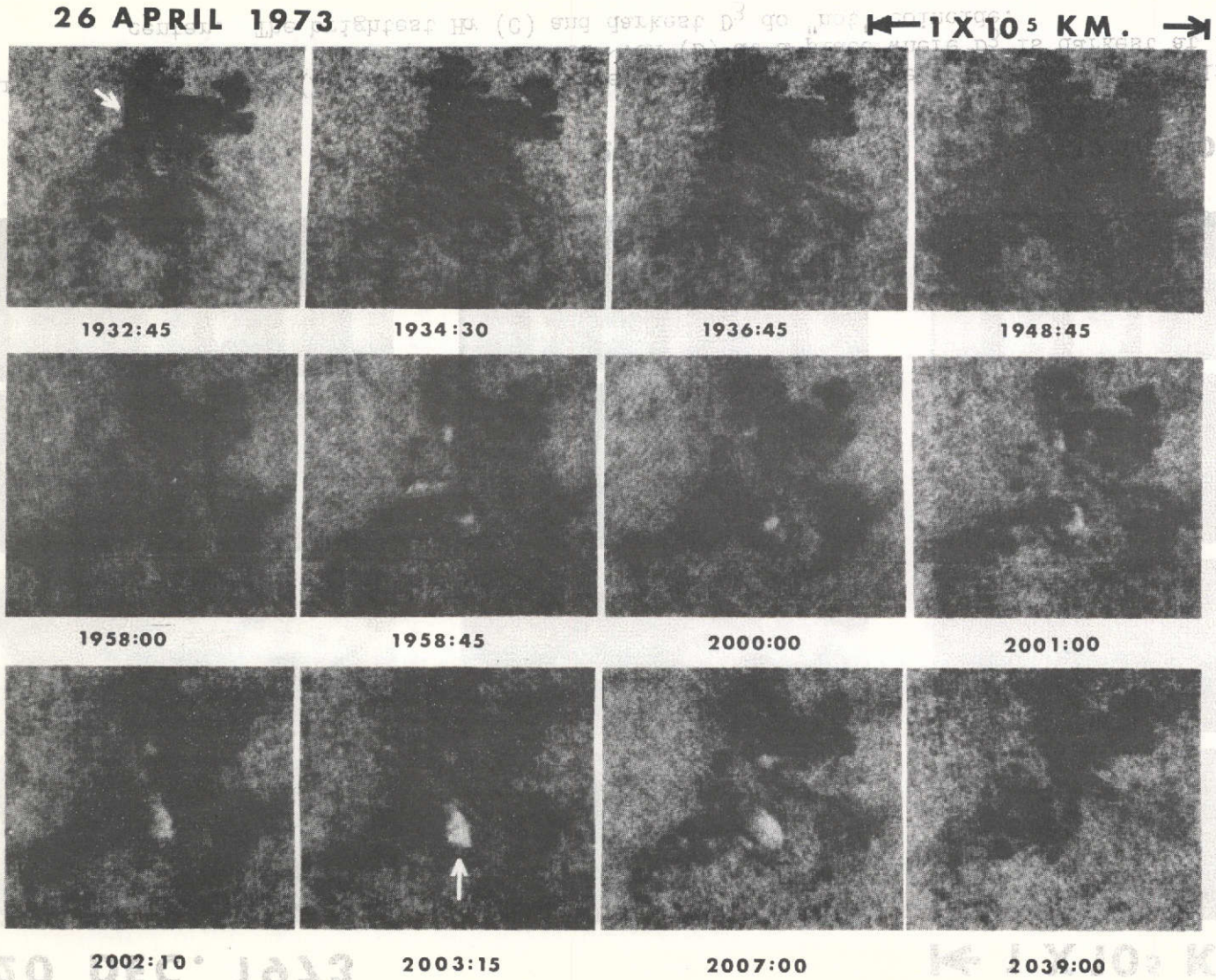

Figure II. A pre-flare filament darkening (1934:30) and abrupt disappearance with an Imp. IIB flare. Bright arches appearing abruptly in the post-maximum phase (2003:15) are probably the tops of a "complex coronal loop system."

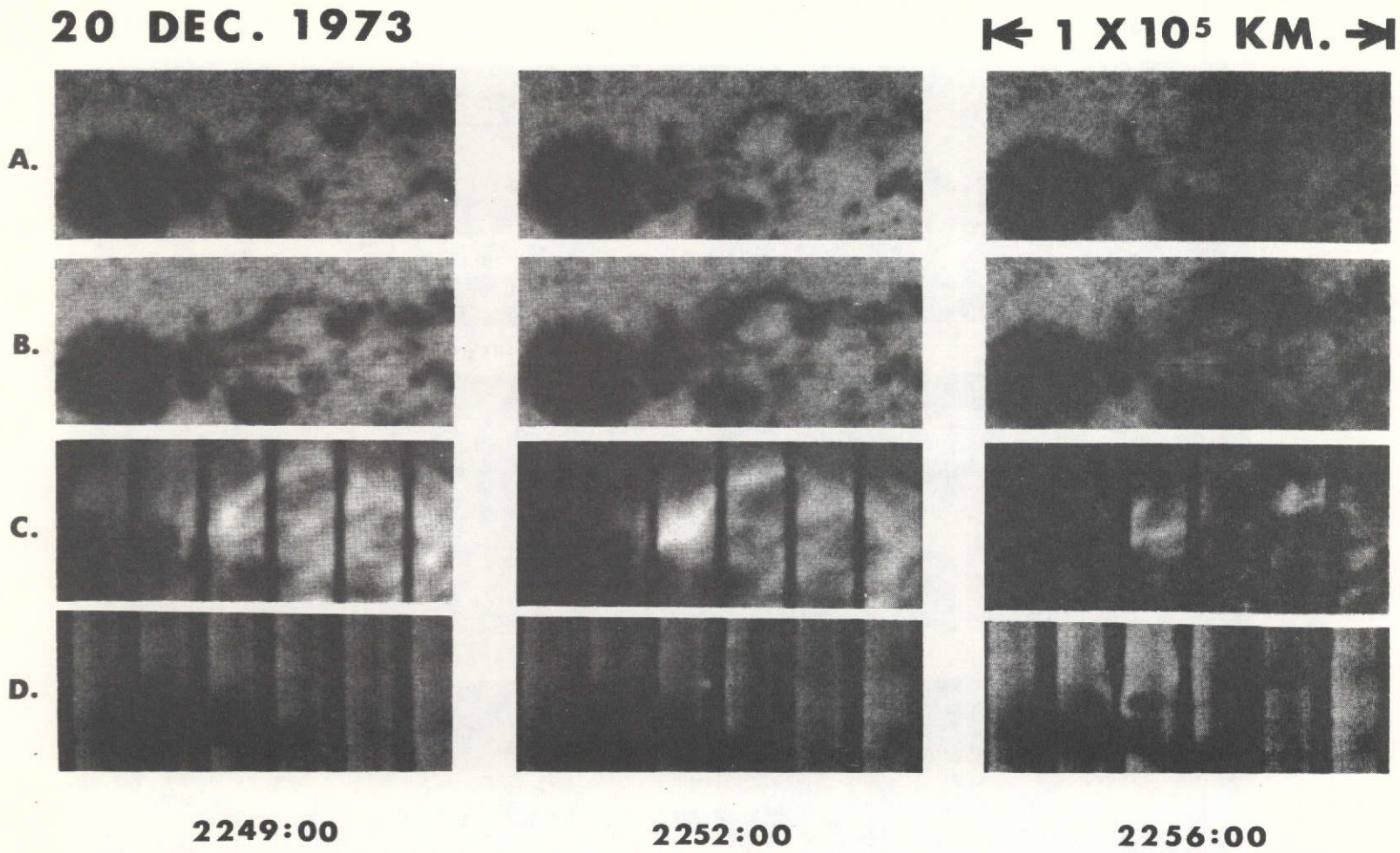

Figure III. At D_3 + .8Å (A) sub-flares are rarely visible. They are best observed at "line center" (B). The Hα flare is red-shifted ~.8Å (D) at a place where D_3 is darkest at line center. The brightest Hα (C) and darkest D_3 do "not" coincide.

(2) Moving ribbons. With major flares we observe large areas of slowly changing absorption features frequently as two parallel ribbons moving apart. Such features coincide extremely well with the Hα emission, Figures I and II.

(3) Fine threads. In high resolution, Figure IC, at 2032 U.T., many absorption features in a major flare resolve into fine parallel filaments connecting dark strings of points. One string of dark points (foot-points) advances as a sharply defined front moving away from the other. This agrees well with some Hα flares observed in high resolution, with the difference that D_3 displays the very fine filament structures resembling coronal condensations.

(4) Foot-points. The darkest observed D_3 absorption features in single pictures, easy to confuse with sunspots, are frequently the apparent foot-points of D_3 condensations. These foot-points frequently occur adjacent to sunspots.

(5) Erupting filaments. The "pre-flare filament darkening" generally observed in the blue wing of Hα (Smith and Ramsey, 1964) (Martin and Ramsey, 1973) has been observed with three major flares in D_3. Exactly as in Hα we observe it as a pronounced darkening, expanding arch, and abrupt disappearance, Figure II. In one of three flares, we observed the breakup of the filament and ejection in a transverse direction at high velocity.

1.3.2 Pre-flare Filament Darkening and the Brightening of Ascending Prominences in D_3

The physical mechanism for observing a brightening of ascending prominences in Hα presented by Hyder, 1970, is one of resonance scattering due to the increased photospheric radiation that a Doppler shifted feature sees when it is experiencing increasing radial velocity (Doppler brightening). In D_3, we have no dense absorbing chromosphere and thus no means of producing increased resonance scattering by radial motion. Consequently, an ascending prominence in D_3 should not brighten as much as Hα if resonance scattering is the primary mechanism.

If we interpret the pre-flare filament darkening against the disk as brightening of an ascending prominence (Smith and Ramsey, 1964), then D_3 does in fact, at least qualitatively, behave very much like Hα (Figure II).

To further test the hypothesis of Doppler brightening we set up a full limb D_3 eclipsing telescope to observe D_3 prominences simultaneously with an Hα prominence patrol. Several ascending prominences were observed, which were judged to be moderately slow, and with these very little brightening was observed in either D_3 or Hα. With all active, rapidly moving prominences, both D_3 and Hα became significantly brighter during periods of increased prominence motion. With the one classic "rapidly" ascending prominence, Figure IV, observed to date, the D_3 prominence brightens in a way which appears identical to Hα. We plan to micro-densitometer this event to more carefully determine their relative brightness increases.

The obvious weakness in these observations, beyond exposure difference, is that the Hα system has a 1Å filter and cannot contain such strong Doppler shifts as the 6Å D_3 filter system.

We plan to rectify this weakness in a new system using two eclipsing telescopes and essentially identical D_3 and Hα filters.

1.3.3 Sunspot Changes and D_3 Activity

Except for the possible temporary obscuration of sunspots by D_3 transient events, the scarcity of the D_3 chromosphere offers a convenient means of relating D_3 events with photospheric sunspots and their changes. As anticipated, we find a strong correlation between the frequency of D_3 events and changing sunspots. This is especially true with the appearance and growth of new spots (growing or emerging active regions).

During the second Skylab mission we observed the rapid growth of such a region, associated with numerous D_3 events. The most interesting aspect of the activity is the suggestion of individual flares associating with rapid

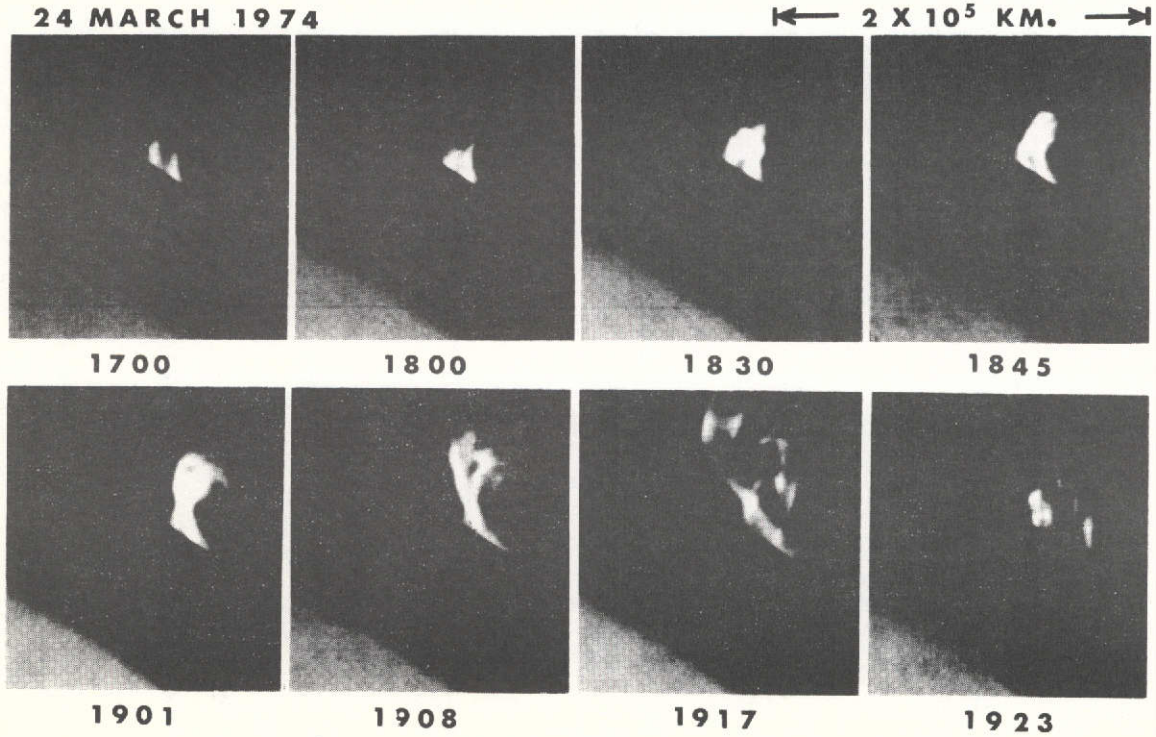

Figure IV. A rapidly ascending prominence observed in D_3 (upper), brightens dramatically in a manner qualitatively consistent with that observed in $H\alpha$ (lower).

changes in small umbrae. We have observed almost continuous D_3 activity adjacent to and over a rapidly growing sunspot for a period of several hours. The suggestion is, however, that sunspot growth may occur in spurts associated with the individual D_3 events. On August 5, 1973, Figure V, we point out several small spots changing rapidly, appearing to coincide with individual D_3 events. With the first event we observe one spot decrease in size while another grows, with the D_3 event spanning between. This is a rapidly growing region, and on the next day, August 6, 1973, Figure VI, we observed several small spots appear and grow rapidly with a large D_3 event. Rapid spot growth did not take place again until later in the day when we observed a second D_3 event.

In Figure VII, October 15, 1973, we observe again rapid appearance of small umbrae associated with a D_3 event.

In Figure VIII, September 1, 1973, under more questionable seeing conditions, we observe the appearance of a small spot in the penumbra of a large spot, coincident with a D_3 event.

Occasionally, small spots can both grow and die coincident with D_3 activity, Figure IX.

We have shown several selected events with excellent conditions to show rapid changes in tiny umbrae, exactly coincident with D_3 activity. Much more frequently, even with major flares and excellent conditions, no spot changes could be detected on a time scale relating directly to the flares.

Our few, but interesting rapid changes in tiny umbrae coincident with D_3 activity, point to the need for observing the "strong" sunspots magnetic fields with the high spatial and time resolution necessary to monitor such changes. Present magnetograph techniques do not sufficiently emphasize such strong fields of small spatial extent. With the recent introduction of the diode array to magnetograph techniques, it is evident that such observations will soon be more practical to obtain.

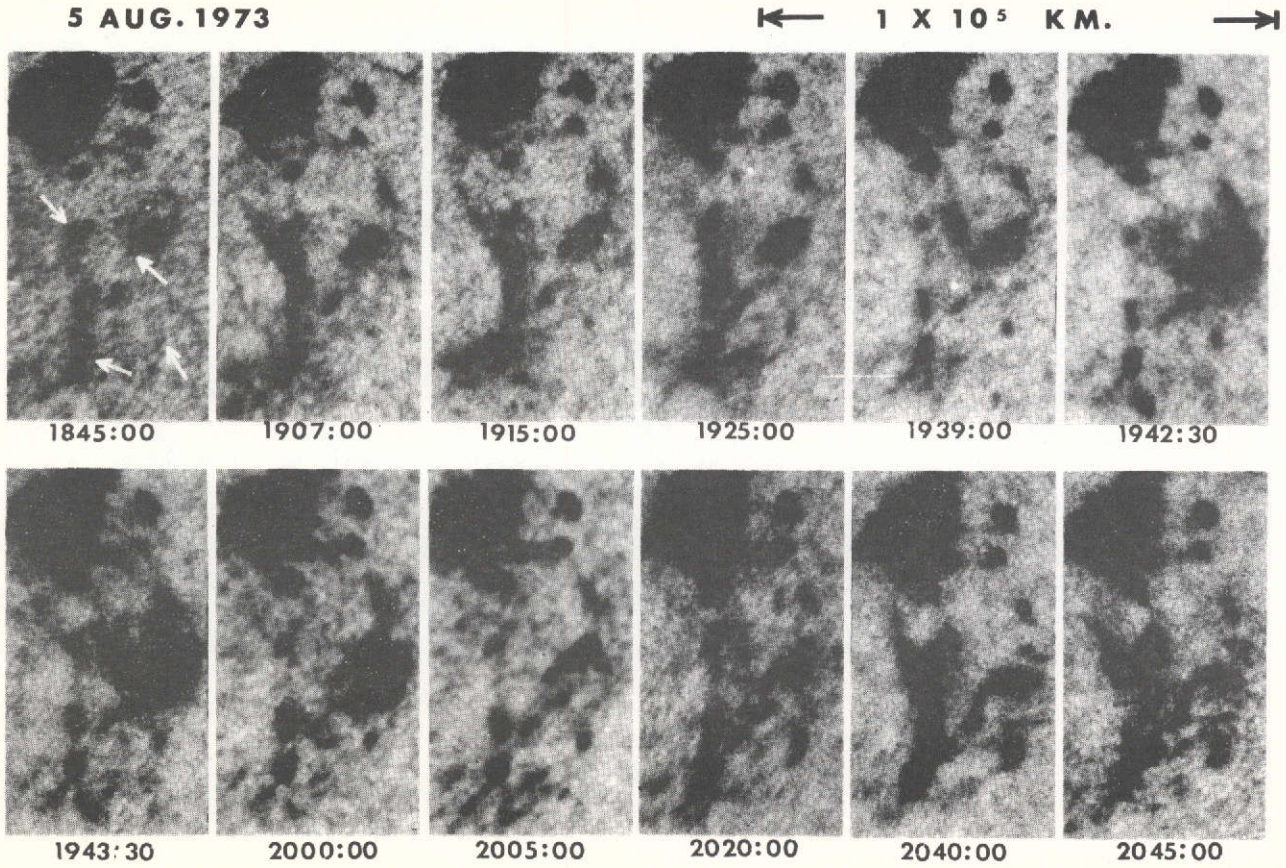

Figure V. D_3 events associated closely with rapid spot changes in a growing region, 5 August 1973.

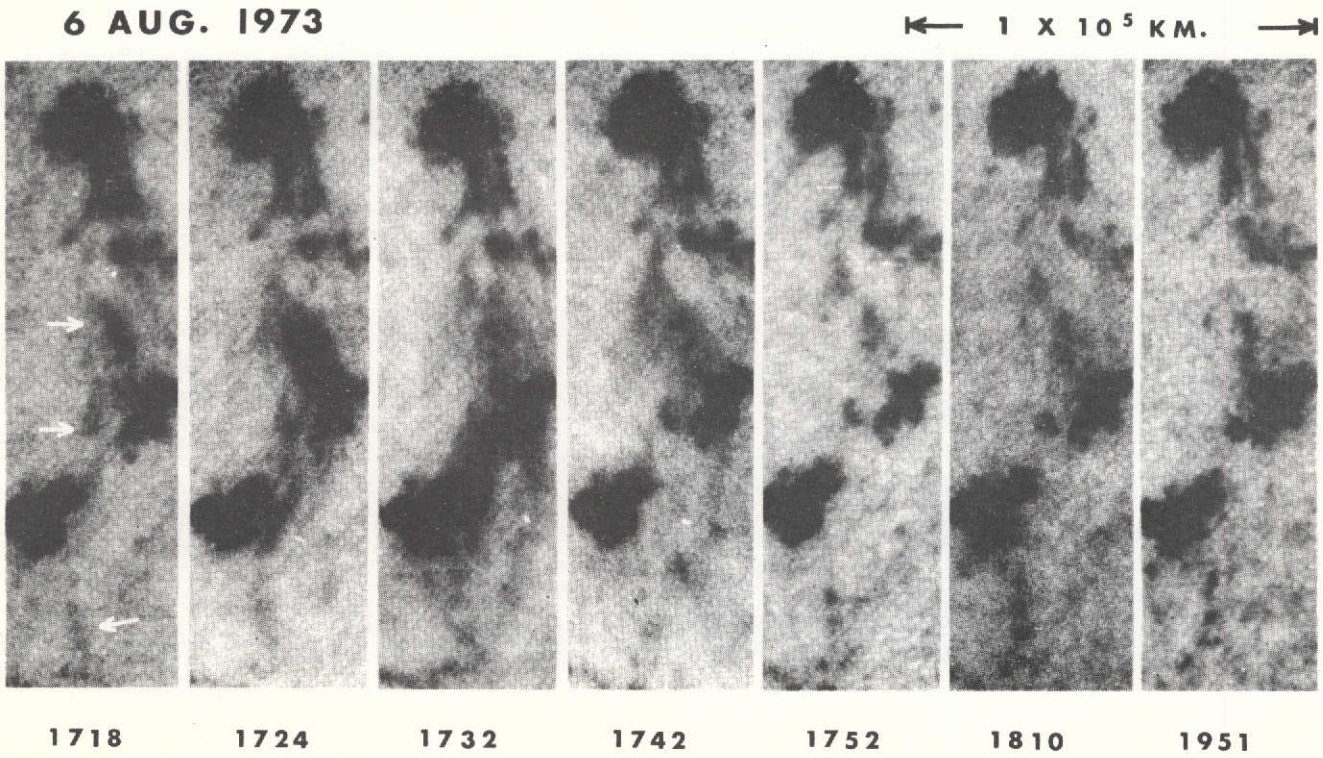

Figure VI. On the next day, 6 August 1973, several small spots suddenly appear, with an Imp. I flare. Rapid spot growth occurs again later in the day with a second D_3 event.

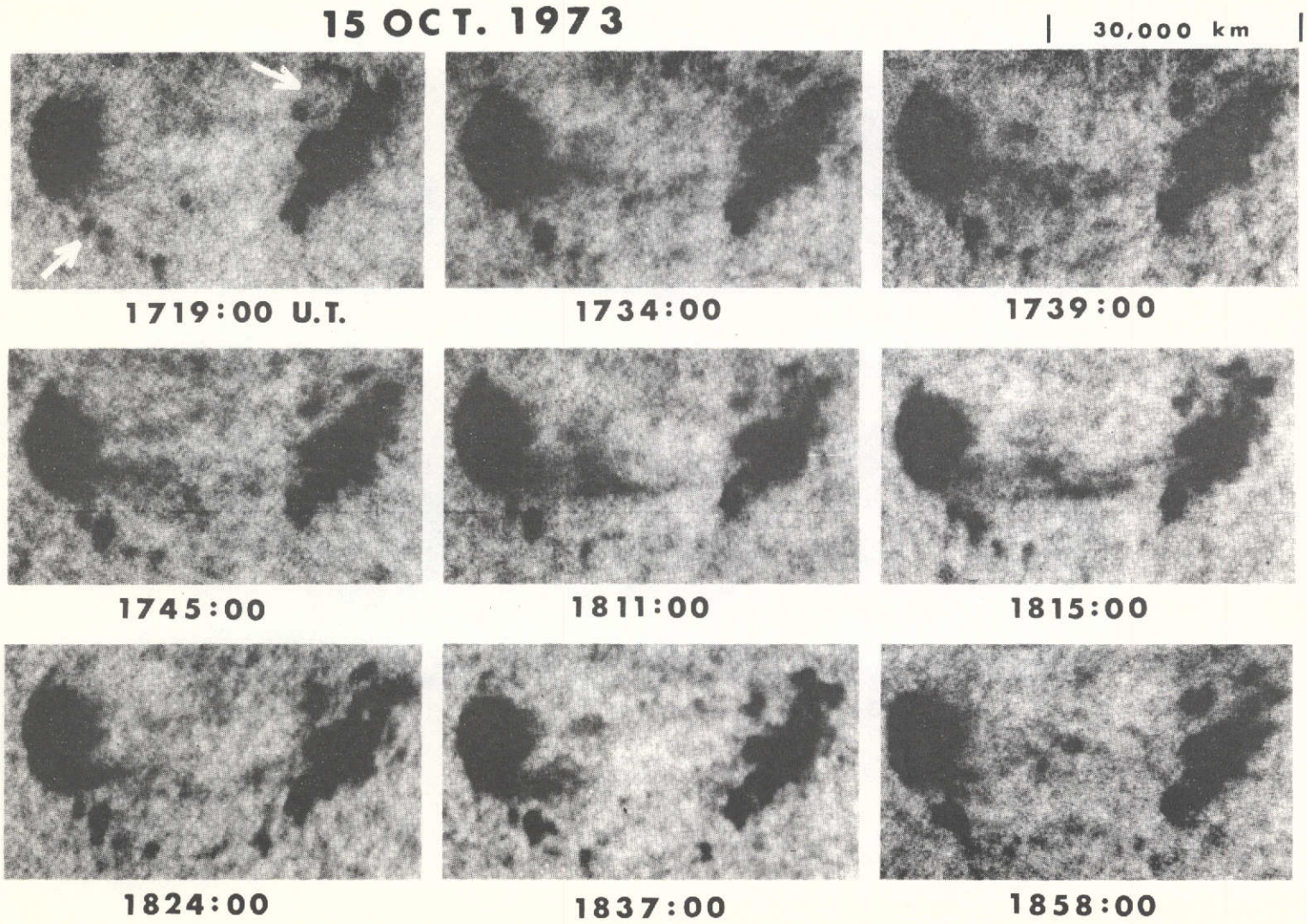

Figure VII. Small spots suddenly appear and grow at either end of a D_3 event.

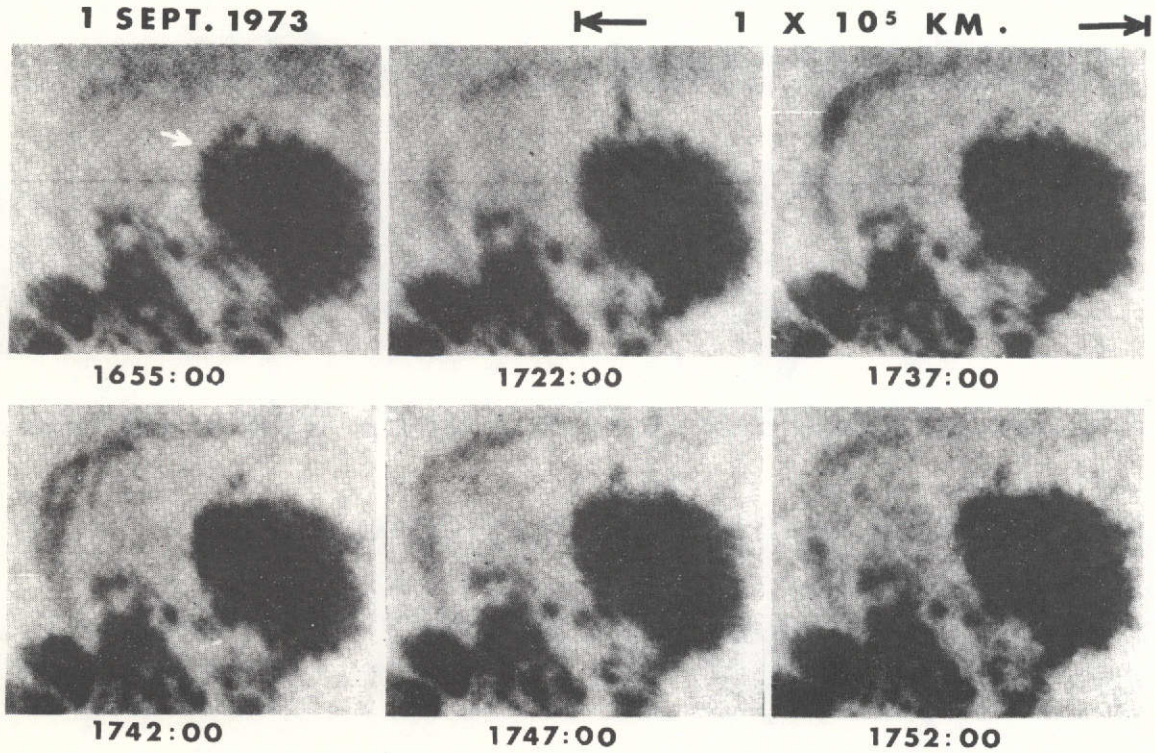

Figure VIII. Under more questionable seeing conditions, a small spot appears in the penumbra of a larger spot, near the terminal of a D_3 event.

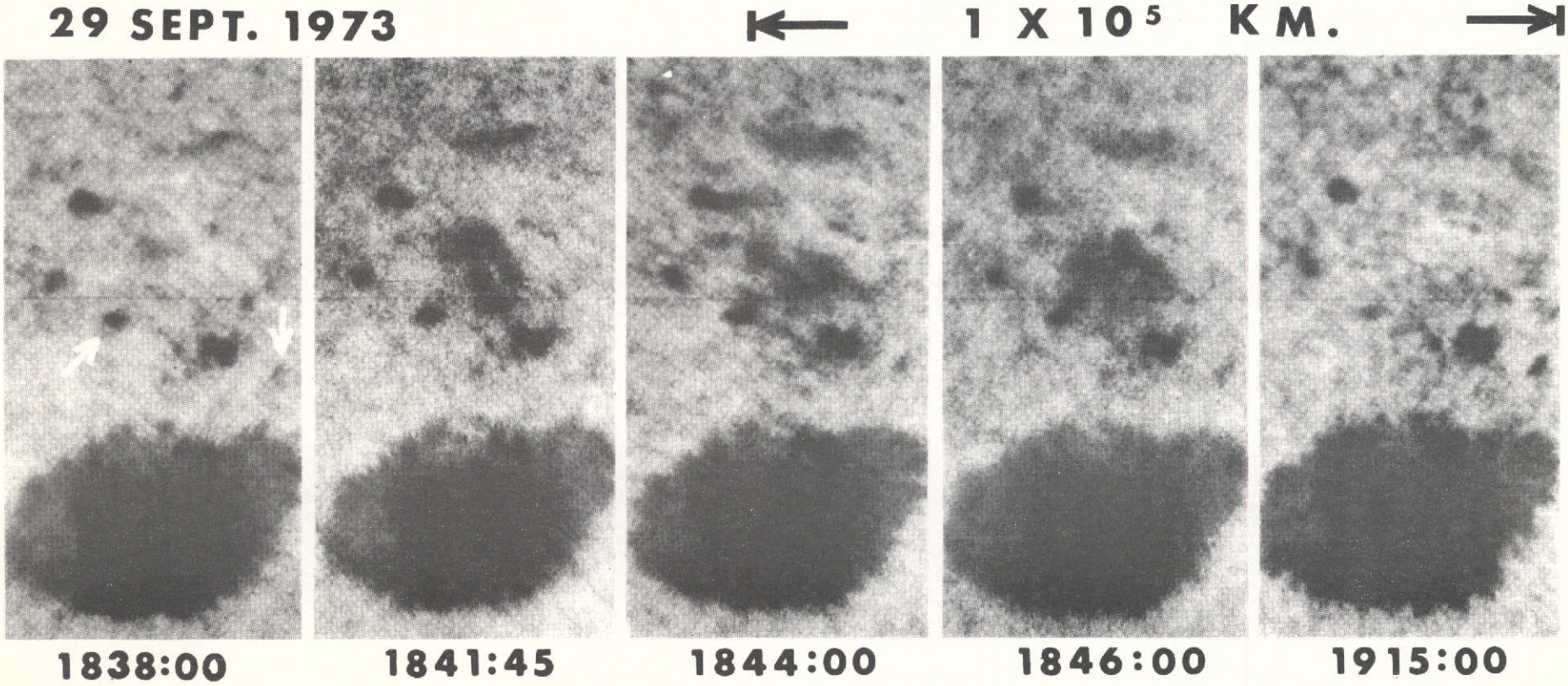

Figure IX. A small filamentary appendage accompanies a dying spot, while nearby a spot grows, with a D_3 event.

1.3.4 The D_3 Chromosphere at the Limb

One of the most interesting aspects of D_3 when observed with a narrow band filter at the solar limb, under good seeing conditions is the D_3 chromosphere. It is concentrated in a raised shell above the photospheric limb. We measured the center of this shell to be 1450 km above the photosphere, confirming measurements of this approximate height made by White, 1963. In Figure X, we picture the D_3 raised shell and how it brightens markedly above an active region directly on the limb. Visually, the D_3 raised shell is evident around the entire limb, but brightens as expected over active regions. The increase in brightness over active regions is much greater than observed for Hα. If this increased brightness of D_3 over active regions corresponds to an increased number of HeI atoms and ions this is a possible source for the increased He abundance observed in space with particles from major solar flares (Hirshberg et al., 1971).

Figure X. The D_3 chromosphere appears as an elevated shell (White, 1963) very much brighter above an active region.

SECTION 2

THE CaII OBSERVATIONS AT 8542Å

2.1 Objectives

A 1/4Å filter for the infrared lines of CaII was built and used for ground-based observations during the Skylab missions. This was an experimental program in that this is the first filter that has ever been constructed for the infrared CaII lines. Our original goal was to take time-lapse observations in the CaII line at 8542Å. This objective was achieved during Skylab III although not during Skylab II or IV. Both the successes and difficulties of this program are described below.

2.2 Description of the Filter

The functioning of this CaII filter built by Spectra Optics, surpasses our original objectives in two respects: (1) The filter is tunable over several hundred angstroms. Thus, it is possible to observe all three of the infrared CaII lines as well as other interesting lines nearby such as the FeI line at 8468Å. (2) Two of the infrared CaII lines (8542Å and 8498Å) can be observed simultaneously or in rapid succession by simply rotating the 8498Å and 8542Å prefilters alternately into the beam. During Skylab III, photographs were only obtained at 8542Å. However, visual assessment of 8498Å and 8542Å were made. No differences could be seen in the two lines, however, it should be noted that visual observations are limited by the quality of image obtained on the TV monitor which shows an interference pattern on the face of the tube. The narrowest passband that the filter can deliver is 1/4Å. However, the filter is versatile in that it can be used as a .37Å filter or a .5Å filter simply by removing one or both polarizers on each end of the filter. The filter can also be used as a Doppler filter by tuning the 1/4Å element out of phase with the rest of the elements. This yields two passbands slightly narrower than 1/4 angstrom, separated by a 1/4Å. If the two passbands are placed symmetrically around a line, one can then observe both ascending and descending mass by use of a polarizing prism behind the filter.

During the construction of the filter we requested two design alterations of the manufacturer, Spectra Optics. Our request was granted with no increase in cost but it did result in a delay in completing the filter. The changes were to: (1) Change the thicknesses of the calcite to provide two passbands centered as close as possible to the lines at 8498Å and 8542Å rather than just the single passband at 8542Å. (2) To incorporate polarizing beamsplitters supplied by us into the filter in place of the sheet polaroid usually used in birefringent filters. This was an important change in order to increase the transmission of the filter. The polarizing coatings were purchased from Perkin-Elmer Corporation using a design specified by Dr. Alan Title.

2.3 The Observational Program

Testing of the completed filter was begun in June, 1973. Two problems were encountered. The filter would not tune properly and the polarizing prisms were found to scatter an excessive amount of light. Spectra Optics took the filter back to solve the tuning problem and Perkin-Elmer agreed to replace the defective polarizing coatings.

Routine observations were begun on August 8, 1973 using the 1/2Å passband. Useful observations were taken until after the end of the second manned mission (Skylab III) using the original set of polarizing prisms.

The replacement prisms were delivered in early December 1973. However, it was not discovered until January 1974, when the new prisms were to be installed in the filter, that they did not meet the size specification and were too large to fit into the filter. This posed an additional problem. The polarizing coatings are soluble in water. Therefore they had to be cut and re-polished in unconventional glass working vehicles such as oil or kerosene. The reworking of the prisms was accomplished after considerable experimentation. The final polish was achieved using ultra-low viscosity silicone oil as an abrasive vehicle. The filter was finally reassembled after the end of Skylab IV.

Photographs taken through the filter with the second set of polarizing prisms are significantly higher in contrast and apparent resolution. Figure XI shows two of the most recent photographs taken through the filter using the .37Å passband centered on 8542Å line. These photographs were printed on the lowest contrast paper available, Agfa Rapid Print No. 1. In comparison, the earlier photographs, taken with the original set of polarizing prisms in the filter, have to be printed on paper 3 grades higher in contrast to achieve a similar appearance.

The photographs in Figure XI were taken with the filter in a telescope having an excellent objective lens 7 inches in diameter. In contrast to D_3 HeI and Hα photographs taken through the same telescope, the CaII photographs show less sharply defined fine structure. To test the visual sharpness of sunspots through the CaII filter, the 8542Å blocking filter was temporarily replaced by an Hα blocking filter. The CaII filter delievered images equal in sharpness to the D_3 observations made on the same day. Thus, the lack of sharply defined fine structure in the CaII photographs relative to Hα is probably not due either to the filter or the telescope. The differences can be attributed to the differences between the IV N emulsion used for the CaII photographs and the ultra fine grain, high contrast, S0392 emulsion used for Hα and to the relative intensity gradient between adjacent structures in the two lines.

IV N, a special order emulsion made by Kodak, was selected because it is the finest grain emulsion available for infrared wavelengths. I N and commercial high speed infrared films were also tested. Although these emulsions are much faster, the grain is so coarse as to inhibit high resolution photography of whole active regions on 35 mm film. During testing of the films, we were advised that the speed of the IV N emulsion could be increased by hypersensitizing the film in a bath of water at approximately 3°C for a few minutes. We followed this recommendation and found that the speed increase was greater than a factor of 4 without appreciable increase in grain size. This reduces the normal exposure through filter with the 1/4Å passband from 1 sec. to less than 1/4 sec.

16 APRIL 1974

17 APRIL

Figure XI. CaII active regions seen near the west limb.

2.4 Preliminary Results of the CaII Observations

On September 5, 1973, an exceptionally good solar flare was recorded on board Skylab III - simultaneously with our ground-based observations on the CaII filter, our Hα Doppler filter and multi-slit spectrograph. This is probably the best flare event recorded during all three Skylab missions. Although the flare was not exceptionally large (Class 1B) it was associated with a filament eruption, a flare-associated shock wave and a large surge.

The CaII observations show no sign of the filament eruption and only a small part of the surge. The wave, however, is as bright or brighter than the bright wave seen in Hα. The arrows in Figure XII point to the curved wave front as it moves out from the flare. The apparent velocity of the wave in the CaII and Hα slit jaw photographs is ~ 400 km/sec. The wave is not visible in the Hα Doppler observations at ±1.2Å in the wings of the Hα in Figures XII and XIII, nor is it readily discernible in the multiple array of Hα spectra (Figures XII and XIII). To our knowledge no other flare-associated waves were recorded during any of the Skylab missions. Several other small flares were recorded in the CaII filter but without any sign of associated events.

Another flare recorded with the CaII filter was under-exposed, and is the only flare in which we can see that the flare has apparent fine structure. This flare, shown in Figure XIV is composed of several small elements. Each element has a relatively short lifetime.

An interesting feature of active regions in the 8542Å line is that the bright plage is surrounded by a region about 30,000 km wide which is darker than the CaII quiet chromosphere. Several examples are shown in Figure XV. The dark band is visible even for relatively young active regions and persists throughout the life of the active region. However, for the oldest, most spread out regions, the dark band seems to be broader and less pronounced. The band apparently corresponds to the outer parts of active regions in Hα where the fibrils appear to lie horizontal to the solar surface. The dark band appears to increase in width with the development of an active region (Figure XV).

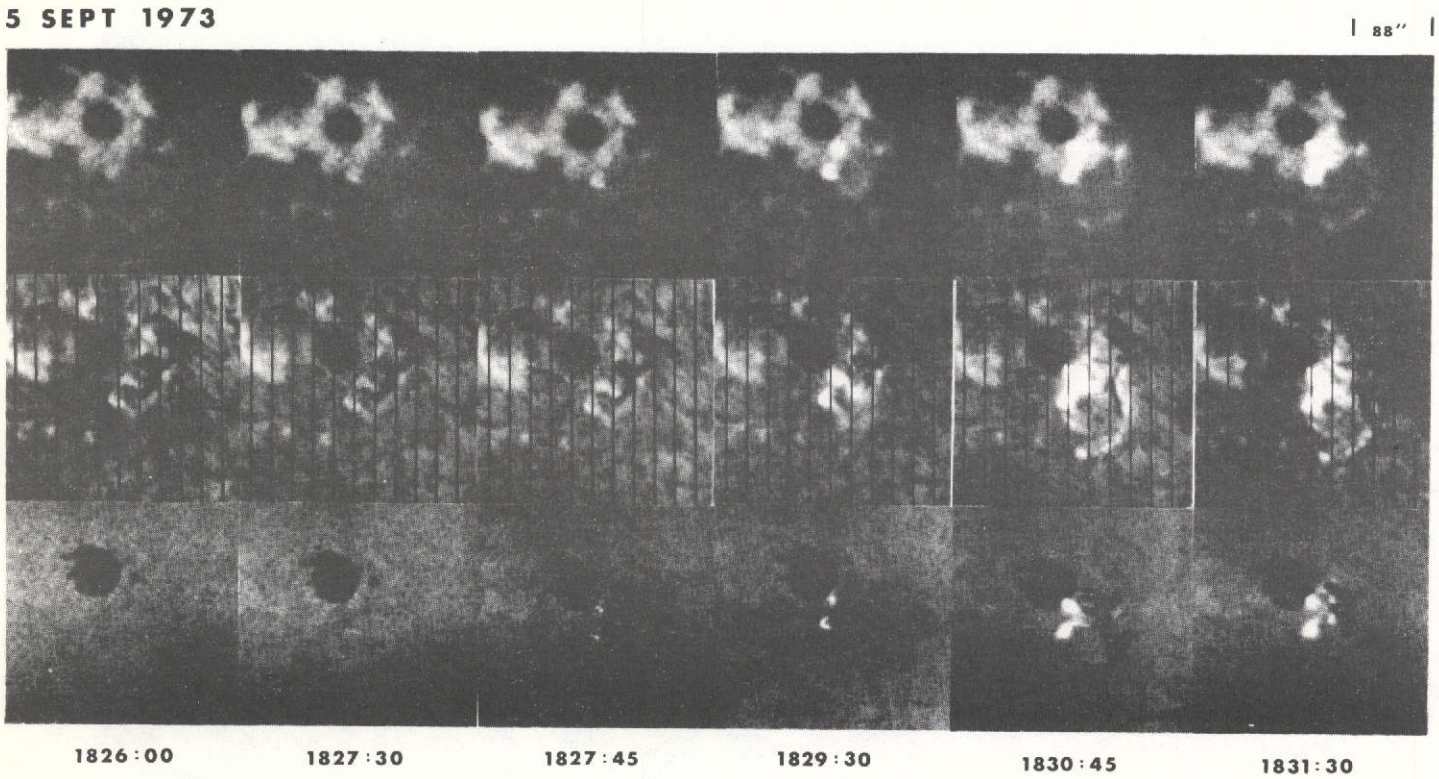

Figure XII. A flare-associated wave in CaII (8542Å) and Hα. Bottom row is Hα + 1.2Å.

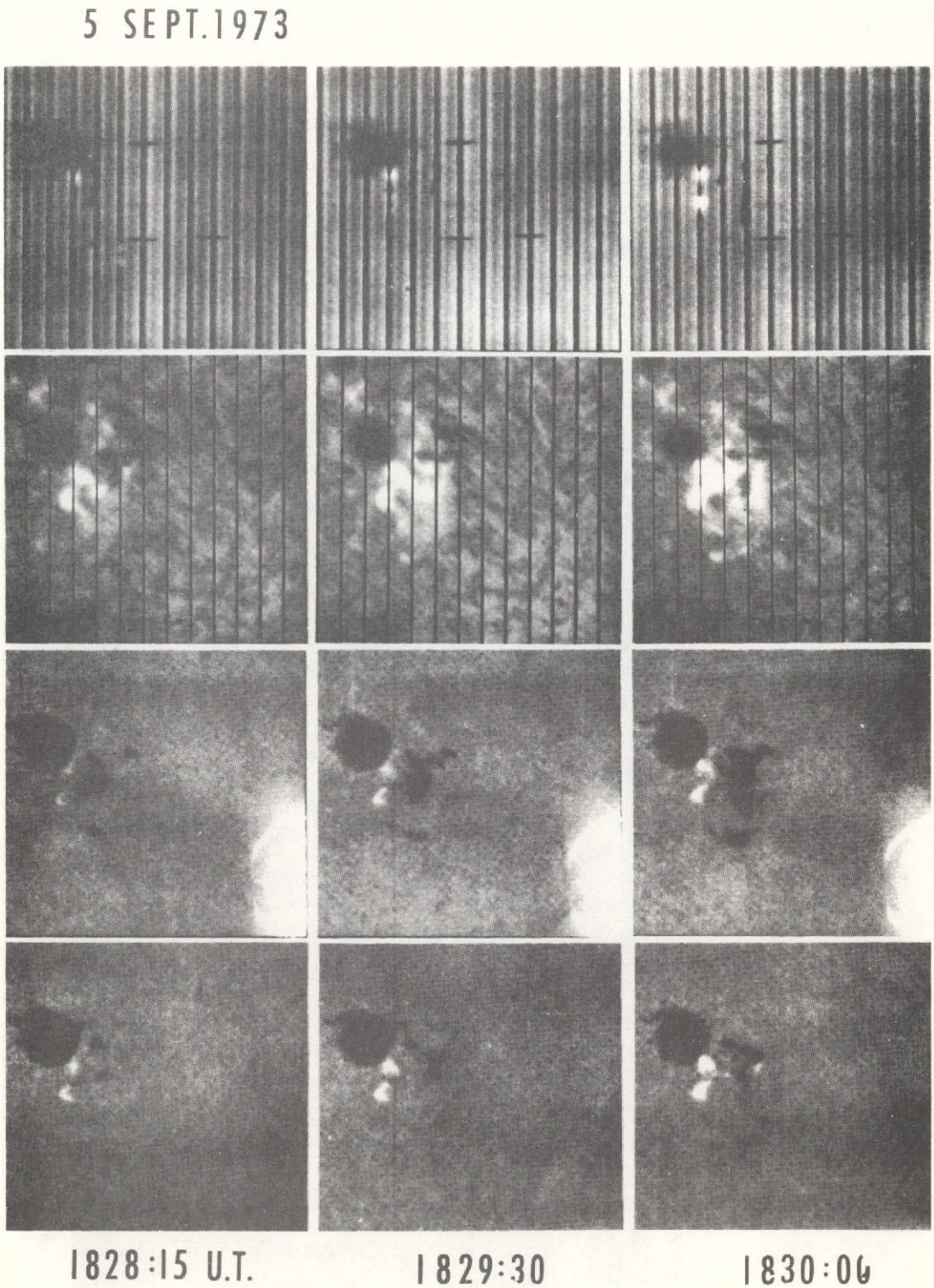

Figure XIIIA. Beginning of Imp. IB flare on 5 September 1973 with the eruption of a filament.

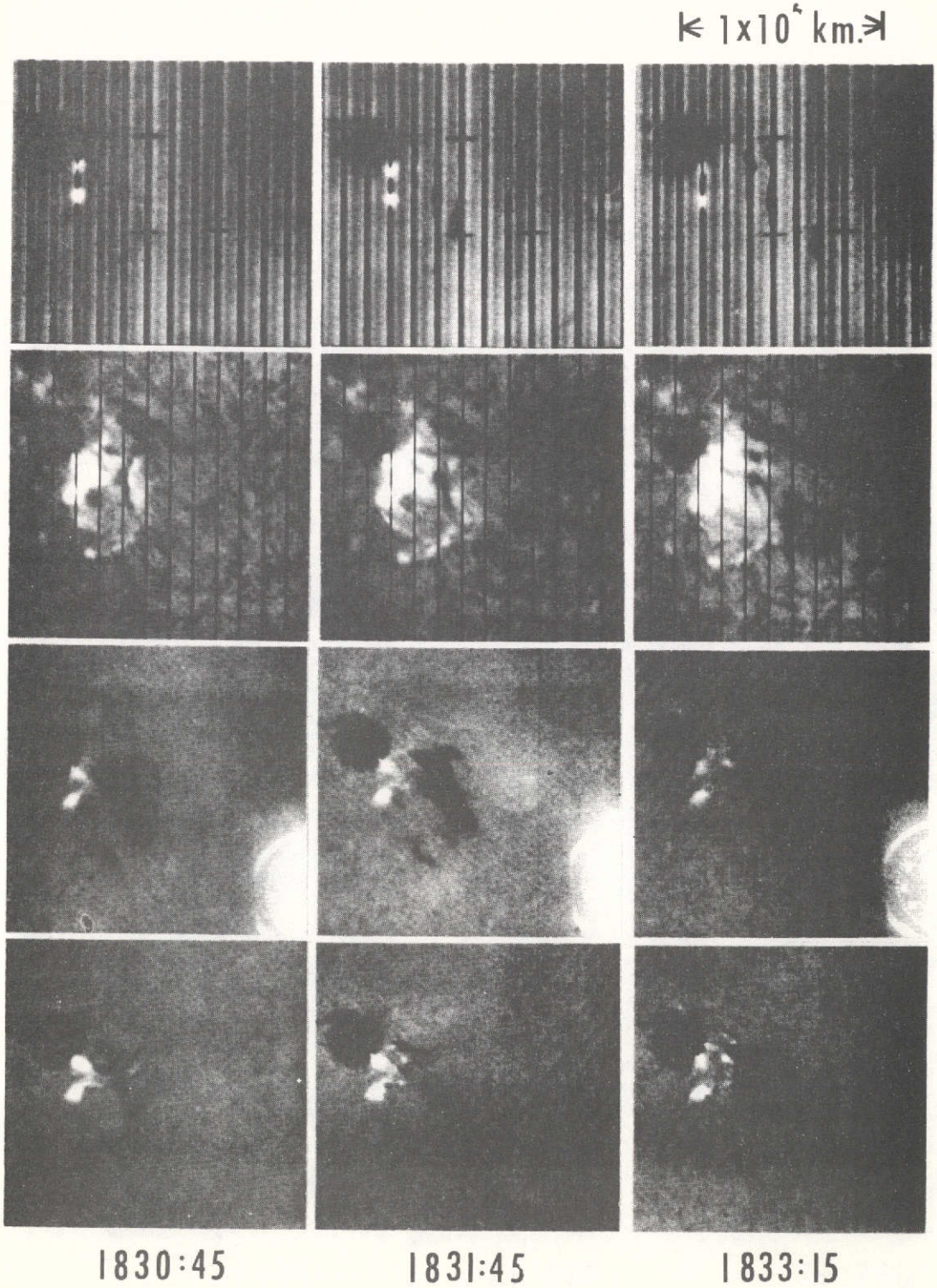

Figure XIIIB. Erupting filament associated with flare on 5 September 1973.

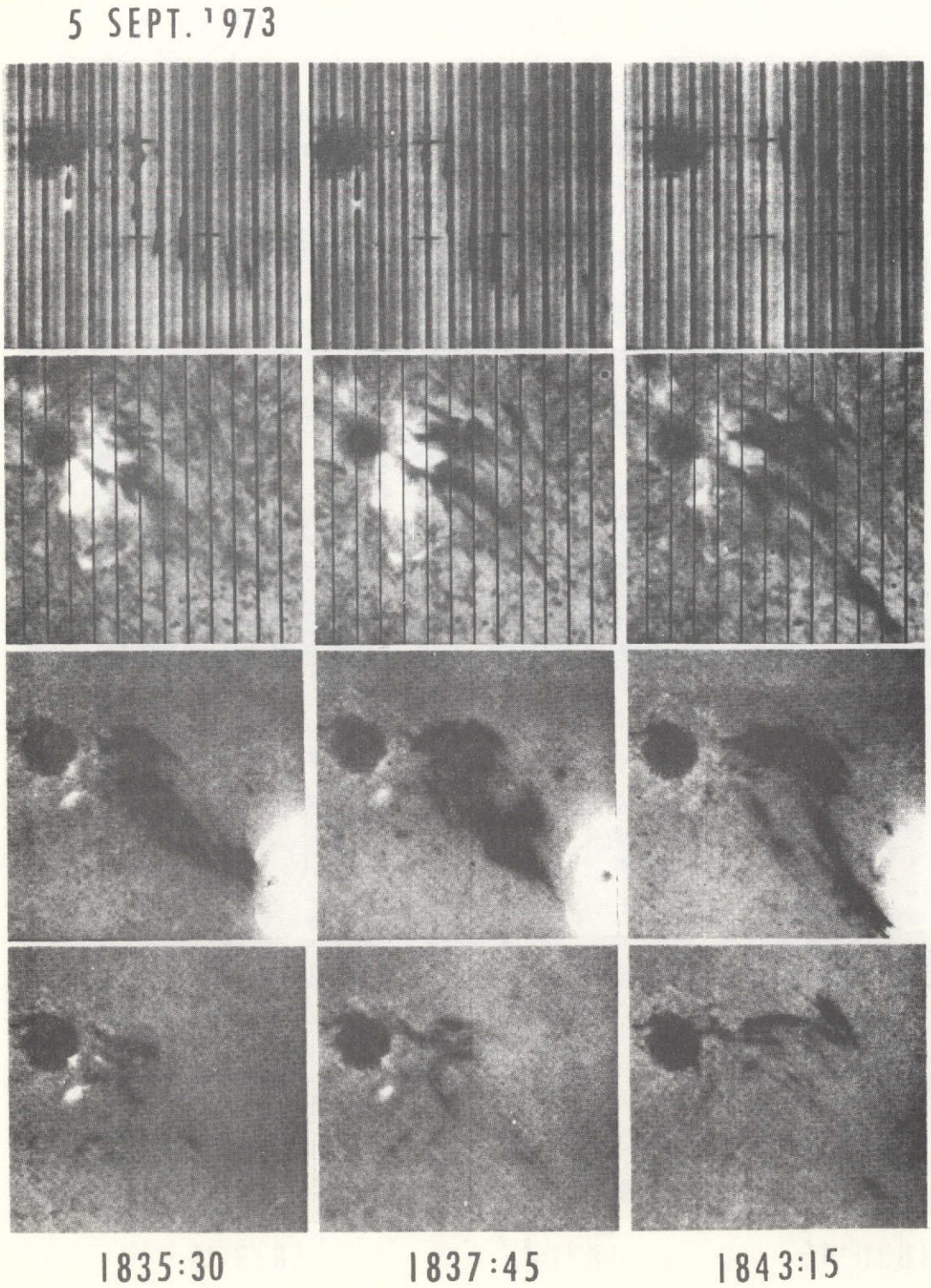

Figure XIIIC. Surge developing with the flare and erupting filament on 5 September 1973.

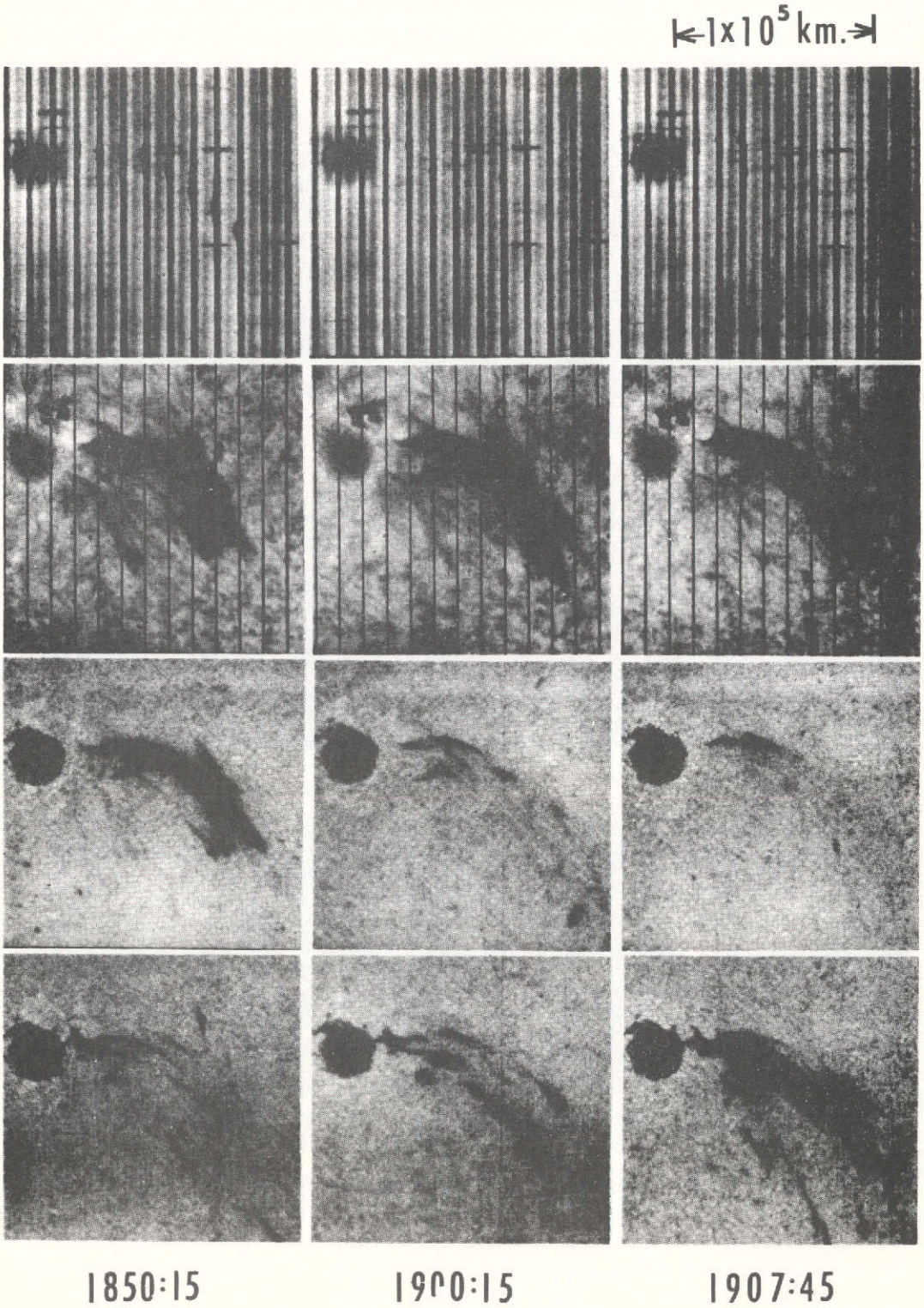

Figure XIIID. Slowing and reversal of surge direction - after the end of the flare on 5 September 1973.

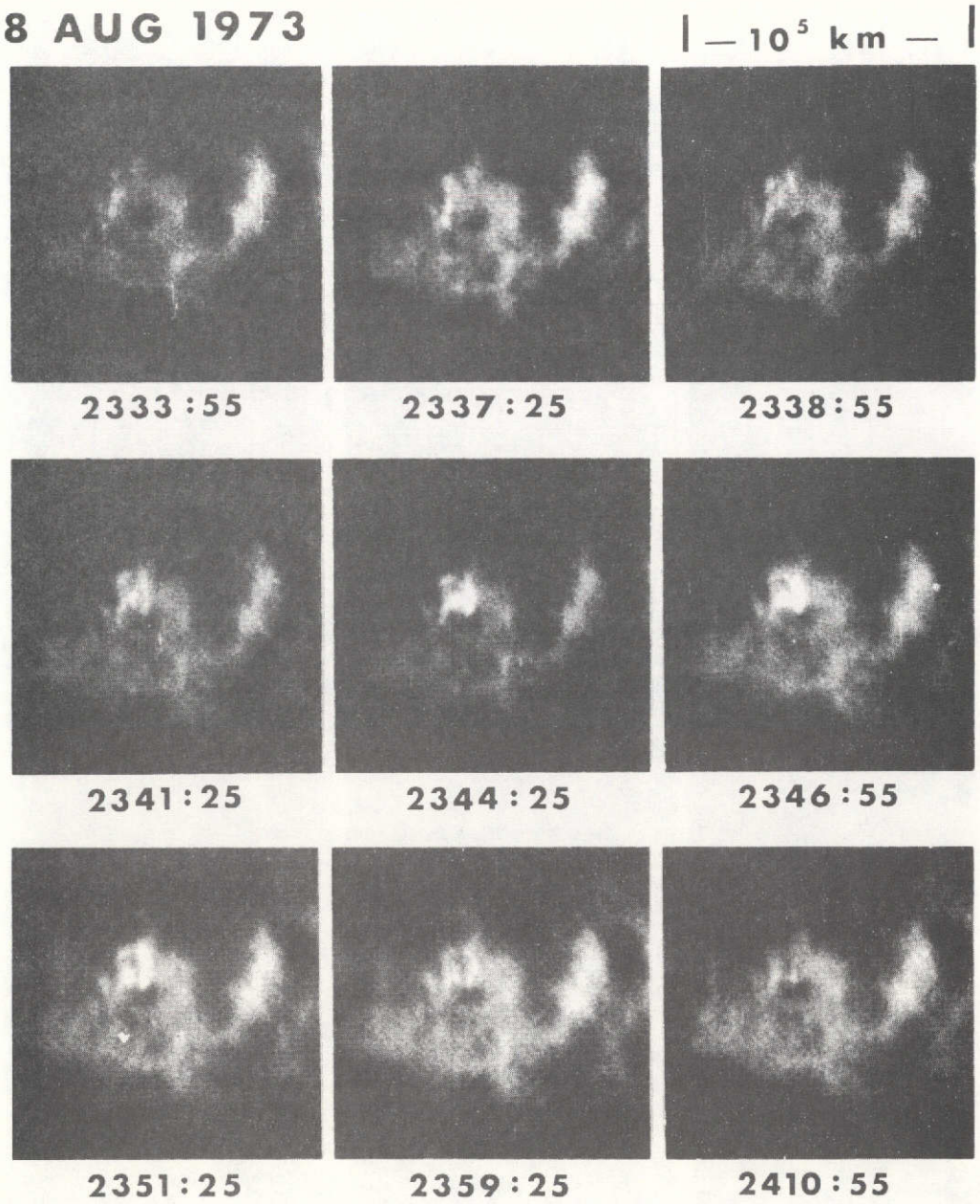

Figure XIV. Flare in CaII showing suggestion of fine structure.

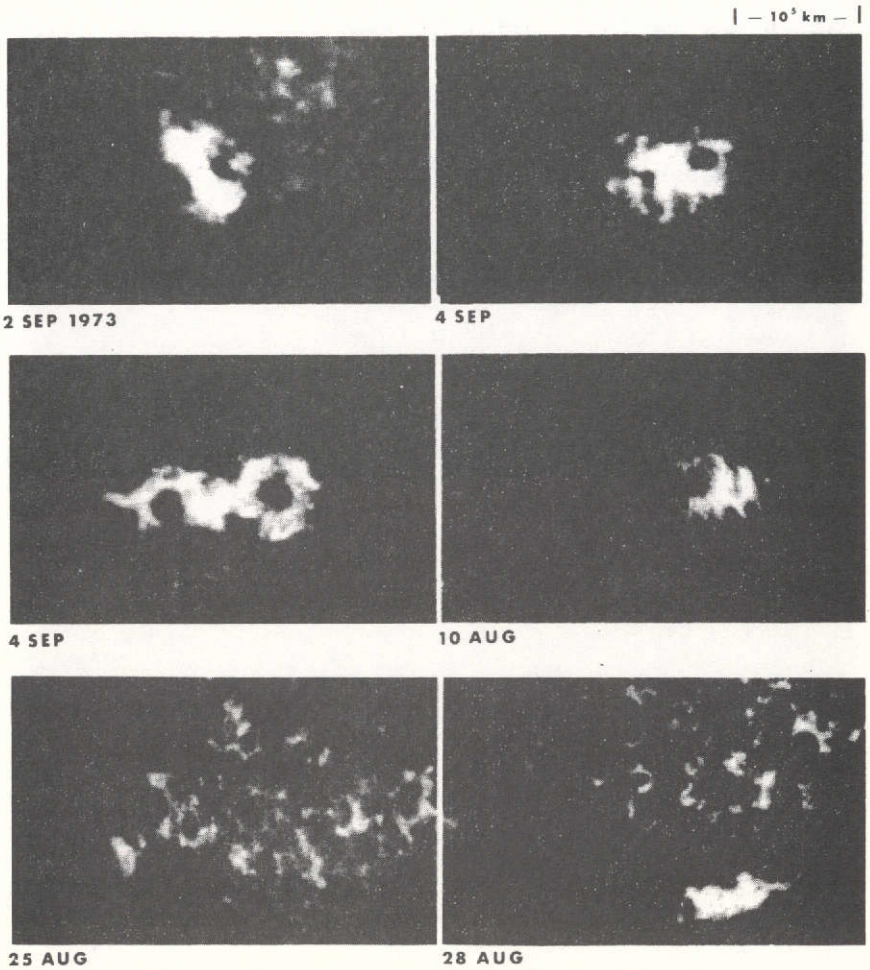

Figure XV. Dark borders are seen around plage of all active regions in CaII at 8542Å.

The CaII at 8542Å observations reveal the existence of umbral flashes. On normal exposures, however, they are at the limit of visibility. Much longer exposures will be required to make these flashes readily visible. Doppler observations of the flashes would be worthwhile for comparison with Hα umbral oscillations.

The development of active regions in CaII is illustrated in Figure XVI. A sunspot in an extensive region appears to change very little in the 7 day period. In contrast a new region, initially seen on 27 August, undergoes great change. This region, probably new on 26 August, is already losing its sunspots and decaying by 30 August. Another new region appears on 30 August and exhibits a rapid increase in size with the development of sunspots. By 31 August the region begins to take on the appearance of the background network, revealing the presence of super granule cells which change very slowly.

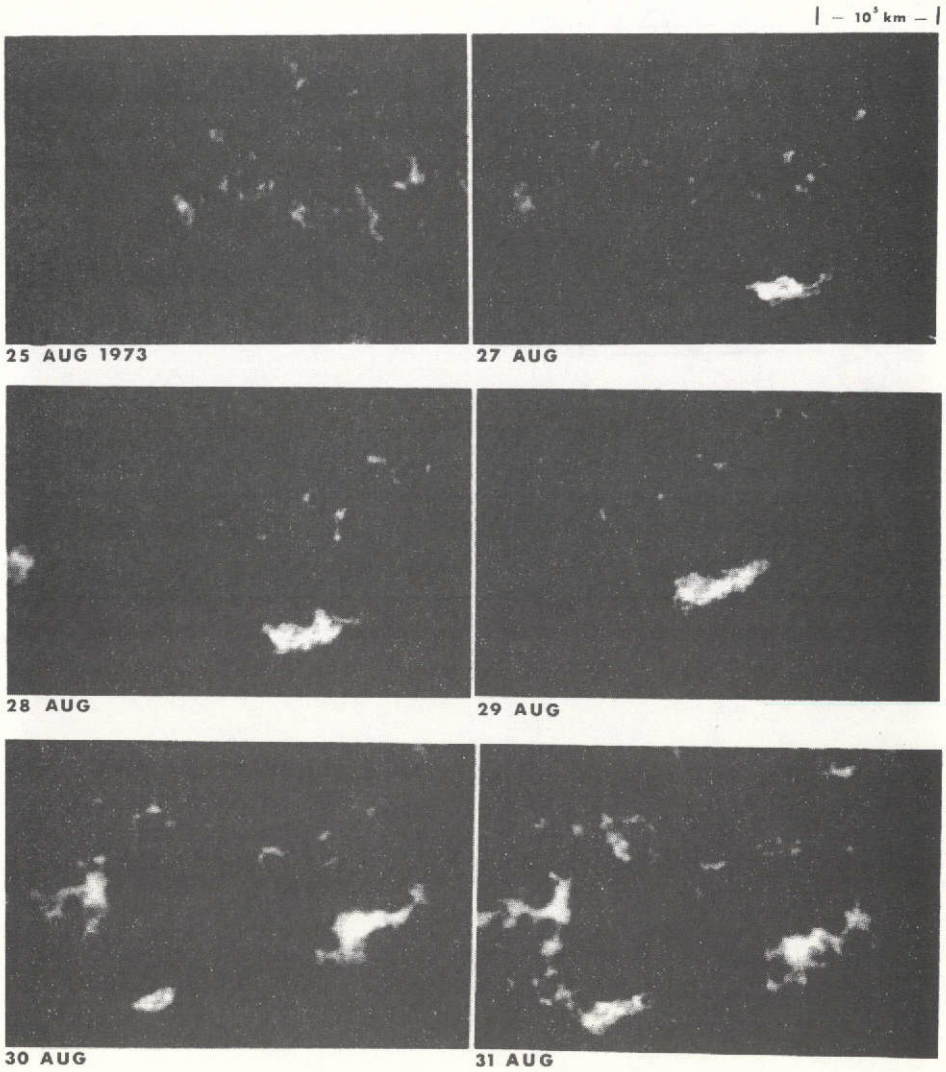

Figure XVI. Development of an active region at 8542Å.

REFERENCES

Hirshberg, J., Asbridge, J.R. and Robbins, D.E.: 1971, Solar Physics 18, 313

Hyder, C.L.: 1970, Solar Physics 14, 147

Martin, S.F. and Ramsey, H.E.: 1972, Solar Activity Observations and Predictions, ed. Murray and McIntosh, p 371

Smith, S.F., and Ramsey, H.E.: 1964, Z. Astrophys. 60, 1

Title, A.: 1974, Submitted to Solar Physics, "Partial Polaroids in Birefringent Filters"

Title, A.: 1973, Solar Physics 33, 521

White, O.R.: 1963, Ap. J. 138, 1316

Appendix E

UCSD Report

Direct Observation of Temperature Amplitude of Solar 300-Second Oscillations

Direct Observation of Temperature Amplitude of Solar 300-Sec Oscillations

H. S. Hudson and C. A. Lindsey

Department of Physics
University of California, San Diego
La Jolla, California 92037

ABSTRACT

The 300-second oscillations form the dominant source of variability of the solar infrared continuum. We have observed them at 20 μ with an amplitude ΔT_{rms} = 3.0 °K over an area with an effective diameter of 33". This new mode of observation of the 300-sec oscillations should make possible a fundamental improvement in our knowledge of their nature and origin.

Intensity variations in the Rayleigh-Jeans portion of the solar continuum spectrum, longward of 1 μ, permit direct observations of the temperature structure of the solar atmosphere. Table 1 indicates the source heights in the HSRA model atmosphere (Gingerich, Noyes, Kalkofen and Cuny 1971) for several of the infrared windows available for ground-based observations. The existence of 300-sec oscillations in the infrared continuum provides a powerful new tool for the exploration of this phenomenon: variation with altitude, spatial structure, relative phase of temperatures and velocity variations, etc.

We report here the initial observations at 20 μ, made with a two-beam photometer at the UCSD-University of Minnesota 60" (152 cm) infrared telescope of the Mt. Lemmon Observatory (altitude 2804 m). The high level of sky noise and atmospheric transparency fluctuations at infrared wavelengths require the use of high, dry site, and a two-beam photometric system to effect sky cancellation. The observations reported here, obtained 1973 June 4 near local noon, utilized circular beams of 23" diameter, separated by ~ 2', and roughly centered at N10 E19. An aperture filter of black polyethylene helped reduce heating of the telescope. An interference filter (OCLI L19420-8) plus a KRS-5 Dewar entrance window (long-wavelength cutoff ~ 40 μ), plus the Earth's atmosphere, determined the spectral passband as approximately 5 μ centered on 22 μ. Subsequent observations under inferior conditions required the use of a KCl window (cutoff ~ 22 μ) to suppress sky noise. The rms amplitude of the variations of the difference signal between the two beams on the solar disk amounted to about 0.06% of the signal obtained with one beam on the disk and one off, for a 1 Hz bandpass. This limb reading calibrates the signal strength

at $\Delta T_{rms} = 6.3$ °K for an assumed brightness temperature of 4900 °K. The corresponding peak-to-peak difference signal with both beams off the Sun amounted to ~ 0.006%, a noise level presumably corresponding to sky noise or to detector noise. Most of this noise occurs at higher frequencies than the 300-sec oscillations. Spatial scans of the temperature structure of the solar atmosphere showed a high degree of reproducibility for short time intervals, so we have little doubt of the solar origin of the bulk of the long-period variations. We assume that the variations in the two beams add independently and that the beam size exceeds the size of an oscillating element, so that the effective beam diameter becomes $\sqrt{2}$ x 23" = 33".

The peak frequency of the oscillatory feature in Figure 1 lies at 3.4×10^{-3} Hz, which corresponds closely to the 300-sec period expected from observations (e.g. Noyes 1967) of the velocity field. The area under the peak in Figure 1 yields an rms temperature fluctuation of 3.0 °K, after integration between 2.5 and 4.1×10^{-3} Hz. The rms amplitude does not have much quantitative significance because of the intrinsic variability of the phenomenon. However, simultaneous temperature and Doppler measurements should enable us to determine the relative amplitude and phase of individual oscillating elements. We have observed the 300-sec oscillations at other wavelengths, ranging from 8.6 μ to 350 μ.

ACKNOWLEDGEMENTS

This work was supported by NASA under contract NAS 8-28015. The authors would like to express their gratitude for the use of the Mt. Lemmon Observatory, which is supported by the National Science Foundation. They have benefited greatly from the advice and assistance of Drs. F. C. Gillett, W. A. Stein, and N. J. Woolf.

TABLE 1

Wavelength (microns)	HSRA Atmosphere Optical Depth (at 5000 Å)	Height (kilometers)
0.5	1.00	0
10.0	0.12	130
20	3.5×10^{-2}	210
35	1.3×10^{-2}	270
350	1.6×10^{-4}	530
1200	7.2×10^{-6}	930

REFERENCES

Gingerich, O., Noyes, R. W., Kalkofen, W., and Cuny, Y. 1971, Solar Phys. 18, 347.

Noyes, R. W. 1967, Proc. I.A.U. Symp. 28 , ed. R. N. Thomas (New York: Academic Press), p. 293.

FIGURE CAPTION

Figure 1 Power spectrum of an 83-minute data sample at 20 μ obtained 1973 June 4, computed from an autocorrelation function 41.5 minutes in length. The observations show temperature fluctuations in an effective aperture of 33" diameter, with an rms amplitude of 1.5 °K between 2.5 and 4.1×10^{-3} Hz.

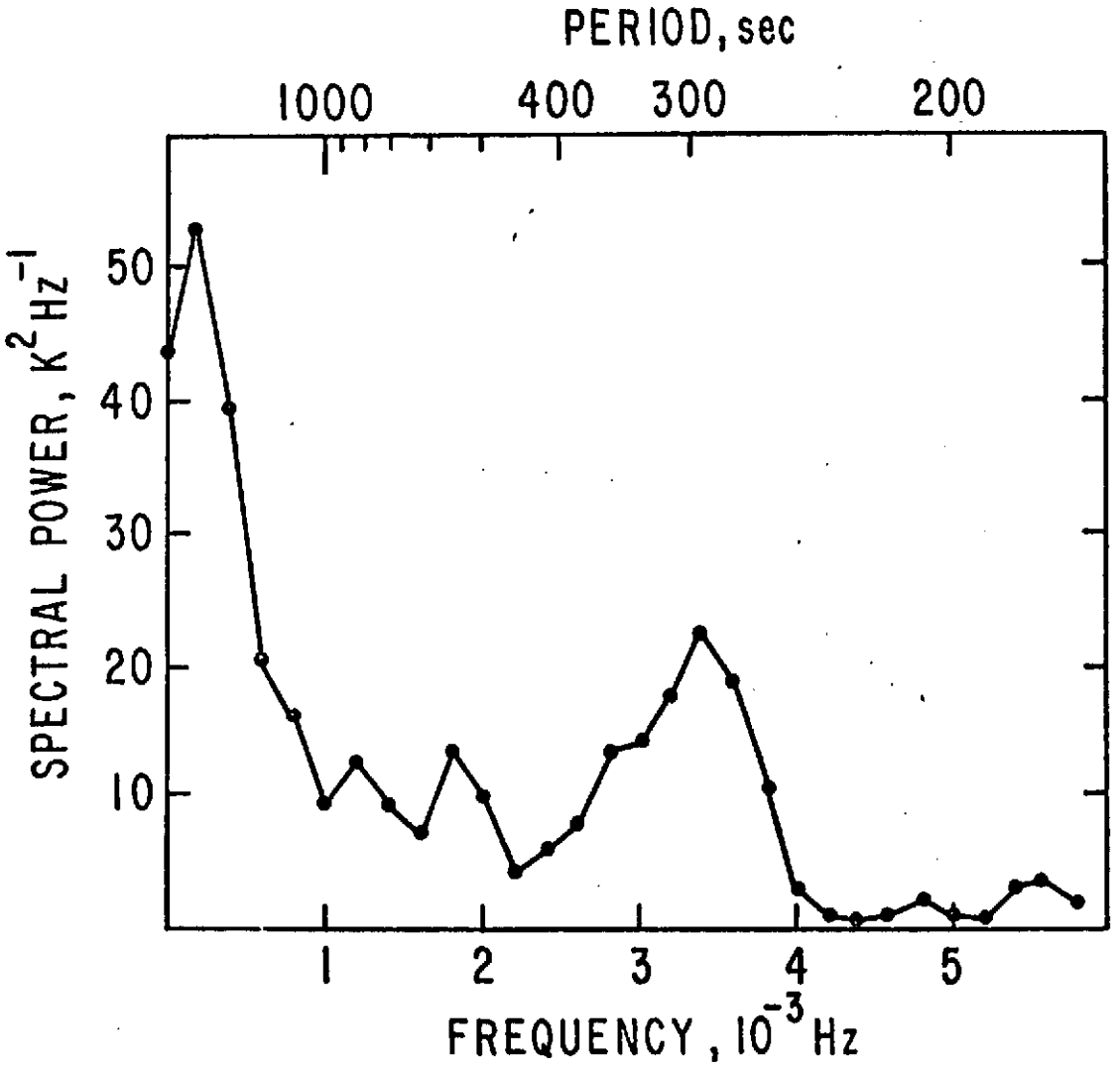
PERIOD, sec
1000
400
300
200
SPECTRAL POWER, $K^2 Hz^{-1}$
50
40
30
20
10
1
2
3
4
5
FREQUENCY, 10^{-3} Hz

Appendix F

LMSC Helium Emission Studies
Final Report

LMSC-D354991

STUDY OF HELIUM EMISSIONS FROM ACTIVE SOLAR REGIONS

Final Summary Report

by

J. L. Kulander

October 1973

Prepared for

George C. Marshall Space Flight Center
Huntsville, Alabama 35812

Contract No. NAS8-27988

Lockheed Missiles & Space Company
Palo Alto Research Laboratory
3251 Hanover
Palo Alto, California 94304

ABSTRACT

A theoretical study is made of the visible and UV line radiation of He I atoms and He II ions from a plane-parallel model flare layer. Codes have been developed for the solution of the statistically steady state equations for a 30 level He I - II - III model, and the line and continuum transport equations. These codes are described and documented in the report along with sample solutions. Optical depths and some line intensities are presented for a 1000 km thick layer. Solutions of the steady state equations are presented for electron temperatures 10^4 - 5×10^4 °K and electron densities 10^{10} - 10^{14} cm^{-3}.

TABLE OF CONTENTS

Section		Page
	ABSTRACT	i
I.	INTRODUCTION	1
II.	THE STEADY STATE EQUATIONS	4
	A. Energy Level Model	4
	B. Population Equations	4
	C. Reaction Rates	13
	D. Sample Solutions	17
III.	LINE TRANSPORT SOLUTION	70
	A. Basic Equations	70
	B. Evaluation of ϵ' and B^s	78
	C. Evaluation of A_k	80
	D. Sample Solution - Two Lines	81
IV.	CONTINUUM TRANSPORT SOLUTION	83
	A. Basic Equations	83
	B. Evaluation of ϵ_i^a and ϵ_i^b	85
	C. Evaluation of A_k'	86
V.	CODES	87
	A. Code 1 - Solution of Statistically Steady State Population Equations	87
	B. Radiative Transfer Codes	91
VI.	REFERENCES	94
Appendices		
A	PROGRAM FOR SOLUTION OF STEADY STATE EQUATIONS	95
B	PROGRAM FOR SOLUTION OF LINE TRANSPORT EQUATION	129
C	PROGRAM FOR SOLUTION OF CONTINUUM TRANSPORT EQUATION	155

HELIUM EMISSION FROM ACTIVE SOLAR REGIONS

I. INTRODUCTION

The purpose of this program has been to develop codes for the simultaneous calculation of He I and II resonance line and He I D_3 line intensities from model flare regions. These lines were chosen because of the spectral ranges of the Skylab high resolution spectrographs and because of the planned program to obtain D_3 filtergrams on a patrol basis at the Lockheed Rye Canyon Observatory during the ATM mission. The NRL spectroheliograms incorporate simultaneous measurements of the He I and II resonance lines.

A plane-parallel layer irradiated on one side by the photospheric radiation field was chosen as the geometric model. A statistically steady state and uniform electron temperature and density with position were assumed. The energy level model consists of all terms through principal quantum number 4. Our study has been confined to conditions we believe characteristic of flare regions, namely electron temperatures between 10^4 and 5×10^4 °K and electron densities between 10^{10} and $10^{14} cm^{-3}$. An extensive compilation of electron impact excitation rates has been made as part of this study. The results were published in Solar Physics (Benson and Kulander, 1972).

The statistically steady state level populations of model He I atoms have been calculated by a number of investigators for temperatures and densities characteristic of the outer solar atmosphere. Almost none of these authors has considered a sufficiently detailed energy level structure in the model atom to accurately obtain the D_3 line emission. Jefferies (1955) e.g. treats the 2s and 2p levels as a single level. De Jager and de Groot (1957) consider the 2s and 2p terms separately but the term structure of higher levels is ignored. This higher term structure is also ignored by Athay and Johnson (1960). They also neglect the effect of the He II ion processes by using other values for the

He I/He II equilibrium. Athay and Johnson arrive at the conclusion that in the temperature range 40,000 - 50,000°K, the D_3 line will appear in emission for $n_e \geqslant 10^{12}$ almost independently of T_e.

Zirin (1956) assumes in his calculations that transitions between terms of a given level are of negligible importance in determining the occupation numbers. This is known to be a poor assumption. Shklovsky and Kononovitch (1958) have calculated the D_3 line intensity but have made a number of unrealistic physical assumptions. More recently Hearn (1969) has calculated the occupation numbers of a 41 level He I atom and one level He II ion but he only presents results for the resonance line intensities. We shall demonstrate that more levels are required in He II to obtain correct line intensities.

Jefferies (1957) has calculated the D_3 line intensity from a layer assumed to be optically thick in the D_3 line. The transport equation was solved assuming incoherent scattering with no photospheric radiation in the line. Jefferies' results are very qualitative since it is known that the D_3 line is probably not optically thick.

To obtain accurate line intensities, simultaneous solution of the line and continuum radiative transfer equations and the steady state populations is required. To accomplish this, we have developed three separate codes. The first code (Code 1) solves the statistical equilibrium equations for a 30 level He I-II-III system given the appropriate rates. The basic equations and sample solutions are given in Section II. The code is described in Section V and a listing is given in Appendix A.

The second code (Code 2) represents a numerical solution of the line transport equations for a finite layer. The solution is of the integral form of the transport equation by expansion of the source function in terms of a finite sum. The mathematical method used is summarized by Avrett and Loeser (1969). Complete frequency redistribution and a Gaussian absorption profile are assumed. The basic equations and sample

solution are given in Section III. The code is described in Section V and a listing is given in Appendix B.

The third code (Code 3) solves the continuum transport equation by expansion of the source function in a very similar manner to the line transport equation. The equations are given in Section IV. The code is described in Section V and a listing is given in Appendix C.

II. THE STEADY STATE EQUATIONS

A. Energy Level Model

The 30 assumed energy levels for the system of ions He I - He III are given in Table II-1. There are 19 levels for He I, 10 for He II and 1 for He III. These levels are shown in Figures II-1 and II-2. The levels are numbered 1 - 30 in order of increasing energy. Levels 1, 20 and 30 are the ground states of He I, II and III, respectively. This model was chosen to provide accurate solution for the first two resonance lines in He I and II and the D3 and 10830 lines of He I. Many other lines are included but were not the primary lines under consideration. The allowed transitions included in the model are listed in Table II.2 together with f numbers and wavelengths. The inclusion of the 4 S,P,D and F levels separately is necessary because at the lower electron densities considered radiative de-excitation rates can become larger than collision rates between the n = 4 levels. At higher electron densities the collision rates between the n = 4 terms dominate all other rates in or out of these terms and the relative populations are Boltzmann.

B. Population Equations

The rate equation describing the population of the bound or continuum state i is

$$S_{\gamma j} \left(R_{\gamma_{ji}} - R_{\gamma_{ij}}\right) = 0 \qquad \text{II.1}$$

where $R_{\gamma ji}$ and $R_{\gamma ij}$ are the total transition rates/cm^3 by process γ from state j to i and from i to j respectively. The sum S represents a sum over discrete states and an integration over continuum states. We shall assume the particle translational distribution-functions to be Maxwellian and the external continuum radiation field to be Planckian, in which case it is possible to integrate over the continuum and replace it by one additional term in the discrete sum. The atomic transition processes are radiative excitation and ionization, collisional excitation and ionization by atoms and electrons and their inverses. Because of their higher velocities, electron collisions generally dominate the collisonal rates and hence only electron inelastic rates will be considered.

TABLE II.1

He I, II Energy Levels

He I - i = 1

j			Energy (ev)	Wave Nos.	St.Wt.
1	$1s^2$	^1S	0	0	1
2	1s2s	^3S	19.821	159850	3
3	1s2s	^1S	20.618	166272	1
4	1s2p	$^3P^0$	20.966	169081	9
5	1s2p	$^1P^0$	21.220	171129	3
6	1s3s	^3S	22.721	183231	3
7	1s3s	^1S	22.923	184859	1
8	1s3p	$^3P^0$	23.009	185559	9
9	1s3d	^3D	23.076	186096	15
10	1s3d	^1D	23.076	186099	5
11	1s3p	$^1P^0$	23.089	186204	3
12	1s4s	^3S	23.596	190292	3
13	1s4s	^1S	23.676	190935	1
14	1s4p	$^3P^0$	23.710	191211	9
15	1s4d	^3D	23.738	191439	15
16	1s4d	^1D	23.739	191441	5
17	1s4f	$^3F^0$	23.739	191447	27
18	1s4f	$^1F^0$	23.739	191447	7
19	1s4p	$^1P^0$	23.744	191487	3

He II - i = 2

1	1s	^2S	0	0	2
2	2s	^2S	40.8099	329179.57	2
3	2p	$^2P^0$	40.8091	329182.02	6
4	3s	^2S	48.3662	390140.76	2
5	3p	$^2P^0$	48.3664	390141.49	6
6	3d	^2D	48.3665	390142.64	10
7	4s	^2S	51.0113	411476.98	2
8	4p	$^2P^0$	51.0114	411477.28	6
9	4d	^2D	51.0115	411477.77	10
10	4f	$^2F^0$	51.0117	411477.95	14

TABLE II.2

He I, II Lines

He I

	Upper Level	Lower Level	Notation	λ(Å)	A (10^8/sec)	f
	4	2	1	10830	.1022	.5391
	5	1	2 UV	584.4	17.99	.2762
	5	3		20582	.01976	.3764
	6	4	10	7065	.278	.0693
	7	5	45	7281	.181	.0480
	8	2	2	3889	.09478	.06446
	8	6		4.30+4	.0108	.896
D3 →	9	4	11	5876	.706	.609
	9	8		1.86+5	1.28-4	.111
	10	5	46	6678	.638	.711
	11	1	3 UV	537.1	5.66	.0734
	11	3	4	5016	.1338	.1514
	11	7		7.43+4	.00253	.629
	12	4	12	4713	.106	.0118
	12	8		21120	.0652	.145
	13	5	47	5049	.0655	.00834
	13	11		21132	.0459	.103
	14	2	3	3188	.0505	.0231
	14	6		12538	.00608	.0429
	14	9		19543	.00597	.0205
	14	12		1.09+5	.0505	1.21
	15	4	14	4472	.251	.125
	15	8		17002	.0668	.482
	15	14		4.39+5	4.16-5	.200
	16	5	48	4922	.202	.122
	16	11		19089	.0711	.647
	17	9		18688	.139	1.02
	17	15		1.43+7	6.01-10	.0033
	18	10		18699	.138	1.01
	18	16		1.67+7	4.34-10	.00253
	19	1	4 UV	522.2	2.46	.030
	19	3	5	3965	.0717	.0507
	19	7		15088	.0137	.140

TABLE II.2 (Continued)

He I

Upper Level	Lower Level	Notation	λ(Å)	A (10^8/sec)	f
19	10		18560	.00277	.00858
19	13		1.81+5	5.78-4	.853
19	16		2.17+6	5.65-7	.024

He II

3	1		303.80	100.	.4162
4	3		1640.5	1.01	.01359
5	1		256.3	26.8	.07910
5	2		1640.4	3.59	.4349
6	3		1640.4	10.3	.6958
7	3		1215.1	.413	3.045-3
7	5		4687.0	.294	.03225
8	1		243.03	10.9	.02899
8	2		1215.1	1.55	.1028
8	4		4686.8	.491	.4847
8	6		4687.2	.056	.01099
9	3		1215.1	3.30	.1218
9	5		4686.9	1.13	.6183
10	6		4687.1	2.21	1.018

Fig. II-1 ENERGY LEVEL DIAGRAM FOR IDEALIZED HeI ATOM

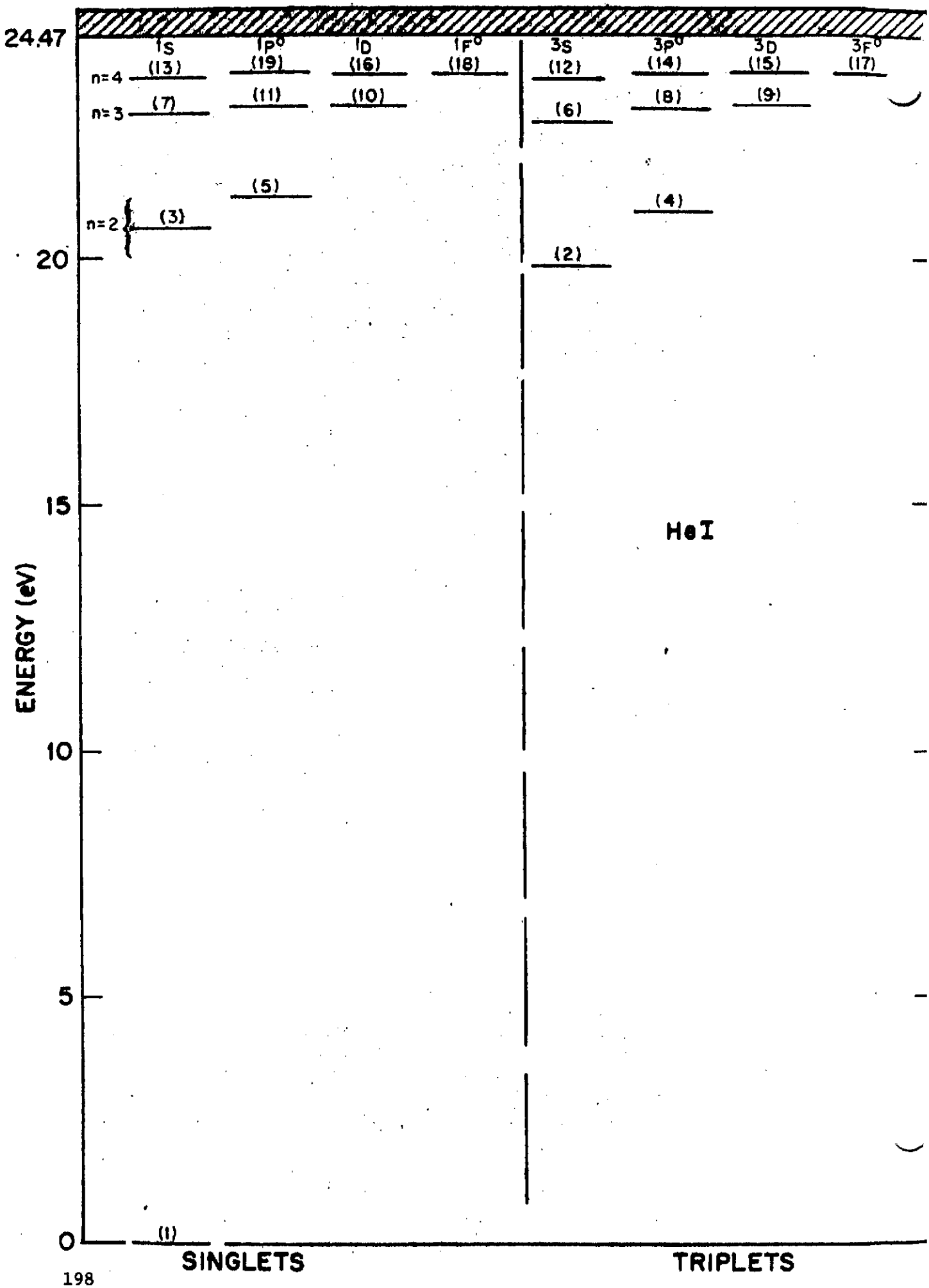

Fig. II-2 ENERGY LEVEL DIAGRAM FOR IDEALIZED He II ION

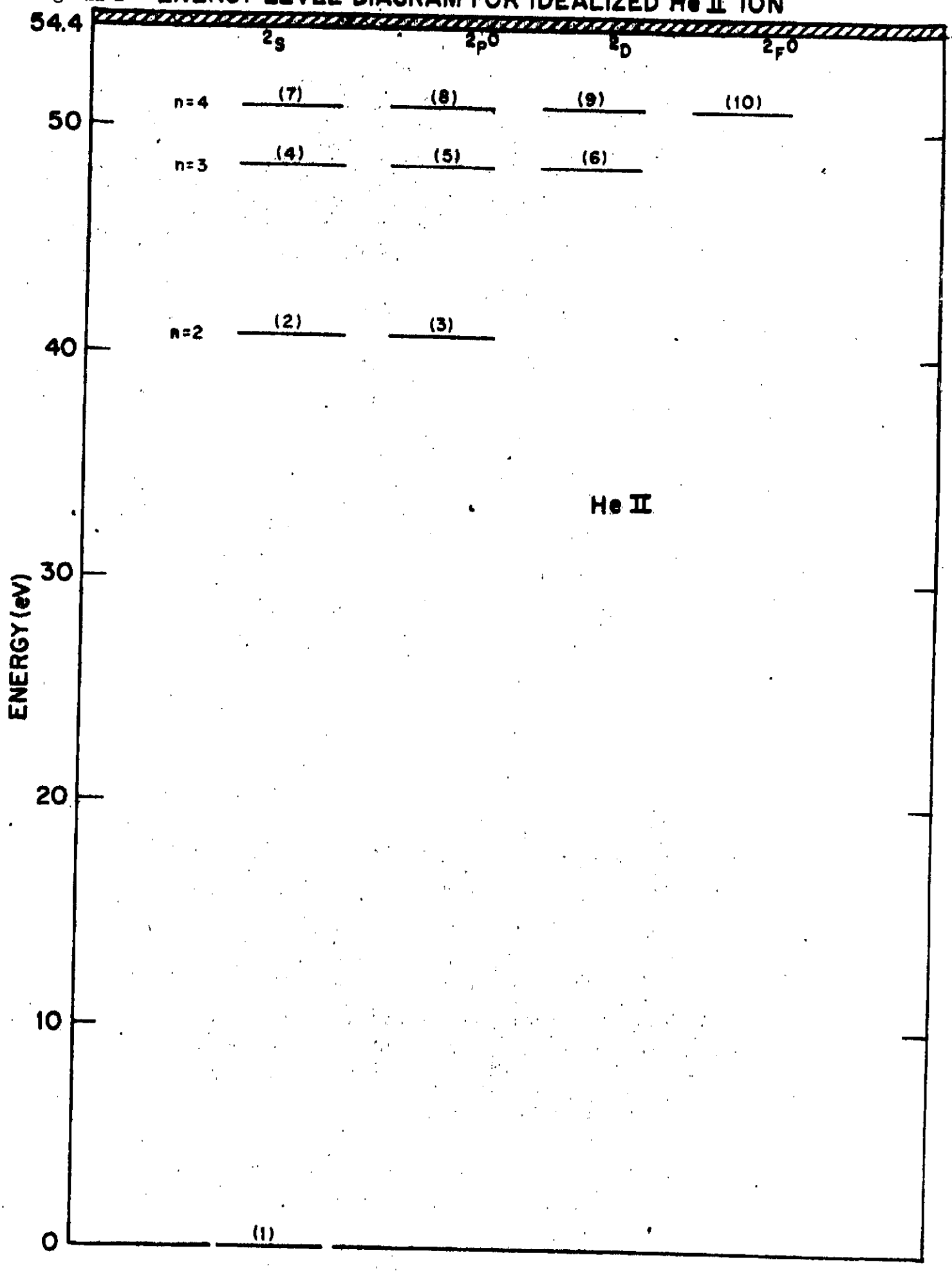

We may write the total rate from i to j more specifically as,

$$R_{yij} = n_i P_{ij} = n_i(A'_{ij} + C_{ij}), \qquad \text{II.2}$$

where A'_{ij} and C_{ij} are the radiative and collisonal transition rates/particle from the ith to the jth state. In the statistically steady state, equation II.1 reduces to

$$\sum_{j\neq i}(n_j P_{ji} - n_i P_{ij}) = \sum_j n_j P_{ji} = 0; \quad P_{ii} \equiv -\sum_{j\neq i} P_{ij}. \qquad \text{II.3}$$

The system of equations represented by II.3 can easily be solved for the populations n_i when all the P_{ij}'s are known. This is the case when the gas is totally optically thin (in all lines), since the external radiation field is specified and the internal radiation field does not produce a significant upward transition rate. We can characterize the system of linear equations (II.3) by a matrix whose coefficients a_{ij} are equal to P_{ji}. The diagonal elements are the P_{ii}.

The general solution of equations (II.3) is given by White (1961)

$$n_i = \lambda_m P^{mi}; \quad \lambda_m = \frac{N}{\sum_i P^{mi}}, \qquad \text{II.4}$$

where P^{mj} is the co-factor of the coefficient of n_j in the mth equation (i.e. the matrix element P_{mj}) and N is the total number of He particles/cm^3. We denote the discrete level corresponding to the continuum, i.e. an ionization or recombination, by c. We may then write the rate equation for level i of ion q as,

$$-(\sum_j P^q_{ij} + \sum_{j'} P^q_{icj'} + \sum_{j'} P^q_{cij'})n_i^q + \sum_{j'} P^{c,q+1}_{j'i}\, n^{q+1}_{j'} + \sum_{j'} P^{q-1,c}_{j'i}\, n^{q-1}_{j'} + \sum_j P^q_{ji}\, n^q_j = 0 \qquad \text{II.5}$$

where j and j' refer to other bound levels in the qth ion and in other stages of ionization, respectively, P^q_{ij} is the total excitation or de-excitation rate in ion q from i-j; $P^q_{icj'}$ and $P^{q+1,c}_{j'i}$ are the total ionization rates from i in q to j' in q + 1 and to i in q from j' in q - 1, respectively; $P^q_{cij'}$ and

$P^{c,q+1}_{j'i}$ are the total recombination rates from i in q to j' in q -1 and to i in q from j' in q+1, respectively. Specifically we may write the P's as follows:

bound-bound

$$i > j \qquad P^q_{ij} = A^q_{ij} + Y^q_{ij} B^q_{ij} B_r + n_e \Omega^q_{ij}$$

$$i < j \qquad P^q_{ij} = Y^q_{ij} B^q_{ij} B_r + n_e \Omega^q_{ij} \qquad \text{II.6}$$

bound-free (from initial state q,i)

ionization $\quad P^q_{icj'} = W \bar{A}^q_{ij'} + n_e \bar{\Omega}^q_{ij'}$ II.7

recombination $\quad P^q_{cij'} = n_e \alpha^q_{ij'} + n_e W \beta^q_{ij'} + n_e^2 \bar{\bar{\Omega}}^q_{ij'}$

bound-free (to initial state q, i)

ionization $\quad P^{q-1,c}_{j'i} = W\bar{A}^{q-1}_{j'i} + n_e \bar{\Omega}^{q-1}_{j'i}$

recombination $\quad P^{c,q+1}_{j'i} = n_e \alpha^{q+1}_{j'i} + n_e W \beta^{q+1}_{j'i} + n_e^2 \bar{\bar{\Omega}}^{q+1}_{j'i}$ II.8

where n_e is the electron density/cm^3; B_r is the Planck function at temperature T_r; W is the dilution factor; Y^q_{ij} is a free parameter, A^q_{ij}, B^q_{ij} are the Einstein transition probabilities; $\bar{A}^q_{ij}$ is the photoionization rate/ion; Ω^q_{ij}, $\bar{\Omega}^q_{ij}$ are the collisional transition rates/electron per ion for bound-bound and bound-free processes, respectively; $\bar{\bar{\Omega}}^q_{ij}$ is the collisional transition rate/electron^2 per ion for free-bound recombination; and α^q_{ij}, β^q_{ij} are the recombination, and stimulated recombination coefficients, respectively.

The basic quantities required for the evaluation of the radiative rates are the oscillator strengths and photoionization cross sections; for the collisional rates the excitation and ionization cross sections. The inverse cross sections and Einstein coefficients can be obtained from the usual detailed balance relations. The quantities Ω, $\bar{\Omega}$, $\bar{\bar{\Omega}}$ and α generally have the form

$$\int vQ(v) f(v)\, dv, \qquad \text{II.9}$$

where v is the electron velocity, $Q(v)$ the cross section and $f(v)$ the electron translational distribution function. $\bar{A}$ may be written in terms of the photoionization cross section $a(\nu)$ as

$$4\pi \int \frac{a(\nu)}{h\nu} B(\nu)\, d\nu. \qquad \text{II.10}$$

β is expressed similarly in terms of the stimulated recombination cross section $b(\nu)$.

Solutions can be obtained for any arbitrary line radiation field by suitable choice of the parameter Y which is closely related to the net radiative bracket (NRB). Y varies between 0 and 1 being 0 for a thin layer (no external radiation) and 1 for a very thick layer where the line radiation field is Planckian. For a thin line with external photospheric radiation $Y = 1/2\ B(T_e)$. Various continuum radiation fields can be considered by suitable choices of $\bar{A}$.

C. Reaction Rates

Oscillator strengths for all of the allowed transitions included in our model (Section II.A) were found in the NBS compilation by Wiese et al. (1966). Photoionization rates were obtained from Hartree-Fock calculations of Stewart and Webb (1963) for the ground state of He I and from calculations by Peach (1967) for the n^1 S, n^3 S, n^1 P and n^3 P levels. For all other levels cross sections were calculated using the quantum-defect method of Burgess and Seaton (1960).

Collisional ionization rates were obtained from measurements of Englander-Golden and Rapp quoted by Kieffer and Dunn (1966) for 1^1 S, from measurements of Long (1967) for 2^3 S and from calculations of Dolder, et al. (1961) for the He II ground state. For other levels the ionization rates were taken from Allen (1961).

The collisional excitation cross sections are crucial to the solution of the steady state equations. For this reason we have made an extensive tabulation and study of rates from many sources. A paper entitled "Electron Impact Excitation Rates for Helium" describing these rates was published in the December 1972 issue of Solar Physics (Benson and Kulander, 1972). Excitation rates were calculated from most available cross section data, and fitted to the empirical formula

$$\Omega = AT^n \exp(-\alpha X_o)$$

where $X_o = E_o/kT$; A, n and α are constants. For He I the temperature range considered was 4000-50,000°K and for He II, 10^4 - 10^5°K. Rates between all levels of the model of Section II.A were calculated. The inverse rates for both radiative and collisional transitions were calculated from standard equilibrium relationships.

We shall discuss briefly some of our conclusions concerning the electron impact rates beginning with the He I rates.

Generally both forbidden and allowed rates are in better agreement for higher temperatures than for lower temperatures. The allowed rates are in much better agreement than the forbidden rates. The allowed rates from ground state or level 2 generally show differences as large as a factor of 10 for low temperatures and as large as 5 for high temperatures. Between other levels ($n \geq 3$) the differences are only as much as factors of 3 at low temperatures and 50-100% at high temperatures.

In He I the forbidden rates generally differ by as much as a factor of 100 at low temperatures, a factor of 20-50 at higher temperatures. Differences as high as a factor of 10^5 are noted in a few cases, differences of factors of 10^3 are not uncommon. If one does not consider the highest and the lowest rate value for each transition the differences are generally reduced to factors of about 10 at lower temperatures and 5 at higher temperatures. Forbidden transitions with lower level $n = 2$ show differences 2-3 times less than those with $n = 1$.

For transitions between the higher levels only the very approximate cross sections of Green (1966) and Allen (1963) are available for forbidden transitions and for allowed transitions those of Seaton (1962), Saraph (1964) and Mihalas and Stone (1968). Comparing the two approximate results for forbidden transitions with the other measured and calculated values we find the approximate results generally lower by factors of 2-10. For higher levels the Green cross sections are generally higher than those of Allen. With regard to the Seaton and Saraph approximations, it is not conclusive which is more often closer to the other values. The Seaton approximation gives values generally higher than the Saraph approximation for lower temperatures while the reverse situation holds for higher temperatures.

For He II there are relatively few cross sections available. The largest differences, being about a factor of 5, are much less than for He I. For both He I and He II experimentally determined cross sections give lower rates than the calculated values.

The actual collisional excitation rates chosen represent mean values of those given in the paper, taken from various sources listed there. To determine the sensitivity of the solution to these rates the statistical equilibrium equations were solved after increasing the individual values of the collision rates per electron Ω between each state by a factor of 100. This was done to determine the sensitivity of the solution to the collision excitation rates. We chose the optically thin case with $T = 20{,}000^{\circ}K$, $n_e = 10^{10}$ for this test. We illustrate in Figure II.3 the effect on the population of the levels 1, 2, 4, 9, 11 and 20 of each perturbation in collision rate. Of course in many instances increasing a particular Ω_{ij} by 100 had little effect on the populations of the levels mentioned. In Figure II.3 we show the 10 transitions i-j which have the largest effect on each of the above levels. The ratio of the population after increasing Ω_{ij} by 100 to that before the perturbation is shown. We note that changes of 10 to 50 in these important populations result from an uncertainty of a factor of 100 in the rates.

All the triplet levels of He I had about the same response to the change in Ω. When the rate from the He I ground state (G.S.) to triplet levels increased the triplet populations increased. When the triplet to singlet rates increased the triplet populations decreased as would be expected. The He I G.S. population is very sensitive to the rate from the G.S. to the metastable $2\ ^3S$ level (and $2\ ^3P$ level). The $1\ ^1S$ level population was decreased by about 20 when $\Omega(1\ ^1S \rightarrow 2\ ^3S)$ was increased by 100. At the same time the He II G.S. pupulation was increased. An increased rate from the triplets to singlets results in increased $1\ ^1S$ population and a corresponding decrease in $1\ ^2S$ population. The populations of the upper levels of the 584 and 537 Å lines are very sensitive to the rate from the $1\ ^1S$ to $2\ ^1S$ level increasing as this rate increases.

ORIGINAL PAGE IS OF POOR QUALITY

Figure II-3 POPULATION CHANGE BY INCREASING Ω BY 100

OPTICALLY THIN CASE $T_e = 2 \times 10^4$ $n_e = 10^{10}$

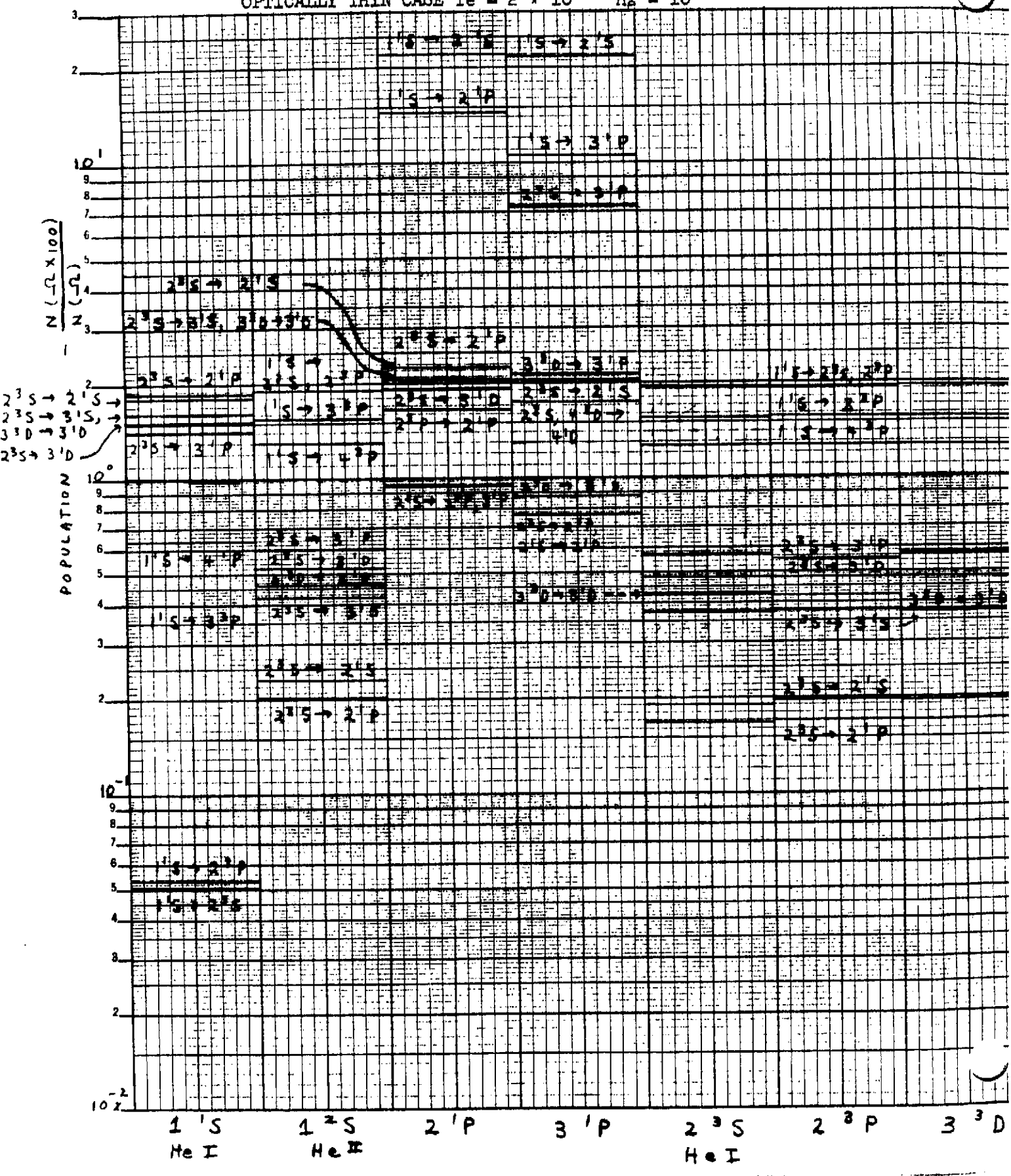

D. Sample Solutions

A code which we shall designate as code 1 has been developed to solve the steady state population equations given in Section II.B. This code is described in Section V. We discuss in this section some sample solutions of the steady state population equations.

The gas is assumed irradiated over 2π ster by a Blackbody spectrum at $6000^{\circ}K$ representing the photospheric radiation field. The gas is assumed to be optically thin for all lines and continuua unless otherwise specified.

1. Ionization Equilibrium

In this section we illustrate results for the ionization equilibrium. Fig. II-4 shows the ratio n_1/n_{20} with $T_e = 30{,}000^{\circ}K$ at various values of n_e. For an atomic model with only levels 1 and 20 the ratio n_1/n_{20} is approximately constant with n_e since both the collisional ionization and recombination rates are proportional to n_e. The optically thin solution for two levels is shown. The results are generally within a factor of 2. For very low n_e, all of the levels of He I except 5, 11 and 19 represent additional paths from level 1 to level 20. This is so because the photoionization rates from these levels exceed almost all collisional rates. n_1/n_{20} is hence lower at $n_e = 10^{10}$ than the two level solution. For somewhat higher electron densities the collisional rates between the singlets and triplets exceed the photoionization rates. Hence, the recombination to intermediate levels results in conversion to the 5, 11 or 19 level and thence to the 1 level by spontaneous emission. The rate from 20 to 1 is now enhanced and n_1/n_{20} exceeds the two level solution. At still higher electron density the collisional ionization rates begin to become greater than either the spontaneous emission or collisional deexcitation rates. Now all intermediate levels represent paths from level 1 to 20 and n_1/n_{20} becomes lower than the two level solution. This is seen to be the case at $n_e = 10^{14}$.

We turn to the solution when the resonance lines are optically thick. The result for detailed balance (db) in the first resonance line is shown

ORIGINAL PAGE IS
OF POOR QUALITY

Figure II-4 HELIUM IONIZATION EQUILIBRIUM

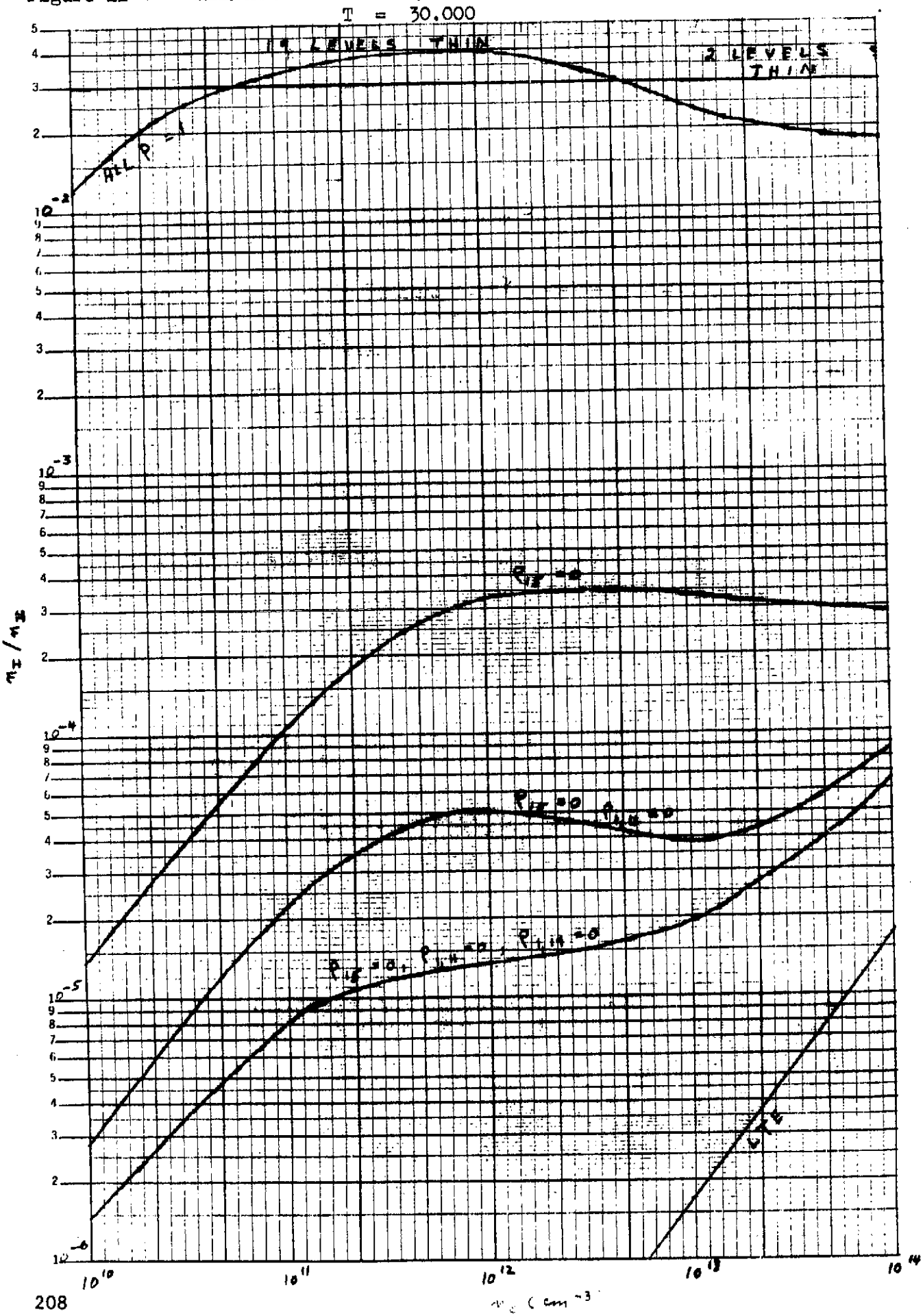

by the curve labeled $\rho_{15} = 0$ (ρ is the net radiative brackett). Also shown are results for db in the second and third resonance lines. Increasing the radiative excitation rate increases the effective ionization rate and the amount of n_{20} by several orders of magnitude. We thus note the important result that the ionization equilibrium is strongly influenced by the optical thickness of the resonance lines. The LTE result is also shown and is labeled LTE.

2. Level Populations

Many sample solutions have been obtained for the level populations or non-equilibrium parameters, b, where $b = n/n_{equil}$.

We have completed a parametric study of the effect of optical thickness in the resonance lines and continuua upon the level populations. Level populations were obtained for various physically meaningful combinations of resonance lines and continuua being optically thick or thin. That is to say each resonance line or continuua was assumed to have a net radiative brackett of either 0 (completely thick) or 1 (thin). The results cover the temperature range T = 10,000 to 50,000°K and electron density range $n_e = 10^{10} - 10^{14}$ cm^{-3}. Due to space limitations we cannot present results for all 30 levels of the model. Hence levels 1, 5, 9, 20 and 27 were chosen to illustrate the results. Referring to section II.A we see that levels 1 and 20 are the ground states of He I and II, level 5 the upper level of the 584Å line, level 9 the upper level of the D3 line and level 27 the upper level of the 4686Å line of He II. Figures II.5-29 show results for each of these 5 levels for electron temperatures 10^4, 2×10^4, 3×10^4, 4×10^4 and 5×10^4°K. In each figure the ratio of the actual population to the equilibrium population, b, is given as a function of n_e.

At each temperature calculations were made for combinations of net radiative brackets corresponding to layers of varying total thickness. There are 3 resonance lines in the model for both He I and He II. These 6 lines together with the Lyman continuua for each ion are allowed to become optically thick in our calculation. Thus, there are eight lines and continuua which can be optically thick or thin depending upon the physical thickness of the layer. Each figure shows a completely optically thin solution labeled T and 8 other solutions labeled 1 - 8 which correspond to the combinations of optical

Figure II-5 b_1

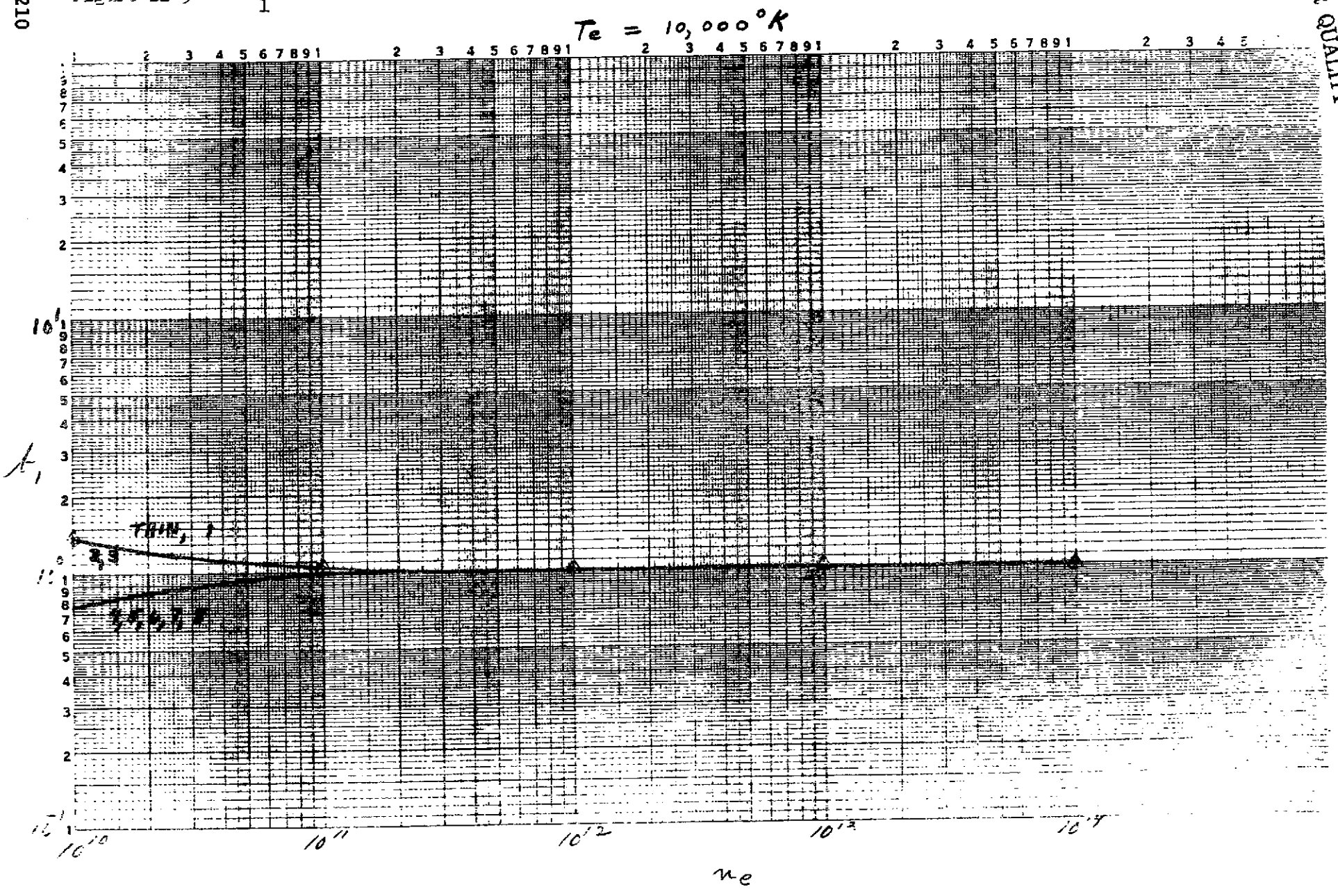

ORIGINAL PAGE IS
OF POOR QUALITY

Figure II-6 b_9

Te = 10,000° K

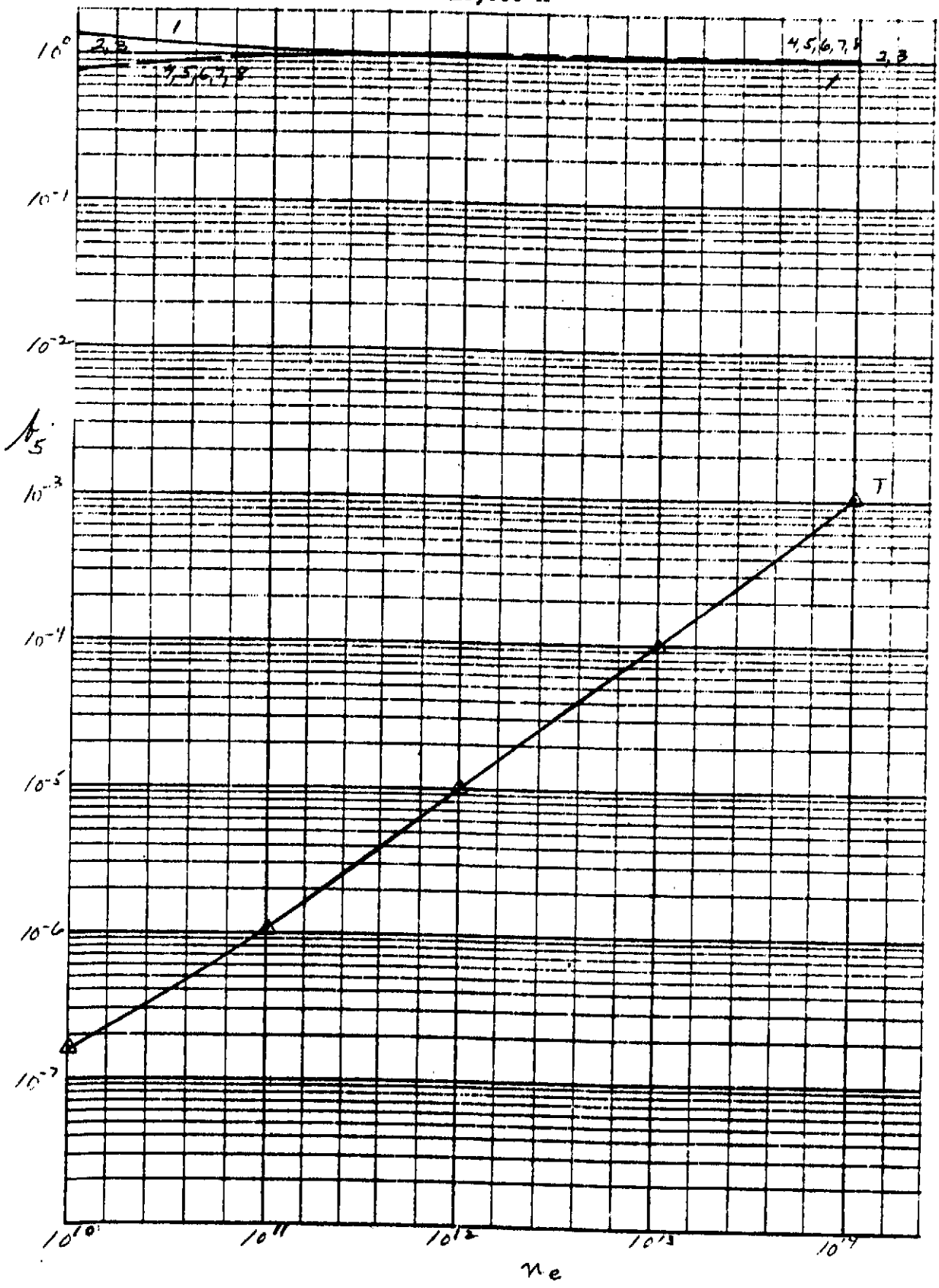

Figure II-7 b_9

Te = 10,000° K

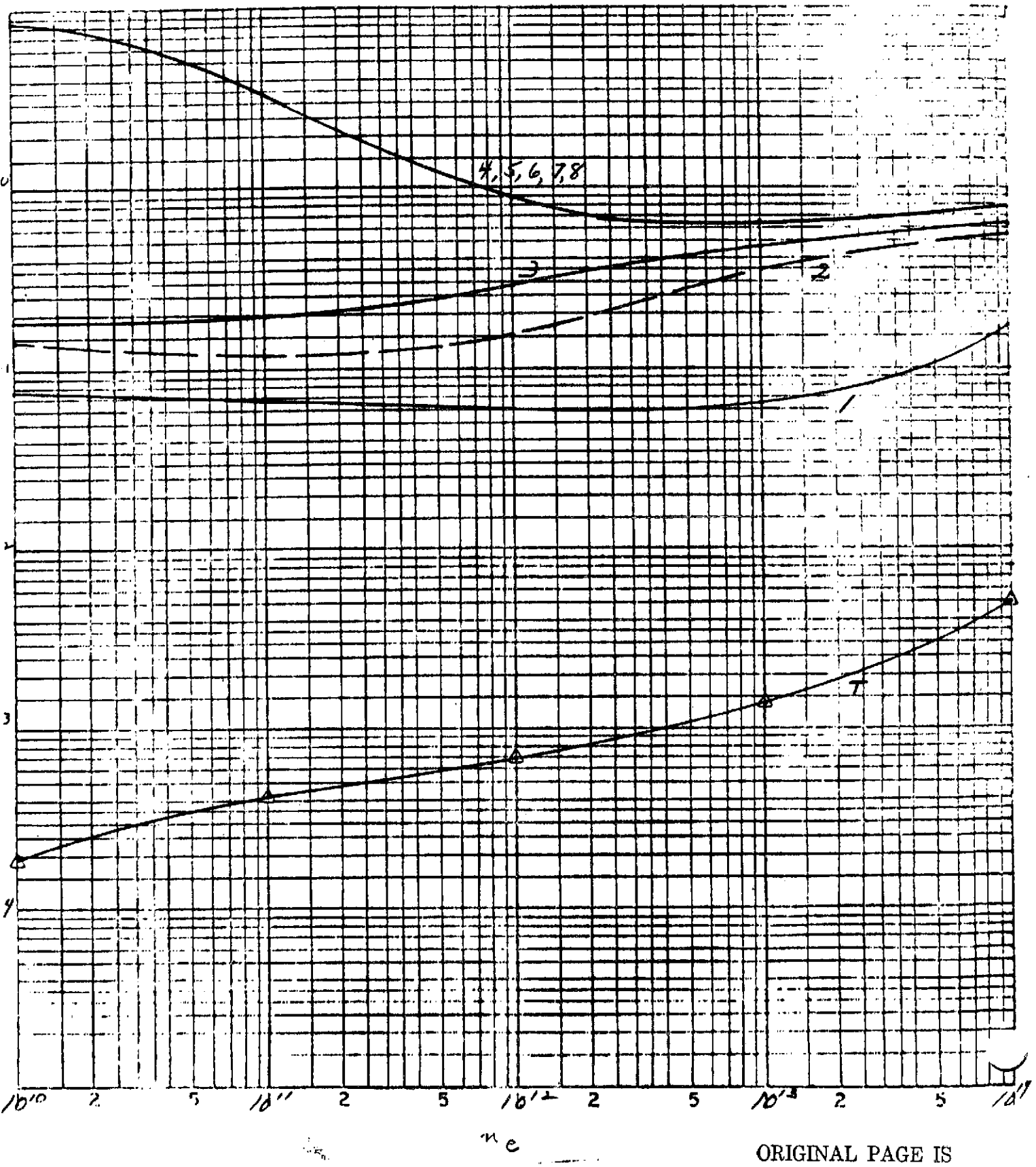

ORIGINAL PAGE IS
OF POOR QUALITY

Figure II-8 b_{20}

Te = 10,000° K

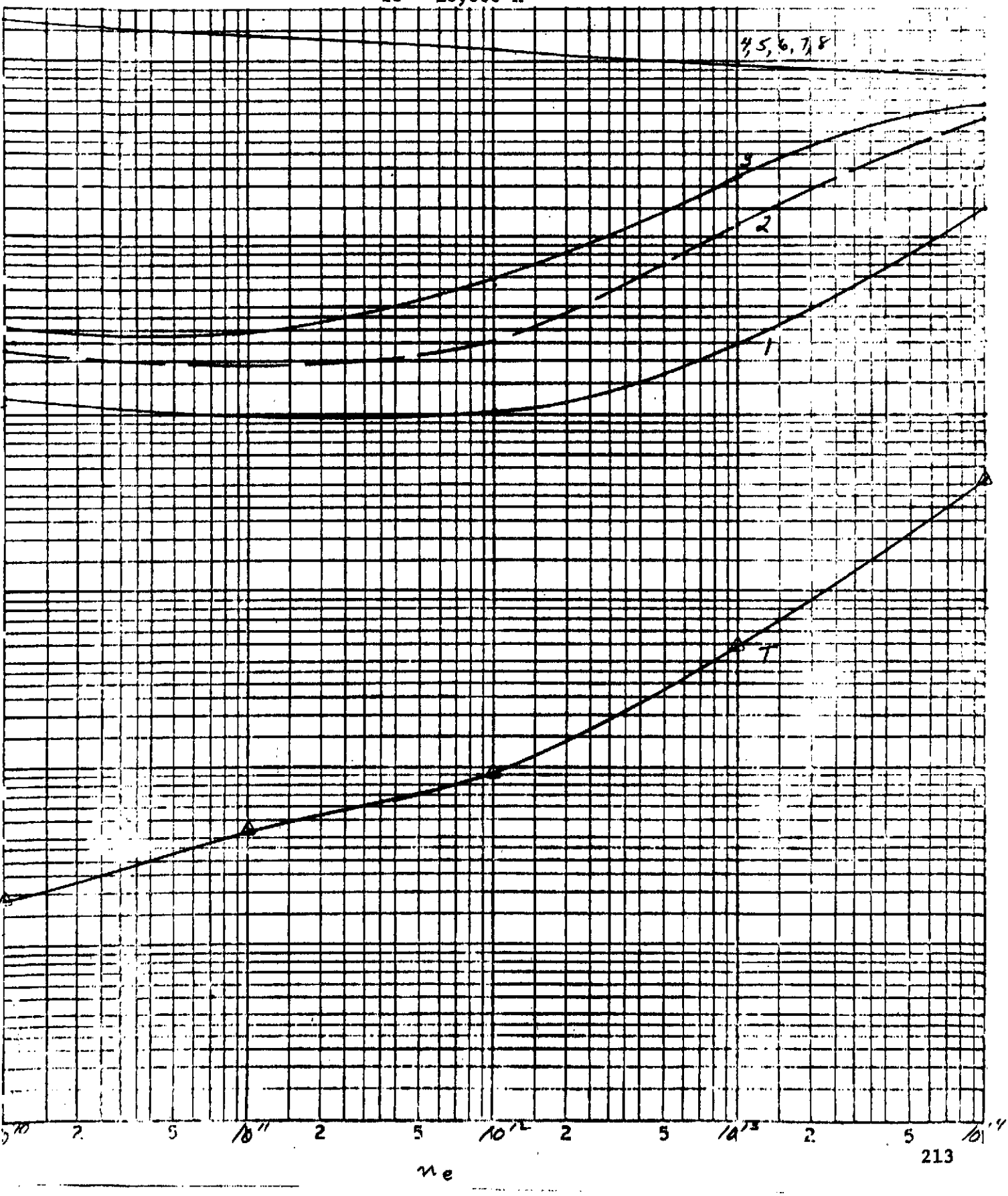

Figure II-9 b_{17}

ORIGINAL PAGE IS
OF POOR QUALITY

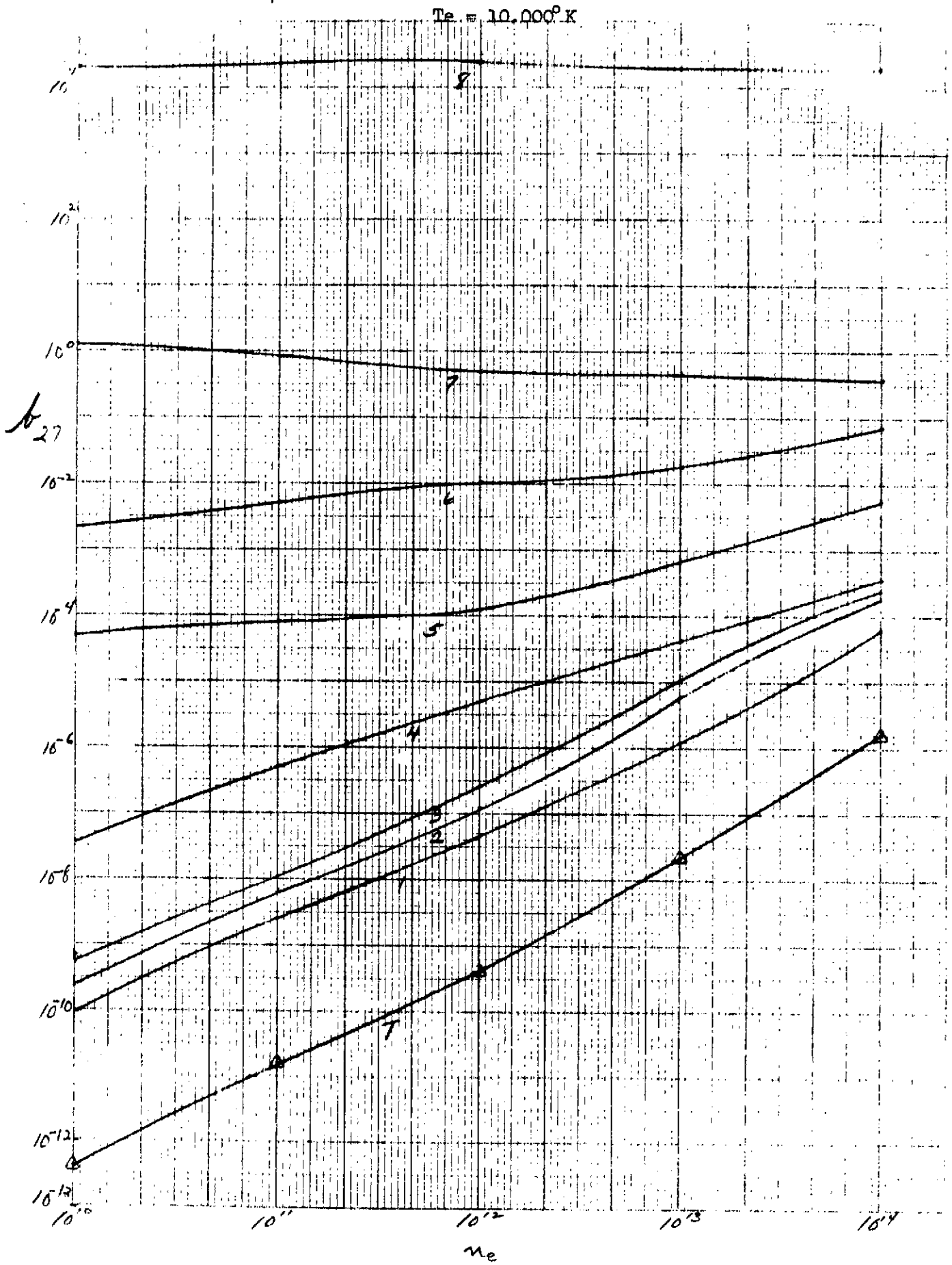

Figure II-10 b_1

Te = 20,000° K

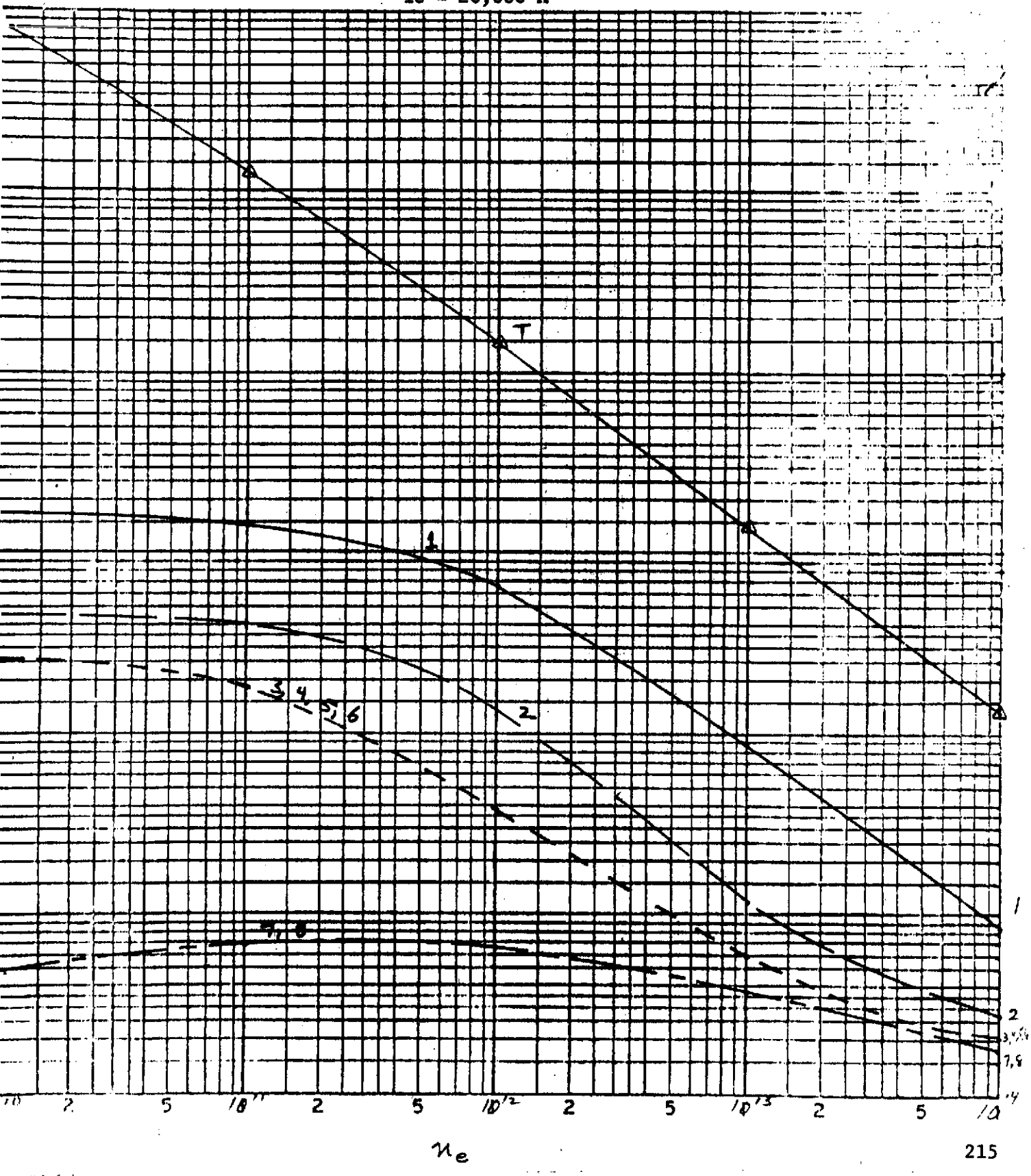

Figure II-11 b_5

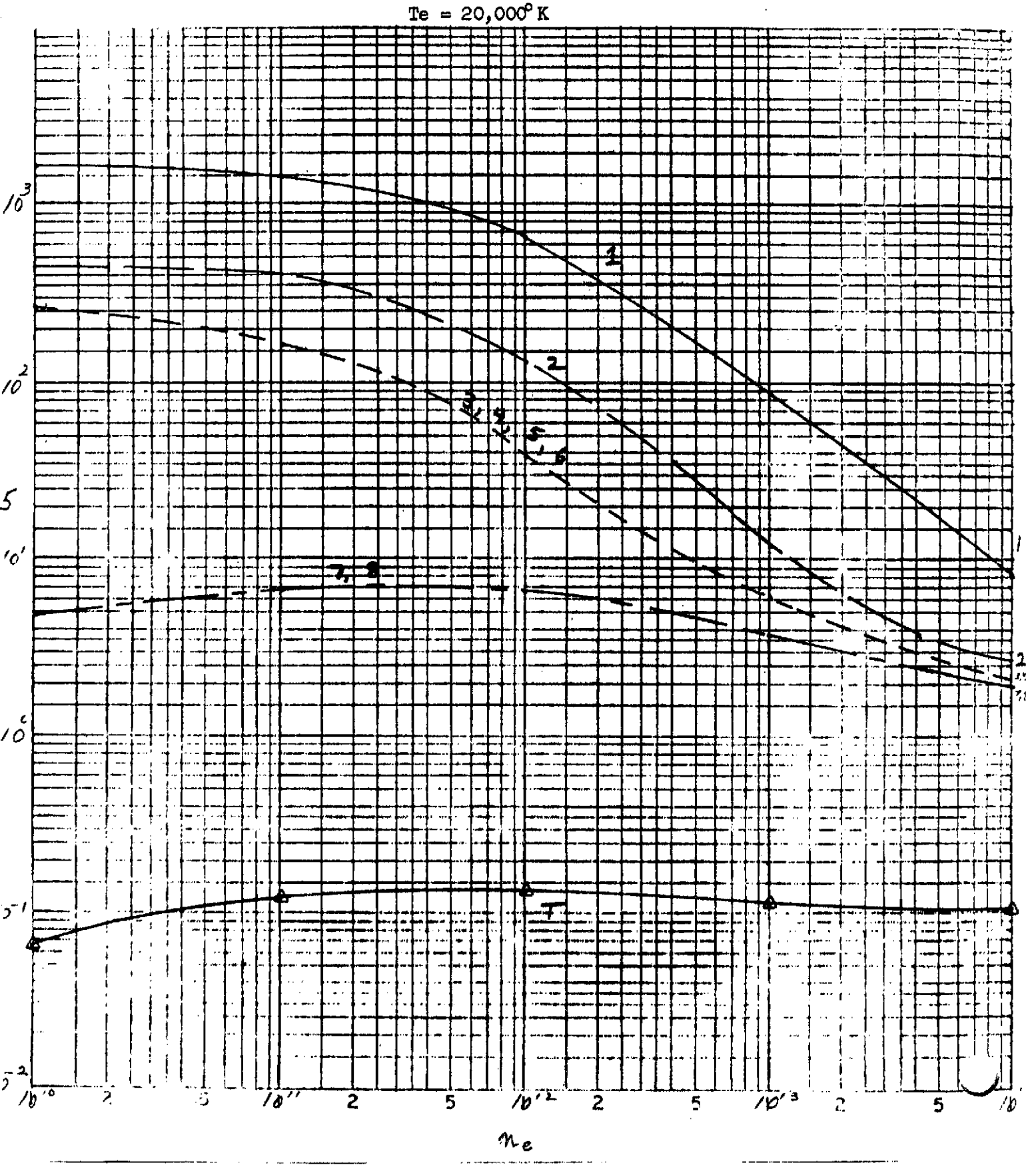

Figure II-12 b_9

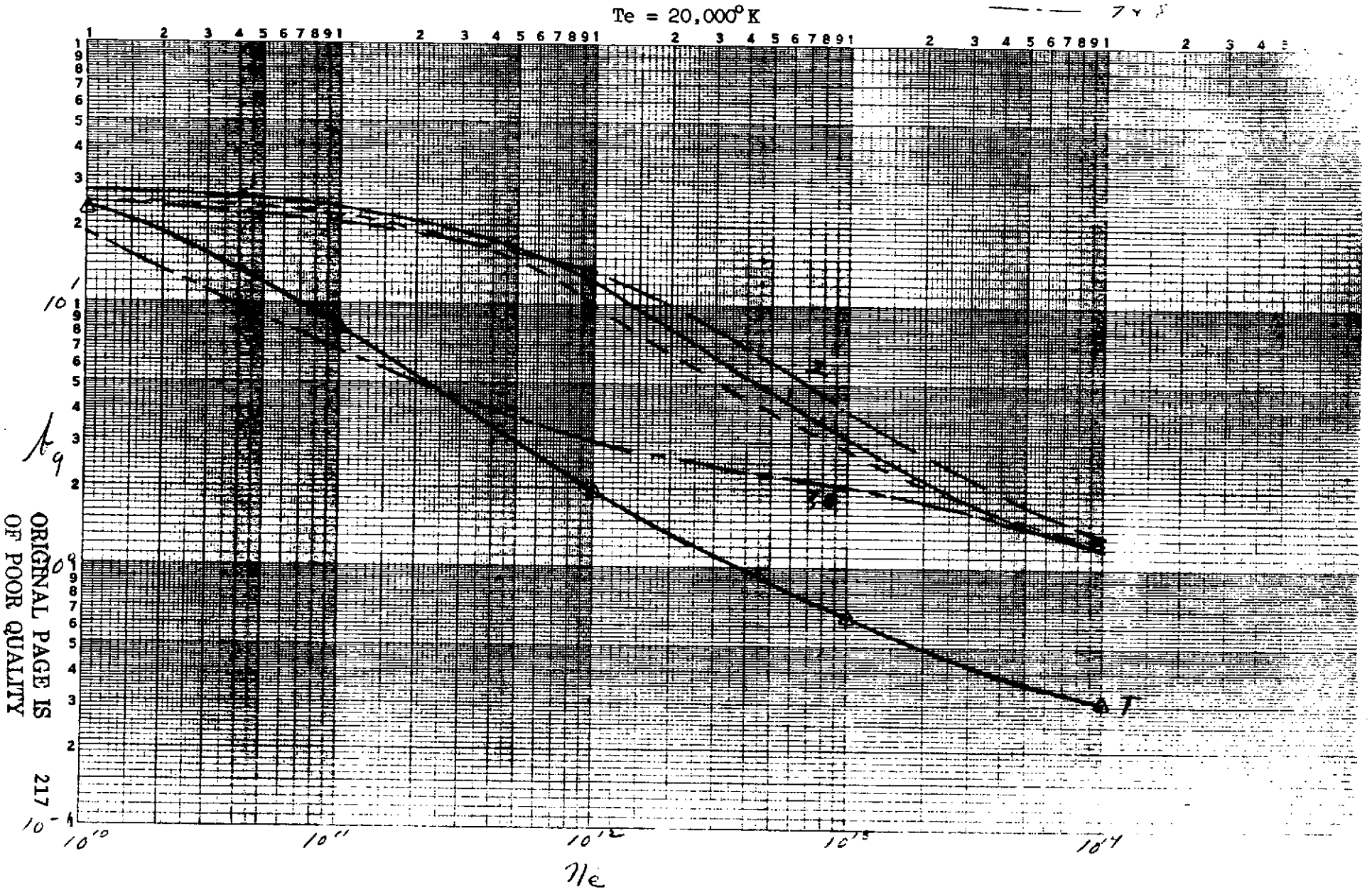

ORIGINAL PAGE IS
OF POOR QUALITY

Figure II-13 b_{27}

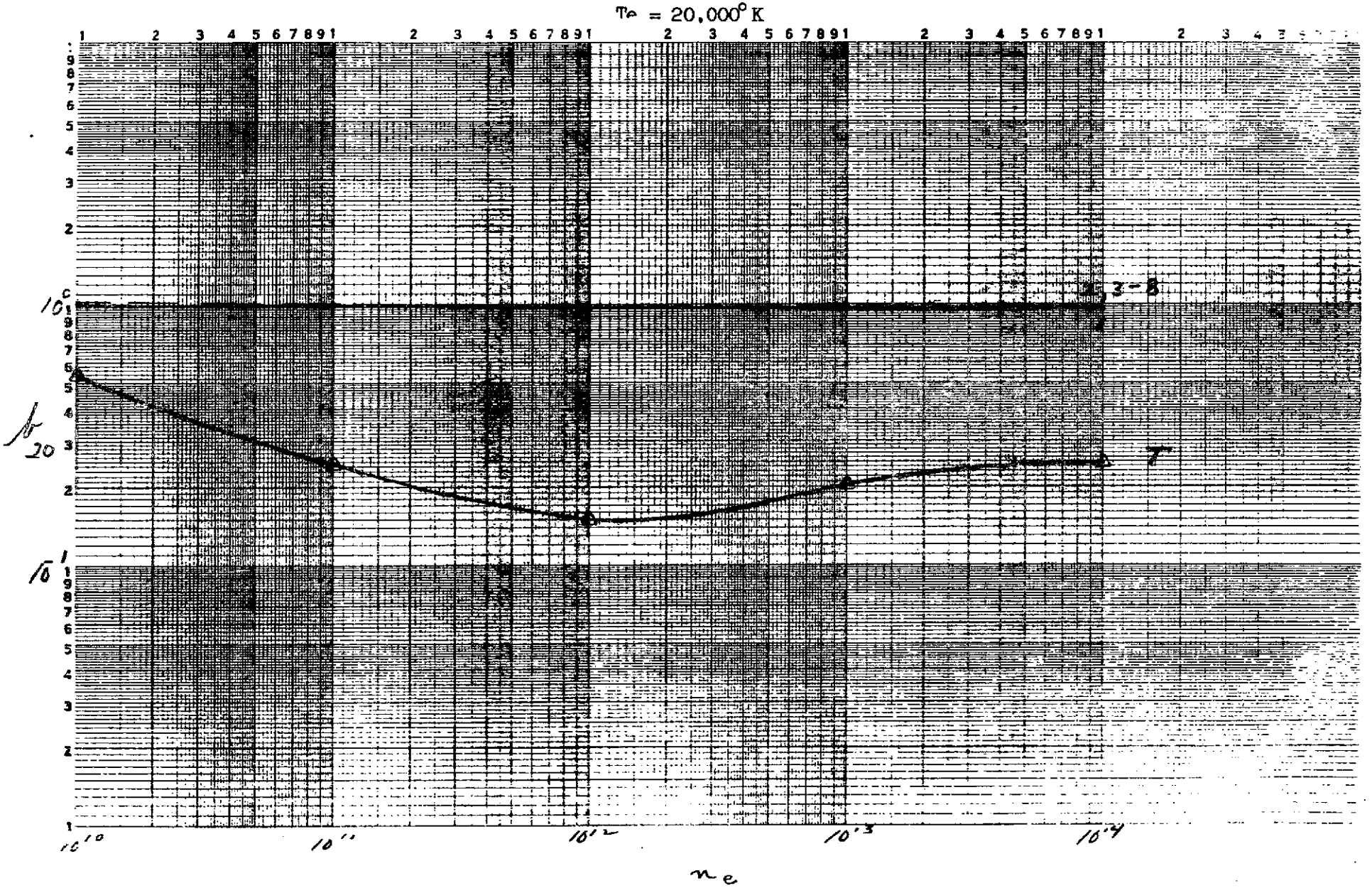

Figure II-14 b_{27}

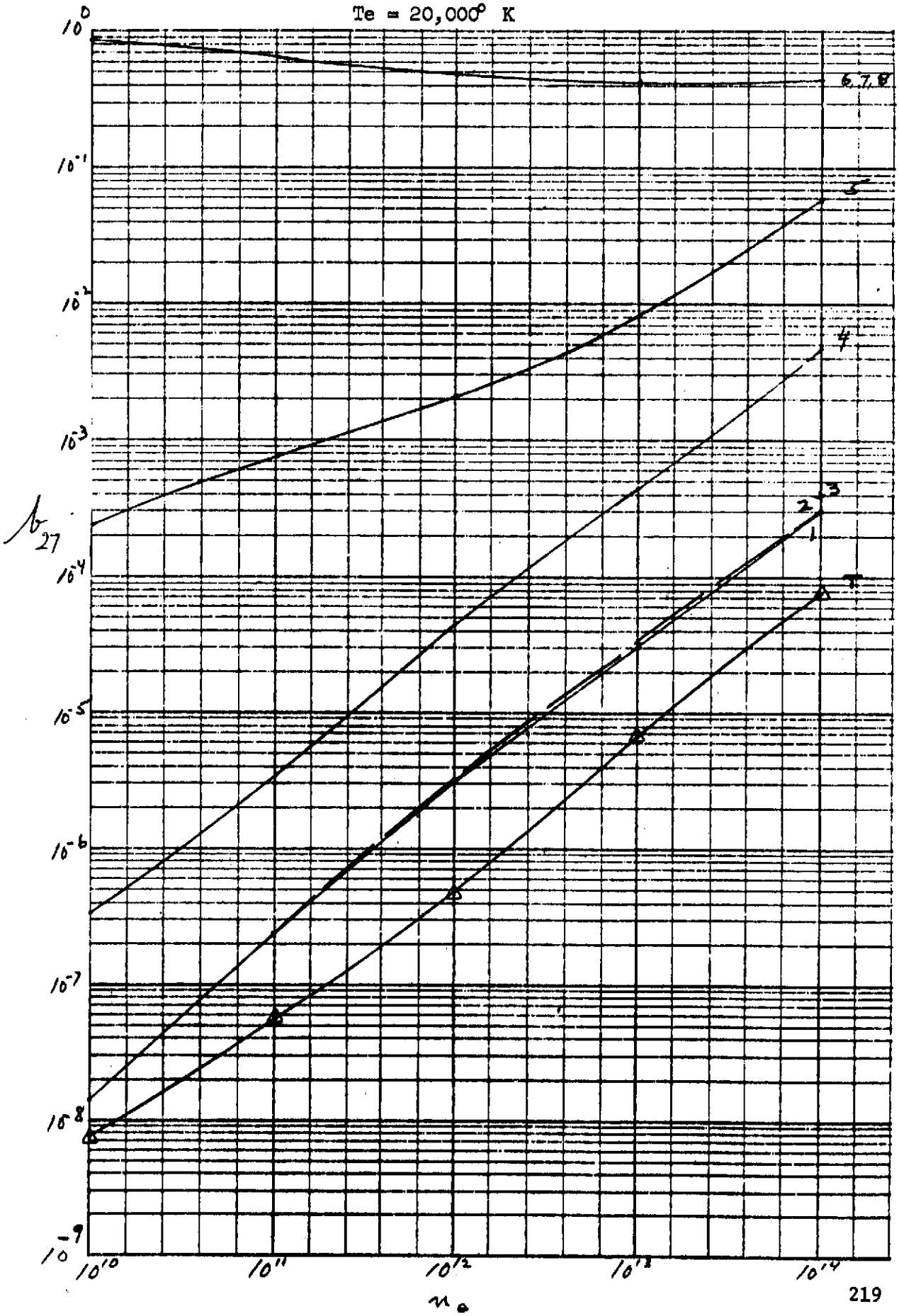

Figure II-15 b_5

ORIGINAL PAGE IS
OF POOR QUALITY

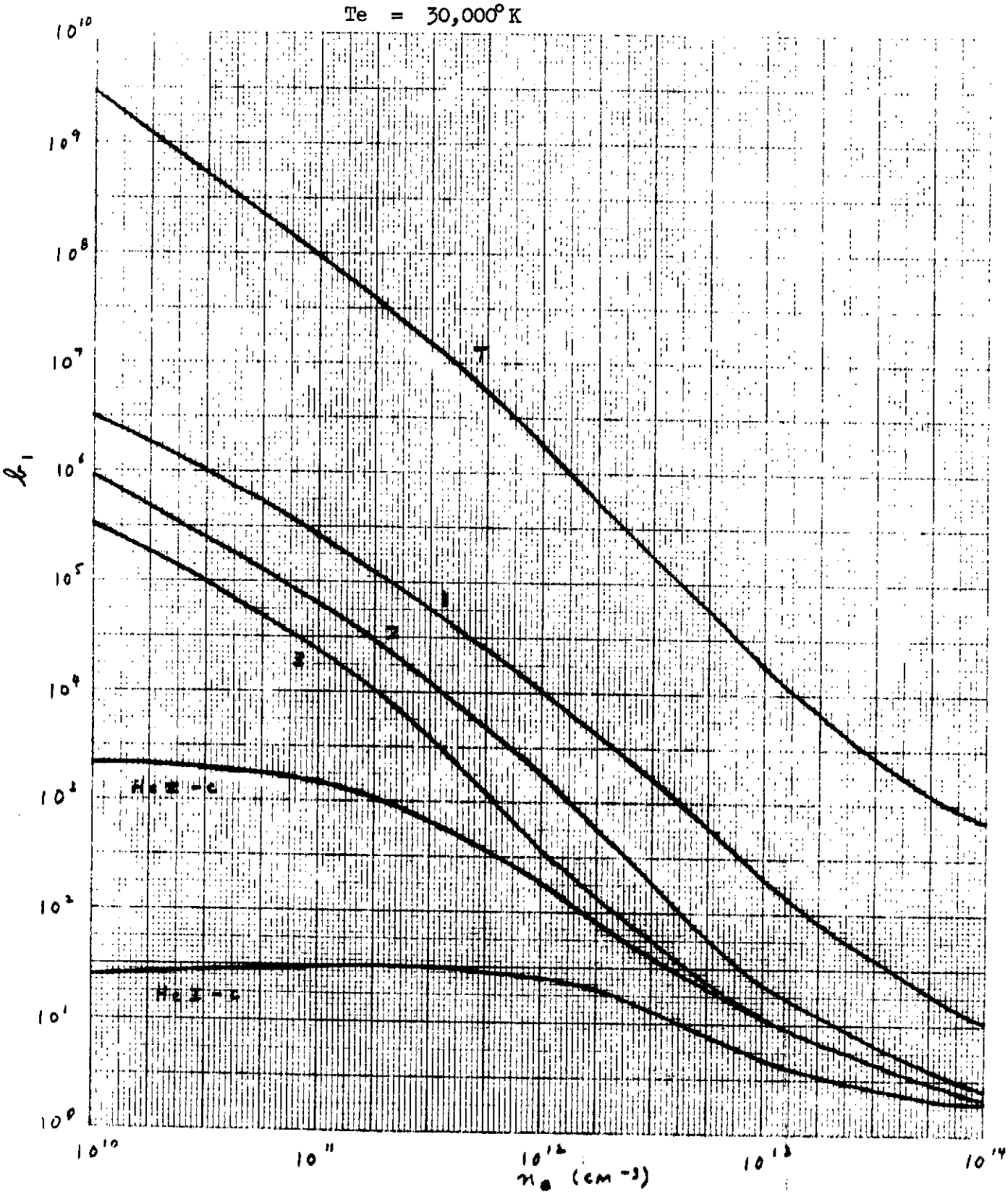

Figure II-16 b_5

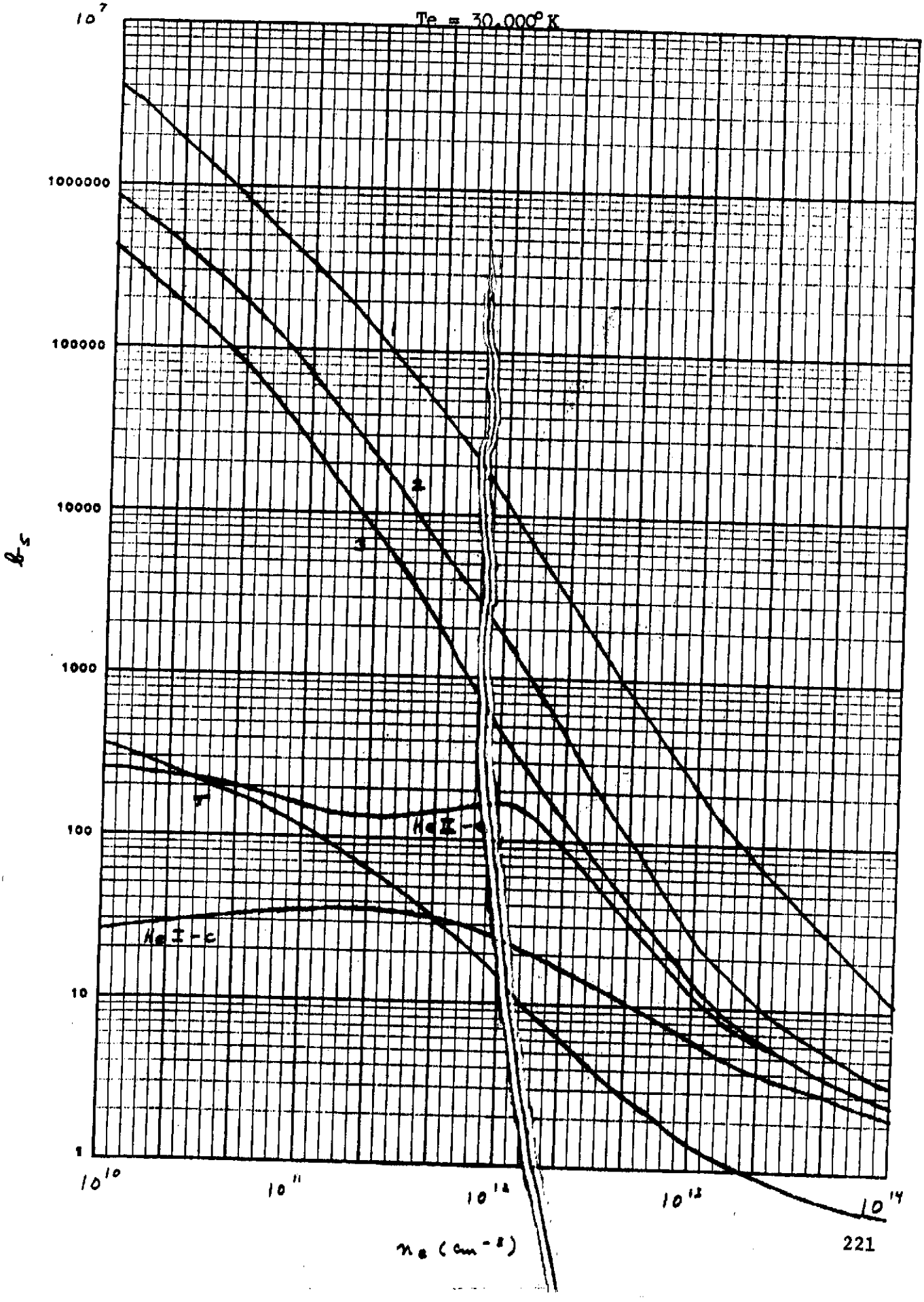

Figure II-17 b_9 $T_e = 30{,}000°K$

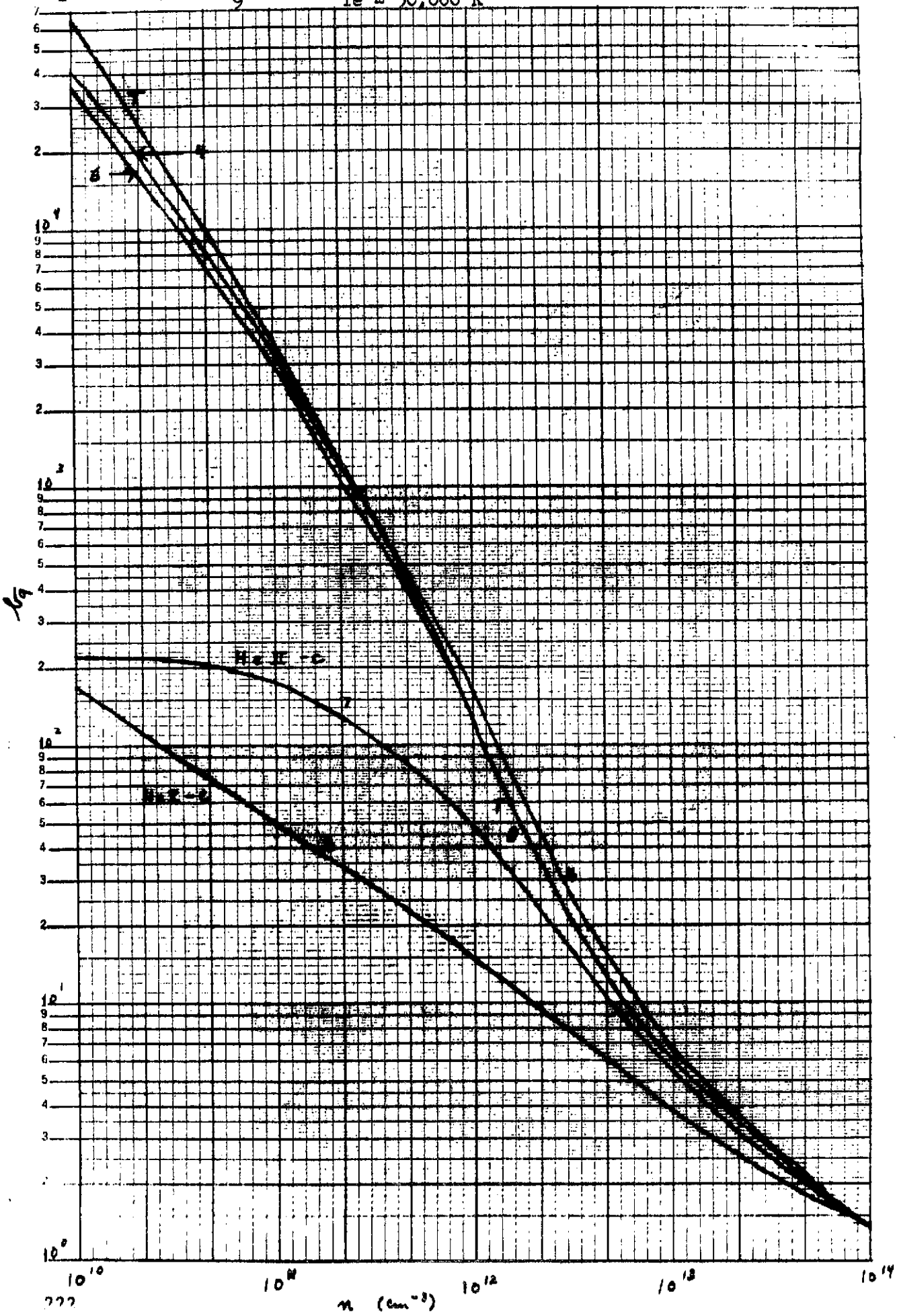

Figure II-18 b_{20}

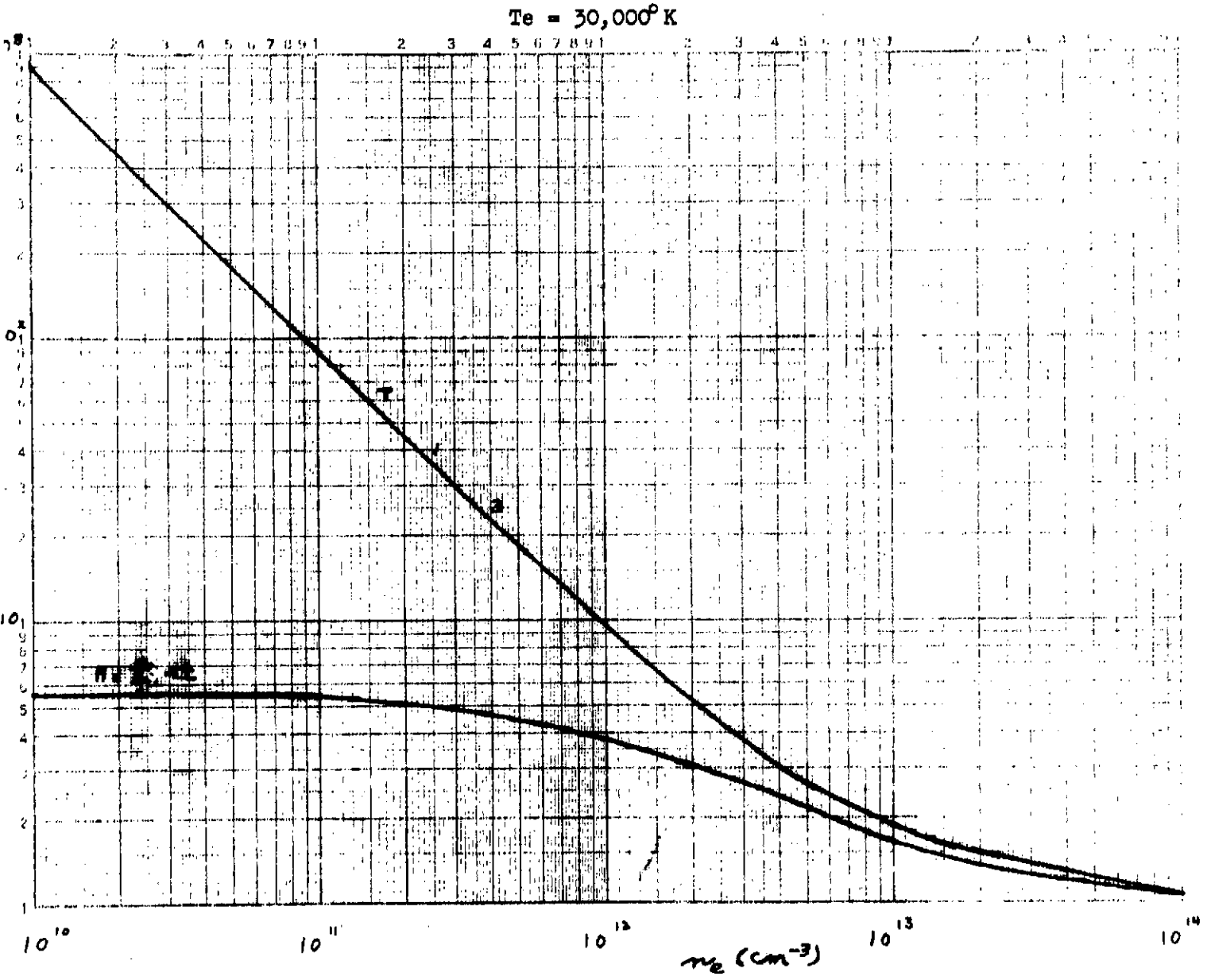

ORIGINAL PAGE IS
OF POOR QUALITY

Figure II-19 b_{27}

Te = 30,000° K

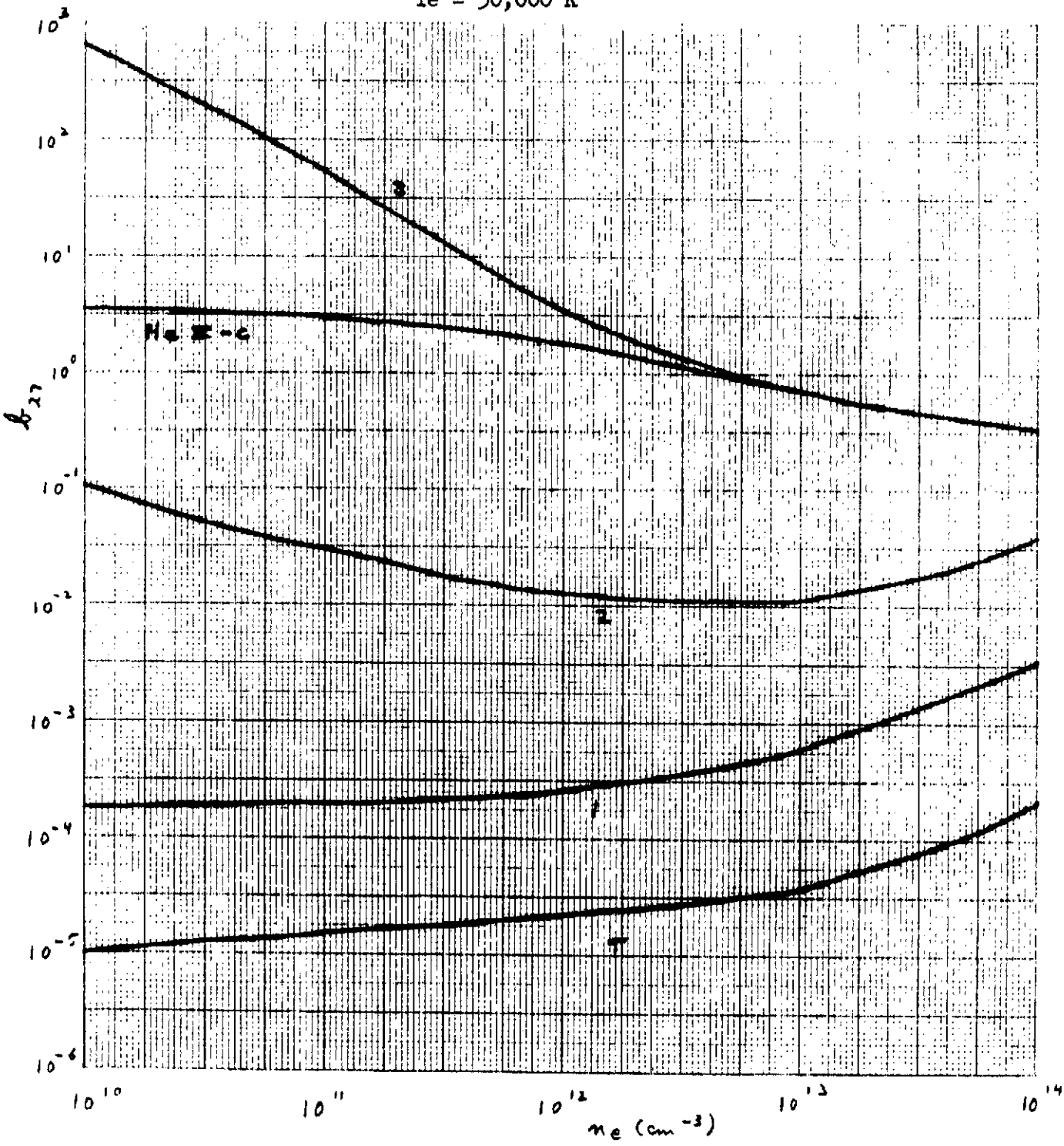

ORIGINAL PAGE IS
OF POOR QUALITY

Figure II-20 b_1

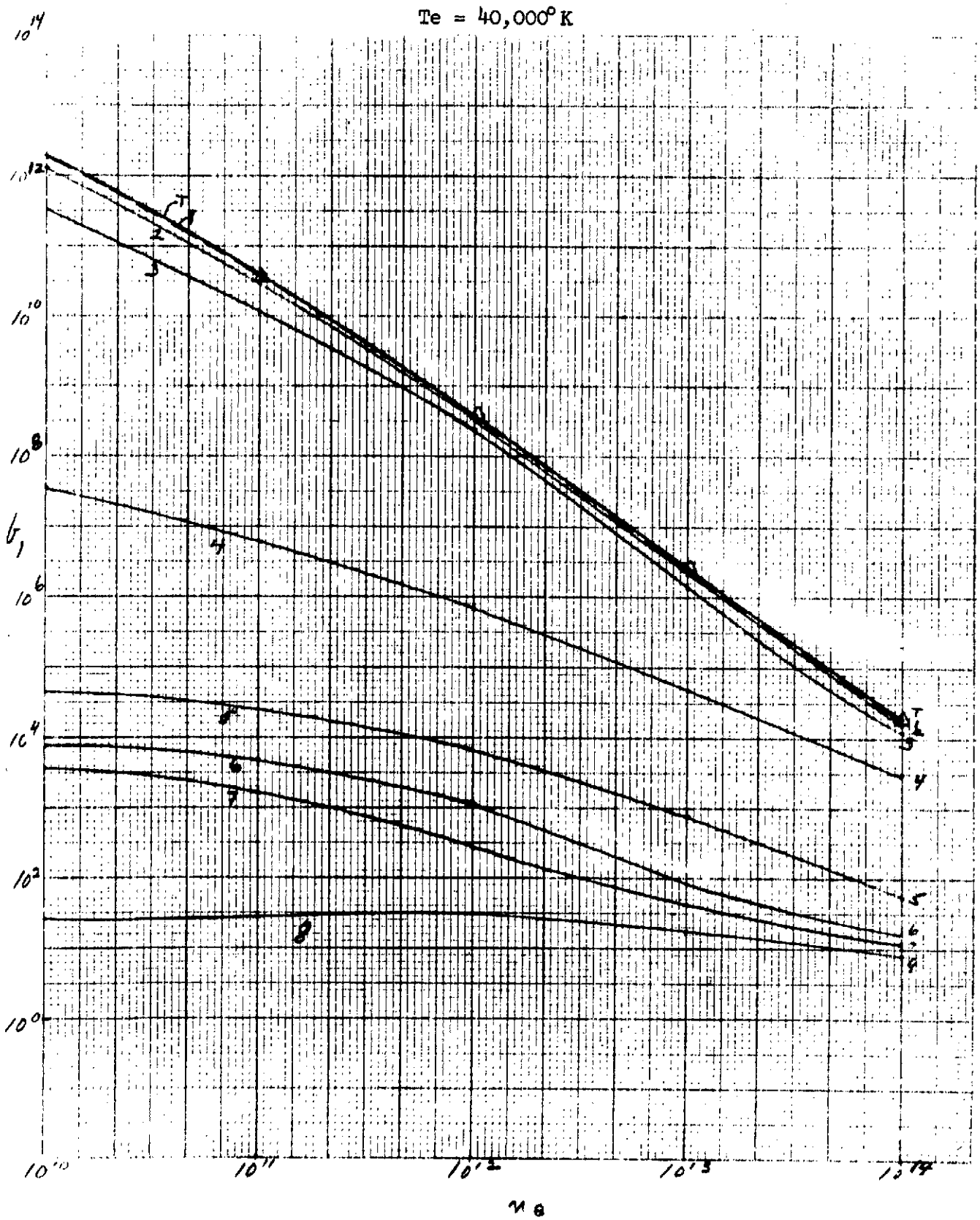

Figure II-21 b_5

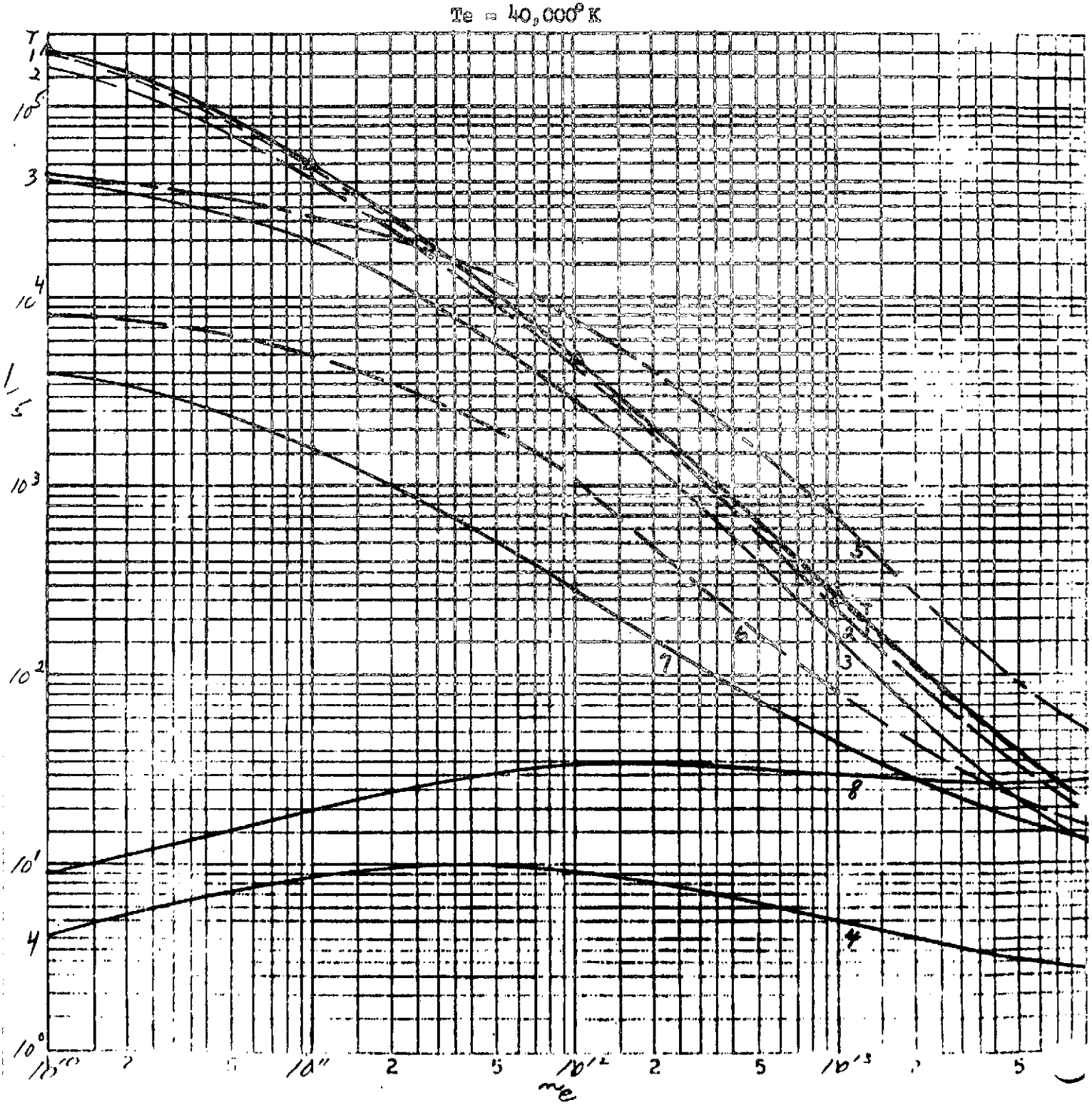

Figure II-22 b_9

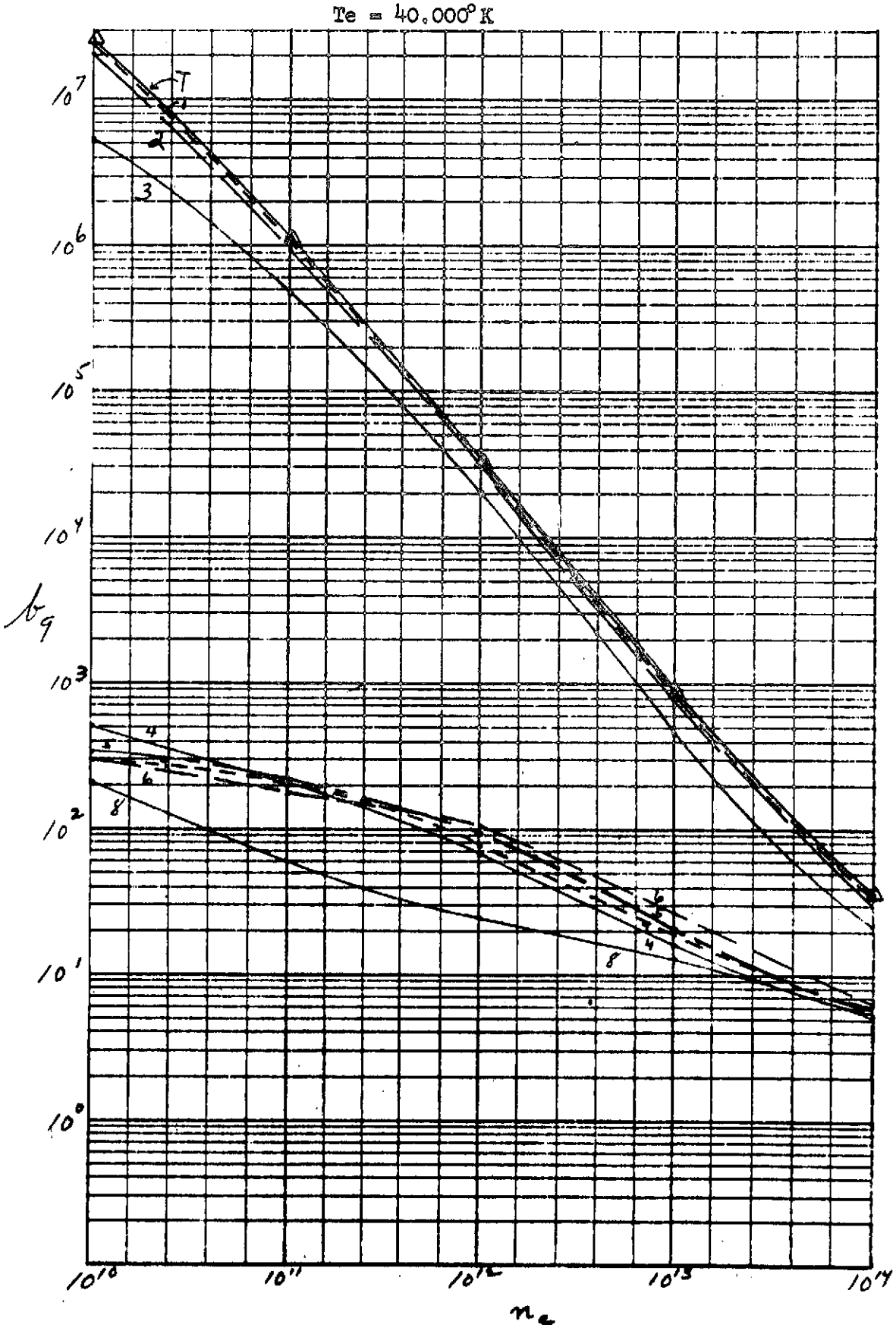

Figure II-23 b_{20}

Te = 40,000° K

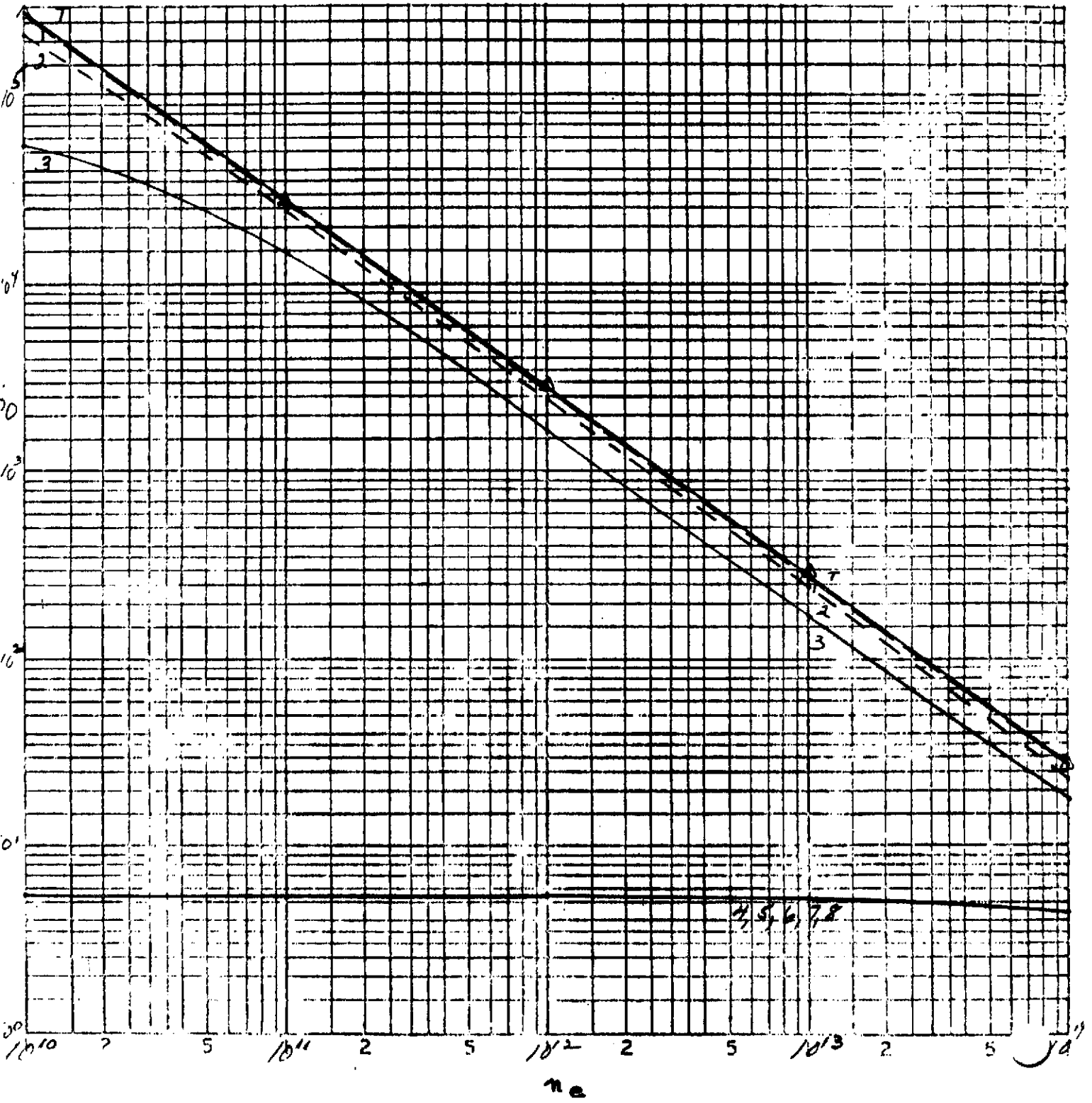

Figure II-24 b_{27}

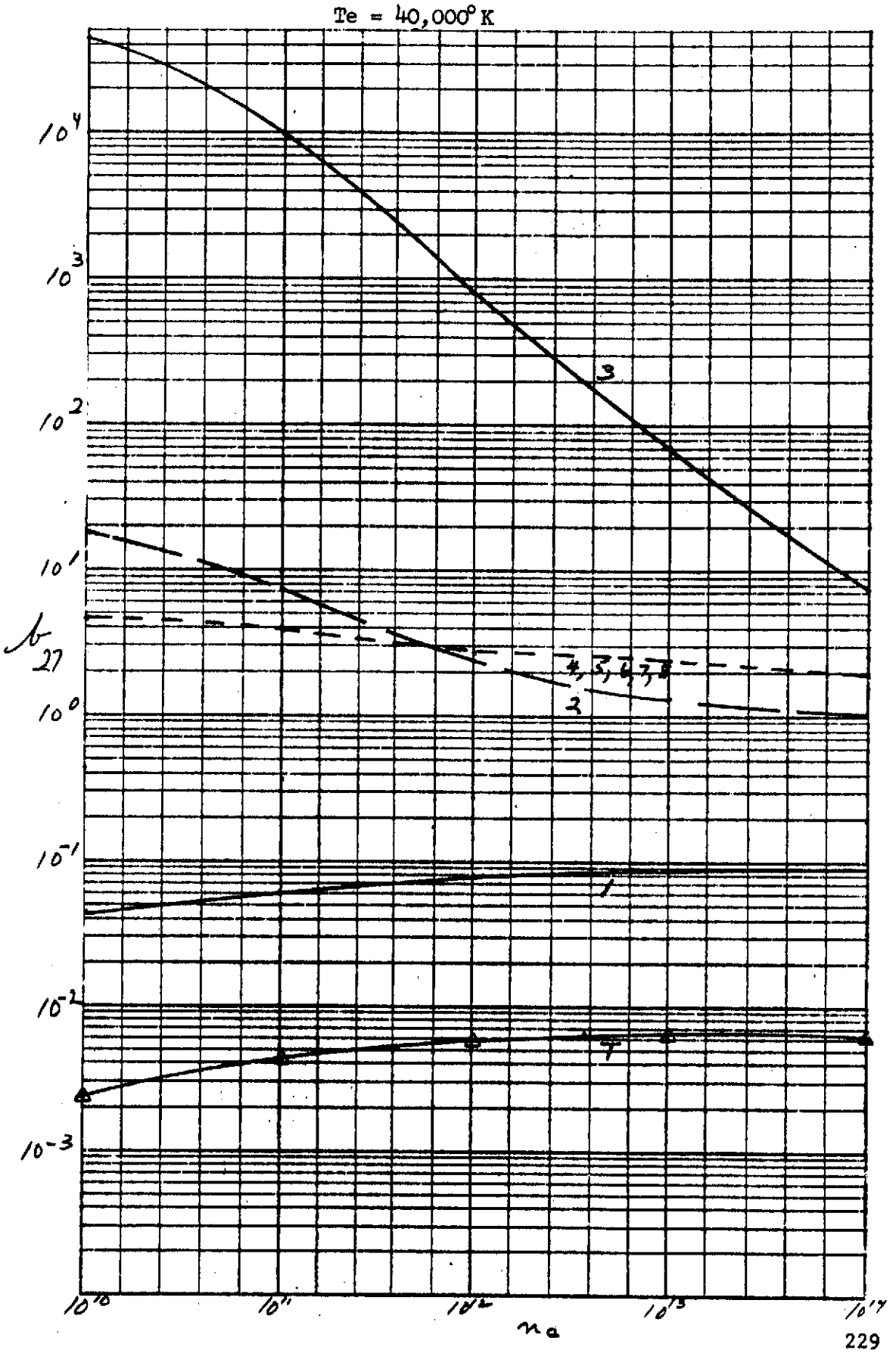

Figure II-25 b_1

Te = 50,000° K

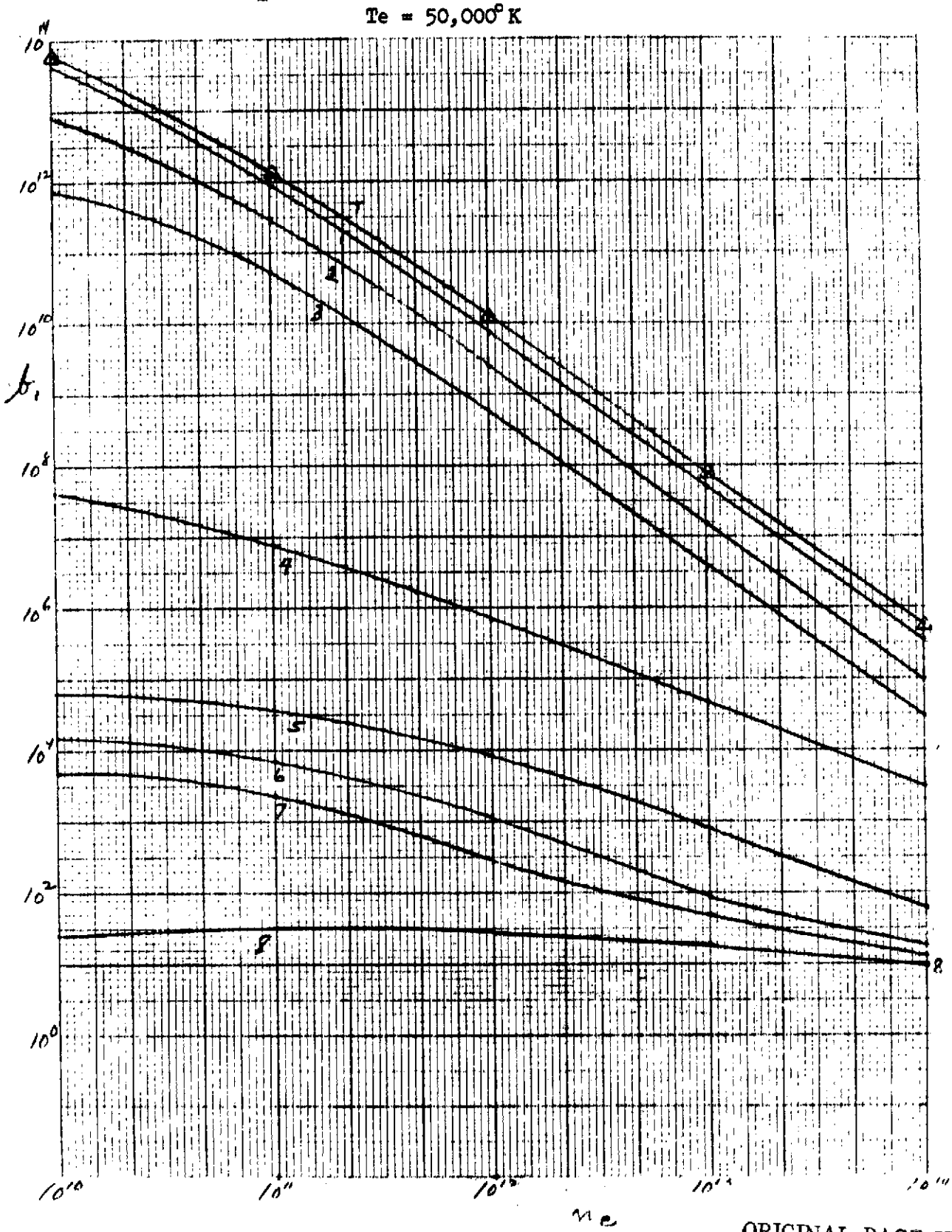

ORIGINAL PAGE IS
OF POOR QUALITY

Figure II-26 b_5

Te = 50,000° K

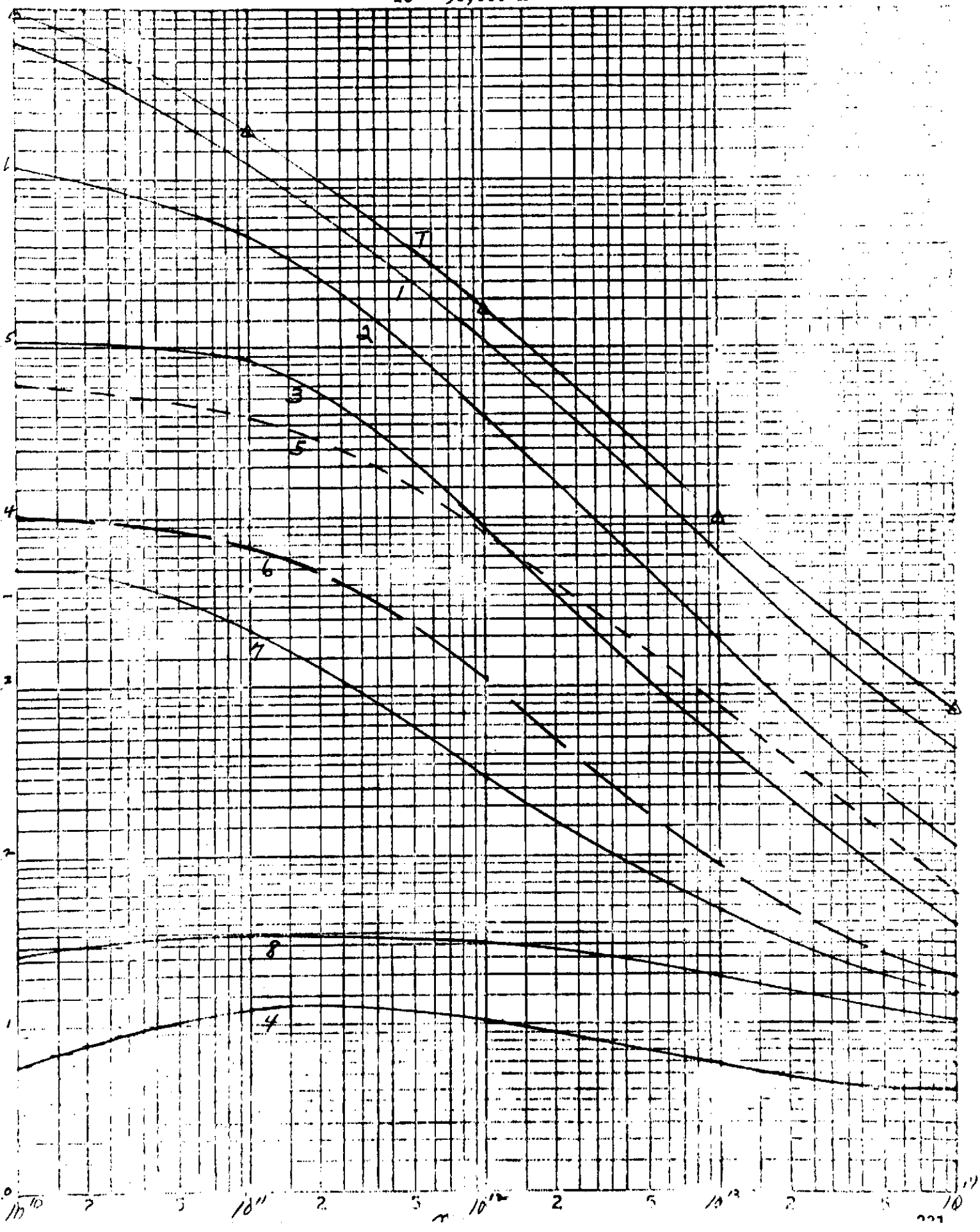

Figure II-27 b_9

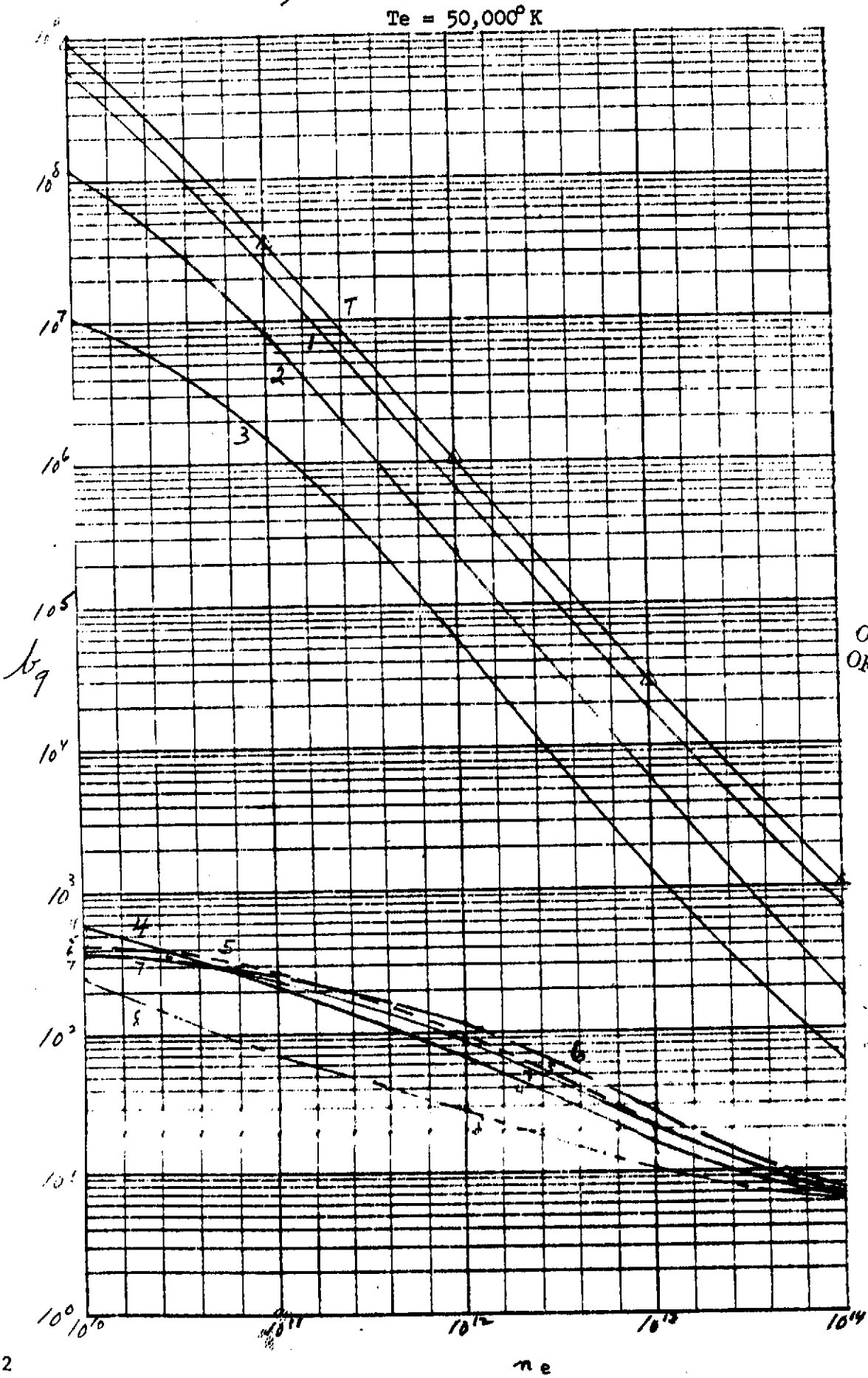

ORIGINAL PAGE IS OF POOR QUALITY

Figure II-28 b_{20}

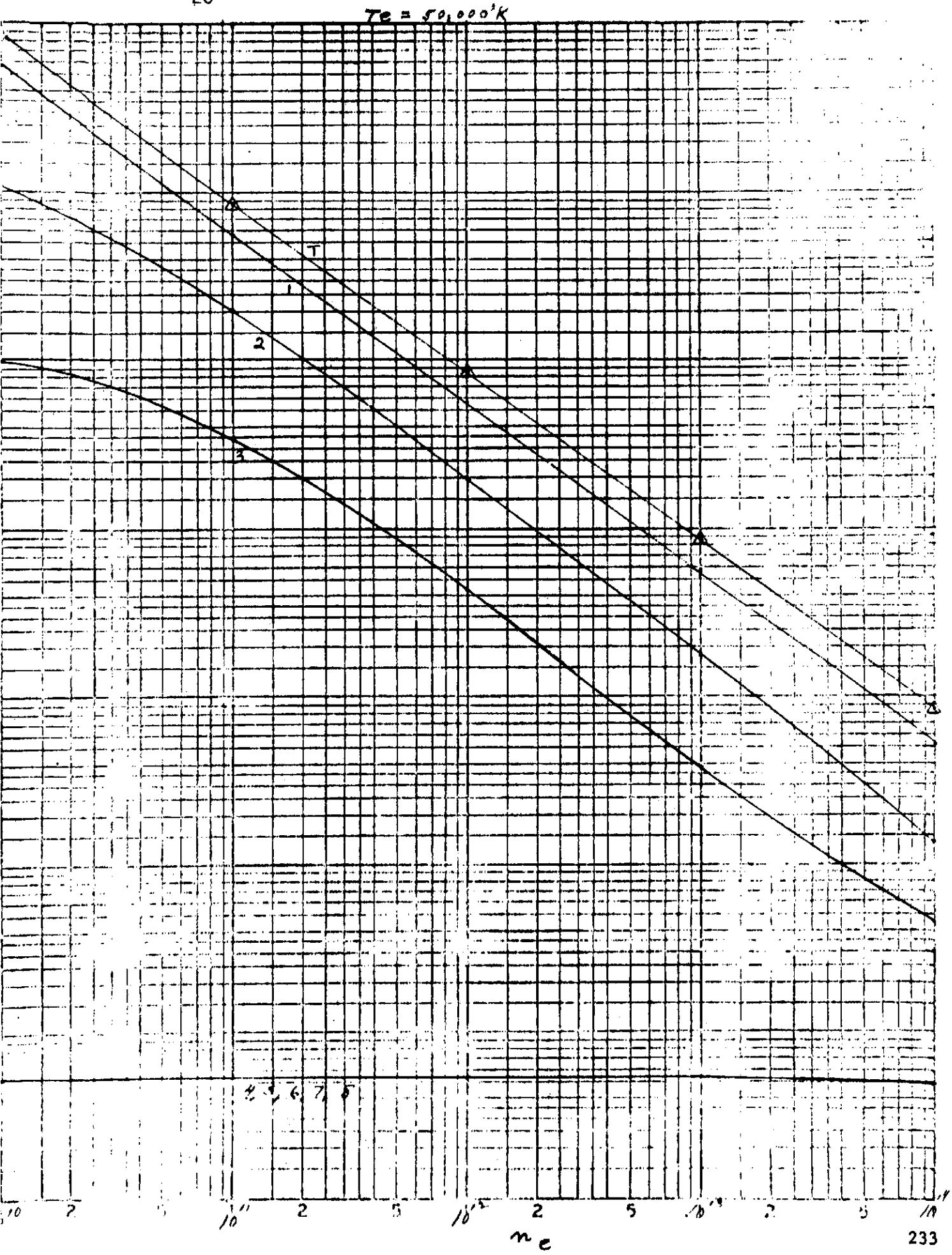

Figure II-29 b_{27} $T_e = 50{,}000°K$

ORIGINAL PAGE IS
OF POOR QUALITY

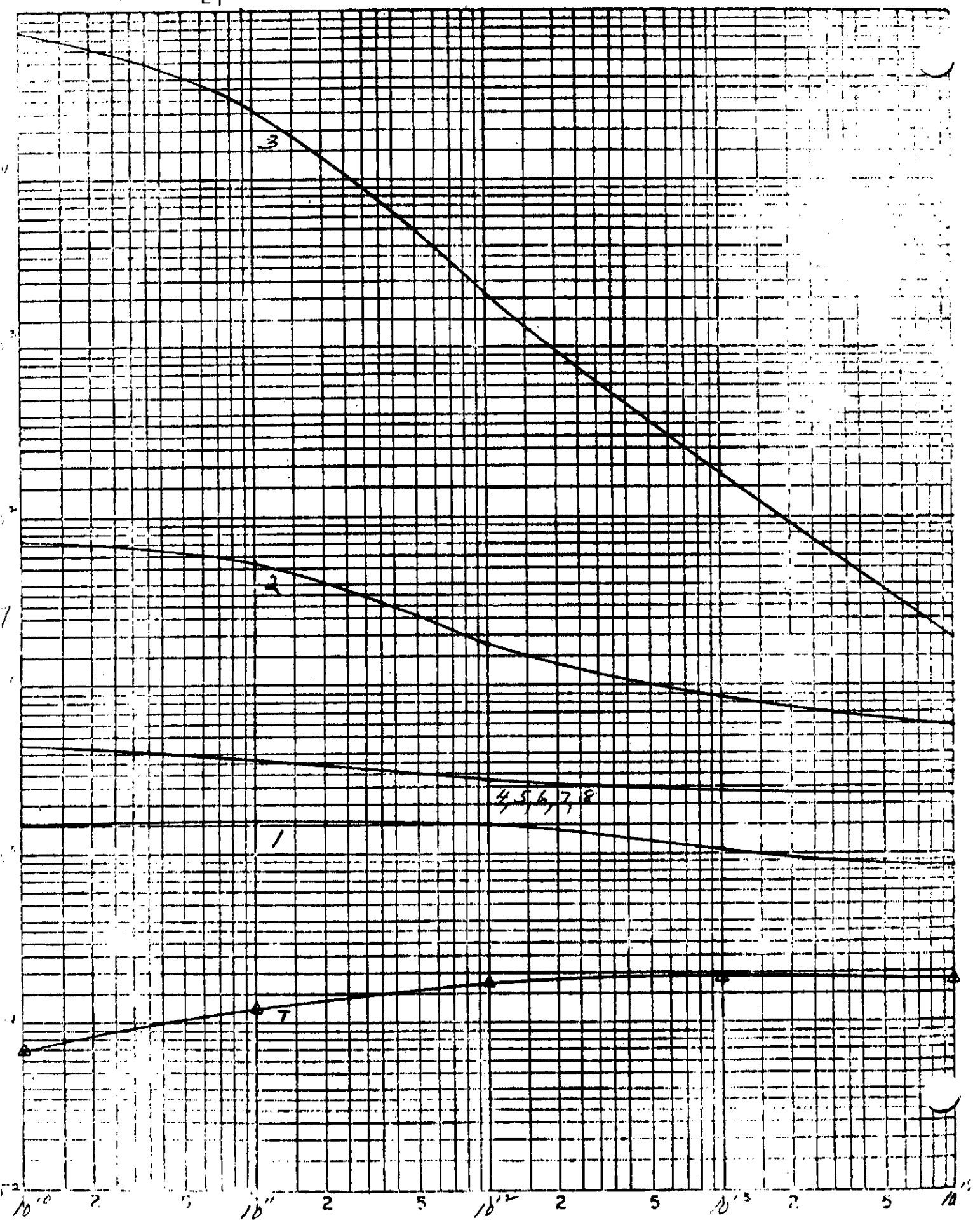

ORIGINAL PAGE IS
OF POOR QUALITY

thicknesses given in Table II.3. On this table (1) refers to the 584Å line, (2) refers to the 537Å line, (3) refers to the 522Å line and (4) refers to the Lyman continuum of He I. Similarly the numbers 5 - 8 refer to the 304, 256, 243Å lines and Lyman continuum of He II. When a number appears in Table II.3 the corresponding transition has been assumed optically thick (i.e. in radiative detailed balance) in obtaining rate coefficients for the level population solutions. Transitions not appearing in the table are assumed optically thin. It is noted that progressing from case 1 to 8 corresponds in general to the layer becoming thicker. Case 8 always corresponds to all 8 lines and continuua becoming optically thick. For example, with $T_e = 30{,}000^{\circ}K$ case 4 represents the NRB = 0 in the first 3 resonance lines of He I and the first resonance line of He II.

We shall discuss briefly the solutions presented in Figures II.5-30. For $T_e = 10^{4}{}^{\circ}K$ most of the He is He I. The He I ground state population is not affected by optical thickness except slightly at $n_e = 10^{10}$. Similarily Figure II.6 shows that once the 584 Å line becomes thick the radiation field in other lines and continuua do not affect it. The D3 line upper level population shown in Figure II.7 is a strong function of the 584 Å line and He I Lyman continuum optical depths and to a lesser extent dependent on the 537 and 522 Å lines. Increasing the singlet populations hence increases the D3 emission. The optical thicknesses of the He II lines and continuua do not affect the D3 line. From Figure II.8 it is seen that the He II ground state exhibits a similar behavior. At $20{,}000^{\circ}K$ the He I and He II densities are very roughly the same. The thin solution shows that He I is greatly overpopulated and He II slightly underpopulated with respect to LTE. Increasing the optical depth in the He I resonance lines and continuua now increases the ionization by absorption of photospheric radiation from upper resonance line levels and thus increases the He II density and decreases the He I density. The D3 line upper level population increases with increasing population of the singlet levels but decreases when the He I Lyman continuum becomes thick due to decreasing total He I density. As before the He II resonance line and continuum radiation fields do not affect the He I level populations.

At $30{,}000^{\circ}K$ both He I and II ground states are overpopulated at the expense of He III. The He II ground state population is sensitive only to the Lyman continuum of He II while the He I population depends upon both continuua and the

Table II-3

OPTICALLY THICK LINES CHOSEN

Temperature	Case Number 1	2	3	4	5	6	7	8
10^4	1	1,2	1-3	1-4	1-5	1-6	1-7	1-8
$2x10^4$	1	1,2	1-3	1-3 5	1-3 5,6	1-3 5-7	1-3 5-8	1-8
$3x10^4$	5	5,6	5-7	1 5-7	1,2 5-7	1-3 5-7	1-3 5-8	1-8
$4x10^4$	5	5,6	5-7	5-8	1 5-8	1,2 5-8	1-3 5-8	1-8
$5x10^4$	5	5,6	5-7	5-8	1 5-8	1,2 5-8	1-3 5-8	1-8

He I resonance lines. The D3 line is sensitive only to the optical thickness in the two Lyman continuua. The level 27 population depends upon the He II resonance lines and continuua only. At $T_e = 40,000°K$ all the levels have a strong dependence on the optical thickness of the He II Lyman continuum. When this continuum is thick thepopulation of He III is greatly increased while those of He I and II are decreased, then decreasing all of the level populations. For levels 9 and 20 this continuum has the largest influence. Levels 1 and 5 are also dependent on the He I resonance line and continuum optical depths. At 50,000° K the level populations have the same behavior as at 40,000° K.

ORIGINAL PAGE IS
OF POOR QUALITY

3. Optical Thickness and Line Intensity

Figures II.5-29 have illustrated the effect of optical thickness in the resonance lines and continuua on certain level populations. We now seek to determine the approximate optical depths of a flare layer. For purposes of illustration we consider a 1000 km thick layer. For each of the same cases given in Table II.3 we have obtained the line center optical thickness in the 584, 304, D3, 10830Å lines and at the threshold of the Lyman continuua of He I and II. Optical depths are not shown for the 537, 522, 256, 245Å lines because they are always simply a constant fraction of the 584 and 304Å line optical thicknesses, namely $\tau(537) = .27\ \tau(584)$, $\tau(522) = .11\ \tau(584)$, $\tau(256) = .19\ \tau(304)$, and $\tau(245) = .070\ \tau(304)$.

The optical thicknesses are given in Tables II.4 - II.8 The He density is assumed to be one tenth of the electron density. The number following each entry is the power of 10 by which the entry is multiplied. We note that the 10830 and D3 lines can become thick for high electron densities even at 50,000°K. These lines do not become thick at 10,000°K. There are many cases in which a number of lines and continuua are optically thick. This does not mean however that simultaneous transport equations must be solved for these lines and continuua. Which line and continuum radiation fields must be obtained simultaneously depends upon the level population being sought as well as the temperature, density and layer optical thickness. To determine the effect of various lines and continuua on levels 1, 5, 9, 20 and 27 we can refer to Figures II.5 - 29. For example, Table II.9 shows the approximate maximum percentage error encountered in the D3 line upper level population by solving only for the lines and continuua given in each box. The effect on any level can be obtained from the output from Code 1. Figures II.5 - 29 illustrate the effect of varying the NRB between 0 and 1. In practice when the layer becomes optically thick it does not usually become so thick that the NRB = 0. In order for the line radiation field to become saturated we require

$$\tau_0 > (\epsilon + \eta)^{-1} ,$$

ORIGINAL PAGE IS
OF POOR QUALITY

Table II-4

OPTICAL THICKNESS - 1000 KM LAYER

T_e = 10,000 °K

TRANSITION	n_e	Case T	1	2	3	4	5	6	7	8
	10^{10}									
584		3.7+4	=	=	=	1.3+4	=	=	=	=
504		7.6	=	=	=	4.1	=	=	=	=
5876		2.8-8	1.1-5	2.1-5	2.7-5	8.0-4	=	=	=	=
10830		2.6-7	1.0-4	1.9-4	2.5-4	7.4-3	=	=	=	=
304		1.5-2	9.6			8.6+2	=	=	=	=
228		1.4-6	9.3-4	1.8-3	2.4-3	8.3-2	=	=	=	=
	10^{11}									
584		3.7+5	=	=	=	=	=	=	=	=
504		76	=	=	=	=	=	=	=	=
5876		1.3-6	1.7-4	2.2-4	3.7-4	6.7-3	=	=	=	=
10830		1.2-5	1.2-3	2.1-3	3.4-3	6.2-2	=	=	=	=
304		.046				1.6+3	=	=	=	=
228		4.4-6	1.0-3	1.9-3	3.1-3	.15	=	=	=	=
	10^{12}									
584		3.7+6	=	=	=	=	=	=	=	=
504		7.6+2	=	=	=	=	=	=	=	=
5876		1.5-5	1.1-3	2.4-3	4.7-3	1.5-2	=	=	=	=
10830		1.2-4	8.6-3	2.0-2	3.7-2	0.12	=	=	=	=
304		0.10				1.3+3	=	=	=	=
228		9.3-6	1.0-3	2.8-3	6.0-3	1.2-1	=	=	=	=
	10^{13}									
584		3.7+7	=	=	=	=	=	=	=	=
504		7.6+3	=	=	=	=	=	=	=	=
5876		2.1-4	1.0-2	3.1-2	4.1-2	6.2-2	=	=	=	=
10830		1.4-3	4.7-2	0.13	0.17	0.26	=	=	=	=
304		0.56		1.3+22	2.5+2	1.1+3	=	=	=	=
228		5.4-5	2.7-3	1.3-2	2.4-2	1.0-1	=	=	=	=
	10^{14}									
584		3.7+8	=	=	=	=	=	=	=	=
504		7.6+4	=	=	=	=	=	=	=	=
5876		5.6-3	0.15	0.24	0.26	0.29	=	=	=	=
10830		1.4-2	0.37	0.54	0.59	0.66	=	=	=	=
304		4.7	1.7+2	5.0+2	6.1+2	9.3+2	=	=	=	=
228		4.5-4	1.6-2	4.8-2	5.9-2	9.0-2	=	=	=	=

Table II-5

OPTICAL THICKNESS - 1000 KM LAYER

$T_e = 2 \times 10^4$ °K

ORIGINAL PAGE IS OF POOR QUALITY

ANSITION	n_e	T	Case 1	2	3	4	5	6	7	8
	10^{10}									
584		1.7+3	3.4	0.92	0.52	=	=	=	7.0-3	=
504		0.36	7.2-4	1.9-4	1.1-4	=	=	=	1.5-6	=
5876		1.7-3	1.8-3	1.7-3	=	=	=	=	9.6-4	=
10830		1.6-2	1.7-2	1.6-2	=	=	=	=	9.3-3	=
304		1.5+3	2.8+3	=	=	=	=	=	2.0+3	=
228		0.10	0.19	=	=	=	=	=	0.13	=
	10^{11}									
584		2.0+4	2.2+2	61.	26.	=	=	=	1.0	=
504		5.7	6.3-2	1.7-2	7.4-3	=	=	=	2.9-4	=
5876		4.3-2	0.11	=	=	=	=	=	3.3-2	=
10830		0.38	1.0	0.86	0.93	=	=	=	2.9-4	=
304		5.1+3	2.1+4	=	=	=	=	=	=	=
228		0.43	1.8	=	=	=	=	=	=	=
	10^{12}									
584		2.3+5	1.0+4	2.0+3	5.6+2	=	=	=	100.	=
504		65.	2.8	0.56	0.16	=	=	=	2.8-2	=
5876		0.90	4.3	4.0	3.1	=	=	=	1.0	=
10830		5.3	24.	22.	17.	=	=	=	=	=
304		3.3+4	2.0+5	=	=	=	=	=	=	=
228		2.7	16.	=	=	=	=	=	=	=
	10^{13}									
584		2.0+6	1.2+5	1.7+4	8.5+3	=	=	=	5.2+3	=
504		6.1+2	37.	5.2	2.6	=	=	=	1.6	=
5876		18.	63.	48.	38.	=	=	=	28.	=
10830		37.	1.3+2	90.	69.	=	=	=	52.	=
304		4.0+5	1.9+6	=	=	=	=	=	=	=
228		36.	170.	=	=	=	=	=	=	=
	10^{14}									
584		2.0+7	1.2+6	3.8+5	3.0+5	=	=	=	2.6+5	=
504		5.8+3	350.	110.	87.	=	=	=	75.	=
5876		2.8+2	7.7+2	5.4+2	5.1+2		=	=	4.8+2	=
10830		[illegible]	8.8+2	5.8+2	5.4+2		=	=	5.1+2	=
304		5.1+6	1.9+7	=	=	=	=	=	=	=
228		450.	1.7+3	=	=	=	=	=	=	=

Table II-6

OPTICAL THICKNESS - 1000 KM LAYER

$T_e = 3 \times 10^4$ °K

TRANSITION	n_e	T	Case 1	2	3	4	5	6	7	8
	10^{10}									
584		23.	=	22.	21.	2.5-2	5.2-3	2.7-3	1.7-5	1.6-5
504		8.4-3	=	=	8.2-3	1.0-6	2.0-7	1.0-7	5.9-6	6.0-11
5876		1.3-3	=	=	1.2-3	7.7-4	7.0-4	=	4.3-6	3.2-6
10830		1.2-2	=	=	1.1-2	7.2-3	6.5-3	6.4-3	4.0-5	3.0-5
304		1.6+3	=	=	=	=	=	=	10.	=
228		0.18	=	=	0.17	=	=	=	1.1-3	=
	10^{11}									
584		6.3+2	=	=	=	2.0	0.43	0.15	8.8-3	2.6-4
504		0.19	=	=	=	7.2-4	1.5-4	5.0-5	3.2-6	1.0-7
5876		6.8-2	=	=	=	5.2-2	4.5-2	=	2.9-3	8.2-5
10830		0.57	=	=	=	0.43	0.37	=	2.4-2	7.0-5
304		1.6+4	=	=	=	=	=	=	1.0+3	=
228		1.7	=	=	=	=	=	=	0.10	=
	10^{12}									
584		7.3+3	=	=	=	62.	9.6	2.5	1.0	0.13
504		2.6	=	=	=	.22	3.4-3	8.9-4	3.6-4	4.6-5
5876		1.5	=	=	=	1.4	=	1.1	0.42	0.15
10830		6.8	=	=	=	6.2	5.9	4.7	1.8	0.63
304		1.6+5	=	=	=	=	=	=	6.4+4	=
228		18.	=	=	=	=	=	=	7.0	=
	10^{13}									
584		4.8+4	=	=	=	6.5+2	76.	38.	32.	17.
504		17.	=	=	=	0.23	2.7-2	1.4-2	1.2-2	6.4-3
5876		22.	=	=	=	18.	15.	12.	10.	7.3
10830		32.	=	=	=	25.	19.	15.	13.	10.
304		1.6+6	=	=	=	=	=	=	1.4+6	=
228		1.8+2	=	=	=	=	=	=	1.5+2	=
	10^{14}									
584		3.1+5	3.3+5	3.7+5	=	5.9+3	1.8+3	1.4+3	=	1.1+3
504		1.2+2	=	1.3+2	=	2.3	0.69	0.48	=	0.38
5876		2.0+2	=	2.4+2	=	1.9+2	1.4+2	1.3+2	=	1.2+2
10830		2.6+2	=	2.1+2	=	1.7+2	1.2+2	1.1+2	=	1.0+2
304		1.5+7	=	=	=	1.6+7	=	=	=	=
228		1.8+3	=	=	=	=	=	=	=	=

Table II-7

OPTICAL THICKNESS - 1000 KM LAYER

$T_e = 4 \times 10^4$ °K

ORIGINAL PAGE IS OF POOR QUALITY

TRANSITION	n_e	T	Case 1	2	3	4	5	6	7	8
	10^{10}									
584		1.9	=	1.5	0.37	1.9-4	1.0-7	1.7-8	8.5-9	5.5-11
504		7.6-4	=	4.5-4	1.5-4	7.6-8	4.0-11	6.8-12	3.4-12	2.2-14
5876		8.3-4	=	6.4-4	1.6-4	1.6-8	1.4-8	1.2-8	=	6.6-9
10830		7.7-3	=	5.9-3	1.5-3	7.7-7	1.3-7	1.0-7	=	6.0-8
304		1.5+3	=	1.2+3	2.9+2	2.9-2	=	=	=	=
228		0.18	=	0.11	.035	3.5-6	=	=	=	=
	10^{11}									
584		40.	38.	33.	15.	6.7-3	4.3-5	8.0-6	2.7-7	4.7-9
504		1.7-2	=	1.5-2	7.0-3	2.8-6	1.8-8	3.4-9	1.1-10	2.0-12
5876		0.32	0.31	0.27	0.13	5.6-6	=	3.8-6	=	1.2-6
10830		0.26	0.25	0.21	0.11	4.5-5	=	3.9-5	=	1.3-5
304		1.4+4	=	1.3+4	7.6+3	2.8	=	=	=	=
228		1.8	=	1.6	0.81	3.6-4	=	=	=	=
	10^{12}									
584		4.2+2	4.1+2	3.7+2	2.5+2	0.82	8.1-3	1.1-3	2.5-4	3.3-5
504		0.17	=	0.15	0.11	3.4-4	3.4-6	4.7-7	1.2-7	1.4-8
5876		0.69	0.67	0.61	0.41	1.4-3	=	=	1.1-3	4.0-4
10830		2.6	2.5	2.3	1.5	5.0-3	=	4.9-3	4.0-3	1.4-3
304		1.5+5	1.4+5	1.3+5	8.7+4	2.9+2	=	=	=	=
228		18.	17.	16.	11.	3.6-2	=	=	=	=
	10^{13}									
584		2.7+3	2.5+3	2.3+3	1.6+3		0.80	0.10	4.5-2	2.0-2
504		1.0	0.92	0.84	0.68	2.2-2	2.1-4	3.6-5	1.8-5	7.7-6
5876		9.1	8.7	8.0	5.6	0.19	0.16	0.13	0.10	8.0-2
10830		11.	10.	9.2	6.5	0.22	0.19	0.14	0.12	8.5-2
304		1.5+6	1.4+6	1.2+6	8.8+5	3.0+4	=	=	=	=
228		180.	170.	160.	100.	3.6	=	=	=	=
	10^{14}									
584		2.1+4	2.0+4	1.7+4	1.2+4	3.1+3				9.0
504		8.4	7.8	6.4	3.0	0.77	1.3-2	4.0-3	3.2-3	2.2-3
5876		90.	85.	84.	58.	15.	12.	10.	9.0	8.3
10830		76.	72.	62.	45.	11.	10.	7.0	6.6	6.0
304		1.4+7	=	1.2+7	9.0+6	2.3+6	=	=	=	=
228		1.8+3	1.7+3	1.4+3	1.2+3	3.0+2	=	=	=	=

Table II-8

OPTICAL THICKNESS - 1000 KM LAYER

$T_e = 5 \times 10^4$ °K

TRANSITION	n_e	Case T	1	2	3	4	5	6	7	8
	10^{10}									
584		0.35	0.21	4.2-2	3.5-3	2.1-7	-	-	-	-
504		1.5-4	9.0-5	1.8-5	1.5-6	9.0-11	-	-	-	-
5876		5.4-4	3.4-4	6.5-5	5.3-6	3.2-10	-	-	-	-
10830		4.9-3	3.0-3	6.0-4	5.0-5	3.0-9	-	-	-	-
304		1.3+3	7.8+2	1.6+2	13.	7.8-4	=	=	=	=
228		0.18	0.11	2.2-2	1.8-3	1.1-7	=	=	=	=
	10^{11}									
584		6.6	4.0	1.3	0.26	4.0-5	-	-	-	-
504		3.0-3	1.8-3	5.9-4	1.2-4	1.8-8	-	-	-	-
5876		1.8-2	1.1-2	3.6-3	7.2-4	1.1-7	-	-	-	-
10830		0.14	8.4-2	2.8-2	5.6-3	8.4-7	-	-	-	-
304		1.3+4	7.8+3	2.6+3	5.2+2	7.8-2	=	=	=	=
228		1.8	1.1	0.36	7.2-2	1.1-5	=	=	=	=
	10^{12}									
584		62.	37.	12.	3.1	3.7-3	-	-	-	-
504		3.0-2	1.8-2	5.8-3	1.5-3	1.8-6	-	-	-	-
5876		0.37	0.22	7.4-2	1.8-2	2.2-5	-	-	-	-
10830		1.2	0.75	0.24	6.0-2	7.2-5	-	-	-	-
304		1.3+5	7.8+4	2.6+4	6.5+3	7.8	=	=	=	=
228		18.	11.	3.6	0.90	1.1-3	=	=	=	=
	10^{13}									
584		4.1+2	2.4+2	82.	20.	0.25	4.0-3	4.5-4	2.3-4	9.0-5
504		0.18	0.11	3.6-2	8.8-3	1.1-4	1.8-6	2.0-7	1.0-7	4.0-8
5876		4.8	2.9	0.96	0.24	2.9-3	2.6-3	2.2-3	1.7-3	1.3-3
10830		4.9	2.9	1.0	0.25	2.9-3	2.6-3	2.1-3	1.7-3	1.3-3
304		1.3+6	7.8+5	2.6+5	6.5+4	7.8+2	=	=	=	=
228		180.	110.	36.	8.8	0.11	=	=	=	=
	10^{14}									
584		3.0+3	1.9+3	5.0+2	160.	19.	0.35	0.11	8.5-2	5.9-2
504		1.4	0.84	0.22	7.0-2	8.9-3	1.6-4	5.1-5	4.0-5	2.8-5
5876		47.	30.	7.8	2.4	0.29	0.25	0.20	=	=
10830		33.	21.	5.6	1.7	0.21	0.18	0.14	=	=
304		1.3+7	7.8+6	2.1+6	6.5+5	7.8+4	=	=	=	=
228		1.3+3	1.1+3	2.9+2	9.0+1	11.	=	=	=	=

Table II-9 ERROR IN D3 Line Intensity

He I - D 3 LINE

Te \ n_e (cm^{-3})	10^{10}	10^{11}	10^{12}	10^{13}	10^{14}
10^4 °K	1, 2, 4 20%	1, 2, 4 40%	1, 2, 4 50%	1, 2 40%	1, 2 25%
2×10^4 °K	T 20%	1, 4 5%	1, 4 20%	1, 4 25%	1 10%
3×10^4 °K	1, 4, 8 10%	4, 8 5%	4, 8 1%	4 30%	T 1%
4×10^4 °K	4, 7, 8 40%	4, 7, 8 5%	4, 7, 8 10%	4, 7, 8 10%	4, 7 10%
5×10^4 °K	4, 5, 6, 7, 8 50%	4, 5, 6, 7, 8 10%	4, 5, 6, 7, 8 15%	4, 5, 6, 7, 8 10%	4, 5, 6, 7 5%

NUMBER	1	2	3	4	5	6	7	8
RFS LINE	1ST He I	2ND He I	3RD He I	Ly-c He I	1ST He II	2nd He II	3RD He II	Ly-c He II

TABLE II.10

CHARACTERISTIC VALUES OF ϵ, η, ζ

T_e (^oK)	n_e (cm^{-3})	ϵ	η	ζ	Line (Å)	Case #
10^4	10^{10}	4.1-9	2.3-4	2.9-18	584	T
		"	"	5.1-14	"	3
		1.2-8	1.2-8	1.8-28	304	T
		"	"	"	"	3
	10^{14}	4.0-5	8.0-3	4.0-14	584	T
		"	"	8.3-13	"	3
		1.2-4	4.8-5	1.8-24	304	T
		"	"	"	"	3
2×10^4	10^{10}	1.1-8	2.3-4	6.1-13	584	T
		"	"	3.8-3	"	3
		8.2-9	1.2-8	2.5-18	304	T
		"	"	"	"	3
	10^{14}	1.1-4	2.2-2	6.4-9	584	T
		"	"	4.9-7	"	3
		8.2-5	5.8-5	2.5-14	304	T
		"	"	"	"	3
3×10^4	10^{10}	1.9-8	2.3-4	4.3-11	584	T
		"	"	"	"	3
		6.7-9	1.4-8	6.1-15	304	T
		"	"	4.2-9	"	3
	10^{14}	6.7-5	1.2-4	5.8-11	584	T
		"	"	1.4-8	"	3
		1.9-4	3.4-2	4.0-7	304	T
		"	"	"	"	3
4×10^4	10^{10}	2.8-8	2.3-4	3.9-10	584	T
		"	2.1-4	2.9-10	"	3
		5.8-9	1.6-8	3.1-13	304	T
		"	"	4.7-7	"	3

TABLE II.10(Continued)

$T_e(^oK)$	n_e (cm^{-3})	ε	η	ζ	Line (Å)	Case #
	10^{14}	2.8-4	4.5-2	3.4-6	584	T
		"	"	"	"	3
		5.8-5	1.9-4	2.8-9	304	T
		"	"	1.9-6	"	3
5×10^4	10^{10}	3.8-8	2.3-4	1.6-9	584	T
		"	2.0-4	9.0-10	"	3
		5.2-9	1.9-8	3.4-12	304	T
		"	"	8.1-6	"	3
	10^{14}	3.8-4	2.7-4	3.0-8	304	T
		"	5.8-2	"	"	3
		5.2-5	2.7-4	3.0-8	304	T
		"	"	2.7-5	"	3

for our assumed Doppler line profile. (For the continuum we require $\tau > \zeta^{-1/2}$ where ζ is the ratio of collisional to radiative recombination.)

Some representative values of the parameters ϵ and η (and ι) for the 584 and 304Å lines are given in Table II.10. Values were obtained for each temperature at $n_e = 10^{10}$ and 10^{14} for the optically thin case and case 3 given in Table II.3. We can see from the optical depth tables that under many conditions the layer is effectively optically thin, i.e.

$$1 < \tau \leq (\epsilon + \eta)^{-1} \quad .$$

In this case the total energy emitted in the line from the surface of a layer of optical thickness t_1 is given approximately by

$$E \sim 2\sqrt{\pi}\ (\epsilon + \iota^*)\ t_1$$

where $\iota^* = \iota/B$.

The values of η and ι vary with optical depth and an integration over depth is required to obtain the total line intensity from the layer.

Using the optical depth tables and estimates of η and ι from code 1 we have obtained approximate solutions for some line intensities. The lines chosen are the 584, 537, 304Å lines and the D3 line. Figures II.30-34 give results as a function of T_e for various n_e while Figures II.35-39 show the variation with n_e for various T_e. We note a considerably different variation with T_e and n_e for the D3, 584 and 304Å line emission. These different variations give some confidence that simultaneous emission measurements of the three lines could yield unique temperatures and densities from the emitting region.

Figure II-30 TOTAL LINE EMISSION

$n_e = 10^{10}$ (cm^{-3})

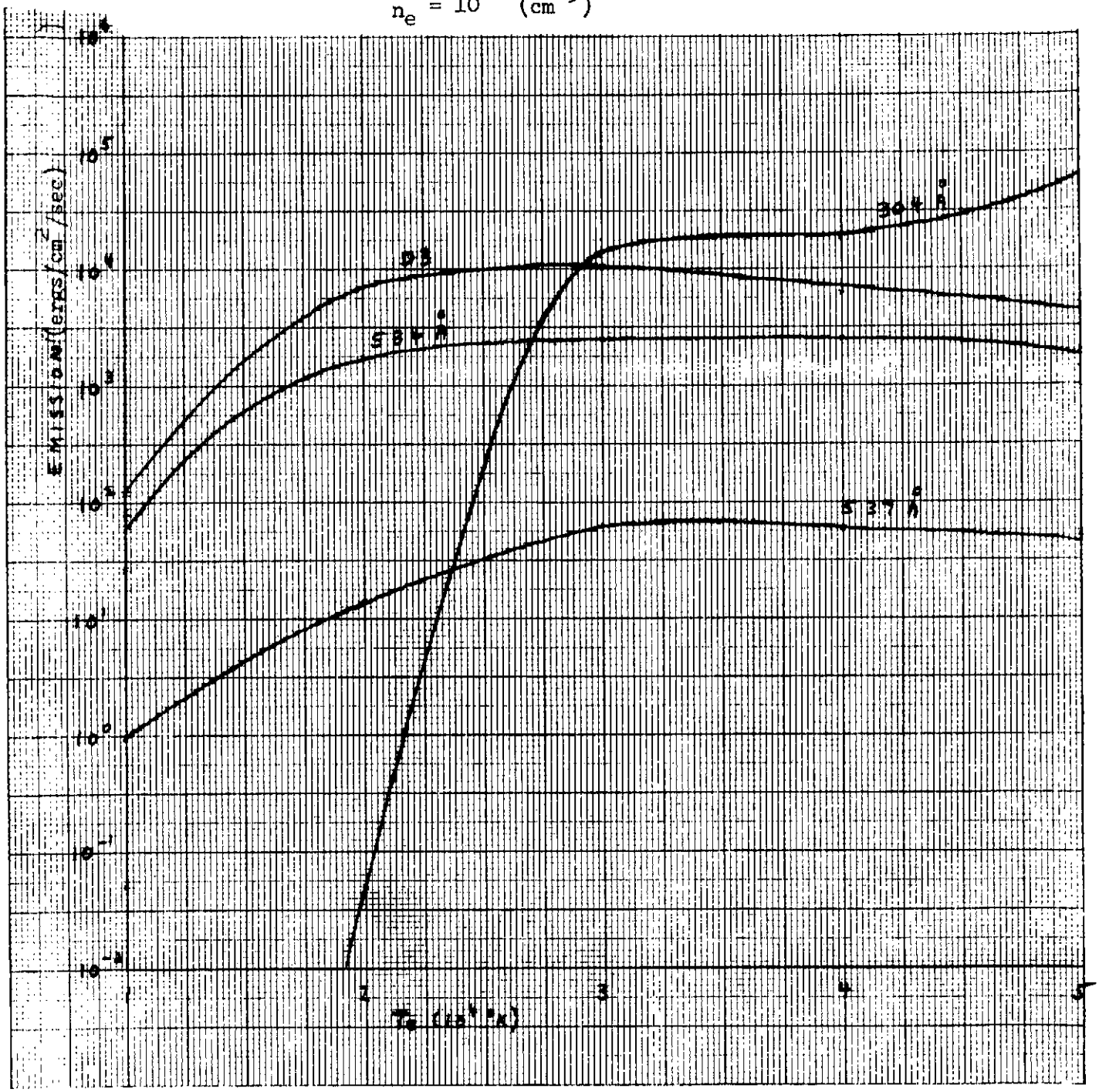

Figure II-31 TOTAL LINE INTENSITY

$n_e = 10^{11}$ (cm^{-3})

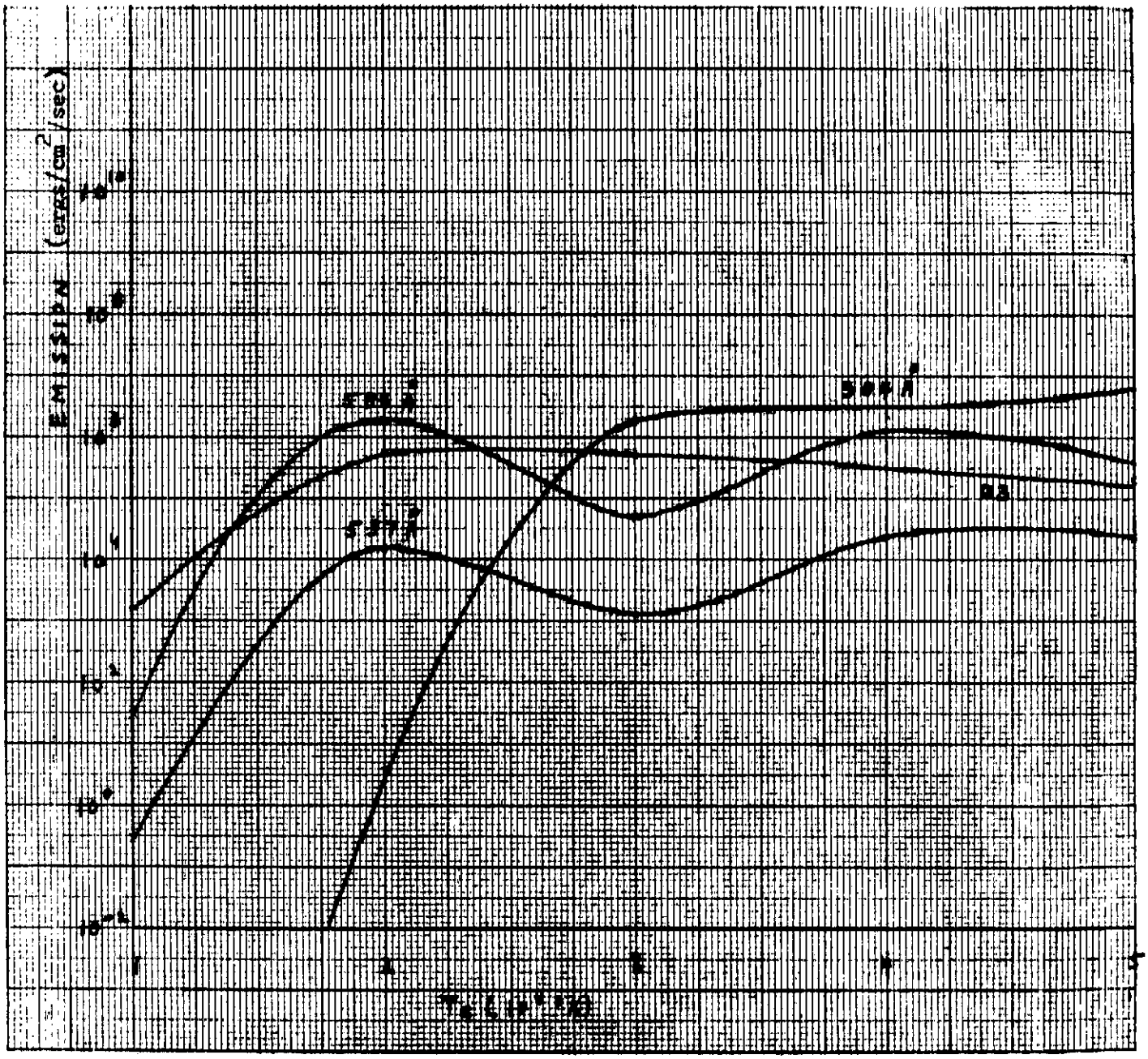

Figure II-32 TOTAL LINE EMISSION

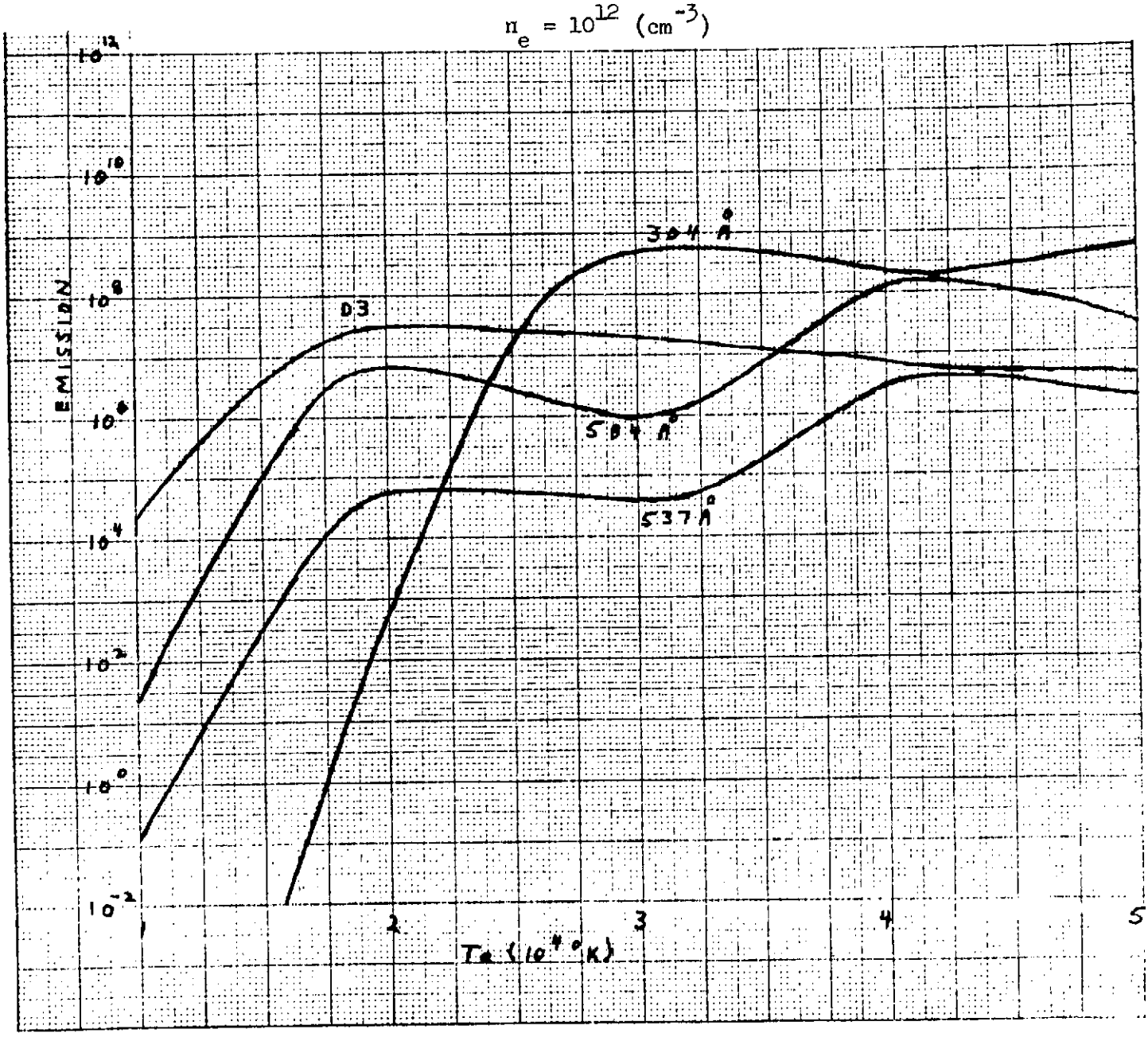

Figure II-33 TOTAL LINE EMISSION

$n_e = 10^{13}$ (cm^{-3})

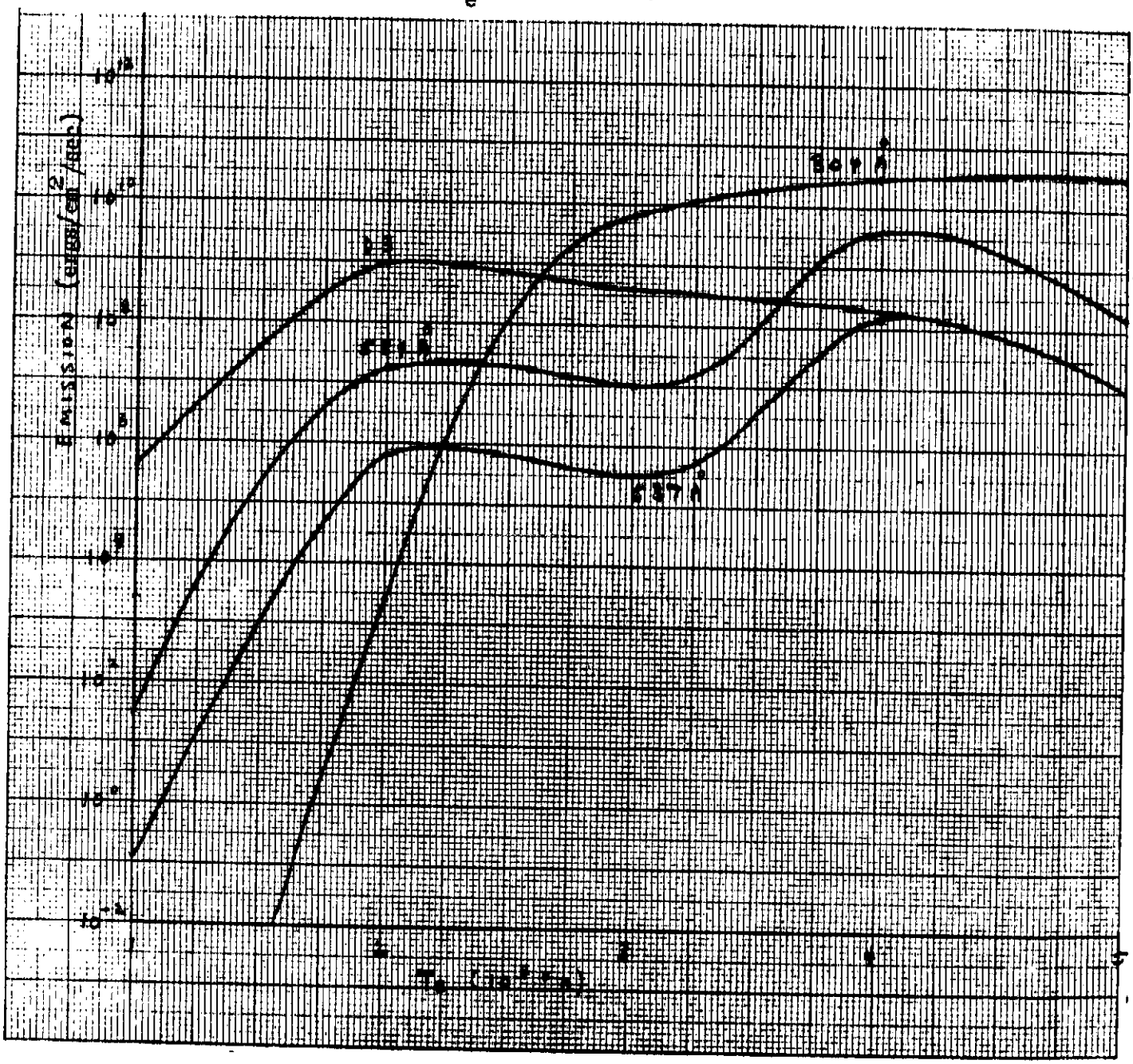

Figure II-34 TOTAL LINE EMISSION

$n_e = 10^{14}$ (cm^{-3})

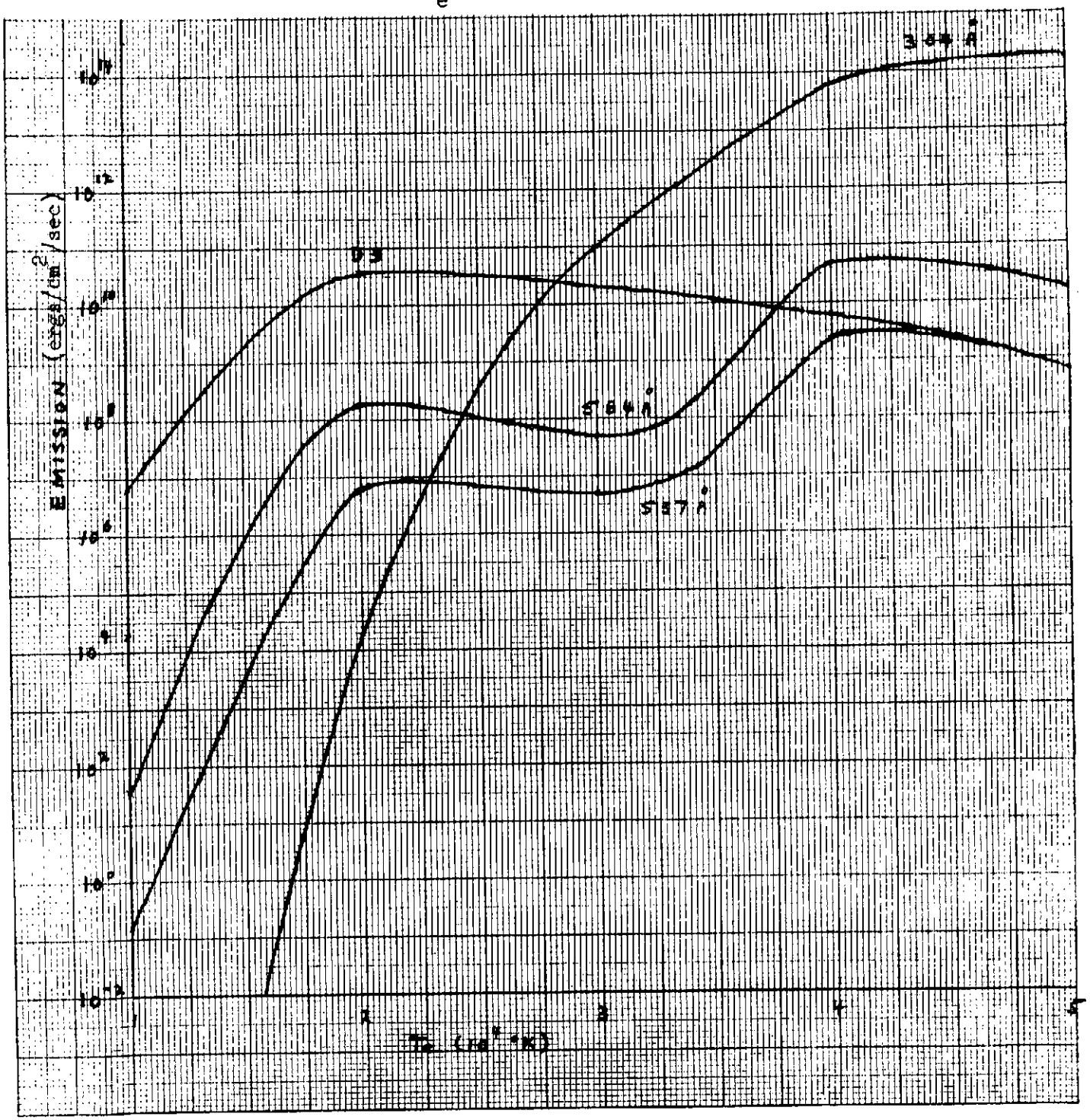

Figure II-35 TOTAL LINE EMISSION

$T_e = 10^4$ °K

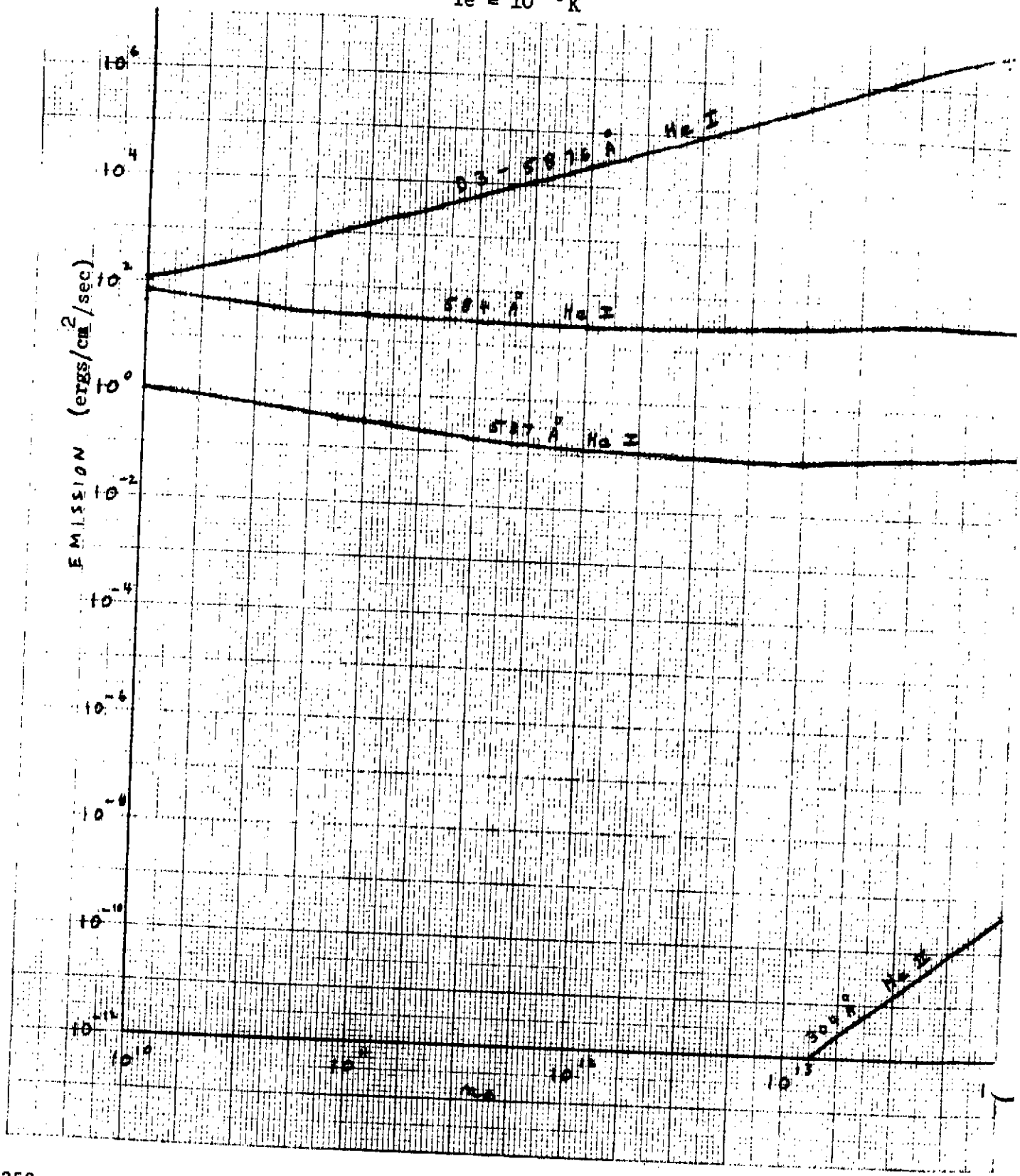

Figure II-36 TOTAL LINE EMISSION

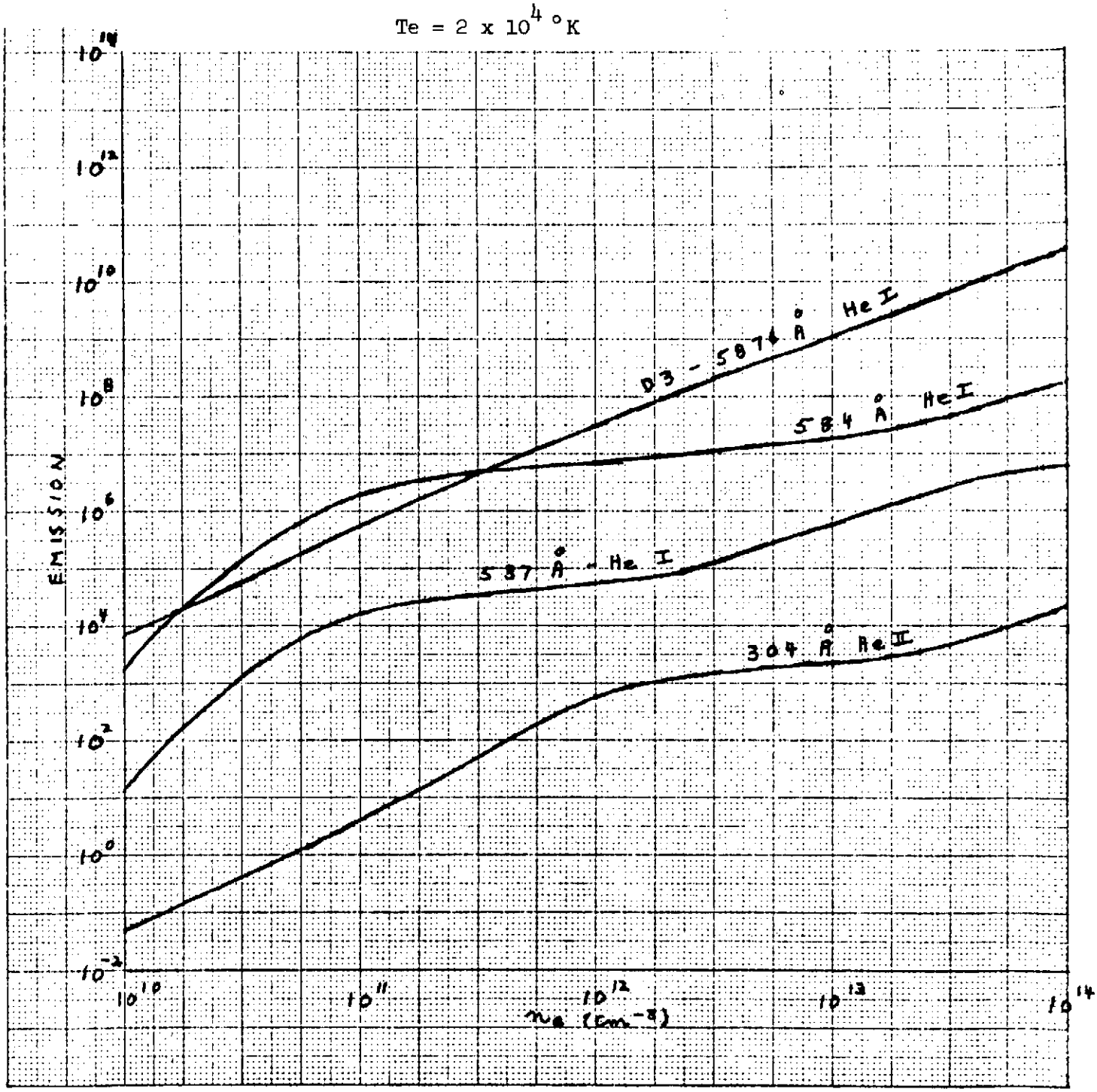

Figure II-37 TOTAL LINE EMISSION

$T_e = 3 \times 10^4\ ^\circ K$

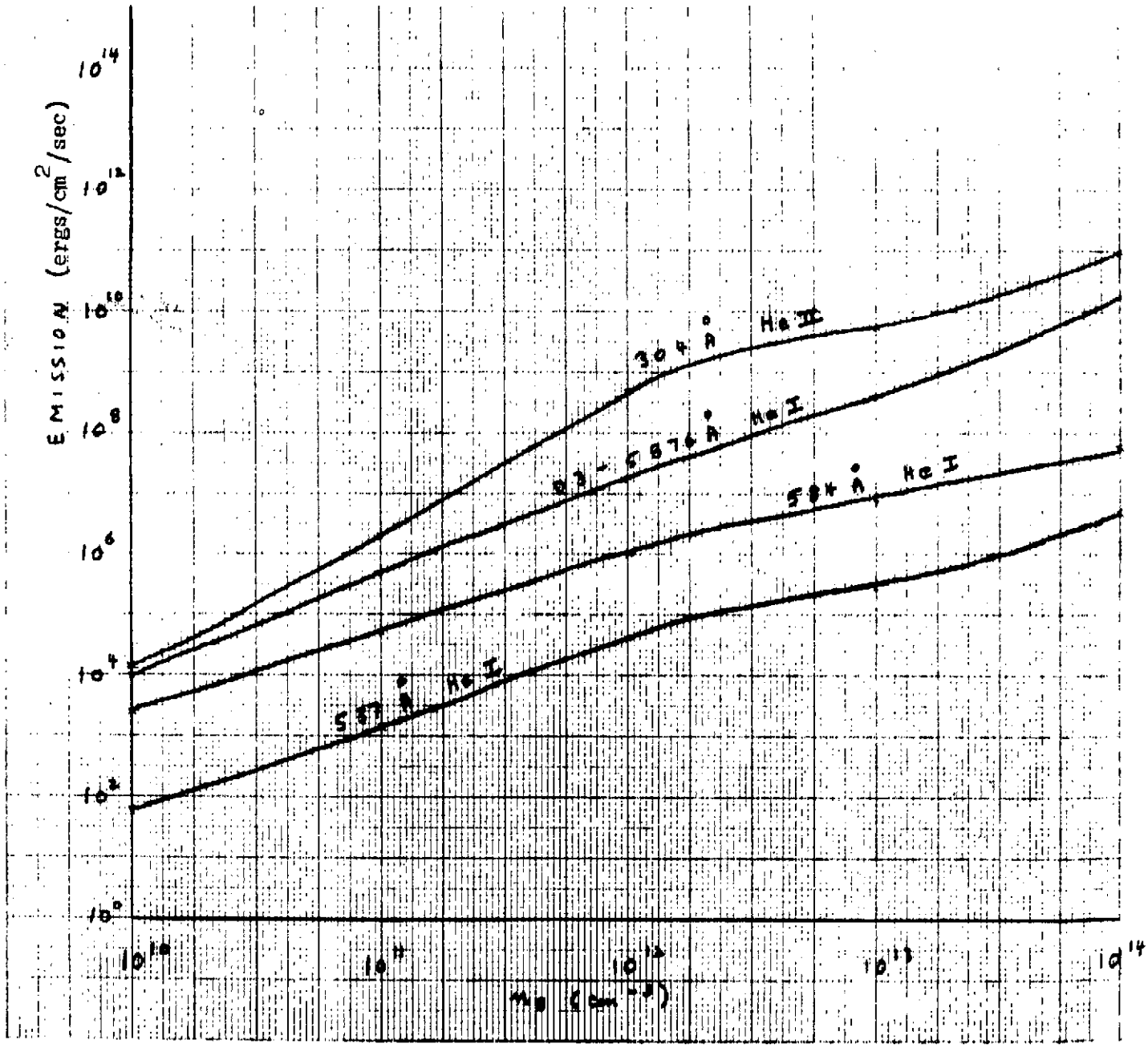

Figure II-38 TOTAL LINE INTENSITY

$Te = 4 \times 10^4\ ^\circ K$

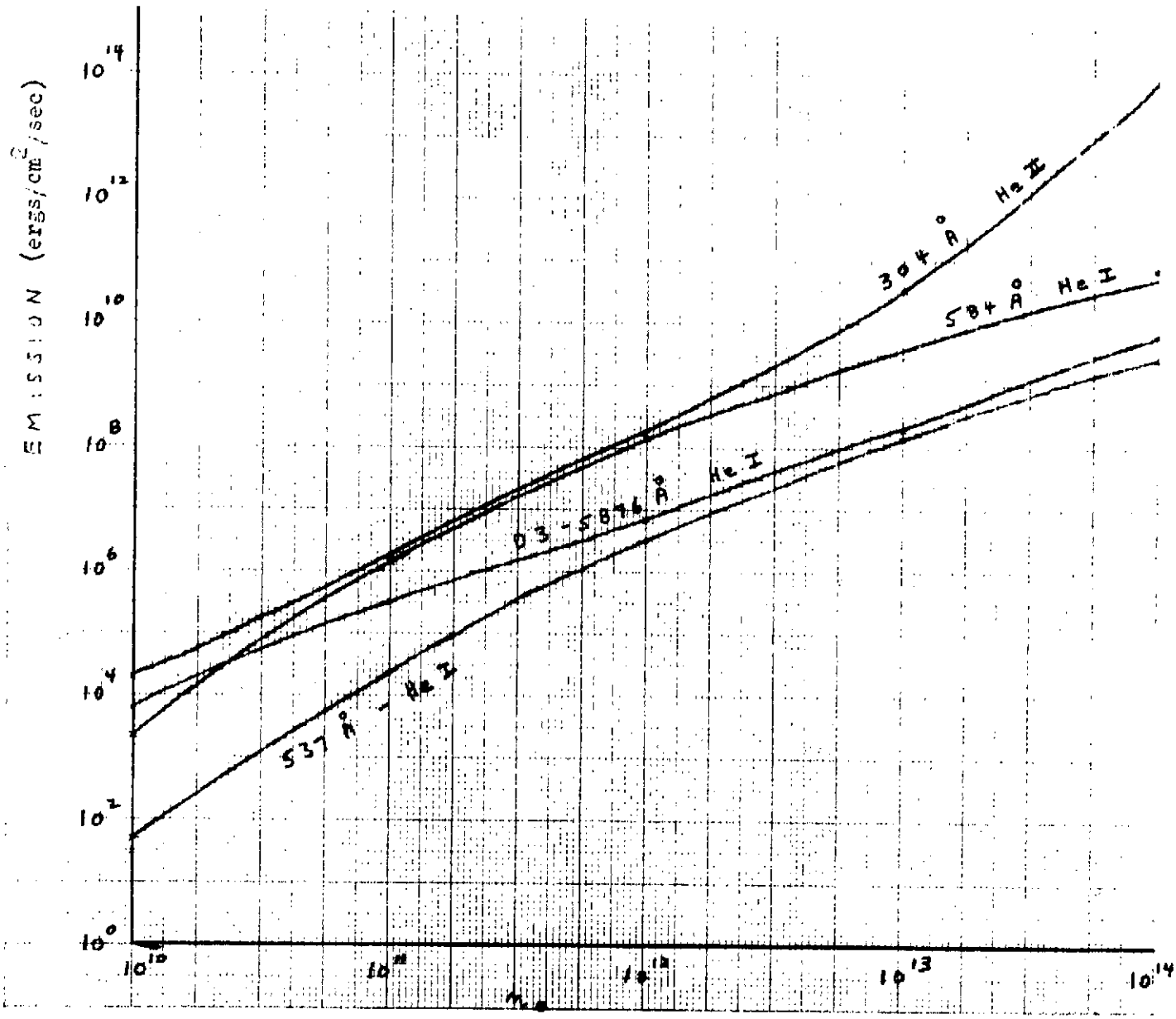

ORIGINAL PAGE IS
OF POOR QUALITY

Figure II-39 TOTAL LINE EMISSION

Te = 50,000° K

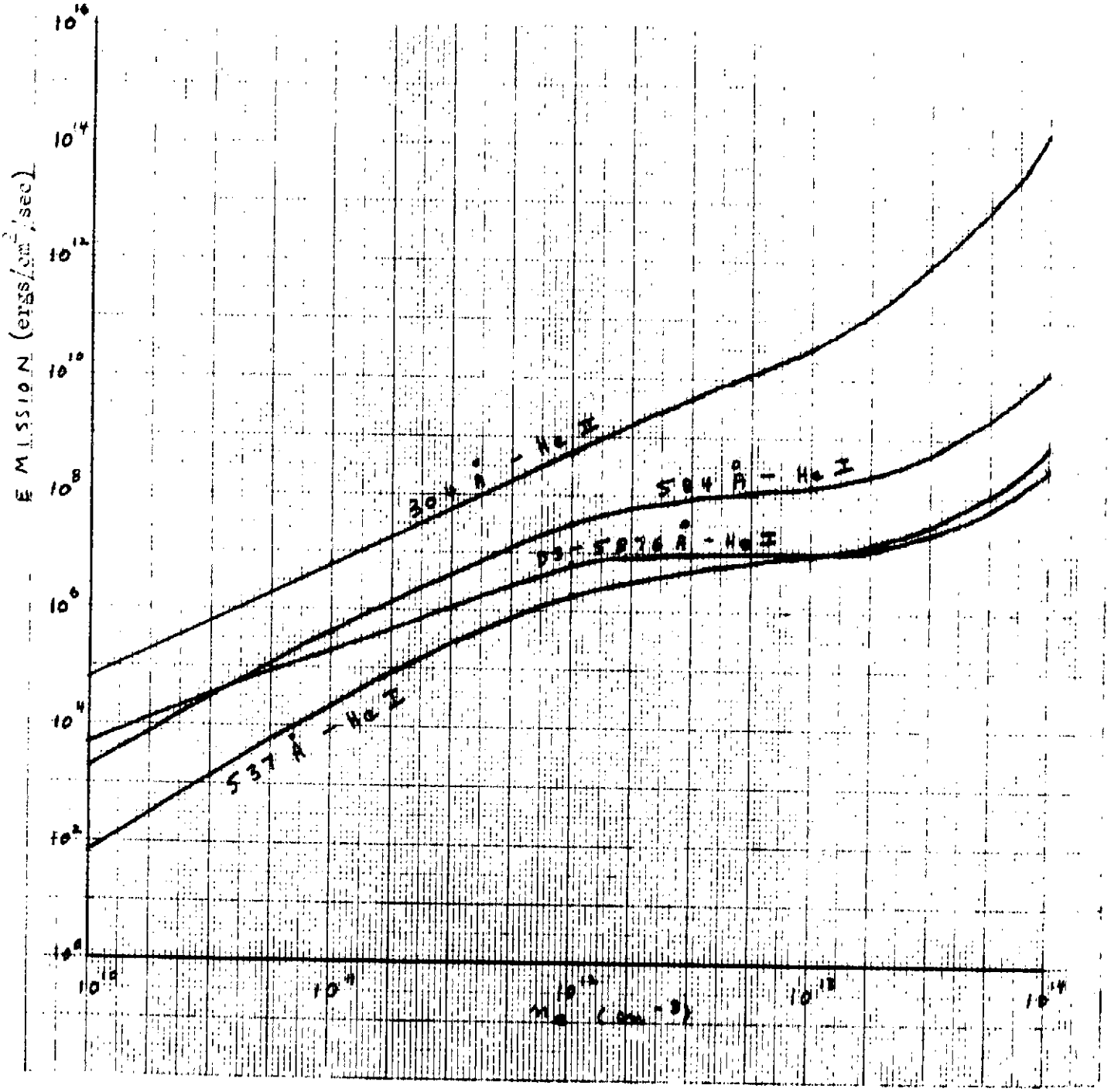

4. Population Rates

It is very instructive to look at the various processes involved in populating and depopulating the upper radiating levels. In other words, to determine the exact processes contributing significantly to the terms η and ϵ in the transport equation. One way to do this is to assume a 3 or 4 level atom and evaluate η and ϵ from the analytic solution choosing different levels for the 3rd or 4th levels. This would give us an approximate answer. Another way is to use the complete solution of the statistical equilibrium equations for the populations to evaluate the rates directly into the upper and lower levels of the lines in question.

Solutions of the full SSS equations were used in obtaining the relative rate processes shown in Figs. II-40 and II-41. Fig. II-40 illustrates the processes populating the 584Å line upper level at $T_e = 40{,}000^{\circ}K$ for various electron densities. Four processes always enter significantly. The largest of these is photoexcitation from the 2^1S level by absorption of photospheric radiation. Direct collisional excitation from the ground state is next, followed by collisional excitation from the 2^3S and radiative decay from the 3^1D. Hence, both the photospheric radiation and coupling to the triplet levels are important.

Fig. II-41 shows relative processes populating the D3 line upper level for the same electron temperature and densities. A much stronger dependence on n_e is noted. Photoabsorption of photospheric radiation in the D3 line itself is the dominant mechanism at low n_e. At high n_e, this process is small and the collisional rate from the 3^1D is dominant with collisional excitation from the 3^3P and 2^3S levels also being significant. Thus, the triplet - singlet interaction is again very important.

Figure II-40 RELATIVE PROCESSES POPULATING 2'P LEVEL OF He I

Te = 40,000°K

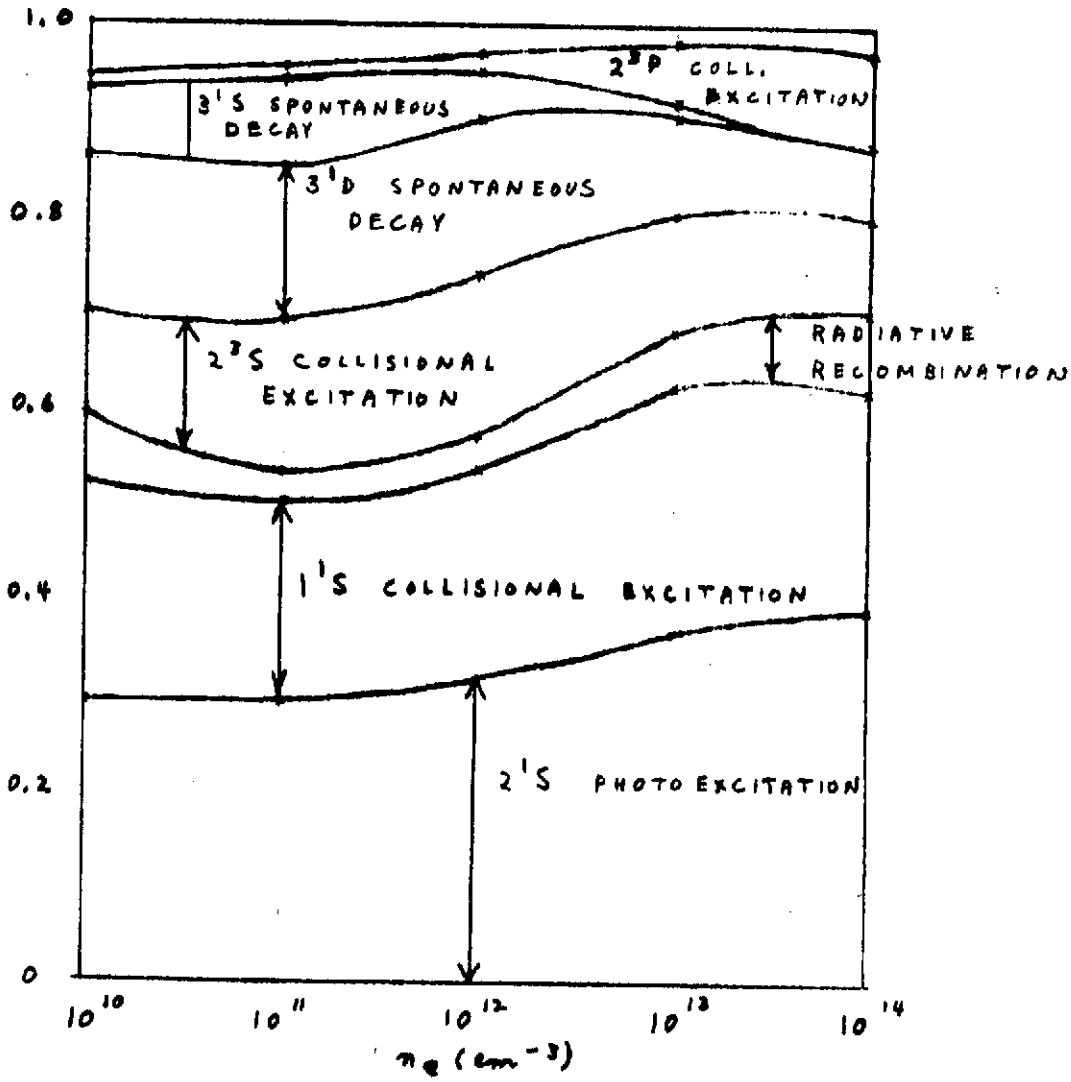

Figure II-41 RELATIVE RATES OF PROCESSES POPULATING THE 3^3 D LEVEL OF He I

Te = 40,000° K

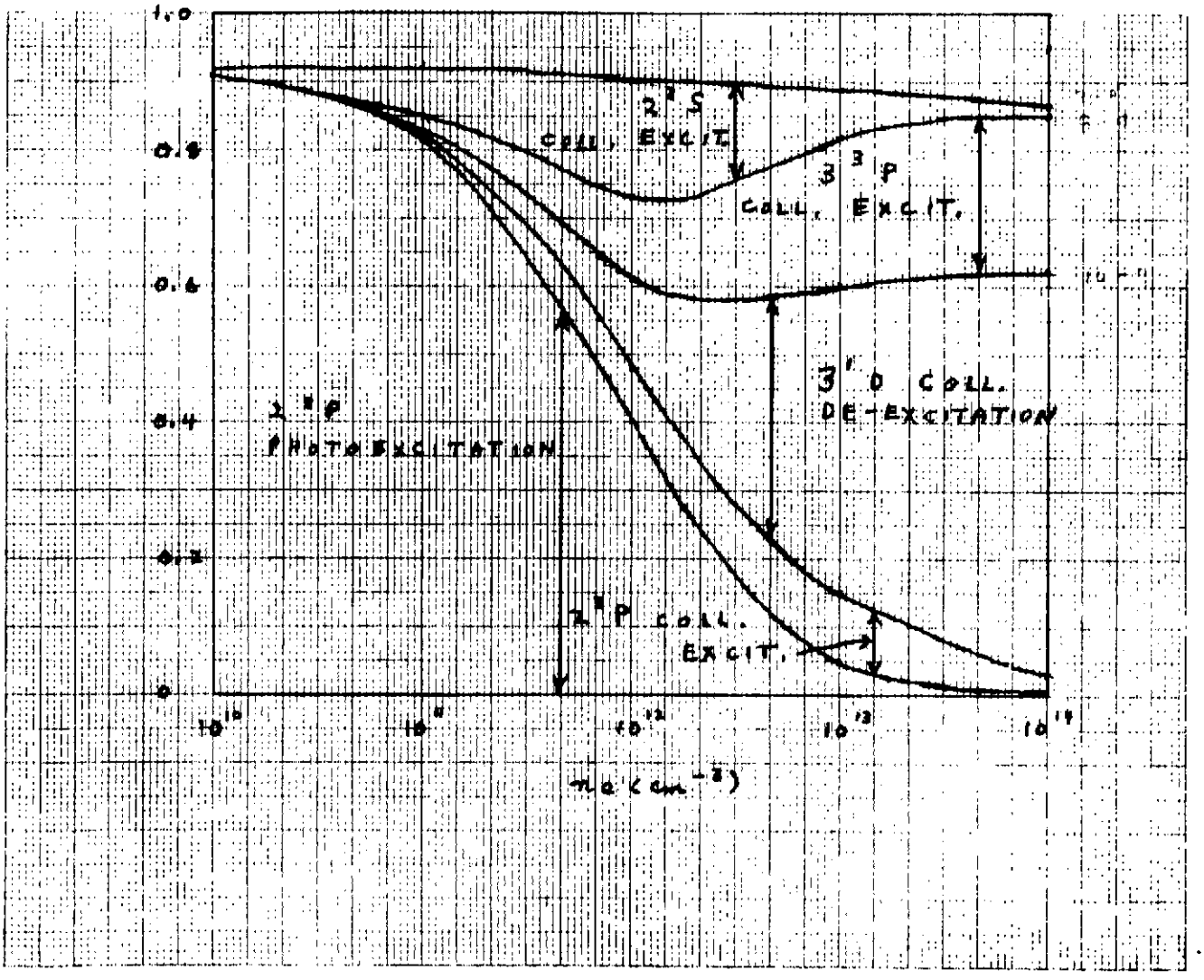

III. LINE TRANSPORT SOLUTION

A. Basic Equations

The solution of the line transport equation that we have used in the code developed (Code 2) is an iterative solution of the integral equation. The details of the method have been developed by Avrett and Loeser (1969) in a manner convenient for the simultaneous solution of both line and continuum transport equations. From Section II.D, we note that solution for the line and continuum radiation field simultaneously is necessary. We will only briefly summarize the method and equations in this report.

In the statistically steady state the rate equation describing the population n_i of the state i is

$$\sum_{j\neq i} (n_j P_{ji} - n_i P_{ij}) = \sum_j n_j P_{ji} = 0$$

$$P_{ii} = -\sum_{j\neq i} P_{ij}, \qquad \text{III.1}$$

where P_{ij} is the total transition rate from i to j per second per particle in the i state. In general, $P_{ij} = R_{ij} + C_{ij}$, where R_{ij} and C_{ij} represent the radiative and collisional transition rates respectively. We shall assume a Maxwellian distribution for the electrons and helium particles and since we also assume a known external radiation field, the transitions involving the continuum can be represented by a single term in Eq. III.1. We can characterize the system of linear equations III.1 by a matrix whose coefficients a_{ij} are equal to P_{ji}. In representing matrix elements and co-factors thereof, we shall always let the first subscript refer to the row and the second to the column. Because of the definition of the transition rate the subscripts of the P's will be reversed when substituted for the matrix elements a. The general solution of Eq. III.1 is

$$n_i = \lambda_m P^{mi} \; ; \qquad \lambda_m = \frac{N}{\sum_j P^{mj}} , \qquad \text{III.2}$$

where P^{mj} is the co-factor of the element $a_{mj} = P_{jm}$ in the coefficient matrix represented by the i equations of type III.1 and N is the total number of helium particles per cm^3. The matrix of coefficients has the property that the co-factor of all the elements in a column are equal, i.e. P^{mj} is independent of m.

When the medium becomes optically non-thin for certain frequencies the radiation field producing internal excitation and ionization for these frequencies is no longer merely the external radiation field but is partly dependent on the internal properties of the gas and must be determined from the radiative-transfer equation

$$\mu \frac{dI_\nu}{d\tau_\nu} = I_\nu - S_\nu, \qquad \text{III.3}$$

where $\cos^{-1}\mu$ represents the angle between the direction of propagation and the outward normal z and $\tau_\nu = \int k_\nu \, dz$, S_ν is the source function, k_ν is the linear absorption coefficient and I_ν is the specific intensity of the radiation. In LTE $S_\nu = B_\nu$, however in the non-LTE case S_ν must be specified in terms of microscopic processes. In terms of such processes the transfer equation governing the spectral line between upper level u and lower level I may be written as

$$- 4\pi\mu \frac{dI_\nu}{dz} = [n_l B_{lu} \Phi_\nu h\nu - n_u B_{ul} \psi_\nu h\nu + 4\pi k_c] \, I_\nu \qquad \text{III.4}$$

$$- n_u A_{ul} j_\nu h\nu - 4\pi k_c S_c(T_e),$$

where k_c represents the continuum absorption coefficient at frequency ν_o and S_c is the continuum source function. B_{lu}, B_{ul} and A_{ul} are the Einstein transition probabilities for absorption, stimulated emission and spontaneous emission. j_ν, ψ_ν and Φ_ν are the normalized emission, stimulated emission and absorption coefficients within the line defined such that

$$\int_0^\infty \Phi_\nu d\nu = \int_0^\infty \psi_\nu d\nu = \frac{1}{4\pi} \int_{4\pi} \int_0^\infty j_\nu d\nu \, d\omega = 1.$$

The continuum absorption coefficient is generally very small compared with the line absorption coefficient near the line center and will be neglected in determining the source function within the line. Using the standard relations between the Einstein coefficients and assuming $j_\nu = \Phi_\nu = \psi_\nu$, the source function becomes

$$S_{ul} = \frac{2h\nu^3}{c^2} \frac{1}{[(g_u/g_l)(n_l/n_u)]-1}, \qquad \text{III.5}$$

where g represents the statistical weight. The minus one term in the denominator represents stimulated emissions.

In evaluating the radiative excitation rate R_{ij} for transitions between bound levels the line radiation field enters as

$$\int_0^\infty J_\nu(\tau)\, \Phi_\nu(\tau)\, d\nu = \bar{J}(\tau)$$

where

$$J_\nu(\tau) = \frac{1}{4\pi} \int_{4\pi} I_\nu(\tau,\mu)\, d\omega$$

is the mean intensity and $d\omega$ represents the solid angle. It is thus convenient to formulate the transfer equation in terms of J_ν rather than I_ν. It is now convenient to separate those components involving the unknown radiation field, J_{ul}, from the co-factors. This is done by expanding the determinant P^{ij} in terms of its co-factors Q^{ij}. Thus

$$P^{lu} = \sum_{k\neq l} P_{lk}Q^{kl} = P_{lu}Q^{ul} + \sum_{k\neq l\neq u} P_{lk}Q^{kl}$$

$$P^{ul} = \sum_{k\neq u} P_{uk}Q^{ku} = P_{ul}Q^{lu} + \sum_{k\neq u\neq l} P_{uk}Q^{ku}. \qquad \text{III.6}$$

Actually, J_{ul} may appear in many of the co-factors since the line u-l may fall in the ionization continuum of some other transition. The influence of J_{ul} as well as the line radiation in general on the bound-free radiative rates will be neglected. Using the standard relationship between the

Einstein coefficients, equation III.6, and remembering that $Q^{ul} = Q^{lu}$ and $A_{lu} = B_{lu} \int J_\nu \Phi_\nu d\nu$ the source function may be written as

$$S_{ul} = \rho_{ul} \frac{P^{lu}}{P^{ul}} = \frac{\int_{ul} J_\nu \Phi_\nu d\nu + \epsilon B + \zeta}{1 + \epsilon + \eta} \qquad \text{III.7}$$

where B is the Planck function

$$B_\nu (T_e) = \rho_{ul} \frac{C_{lu}}{C_{ul}}$$

$$\epsilon = \frac{C_{ul}}{A_{ul}} \qquad \rho_{ul} = \frac{2h\nu^3}{c^2} \frac{g_l}{g_u}$$

$$\zeta = \rho_{ul} \frac{1}{A_{ul} Q^{ul}} \sum_{k \neq u \neq l} P_{lk} Q^{kl} \qquad \text{III.8}$$

$$\eta = \frac{1}{A_{ul} Q^{ul}} \sum_{k \neq u \neq l} P_{uk} Q^{ku}.$$

The terms entering the numerator of Eq. III.7 each represent a method of populating the upper level from the lower level. The first term represents direct radiative excitation, the second direct collisional excitation and the third any combination of radiative or collisional processes involving one or more intermediate levels in going from the lower to the upper level. The denominator, on the other hand, consists of terms indicating transition paths from the upper to the lower level. All the terms are normalized with respect to A_{21}. The first term represents direct radiative de-excitation, the second direct collisional de-excitation and the third any indirect process going from the upper to the lower state.

Equation III.7 is solved using a discrete ordinate method for the frequency integral in which we assume

$$\int_0^\infty F(x)dx = \sum_{k=1}^{K} A_k F_k. \qquad \text{III.9}$$

The coefficients are to be found from a given set of dimensionless frequency values x_k, $k = 1,2...K$; F_k is the value of F at $x = x_k$. The solution for A_k is given in Section III.C.

We shall assume Φ_ν to be Gaussian, i.e.

$$\Phi_\nu = \frac{\exp(-v^2)}{(\pi)^{1/2}\Delta\nu_D}; \quad v = \frac{\Delta\nu}{\Delta\nu_D}. \qquad \text{III.10}$$

$\Delta\nu_D$ is the Doppler half width given by

$$\frac{\nu_o}{c}\left(\frac{2kT}{M}\right)^{1/2} \qquad \text{III.11}$$

where M is the Helium particle mass.

The source function is obtained at N depth points (i = 1 --- N) within the assumed layer. The depth points are located at specified physical depths which do not change during the calculation. The values of S_i are obtained from the matrix equation

$$\sum_{j=1}^{N} M_{ij} S_j = C_i \qquad \text{III.12}$$

where i and j refer to depth points.

The coefficients M_{ij} are given by

$$M_{ij} = \Delta_{ij} - \frac{1}{1+\epsilon_i'} \bar{W}_{ij}^{(\Lambda)} \qquad \text{III.13}$$

where

$$\Delta_{ij} = \begin{cases} 1, & j = i \\ 0, & j \neq i \end{cases}$$

$W_{ij}^{(\Lambda)}$ are weighting functions, ϵ' is a coupling parameter.

C_j are given by

$$C_j = \frac{\epsilon'_i}{1+\epsilon'_i} B_i^S - \frac{1}{1+\epsilon'_i} \sum_{j=1}^{N} w_{ij}^{(\Lambda)} S_j^c \quad . \qquad \text{III.14}$$

In these equations, B_i^S is a coupling parameter,

$$\bar{W}_{ij}^{(\Lambda)} = \frac{2}{\sqrt{\pi}} \sum_{k=1}^{K} A_k W_{ijk}^{(\Lambda)} \frac{\phi_{ik} \phi_{jk}}{\phi_{ik}+r_j} \qquad \text{III.15}$$

and

$$w_{ij}^{(\Lambda)} = \frac{2}{\sqrt{\pi}} \sum_{k=1}^{K} A_k W_{ijk}^{(\Lambda)} \frac{\phi_{ik} r_j}{\phi_{jk}+r_j} \qquad \text{III.16}$$

where k refers to a specific frequency, A_k are weighting functions. The profile function ϕ_{ik} is simply

$$\phi_{ik} = e^{-v_k^2} \quad .$$

The optical depth values τ_{ik} are given by

$$\tau_{ik} = \int_0^{\tau_i} (\phi_{ik}+r_i)\, d\tau \quad .$$

$$d\tau = k^L dz$$

$$k^L = \frac{h\nu_0}{4\pi^{3/2} \Delta\nu_D} n_1 B_{12} \quad .$$

The weighting coefficients $W_{ijk}^{(\Lambda)}$ represent an expansion of the mean intensity $J_\nu(\tau_{\nu i})$ in terms of the source function $S_\nu(\tau_{\nu j})$

$$J_\nu(\tau_{\nu i}) = \sum_{j=1}^{N} W_{ijk}^{(\Lambda)} S_\nu(\tau_{\nu j}) \qquad \text{III.17}$$

Substituting the solution of the radiative transport equation for J_ν we obtain

$$\frac{1}{2}\int_0^{T_1} E_1(|t-\tau_i|)\, S(t)\, dt = \sum_{j=1}^{N} W_{ij}^{(\Lambda)} S(\tau_i) \qquad \text{III.18}$$

where the frequency subscript has been dropped. To evaluate $W_{ij}^{(\Lambda)}$ we assume that S_i is represented by linear segments between optical depth points n and n + 1. S(t) in the interval $n \le t \le \tau_{n+1}$ is given by

$$S(t) = S_n \left(\frac{\tau_{n+1} - t}{\tau_{n+1} - t_n}\right) + S_{n+1} \left(\frac{t - \tau_n}{\tau_{n+1} - \tau_n}\right) \qquad \text{III.19}$$

Equations for $W_{ij}^{(\Lambda)}$ are obtained by substituting Eq. IL19 into Eq. II.18. The $W_{ij}^{(\Lambda)}$ so obtained depend only on the set of τ_i values chosen. Different expressions for $W_{ij}^{(\Lambda)}$ are obtained for $j > i$, $j < i$, and $j = 1$. We give these expressions in order.

W_{ij}^{Λ} depends only on the coefficient of S_n

$$2\, W_{in} = \int_{\tau_{n-1}}^{\tau_n} E_1|t-\tau_i| \; \frac{(t-\tau_{n-1})dt}{\tau_n - \tau_{n-1}} + \int_{\tau_n}^{\tau_{n+1}} E_1|t-\tau_i| \; \frac{(\tau_{n+1} - t)}{\tau_{n+1} - \tau_n}\, dt. \qquad \text{III.20}$$

For $n > i$,

$$2\,W_{in} = \Big[\ \frac{\tau_i(E_2|\tau_{n-1}-\tau_i| - E_2|\tau_n-\tau_i|) + e^{-|\tau_{n-1}-\tau_i|} - e^{-|\tau_n-\tau_i|} + E_3|\tau_n-\tau_i| - E_3|\tau_{n-1}}{(\tau_n - \tau_{n-1})}$$

$$- \frac{\tau_{n-1}}{\tau_n - \tau_{n-1}}\,[E_2|\tau_{n-1}-\tau_i| - E_2|\tau_n-\tau_i|] + \frac{\tau_{n+1}}{\tau_{n+1}-\tau_n}\,[E_2|\tau_n-\tau_i| - E_2|\tau_{n+1}-\tau_i|\ ]$$

$$-\Big[\frac{\tau_i(E_2|\tau_n-\tau_i| - E_2|\tau_{n+1}-\tau_i|) + e^{-|\tau_n-\tau_i|} - e^{|\tau_{n+1}-\tau_i|} + E_3|\tau_{n+1}-\tau_i| - E_3|\tau_n-\tau_i|}{(\tau_{n+1}-\tau_n)}\Big].$$

III.21

For $n < i$,

$$2W_{in} = \frac{(\tau_i-\tau_{n-1})}{(\tau_n-\tau_{n-1})}\,[E_2(\tau_i-\tau_n) - E_2(\tau_i-\tau_{n-1})] + \frac{(\tau_{n+1}-\tau_i)}{(\tau_{n+1}-\tau_n)}\,[E_2(\tau_i-\tau_{n+1}) - E_2(\tau_i-\tau_n)]$$

$$+ [e^{-(\tau_i-\tau_{n+1})} - e^{-(\tau_i-\tau_n)} + E_3(\tau_i-\tau_n) - E_3(\tau_i-\tau_{n+1})]/(\tau_{n+1}-\tau_n)$$

$$- [e^{-(\tau_i-\tau_n)} - e^{-(\tau_i-\tau_{n-1})} + E_3(\tau_i-\tau_{n-1}) - E_3(\tau_i-\tau_n)]/(\tau_n-\tau_{n-1}).$$

III.22

For $i = n$,

$$2W_{in} = \frac{(\tau_i-\tau_{n-1})}{(\tau_n-\tau_{n-1})}\,[1-E_2(\tau_i-\tau_{n-1})] + \frac{(\tau_{n+1}-\tau_i)}{(\tau_{n+1}-\tau_n)}\,[1-E_2(\tau_{n+1}-\tau_i)]$$

$$- \frac{[1/2 - e^{-(\tau_i-\tau_{n-1})} + E_3(\tau_i-\tau_{n-1})]}{\tau_n - \tau_{n-1}} - \frac{[1/2 - e^{-(\tau_{n+1}-\tau_i)} + E_3(\tau_{n+1}-\tau_i)]}{\tau_{n+1} - \tau_n}$$

III.23

B. Evaluation of ϵ' and B^s

ϵ' and B^s appearing in Eqs. III.13 and III.14 are related to the source function parameters ϵ, η and ι as follows:

$$\epsilon' B^s = \epsilon B + \iota$$
$$\epsilon' = \epsilon + \eta \qquad \text{III.24}$$

where B is the Planck function. The values of ϵ' and B^s depend upon the levels included in the model other than the upper and lower line levels. For two bound levels (1,2) and one continuum level (k) ϵ' and $\epsilon' B^s$ are given by:

$$\epsilon' = \frac{C_{21}}{A_{21}}(1-\beta) + \frac{\bar{P}_{21}}{A_{21}} - \frac{\bar{\omega}_1}{\bar{\omega}_2}\frac{\bar{P}_{12}}{A_{21}}$$
$$\epsilon' B^s = \frac{C_{21}}{A_{21}}(1-\beta)\,B + \alpha\frac{\bar{\omega}_1}{\bar{\omega}_2}\frac{\bar{P}_{12}}{A_{21}} \qquad \text{III.25}$$

where $\alpha = \dfrac{2h\nu_{21}^3}{c^2}$, $\beta = e^{-h\nu_{21}/kT}$

$$\bar{P}_{ij} = P_{ik}P_{kj}/(P_{ki} + P_{kj}) \qquad \text{III.26}$$

For three bound levels and a continuum level

$$\epsilon' = X - Y$$
$$\epsilon' B^s = \alpha Y \qquad \text{III.27}$$

where

$$X = \frac{1}{A_{21}}\left(C_{21} + \bar{P}_{21} + P_{23} + \bar{P}_{23} - \frac{M_{12}M_{21}}{M_{22}}\right) \qquad \text{III.28}$$

$$Y = \frac{1}{A_{21}} \frac{\bar{\omega}_1}{\bar{\omega}_2} \left(C_{12} + \bar{P}_{12} - \frac{M_{12} R_2}{M_{22}}\right) \qquad \text{III.29}$$

$$\begin{aligned} M_{12} &= P_{32} + \bar{P}_{32} \\ M_{21} &= P_{23} + \bar{P}_{23} \\ M_{22} &= P_{31} + \bar{P}_{31} + P_{32} + \bar{P}_{32} \\ R_2 &= P_{13} + \bar{P}_{13} \end{aligned} \qquad \text{III.30}$$

For some applications it is convenient to solve for two line radiation fields simultaneously using only the four levels in Code 2. The two lines are then represented by the 3 - 1 and 2 - 1 transitions. The corresponding X and Y values for the 3 - 1 lines are

$$\begin{aligned} X &= \frac{1}{A_{31}} \left(C_{31} + \bar{P}_{31} + P_{32} + \bar{P}_{32} - \frac{M_{12} M_{23}}{M_{11}}\right) \\ Y &= \frac{1}{A_{31}} \frac{\bar{\omega}_1}{\bar{\omega}_3} \left(C_{13} + \bar{P}_{13} - \frac{M_{21} R_1}{M_{11}}\right) \end{aligned} \qquad \text{III.31}$$

where

$$\begin{aligned} M_{11} &= P_{21} + \bar{P}_{21} + P_{23} + \bar{P}_{23} \\ R_1 &= P_{12} + \bar{P}_{12} \quad . \end{aligned} \qquad \text{III.32}$$

In the general case ϵ' and B^s are obtained from Code 1 at each optical depth. Code 1 can be run for arbitrary values of $\bar{J}$ for the lines or $\bar{A}$ for the continuum rates.

C. Evaluation of A_k

The evaluation of A_k follows that of Avrett and Loeser (1969) which is recommended for further details. $F_k(x)$ is represented by

$$F_k = \sum_{j=1}^{K} f(x_k)_j \, C_j \qquad 0 \le x \le x_K$$

where III.33

$$f(x)_j = 1, \quad 0 \le x \le x_K$$

when $j = 1$, and

$$f(x)_j = \begin{cases} (1 - \frac{x}{x_j})\,(1 - y\,\frac{x}{x_j}), & 0 \le x \le x_j \\ 0, & x_j \le x \le x_K \end{cases} \qquad \text{III.34}$$

when $j = 2,3,\ldots K.1$ y is an adjustable parameter.

A_k is given by

$$A_k = \sum_{j=1}^{K} g_j \, f_{jk}^{-1} \qquad \text{III.35}$$

where f_{jk}^{-1} is the inverse of $f(x_k)_j$ and

$$g_j = \begin{cases} x_K, & j = 1 \\ \frac{1}{2}\, x_j\,(1 - \frac{y}{3}), & j = 2,3 \ldots K. \end{cases} \qquad \text{III.36}$$

D. Sample Solution - Two Lines

The inputs to code 2 to begin the iterative solution are the n_j/n_1. Approximate starting values are obtained from code 1. We shall illustrate the solution by discussing the populations n_2/n_1, n_3/n_1 and n_K/n_1, where 1, 2 and 3 designate the lower level and two upper line levels for which the transport equations are solved and K the continuum level. ϵ_i and B_i^s are obtained as described in Section III.B. n_1 and the optical depths at the geometric depth points are calculated by the code from the given population ratios and n_{TOTAL}. For the initial run, the upward radiative rates are those given by the optically thin case. S_j values are calculated from Eq. III.12. $\bar{J}_j$ is found from the S_j and the new radiative excitation rate based on $\bar{J}_j$ is used to obtain new values of n_j/n_1 through code 1 or a simpler 3 or 4 level solution. The new values of n_j/n_1 and $\bar{J}$ are used as input to code 2 (or 3) to obtain the other line intensity.

We illustrate the solution for two lines in Fig. III-1 for $T_e = 2 \times 10^4$ °K and $n_e = 10^{12}$ cm^{-3}. The Figure shows results for n_2/n_1, n_3/n_1 and n_K/n_1 as a function of the number of iterations. The initial values of n_2/n_1 and n_3/n_1 are 10^{-6} and n_K/n_1 is 10^2. The solutions have essentially converged after 2-3 iterations. Solutions at the surface of the layer are labeled -O; solutions at the center of the layer are labeled -C. The codes have been tested for a number of simultaneous line and continuum transfer problems. There have been no convergence difficulties provided the lines and continuua chosen for solution do significantly effect each other.

Figure III-1 2 LINE SOLUTION - CONVERGENCE

Te = 20,000° K

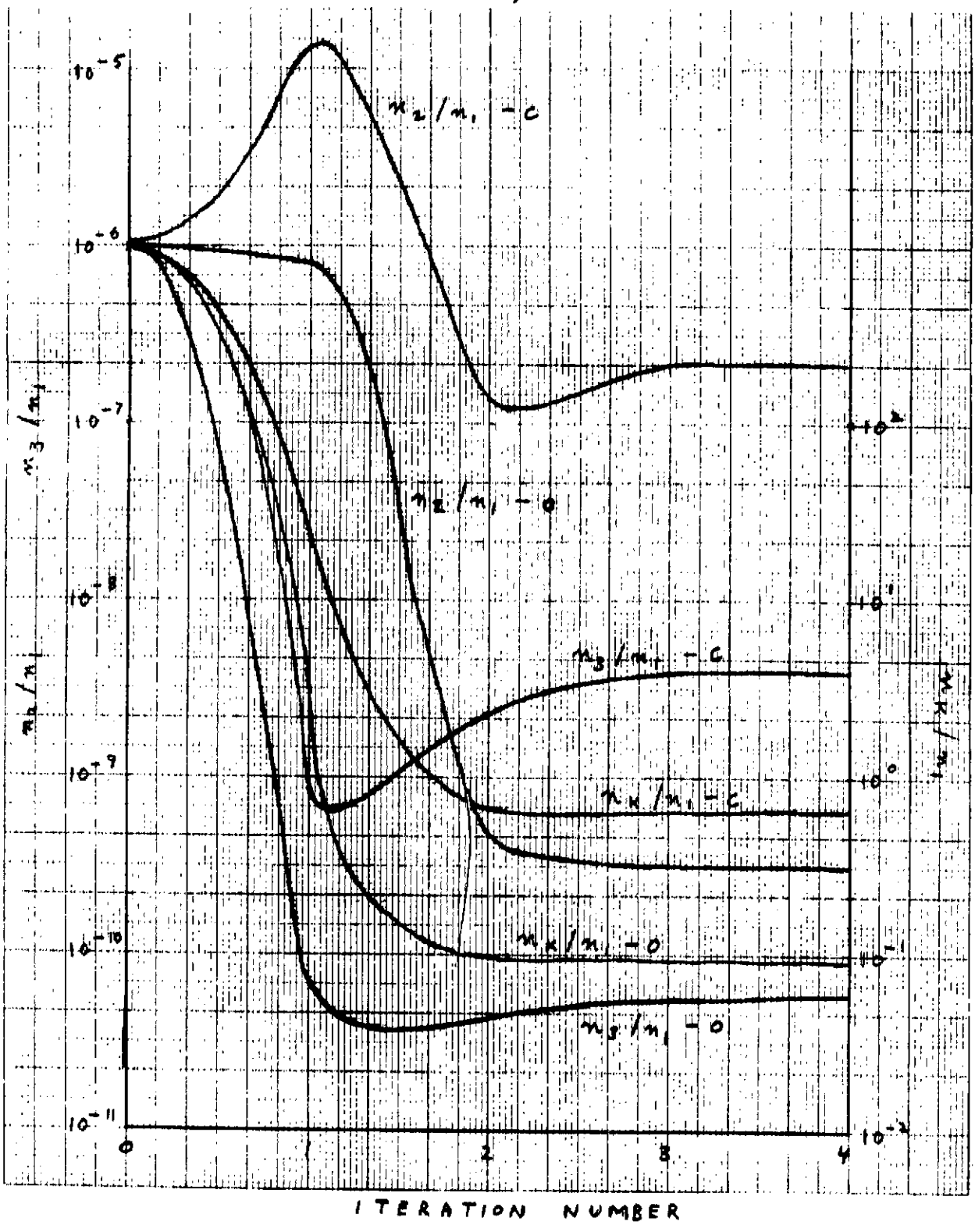

IV. CONTINUUM TRANSPORT SOLUTION

A. Basic Equations

The statistical equilibrium equation for one bound level (n_1) and one contiuum level (n_k) is

$$\frac{n_1}{n_1^*}\left[4\pi \int_{\nu_1}^{\infty} \frac{a_\nu}{h\nu} J_\nu d\nu + C_{1k}\right] =$$

$$\frac{n_k}{n_k^*}\left[4\pi \int_{\nu_1}^{\infty} \frac{a_\nu}{h\nu} e^{-h\nu/kT} \left(\frac{2h\nu^3}{c^2} + J_\nu\right) d\nu + C_{1k} \right], \qquad \text{IV.1}$$

where the * refers to the LTE population at a given electron temperature and density. It is convenient to express the population ratio n_1/n_k in terms of the non-equilibrium parameter b_1,

$$b_1 = (n_1/n_1^*) \;/\; (n_k/n_k^*). \qquad \text{IV.2}$$

The radiative transport equation for $\nu > \nu_1$ can be written

$$\mu \frac{dI_\nu}{d\tau_\nu} = I_\nu - \frac{B_\nu^*}{b_1} \qquad \text{IV.3}$$

where neglecting stimulated recombination (which is justified for He for the temperatures considered)

$$B_\nu^* = \frac{2h\nu^3}{c^2} e^{-h\nu/kT}$$

$$d\tau_\nu = k_\nu dz \qquad \text{IV.4}$$

$$k_\nu = n_1 a_\nu$$

The values of b_{1i} at depth i are found by solving the set of equations

$$\sum_{j=1}^{N} M_{ij} \frac{1}{b_{ij}} = \frac{\epsilon_i^b}{\epsilon_i^a} \qquad i = 1, 2. \ldots N \qquad \text{IV.5}$$

where

$$M_{ij} = \Delta_{ij} - \frac{1}{\epsilon_i^a R_i'} \sum_{k=1}^{K} A_k' \; W_{ijk}^{(\Lambda-1)} \frac{g_k}{y_k} e^{-y_k \theta_j}$$

IV.6

$$\Delta_{ij} = \begin{cases} 1, & j = i \\ 0, & j \neq i \end{cases}$$

and

$$R_i' = \sum_{k=1}^{K} A_k' \frac{g_k}{y_k} e^{-y_k \theta_i}. \qquad \text{IV.7}$$

τ_i is the optical depth at the continuum threshold at depth i, $\theta_i = h\nu_1/kT_i$, $y_k = \nu_k/\nu_1$, k = 1, 2, ...K, a set of dimensionless frequency values and g_k are values such that $g_k y_k^{-3}$ represents the frequency dependence of the photoionization cross section. The optical depth is given by

$$\tau_{ik} = \frac{g_k}{g_1} \frac{1}{y_k^3} \tau_i. \qquad \text{IV.8}$$

ϵ_i^a and ϵ_i^b are coupling parameters whose calculation is described in the next section. The values of $w_{ijk}^{(\Lambda-1)}$ are related to $w_{ijk}^{(\Lambda)}$ as follows,

$$w_{ijk}^{(\Lambda-1)} = \begin{cases} w_{ijk}^{(\Lambda)} - 1, & j = 1 \\ w_{ijk}^{(\Lambda)}, & j \neq i. \end{cases} \qquad \text{IV.9}$$

The mean intensity of the radiation field is given by

$$J_{ik} = \sum_{j=1}^{N} w_{ijk}^{(\Lambda)} \frac{B_{jk}^*}{b_{ij}} . \qquad \text{IV.10}$$

B. Evaluation of ϵ_i^a and ϵ_i^b

ϵ_i^a and ϵ_i^b follow from the statistical equilibrium equation solution for b_1,

$$\frac{1}{b_1} = \frac{(R_{1k}/R_{1k}^*) + \epsilon^b}{1 + \epsilon^a} \qquad \text{IV.11}$$

where

$$R_{1k} = 4\pi \int_{\nu_1}^{\infty} \frac{a_\nu}{h\nu} J_\nu d\nu$$

$$R_{1k}^* = 4\pi \int_{\nu_1}^{\infty} \frac{a_\nu}{h\nu} B_\nu d\nu \, . \qquad \text{IV.12}$$

For two bound levels (1,2) and a continuum level k, ϵ_i^a and ϵ_i^b are

$$\epsilon^b = \frac{1}{R_{1k}^*} \left(C_{1k} + \frac{P_{12} P_{2k}}{P_{21} + P_{2k}} \right)$$

$$\epsilon^a = \frac{1}{R_{1k}^*} \left(C_{1k} + \frac{(n_2^*/n_1^*) P_{21} (n_k^*/n_2^*) P_{k2}}{P_{21} + P_{2k}} \right) . \qquad \text{IV.13}$$

For an N level model the corresponding equations are

$$\epsilon^b = \frac{1}{R_{1k}} \left(C_{1k} + \frac{1}{Q^{k1}} \sum_{\ell \neq 1 \neq k}^{N} P_{1\ell} Q^{\ell 1} \right)$$

$$\epsilon^a = \frac{1}{R_{1k}^*} \left(C_{1k} + \frac{1}{Q^{1k}} \sum_{\ell \neq 1 \neq k}^{N} P_{k\ell} Q^{\ell k} \right). \qquad \text{IV.14}$$

ϵ^a and ϵ^b can easily be obtained from program 1.

C. Evaluation of A_k'

The A_k' coefficients are defined such that

$$\int_1^{y_k} F(y)dy = \sum_{k=1}^{K} A_k' F_k \qquad \text{IV.15}$$

where F_k is the value of F at $y = y_k$. Here, $1 \le y_k \le y_K$. With unity instead of zero as the lower integration limit, we determine the A_k' coefficients as follows.

Let $f'(y)_j = 1, \quad 1 \le y \le y_k,$

when $j = 1$, and

$$f'(y)_j = \begin{cases} (1-\frac{y-1}{y_j-1})\,(1 - Y\,\frac{y-1}{y_j-1}), & 1 \le y \le y_j \\ 0\,, & y_j \le y \le y_K, \end{cases} \qquad \text{IV.16}$$

when $j = 2,3,\ldots K$. Let f'^{-1}_{jk} be the inverse of $f'(y_k)j$. Then

$$A_k' = \sum_{j=1}^{K} g'_j\, f'^{-1}_{jk}, \qquad \text{IV.17}$$

where

$$g'_j = \begin{cases} y_K-1, & j = 1 \\ \frac{1}{2}\,(y_j-1)(1-\frac{Y}{3}), & j = 2,3,\ldots N. \end{cases} \qquad \text{IV.18}$$

Y is an adjustable parameter.

V. CODES

A. Code 1 - Solution of Statistically Steady State Population Equations

1. Main Program

In our own internal notation, this code is designated as P48. The main program reads f numbers, wavelengths (lambda), electron and radiation temperatures, the energy level model, recombination coefficients, converts energy differences from wave numbers to electron volts, and writes all the above before entering subroutine CONSTS. The subroutine CONSTS as well as other subroutines are described in the next section. The radiation temperature is that characterizing the external Blackbody radiation field incident upon the layer. The indices on the f numbers refer to the ion and the upper and lower line levels respectively.

On return to the main program, more quantities are read in and printed out, such as: the total line center optical depth of the layer, the dilution factor for the external radiation, the electron density, the indeces of the chosen thick line, the depth points at which solutions are to be obtained, a constant divisor for the elements of the main matrix to prevent overflow, Y values for thick lines, and various control numbers. These quantities are entered here in order to be able to run a series of different solutions by changing any or all of them without changing the electron or radiation temperatures and, thereby, having to recalculate the many reaction rates.

After the above have been printed and the ratio of B_o/B_{T_r} calculated the subroutine AMAT is entered to calculate the elements and cofactors of the A matrix for the optically thin case. The rate equation matrix represented by Eq. II-3 is printed out. The matrix is 30 x 30 corresponding to the number of energy levels. Selected cofactors are printed out. The accuracy of the solution can be checked by comparison of cofactors with the same j values.

The solution for the non-equilibrium populations n_i is obtained in AMAT. The solutions are printed for the optically thin case along with LTE solutions for the same temperature and density. The optical depth at the center of each line is calculated and printed out for a layer of optical thickness T_1 in the line specified in the input. Some further quantities such as the physical thickness of the layer H are calculated and the subroutine ELIM is entered to compute ε, η and ζ.

The program now repeats the calculation with the specified set of Y values read in. Next, a DO loop on depth is set up. In the listing given there is no depth variable. In calling for one to obtain values of η and ζ for example, it would enter into the calculation of the quantity FF, which is used to alter the Y value for the thick line.

2. Description of Sub-Programs

Subroutine AMAT(KK)

AMAT calculates elements of the A matrix using quantities determined by CONSTS. Once all the elements are found, they are divided by a constant to prevent overflow. Cofactors are calculated, summed, and used to determine λ. From this the n_i are found. Next the n_{eqi} are found and the ratio n_i/n_{eqi}. Last, before returning to the main program, the optical depths are calculated and printed for each f value.

KK = 0 , optically thin solution

KK = 1 , optically thick solution for any $Y \neq 0.0$.

Function COFACT (NR, NC, NE, D)

COFACT finds the cofactor of matrix D for row NR, column NC. NE is the number of rows and columns in D.

Function CØLL (T, I, J, K, N)

Function CØLL calculates certain electron collisional excitation and ionization coefficients for special points.

T = electron temperature ($^{\circ}$K)

I, J, K = indeces of coefficient

N = 1 , excitation coefficient calculated

N = 2 , ionization coefficient calculated

Subroutine CONSTS

Initially, if the radiation temperature is different from the electron temperature, CONSTS reads in new values of β_{ijk} calculated at T_r. It then calculates the electron collisional ionization and recombination coefficients, the radiative ionization rate, the B_{ijk} and B_{ikj}, the electron collisional excitation coefficient, the Einstein spontaneous transition probability, and the Einstein absorption transition probability multiplied by the Planck function. The subscript i refers to the ion, the second subscript the beginning level and the last subscript the ending level of the transition.

ORIGINAL PAGE IS
OF POOR QUALITY

Subroutine ELIM (RHO, AP)

AP = Einstein spontaneous transition probability for the thick line (K7, K8, K9)

RHO = $h\nu^3/c^2$, where ν is calculated at (K7, K8, K9)

This computes double cofactors for use in calculating eta and iota. It is called from the main program and uses the function ELM2.

Function ELM2 (IRA, ICA, KRA, KCA, RMAT, Z)

IRA = row index of 1st row to be eliminated

ICA = column index of 1st column to be eliminated

KRA = row index of second row to be eliminated

KCA = column index of second column to be eliminated

RMAT = contains reduced matrix

Z = sign of cofactor ($Z = \pm 1$).

ELM2 eliminates two rows and two columns from the A matrix and places the reduced matrix in RMAT.

B. Radiative Transfer Codes

Two codes have been developed under this program. The first (code 2) represents a numerical solution of the line transport equation given in Section III. The second (code 3) represents a numerical solution of the continuum transport equation. Listings of these codes appear in Appendices B and C. The simultaneous solution of several line and/or continuum transport eqs. with the population eqs. is accomplished by iteration. Initial values for population ratios are estimated from various solutions obtained from code 1 (see Section II). After obtaining the radiation intensities from codes 2 and 3 the new radiative rates are used as input to code 1 to obtain new population ratios to be used in the next iteration.

Code 2 requires the specification of certain quantities involving ϵ_i' and B_i^s while code 3 requires ϵ_i^a and ϵ_i^b. There are two methods provided for determining these quantities. One option is to calculate them in code 1 and simply read them in. (Code 1 is now set up to calculate the quantities η and ι which are read in and are related in a simple manner -- see Eq. III.24. The quantities ϵ^a and ϵ^b are easily related to the cofactors generated by code 1. Code 1 will generate arbitrary cofactors depending upon input parameters.)

A more approximate method of calculating these quantities is provided directly in the two codes. Code 2 will obtain the solution for ϵ' and B^s from a 4 level model (3 bound levels and 1 continuum level). Code 3 has the option of solving for ϵ^a and ϵ^b from a 3 level model (2 bound levels and 1 continuum level). These approximate solutions can be very useful for some purposes.

A symmetrical (about the center of the layer) geometrical grid (called Z in the program) is set up given the total geometric depth and number of desired decades. Currently, the maximum number of decades is set at 5 giving a total number of points of 31. This calls for solution

ORIGINAL PAGE IS
OF POOR QUALITY

of a 31 x 31 matrix and may create underflow or overflow problems. The number of decades required for convergence must be tested for each problem.

Optical depth points at each geometric depth are next calculated from an integration over geometric depth at a given frequency.

Steps in frequency are now calculated using the quantities $x = \frac{\nu - \nu_o}{\Delta \nu_D}$ in the bound level cases and $y = \nu/\nu_{K1}$ in the continuum. Step sizes are input quantities and are constant in x and y. The maximum x is found by choosing the first value of x such that $e^{-x^2} \tau_{max} \leq 1.0$, and the maximum y such that $\tau_{max}/y^3 \leq 1.0$.

Certain quantities uniquely dependent on frequency are now calculated, such as f(y), g(y), A(y), f'(x), g'(x), and A'(x). A loop over frequency is set up with index k to compute the $W_{ijk}^{(\Lambda)}$ and $W_{ijk}^{(\Lambda-1)}$ (by means of the subroutine WMAT) and then sums over frequency are taken within the loop to arrive at the coefficients in the final equations: $\overline{W}_{ij}$ in the bound case and M_{ij} in the continuum.

Once the integration over frequency is completed, the program sets up a matrix, called EM, for solution of the simultaneous equations to get S_j or $1/b_{ij}$. These are then punched in cards along with the population ratios to be used as inputs to the next step in the iteration.

The S_j or b_{ij} are used to determine new line or continuum radiative rates which are then used as input to code 1. New values for the populations and the parameters ϵ_i, B_i^s, ϵ_i^a and ϵ_i^b are obtained and are used in beginning the next step of the iteration.

DESCRIPTION OF SUBPROGRAMS

SUBROUTINE WMAT (NZ, TCUT)

WMAT calculates $W_{ij}^{(\Lambda)}$ and $W_{ij}^{(\Lambda-1)}$ for those areas of the matrices where $|\tau_i-\tau_j|$ is less than TCUT.

FUNCTION NOSONI (A, X, L, LMAX)

NOSONI is a matrix inversion routine using the method outlined on page 434 of Hildebrand, Introduction to Numerical Analysis (New York, 1956).

A is a matrix of order L with column dimension LMAX. Its elements are assumed to be stored columnwise in the usual Fortran manner. X is working storage of length L. The inverse of A will replace A. Upon return, NOSONI = 1 if inversion went properly, = 0 if a divisor is zero, in which case, A may contain garbage.

FUNCTION ESB (X, N)

This routine uses the function EXIN to obtain $E_1(X)$, the exponential integral of order 1 in X. It then calculates $E_N(X)$, where N = 2, 3 or 4 from the rec recurrence relation $E_{N+1}(X) = \frac{1}{N}[e^{-X} - XE_N(X)]$

FUNCTION EXIN (Y)

EXIN obtains $E_1(Y)$ from polynomial approximations shown in sections 5.1.53 and 5.1.56 of the Handbook of Mathematical Functions, National Bureau of Standards, 1964.

VI. REFERENCES

Allen, C. W.: 1961, Mem. Soc. R. Sci. Liege, 5th Sec., 4, 241

Allen, C. W.: 1963, "Astrophysical Quantities," 2nd Ed., The Athlone Press, London, p 41

Athay, R. G., and Johnson, H. R.: 1960, Ap. J., 131, 413

Avrett, E. H. and Loeser, R.: 1969, SAO Special Report No. 303, Cambridge, Mass.

Benson, R. S. and Kulander, J. L.: 1972, Solar Physics, 27, 305

Burgess, A. and Seaton, M. J.: 1960, M. N., 120, 9

DeJager, C. and DeGroot, C.: 1957, B.A.N., 14, 21

Dolder, K. T., Harrison, M. F. A. and Thonemann, P. C.: 1961, Proc. R. Soc., A264, 367

Green, A. E. S.: 1966, AIAA J. 4, 769

Hearn, A. G.: 1969, M. N., 142, 53

Jefferies, J. T.: 1955, Aust. J. Phys., 8, 335

Jefferies, J. T.: 1957, M. N., 117, 493

Kieffer, L. J. and Dunn, G. H.: 1966, Rev. Mod. Phys., 38, 1

Long, D. R.: 1967, Thesis, Univ. of Wash., Seattle, Wash.

Mihalas, D. and Stone, M. E.: 1968, Ap. J., 151, 293

Peach, G.: 1967, Mem. Roy. Ast. Soc., 71, 13

Saraph, H. E.: 1964, Proc. Phys. Soc., 83, 763

Seaton, M. J.: 1962, "Atomic and Molecular Processes"(ed. by D. R. Bates), Academic Press, N.Y., p 414

Shklovsky, I. S. and Kononovitch, E. W.: 1958, Russ. Ast. J., 35, 37

Stewart, A. L. and Webb, T. G.: 1963, Proc. Phys. Soc., 82, 532

White, R. O.: 1961, Ap. J., 134, 85

Wiese, W. L., Smith, M. W. and Glennon, B. M.: 1966, Atomic Transition Probabilities, NSR DS-NBS4

Zirin, H.: 1956, Ap. J., 123, 536

Appendix G

John Hopkins Solar Radio Observations
Final Report

TSSD-4515
Enclosure (1)
S1P-198-74

SOLAR RADIO OBSERVATIONS IN SUPPORT OF SKYLAB - A

by

Bruce L. Gotwols

Final Report Submitted to the
National Aeronautics and Space Administration

Grant No. : NGR 21-001-024
Period Covered: 1 Oct., 1972 - 31 March, 1974
NASA Technical Officer: Charles R. Baugher (MSFC)

Principal Investigator: Bruce L. Gotwols

Introduction

This Final Report summarizes the research performed under NASA grant NGR 21-001-024, from 1 Oct., 1972 thru 31 March, 1974. This grant allowed the continuation of solar radio observations which had previously been funded with "in-house" research funds.

The research was performed under the direction of B. L. Gotwols. Antenna control, circuit construction, and routine cataloging of data were performed by R. J. Sneeringer.

Observations and Data Reduction

Observations commenced in November, 1972 (after a month of receiver improvement), and continued until the end of the last manned Skylab mission in February, 1974. As explained in our original proposal, it was not possible to obtain uninterruped sunrise to sunset coverage, due to the sharing of the 60 ft. antenna with other laboratory programs. Despite this limitation, 1408 hours of observations were obtained.

The spectra were recorded in real time, both on film and magnetic tape. The filming was performed with a continuous motion camera running at 0.8 in/min. This rate of film travel will only allow 0.2 s to be resolved, but this is sufficient to identify intervals which require further study with the full time resolution of 0.01s that is preserved on the magnetic tapes. High speed replays of all bursts were subsequently made at times which caused the least interruption to the observing program, i.e., during periods of exceptionally low solar activity, during the unmanned portions of the Skylab flight, etc.

A catalog of the observations is given in Appendix I. A similar catalog covering the period May, 1973 - February, 1974, has been submitted to World Data Center - A (NOAA), for inclusion in a catalog of ground based observations in support of Skylab.

Equipment Modification

Our CRT display was modified so as to greatly improve the contrast obtainable on weak solar bursts, at the expense of decreasing the dynamic range displayed to 10 dB. The display was run in this high contrast mode throughout the period November, 1972 - February, 1974. For non-saturated filming of very strong bursts, the CRT controls are easily readjusted and the magnetic tape replay through the spectrograph display.

An automatic intensity calibration scheme (hourly) was constructed and installed in November, 1973. Up until this time intensity calibrations were performed manually once or twice a day.

Research Results

Preliminary reduction of our high time resolution observations has revealed the fact that there is often considerable curvature present at the low frequency extremity of the fast-drift bursts in our frequency range (see Figure 1). The entire burst occurs on a time scale of 0.5 s, so the detection of this curvature would have been impossible with the 0.2 s or greater scanning period of former studies. Stimulated by this new finding we are currently considering the following hypothesis: The majority of fast-drift decimetric wavelength bursts are the result of streams of electrons that are guided along closed magnetic field lines. This hypothesis appears to be capable of explaining the surprisingly loose correlation between type III bursts at decimeter and meter wavelengths. It can also account for the observation[1] that shorter lived decimeter wavelength type III bursts exhibit higher drift rates.

On the theoretical side, we have studied pulsating type IV solar radio bursts.[2] The most interesting result of this study

---

1. Young, C. W., Specer, C. L. Moreton, G. E., and Roberts, J. A.: 1961, Astrophys, J., 133, 243.

2. Gotwols, B. L.: 1973, Solar Phys., 33, 475 (reprinted in Appendix II).

was the way in which the Razin effect enhances the depth of modulation of the pulsations. Also of interest is the fact that when significant synchrotron self-absorption is present, the pulsations break up into two distinct bands which pulsate 180° out of phase with each other.

Colloboration with Other Groups

Our Data has been supplied directly to two of the investigators on Skylab. These are: Dr. E. B. Mayfield of the Aerospace Corporation (experiment S-056), and Dr. A. S. Krieger of AS & E (experiment S-54). Data has also been furnished to Dr. J. C. Brown who is currently visiting the Astronomical Institute at Utrecht.

A catalog of our observations during the first manned Skylab flight was included as part of a NOAA publication[3]. A complete catalog covering the entire Skylab flight has recently been submitted through the same channels.

Scientific Meetings and Publications

Gotwols, B. L. : "Pulsating Type IV Solar Radio Bursts", presented at the 140th meeting of the AAS, June 27, 1973, Columbus, Ohio. Abstract - BAAS, 5, 340, 1973

Gotwols, B. L. : "Solar Radio Pulsations", presented at IAU Symposium no. 57 on The Solar Corona, September 13, 1973, Surfers Paradise, Australia. Abstract - to be published in the Proceedings.

Gotwols, B. L. : 1973, Solar Phys. 33, 475 (reprinted in Appendix II).

---

3. Coffey, H.: 1973, "Preliminary Catalog of Ground-Based Skylab-Coordinated Solar Observing Programs for the Period May 28 to July 26, 1973", World Data Center - A for Solar - Terrestrial Physics, NOAA, Boulder, Colorado.

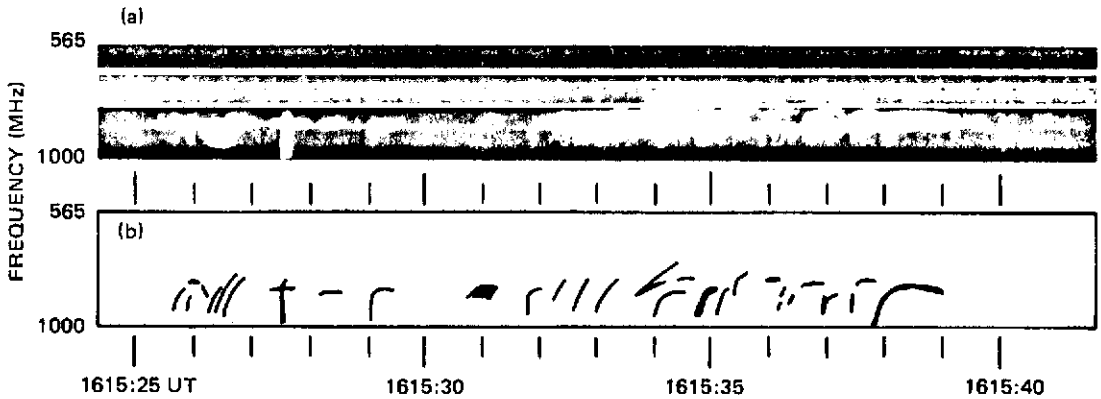

Fig. 1 Solar bursts recorded on 21 Nov. 1972: (a) high time resolution dynamic spectra of fast drift bursts, many of which exhibit a low frequency turnover. Much detail has been lost in the process of reproduction. (b) schematic tracing of the original film from which Figure 2a was produced.

C4

APPENDIX I

CATALOG OF SOLAR RADIO OBSERVATIONS

TAKEN AT THE APPLIED PHYSICS LABORATORY

November, 1972 - February, 1974

ORIGINAL PAGE IS
OF POOR QUALITY

A Guide for Classification of Solar Radio Bursts Observed with the APL Spectrograph[1] (565-1000 MHz)

TABLE I - Description of the various types of spectra

SPECTRAL TYPE	APL SYMBOL	DESCRIPTION AND COMMENTS
I	1	Storm bursts
II	2	Slow drift bursts
III	3	Fast drift bursts; $\dot{\nu} >$ 100 MHz/sec
IV	4	Prolonged continuum
V	5	Brief continuum (normally following type III bursts)
-	6	Intermediate drift bursts; $\dot{\nu} \sim$ 30-100 MHz/sec
UNCLF	UNCLF	Unclassified activity.

TABLE II - Symbols appended to the spectral type

SYMBOL	DESCRIPTION
P	Pulsations
G	Small group (< 10) of bursts
GG	Large group ($\geq$ 10) of bursts
C	Underlying continuum
U	U-shaped burst of type III
RS	Reverse-slope burst
DP	Drifting pair
N	Intermittent activity in this period

TABLE III - Intensity Scale

SYMBOL	FLUX DENSITY $X10^{-22}$ Wm^{-2} Hz^{-1}
1	25 - 65
2	65 - 650
3	> 650

1 Gotwols, B. L. and Phipps J., 1972, Solar Phys. 26, 386.

SOLAR RADIO EMISSION
SPECTRAL OBSERVATIONS (565-1000 MHZ)

NOV. 1972

	TIMES OF OBS. (UT)		BURSTS				
DATE	START	END	START(UT)	END(UT)	INT.	TYPE	REMARKS
15	2039	2054					
16	1329	1447					
	1510	2052					
17	1328	1725					
	1727	2016					
20	1520	1832	1933.2	1933.4	1	3G	
	1836	2053					
21	1340	2053	1347.8	1348.1	2	3G	
			1349.5	1349.7	1	3G	
			1351.0	1351.1	1	3G	
			1432.9	1435.5	3	3GG	
			1519.0	1519.4	2	3GG	
			1525.2	1525.3	1	3	
			1529.0	1536.4	2	3GG	
			1615.0	1616.2	3	3GG	
			1617.5	1619.7	3	3GG	
			1640.4	1640.9	2	3G	
			1642.2	1642.4	2	3G	
			1728.0	1728.1	1	3G	
			1730.1	1732.7	3	3GG	
			1756.3	1758.2	3	3GG	
			1817.5	1817.6	1	3G	
			1833.2	1833.4	2	3G	
			1850.1	1850.2	2	3G	
			1902.8	1903.9	3	3GG	
			1905.2	1905.8	2	3GG	
22	1342	1755	1422.6	1423.0	1	3G	
	2016	2051	1631.1	1631.6	1	UNCLF	
27	1311	1456					
	1525	2050					
28	1314	2013					
29	1305	1539					
	1623	2051					

SOLAR RADIO EMISSION
SPECTRAL OBSERVATIONS (565-1000 MHZ)

NOV. 1972

	TIMES OF OBS. (UT)		BURSTS				
DATE	START	END	START(UT)	END(UT)	INT.	TYPE	REMARKS
30	1301	2046	1522.0	1523.6	2	UNCLF	
			1711.7	1711.9	1	3G	
			1715.5	1715.5	1	3G	
			1916.4	1917.3	2	3GG	

SOLAR RADIO EMISSION
SPECTRAL OBSERVATIONS (565-1000 MHZ)

DEC. 1972

	TIMES OF OBS. (UT)		BURSTS				
DATE	START	END	START(UT)	END(UT)	INT.	TYPE	REMARKS
05	1259	1358					
	1431	1606					
08	1953	2049					
11	1304	1634					
	1723	1910					
12	1308	1914	1615.0	1615.2	1	3G	LOW FREQ END
	1950	2006	1742.2	1742.6	3	3GRS	
13	1327	1456					
	1459	1516					
	1659	1900					
	2010	2113					
14	1257	1857					
	1901	2033					
15	1301	1427					
	1503	1539					
	1602	2009					
18	1257	1447					
	1518	2 26					
19	1257	1410					
	1414	1443					
20	1331	1617					
	1711	1924					
	1956	2040					
	2104	2114					
21	1257	1525					
	1530	1856					
	1924	2050					
22	1304	1855	1321.6	1321.8	1	3G	
26	1301	1500	2015.1	2016.1	3	3G	
	1529	1945					

SOLAR RADIO EMISSION
SPECTRAL OBSERVATIONS (565-1000 MHZ)

DEC. 1972

	TIMES OF OBS. (UT)		BURSTS				
DATE	START	END	START(UT)	END(UT)	INT.	TYPE	REMARKS
26	2015	2054					
27	1301	1407					
	1703	1915					
	2013	2042					
29	1307	1522					
	1643	1819					
	1845	2048					

SOLAR RADIO EMISSION
SPECTRAL OBSERVATIONS (565-1000 MHZ)

JAN. 1973

	TIMES OF OBS. (UT)		BURSTS				
DATE	START	END	START(UT)	END(UT)	INT.	TYPE	REMARKS
04	1306	1500					
	1519	1835					
	1906	2051					
05	1311	1434	1955.8	1957.2	3	3G	
	1920	2058					
08	1304	1617					
	1625	1634					
09	1537	1607					
17	1323	1546					
	1559	1710					
	2016	2043					
18	1321	1810					
	1925	2055					
19	1307	1735					
	1819	1947					
22	1414	1446					
	1454	1608					
	1645	1752					
	1826	1933					
	2006	2126					
23	1308	1725					
	1850	2050					
24	1307	1656					
	1725	2003					
	2034	2054					
25	1309	1937					
26	1307	1438					
	1613	1732					
	1806	2000					
	2032	2051					

SOLAR RADIO EMISSION
SPECTRAL OBSERVATIONS (565-1000 MHZ)

JAN. 1973

	TIMES OF OBS. (UT)		BURSTS				
DATE	START	END	START(UT)	END(UT)	INT.	TYPE	REMARKS
29	1306	1745					
	1817	1937					
30	1339	1355					
	1949	2000					
31	1337	1646					
	1715	1732					

SOLAR RADIO EMISSION
SPECTRAL OBSERVATIONS (565-1000 MHZ)

FEB. 1973

DATE	TIMES OF OBS. (UT) START	END	BURSTS START(UT)	END(UT)	INT.	TYPE	REMARKS
01	1304	1508	2017.6	2017.7	2	3U	
	1546	1616					
	1646	1734					
	1813	2038					
02	1305	1514					
	1618	1727					
	1758	1834					
	1914	1933					
	1950	2053					
05	1313	1538					
	1627	1737					
	1843	2053					
06	1305	1702					
	1735	1912					
	1945	1953					
09	1638	1713					
	1943	2050					
12	1424	1549	2038.3	2038.3	1	3	
	1615	1640					
	1703	2136					
13	1306	1517					
	1544	2050					
14	1257	1627					
	1656	2 56					
15	1302	1615					
	1626	2 54					
16	1422	1527					
	1557	2106					
22	1511	1546					
	1656	1818					
	1847	2053					

SOLAR RADIO EMISSION
SPECTRAL OBSERVATIONS (565-1000 MHZ)

FEB. 1973

	TIMES OF OBS. (UT)		BURSTS				
DATE	START	END	START(UT)	END(UT)	INT.	TYPE	REMARKS
23	1321	1410					
	1445	1517					
	1546	1847					
	1921	1943					
	2010	2055					
26	1307	1528	2012.1	2013.3	1	UNCLF	
	1603	1702					
	1732	2054					
28	1305	1427	1733.0	1733.0	2	UNCLF	
	1459	1607	1735.4	1735.4	2	3G	
	1650	1805					
	1839	2035					
	2041	2050					

SOLAR RADIO EMISSION
SPECTRAL OBSERVATIONS (565-1000 MHZ)

MAR. 1973

DATE	TIMES OF OBS. (UT) START	END	BURSTS START(UT)	END(UT)	INT.	TYPE	REMARKS
01	1324	1359					
	1429	1501					
	1602	1635					
	1708	1849					
02	1253	1432					
	1633	1743					
05	1314	1508					
	1552	1650					
	1711	2056					
08	1301	1348					
	1419	1532					
	1611	1647					
	1724	2047					
09	1518	1603					
	1636	1805					
10	1553	1644					
	1651	2030					
11	1306	1351					
17	1308	2009					
18	1312	2 23					
19	1301	1321	1820.0	1820.0	1	3G	
	1346	1459					
	1621	2 44					
22	1301	1327					
	1356	2 51					
23	1326	1440	1404.8	1404.8	3	3G	
	1504	1634	1919.2	1919.4	1	UNCLF	
	1659	2041	2040.8	2041.2	3	3GG	
24	1304	1628	1314.1	1314.5	2	3G	

SOLAR RADIO EMISSION
SPECTRAL OBSERVATIONS (565-1000 MHZ)

MAR. 1973

	TIMES OF OBS. (UT)		BURSTS				
DATE	START	END	START(UT)	END(UT)	INT.	TYPE	REMARKS
25	1310	2013	1616.8	1618.2	1	3GG	
30	1338	1453	1439.2	1439.4	1	UNCLF	
	1524	2042	1526.8	1530.1	3	3GG	
			1613.6	1614.2	2	3GG	
			1717.8	1718.2	1	UNCLF	

SOLAR RADIO EMISSION
SPECTRAL OBSERVATIONS (565-1000 MHZ)

APR. 1973

	TIMES OF OBS. (UT)		BURSTS				
DATE	START	END	START(UT)	END(UT)	INT.	TYPE	REMARKS
01	1740	1900	1747.3	1747.8	3	3GRS	
			1842.1	1842.3	2	3GU	

SOLAR RADIO EMISSION
SPECTRAL OBSERVATIONS (565-1000 MHZ)

MAY 1973

	TIMES OF OBS. (UT)		BURSTS				
DATE	START	END	START(UT)	END(UT)	INT.	TYPE	REMARKS
17	1749	2026	1749.0F	1750.5	2	3GG	
			1825.3	1827.1	2	3GG	
			1827.9	1828.5	1	3GG	
			1915.3	1917.9	3	3GG	
18	1203	1958	1527.4	1531.6	2	4P	
19	1210	1926					
20	1211	1936	1654.3	1654.4	1	3G	
21	1211	1653					
	1714	1749					
	1754	1852					
	1855	1955					
24	1345	1415					
	1424	1558					
	1601	1957					
25	1201	1635					
	1639	1816					
	1823	1959					
26	1155	1310					
	1322	1619					
	1639	1718					
	1725	1927					
27	1205	1543	1331.2	1331.6	1	3G	
	1550	1931	1606.2	1607.0	2	3GG	
28	1224	1929					
29	1638	1956					
31	1206	1957					

SOLAR RADIO EMISSION
SPECTRAL OBSERVATIONS (565-1000 MHZ)

JUN. 1973

DATE	TIMES OF OBS. (UT) START	END	BURSTS START(UT)	END(UT)	INT.	TYPE	REMARKS
01	1157	1955					
03	1231	1906					
04	1234	1453					
	1459	1751					
	1822	2019					
09	1231	1926					
10	1156	1918					
11	1219	1955					
12	1245	1516					
	1523	2000					
	2004	2047					
13	1201	1950	1322.0	1322.0	2	UNCLF	NARROW BANDWIDTH
14	1201	1432					
	1503	1953					
15	1208	1954	1409.3	1409.4	2	3G	
16	1224	1535	1422.0	1426.0	3	4[illegible]	
	1539	1926	1427.9	1428.4	2	3G	
17	1203	1926					
18	1220	1440					
	1510	1952					
21	1226	1507					
	1510	1956					
22	1159	1930					
23	1238	1852					
25	1214	1356					
	1433	1746					

SOLAR RADIO EMISSION
SPECTRAL OBSERVATIONS (565-1000 MHZ)

JUN. 1973

	TIMES OF OBS. (UT)		BURSTS				
DATE	START	END	START(UT)	END(UT)	INT.	TYPE	REMARKS
28	1858	1920	1858.9	1859.7	2	3GG	
29	1202	1919	1310.0	1311.5	2	3G	
	1855	1931	1515.4	1517.4	2	4P	
			1908.6	1909.5	1	4	
30	1214	1918	1516.3	1518.8	3	3GG	

SOLAR RADIO EMISSION
SPECTRAL OBSERVATIONS (565-1000 MHZ)

JUL. 1973

	TIMES OF OBS. (UT)		BURSTS				
DATE	START	END	START(UT)	END(UT)	INT.	TYPE	REMARKS
01	1210	1925					
02	1238	1530					
	1600	1953					
06	1155	1920					
07	1229	1449					
	1456	1930					
08	1217	1930					
09	1211	1752	1650.3	1650.3	2	3U	
	1820	1938					
12	1154	1251					
	1307	1432					
	1502	1805					
	1832	1916					
	1938	1954					
13	1156	1918					
14	1139	1845					
15	1131	1849					
16	1243	1334					
	1357	1649					
	1809	1947					
21	1129	1725					
22	1126	1237					
	1250	1855					
23	1226	1314					
	1352	1544					
	1547	1731					
	1825	2000					
26	1209	1458					

SOLAR RADIO EMISSION
SPECTRAL OBSERVATIONS (565-1000 MHZ)

JUL. 1973

	TIMES OF OBS. (UT)		BURSTS				
DATE	START	END	START(UT)	END(UT)	INT.	TYPE	REMARKS
29	1128	1856	1309	1353	2	4	
30	1219	1600					
	1656	1726					
	1751	1829					
	1901	1955					

SOLAR RADIO EMISSION
SPECTRAL OBSERVATIONS (565-1000 MHZ)

AUG. 1973

DATE	TIMES OF OBS. (UT) START	END	BURSTS START(UT)	END(UT)	INT.	TYPE	REMARKS
01	1155	1446					
	1729	1811					
	1911	1955					
02	1203	1329					
	1554	1732					
	1801	1955					
03	1244	1423					
04	1130	1942					
05	1132	1416					
	1423	1845					
06	1214	1712					
	1740	1920					
09	1151	1450	1151.0F	1151.8	3	3GU	
	1456	1727	1153.4	1154.1	1	UNCLF	
	1844	1945	1414.9	1415.9	2	3GU	
			1550.4	1552.6	2	3GGU	
10	1156	1657					
	1723	1748					
	1805	1826					
	1855	1943					
11	1134	1845					
12	1137	1847					
13	1218	1406					
	1412	1700					
	1803	1941					
16	1203	1533					
	1603	1952					
17	1157	1429					
	1436	1643					
	1820	1958					

SOLAR RADIO EMISSION
SPECTRAL OBSERVATIONS (565-1000 MHZ)

AUG. 1973

	TIMES OF OBS. (UT)		BURSTS				
DATE	START	END	START (UT)	END (UT)	INT.	TYPE	REMARKS
18	1149	1845					
19	1151	1244					
	1254	1844					
20	1217	1247					
	1318	1449					
	1637	1925					
23	1156	1418					
	1450	1524					
	1550	1912					
	1842	1954					
24	1201	1454					
	1519	1535					
30	1213	1955	1503.5	1503.8	1	3G	
31	1204	1219					
	1225	1941					

SOLAR RADIO EMISSION
SPECTRAL OBSERVATIONS (565-1000 MHZ)

SEP. 1973

	TIMES OF OBS. (UT)		BURSTS				
DATE	START	END	START(UT)	END(UT)	INT.	TYPE	REMARKS
01	1204	1526					
	1747	1925					
02	1209	1219					
	1422	1535					
06	1215	1226					
	1346	1359					
	1422	1458					
	1622	1647					
	1746	1844					
	1930	1946					
07	1211	1320	1218.9	1223.4	2	3GG	
	1519	1937	1823.1	1823.3	1	UNCLF	
09	1217	1918					
10	1225	1443	1635.7	1635.7	2	3	
	1510	1748					
13	1215	1338					
	1341	1457					
	1615	1810					
	1818	1944					
14	1208	1423					
	1454	1938					
15	1206	1846					
16	1512	1727					
17	1217	1422					
	1502	1642					
	1657	1950					
20	1522	1638					
21	1206	1413					
	1442	1510					
	1601	2017					

SOLAR RADIO EMISSION
SPECTRAL OBSERVATIONS (565-1000 MHZ)

SEP. 1973

DATE	TIMES OF OBS. (UT) START	END	BURSTS START(UT)	END(UT)	INT.	TYPE	REMARKS
22	1216	1404					
	1424	1924					
23	1220	1919	1749.9	1750.0	2	3G	
24	1339	1425	1759.1	1759.2	1	3G	
	1451	1708					
	1730	1813					

SOLAR RADIO EMISSION
SPECTRAL OBSERVATIONS (565-1000 MHZ)

OCT. 1973

DATE	TIMES OF OBS. (UT) START	END	BURSTS START(UT)	END (UT)	INT.	TYPE	REMARKS
01	1242	1404					
05	1502	1846					
	1850	1946					
12	1224	1944	1450.8	1450.9	1	3	
13	1217	1927					
14	1216	1925					
15	1631	1755					
	1829	2000					
18	1251	1955					
19	1219	1332					
	1405	1930					
20	1227	1923					
21	1219	1830					
22	1243	1945					
25	1232	1318	1552.8	1553.0	1	3G	
	1352	1505					
	1540	1948					
26	1224	1447					
	1450	1945					
27	1224	1742	1550.0	1550.0	2	UNCLF	
			1555.5	1559.1	2	6GRS	
			1607	1633	2	4	
28	1227	1839					
	1845	1938					
	1950	2056					

SOLAR RADIO EMISSION
SPECTRAL OBSERVATIONS (565-1000 MHZ)

NOV. 1973

	TIMES OF OBS. (UT)		BURSTS				
DATE	START	END	START(UT)	END(UT)	INT.	TYPE	REMARKS
16	1308	1342					
	1408	1428					
	1511	1600					
17	1351	2023					
18	1308	1321					
	1324	1336					
19	1323	1639					
	1737	1838					
	1914	2026					
20	1333	1345					
	1405	1423					
	1708	1803					
	2014	2047					
24	1324	1351					
	1814	1847					
	1852	2020					
25	1303	1340					
27	1406	1914					
	1917	2106					
28	1431	2107					
29	1308	2031	1750.7	1750.7	1	3	
30	1305	1726					

ORIGINAL PAGE IS
OF POOR QUALITY

SOLAR RADIO EMISSION
SPECTRAL OBSERVATIONS (565-1000 MHZ)

DEC. 1973

	TIMES OF OBS. (UT)		BURSTS				
DATE	START	END	START(UT)	END(UT)	INT.	TYPE	REMARKS
01	1307	1916					
02	1318	2004					
03	1327	1602					
	1632	2040					
04	1319	1431	1349.0	1349.0	2	3	
	1623	2050	1949.6	1950.9	1	3G	
			1950.0	1950.1	1	3RS	
05	1323	1411					
	1424	1612					
	1620	1655					
	1745	1941					
	2008	2040					
06	1325	1714					
	1718	1930					
	2016	2046					
07	1305	2020					
08	1313	2015					
09	1332	2014					
10	1325	2030					
11	1330	1432					
12	1512	1545					
	1938	2110					
13	1318	1342					
	1521	1907					
	1910	2040					
14	1301	1600					
	1603	1734					
15	1258	1434					

SOLAR RADIO EMISSION
SPECTRAL OBSERVATIONS (565-1000 MHZ)

DEC. 1973

	TIMES OF OBS. (UT)		BURSTS				
DATE	START	END	START(UT)	END(UT)	INT.	TYPE	REMARKS
15	1820	2023					
16	1301	1411					
17	1619	1923					
	1927	2020					
18	1328	1949					
	2020	2048					
19	1322	1921					
20	1318	2030					
21	1314	1619					
	1624	1935					
22	1309	1922					
23	1303	1503					
	1542	1931					
24	1322	2110	1521.2	1521.3	3	3G	
26	1327	2050					
27	1715	2057					
28	1311	1906					
30	1335	1516					
	1553	2027					
31	1310	1540					
	1545	1600					
	1604	1959					

SOLAR RADIO EMISSION
SPECTRAL OBSERVATIONS (565-1000 MHZ)

JAN. 1974

	TIMES OF OBS. (UT)		BURSTS				
DATE	START	END	START(UT)	END(UT)	INT.	TYPE	REMARKS
01	1418	2122					
02	1343	2052					
03	1322	1908					
04	1316	1422					
	1432	1605					
	1620	1818					
	2009	2043					
05	1318	1945					
06	1330	2027					
07	1313	1935					
09	1429	1746					
10	1504	1957					
	2031	2046					
11	1319	1354					
	1449	1712					
	1716	1852					
12	1304	1822					
	1826	1947					
13	1311	1945					
14	1312	1726					
	1819	1942					
	2007	2040					
15	1307	1733					
	1759	1945					
17	1305	2100					
18	1304	1321					
	1935	2054					

SOLAR RADIO EMISSION
SPECTRAL OBSERVATIONS (565-1000 MHZ)

JAN. 1974

	TIMES OF OBS. (UT)		BURSTS				
DATE	START	END	START(UT)	END(UT)	INT.	TYPE	REMARKS
19	1312	1949					
20	1320	1606					
	1614	1929					
21	1307	1335					
	1341	1640					
	1648	1748					
	1829	1841					
	1859	1921					
22	1305	1800					
	1835	1900					
	1928	2048					
23	1344	1522					
	1526	1702					
	1712	1832					
	1929	1946					
	1950	2055					
24	1310	1340					
	1344	1425					
	1505	1538					
	1617	1800					
	1829	2053					
25	1316	1411					
	1417	1548					
	1702	1729					
	1758	2040					
26	1309	1937					
27	1305	1942					
28	1304	1738					
	1809	2029					
30	1417	1909					
	1912	2105					

SOLAR RADIO EMISSION
SPECTRAL OBSERVATIONS (565-1000 MHZ)

JAN. 1974

TIMES OF OBS. (UT)			BURSTS				
DATE	START	END	START(UT)	END(UT)	INT.	TYPE	REMARKS
31	1819	1956					

ORIGINAL PAGE IS
OF POOR QUALITY

SOLAR RADIO EMISSION
SPECTRAL OBSERVATIONS (565-1000 MHZ)

FEB. 1974

	TIMES OF OBS. (UT)		BURSTS				
DATE	START	END	START(UT)	END(UT)	INT.	TYPE	REMARKS
01	1303	1709					
	1812	2038					
02	1308	1552					
	1558	2033					
03	1324	2034					
04	1303	1733					
	1801	2029					
05	1302	1411					
	1428	1654					
	1729	1945					
	1849	2039					
06	1332	1439					
	1444	1628					
	1658	2039					
07	1305	1600					
	1628	2040					

NASA TMX-64882

APPROVAL

MSFC
SKYLAB GROUND-BASED ASTRONOMY PROGRAM

BY

B.J. Duncan

The information in this report has been reviewed for security classification. Review of any information concerning Department of Defense or Atomic Energy Commission programs has been made by the MSFC Security Classification Officer. This report, in its entirety, has been determined to be unclassified.

This document has also been reviewed and approved for technical accuracy.

W.C. Snoddy
Chief,
Astronomy and Solid State Physics Division

R. Ise 1/31/75
Manager,
Skylab Program Office

C.A. Lundquist
Director,
Space Sciences Laboratory

☆ U.S. GOVERMENT PRINTING OFFICE 1975–640-451/205 REGION NO. 4